

**Developing Pyrometric and Chemiluminescence Optical
Diagnostics for Investigation of Modern Alternative CI
Engine Combustion Strategies**

by

Mahdiar Khosravi

B.A.Sc., K.N.Toosi University of Technology, 2008

M.A.Sc., University of Tehran, 2011

A THESIS SUBMITTED IN PARTIAL FULFILLMENT
OF THE REQUIREMENTS FOR THE DEGREE OF

Doctor of Philosophy

in

THE FACULTY OF GRADUATE AND POSTDOCTORAL
STUDIES

(Mechanical Engineering)

The University of British Columbia

(Vancouver)

June 2019

© Mahdiar Khosravi, 2019

The following individuals certify that they have read, and recommend to the Faculty of Graduate and Postdoctoral Studies for acceptance, the dissertation entitled:

Developing Pyrometric and Chemiluminescence Optical Diagnostics for Investigation of Modern Alternative CI Engine Combustion Strategies

submitted by Mahdiar Khosravi in partial fulfillment of the requirements

for the degree of Doctor of Philosophy

in Mechanical Engineering

Examining Committee:

Patrick Kirchen, Mechanical Engineering

Supervisor

Kendal Bushe, Mechanical Engineering

Supervisory Committee Member

Martti Larmi, Mechanical Engineering

External Examiner

Xiaotao Bi, Chemical and Biological Engineering

University Examiner

Dana Grecov, Mechanical Engineering

University Examiner

Abstract

Its inherent economic and environmental advantages as a compression ignition (CI) engine fuel make natural gas (NG) an attractive alternative to diesel fuel. Limited optical studies of the NG combustion strategies have been reported in literature. The current work focused on developing optical characterization techniques to study in-cylinder processes in cleaner combustion strategies, such as those involving natural gas. An experimental facility supporting optical diagnostics via a Bowditch piston arrangement in a 2-litre, single-cylinder research engine was used in this study.

In order to facilitate quantitative soot analysis for low soot combustion strategies, the performance of the pyrometric method was improved by nearly 40% increase in the resolved signal fraction through modifications in numerical algorithm, calibration and implementation of the method, and image processing. The enhanced pyrometry method was implemented simultaneously with high-speed OH* chemiluminescence imaging to pilot-ignited direct-injected natural gas (PIDING) combustion for the first time. The results revealed that a standard PIDING operation can be characterized by low-sooting non-premixed combustion of the NG along the jet axes and of a partially-premixed charge at the wall region, followed by onset of detectable soot at the points of NG jet impingement on the bowl wall. This results in formation of a soot cloud adjacent to the wall, which then grows towards the center with continued soot formation and reflected momentum of the NG jets impinging on the bowl wall. The relative timing between NG injection pulse and peak HRR, and the P_{inj} , showed strong influence in the rate and extent of soot formation and peak concentration levels.

Rugged probe designs afford optical measurements from all-metal engines.

Comparisons between 2D and probe based 0D pyrometry measurements were made under optical engine configuration, for the first time, to better characterize the 0D probe signal. The 2D and 0D results showed reasonable agreements, especially when field-of-view geometry differences were taken into account. 0D two-color pyrometry measurements in an all-metal engine led to similar conclusions on soot in-cylinder processes, albeit with signs of enhanced late-cycle soot oxidation, attributed to the conventional omega shaped piston bowl geometry.

Lay Summary

The increasingly strict emission regulations for heavy-duty diesel truck engines have driven the development of new engine technologies towards reducing greenhouse gas and soot emissions. These technologies possess fundamentally different energy production and pollutant formation characteristics, and dedicated research to understand these phenomena is critical for optimization. High-speed imaging systems were developed to investigate the combustion processes inside an optical engine and improvements were identified to an optical diagnostic technique to facilitate its application for low-sooting combustion conditions. The method was implemented to a direct-injected diesel-natural gas combustion strategy to evaluate soot concentration and temperature distributions. Based on these results and other simultaneous diagnostics, a conceptual understanding of the soot processes and the influence of the operating parameters thereof was proposed. In addition, the developed imaging tools were used to characterize the signal from a rugged optical probe design, which can be implemented for optical measurements in less-idealized all-metal engines.

Preface

The original vision of this research work with regards to the implementation of two-color pyrometry to natural gas combustion strategies in compression ignitions, as well as the thermo-optical methodology was developed by my supervisor Dr. Patrick Kirchen. However, the direction I took with regards to the design of the simultaneous two-color pyrometry and OH* chemiluminescence imaging system, and analysis algorithms, were largely my own undertaking along with the implementation of the developed imaging tools to the PIDING combustion strategy in the optical engine.

Commissioning of the single-cylinder research engine facility was a collaborative effort involving several people. Jeremy Rochussen designed and commissioned the main mechanical, fuel, and safety systems for the Ricardo Proteus single-cylinder research engine. Jeff Yeo commissioned both the hardware and software associated with engine control and data acquisition systems. I was responsible for commissioning of the high-speed optical imaging systems.

Optical engine tests were a combined effort between Jeremy Rochussen, Jeff Yeo, and myself. I was solely responsible for the calibration of the pyrometric imaging system and post-processing of all high-speed imaging results, while Jeremy Rochussen and Jeff Yeo completed processing thermodynamic and probe data, respectively. Jeff Yeo wrote the scripts to process the probe data based on the developed imaging pyrometric algorithm, and I modified these to integrate them with the imaging results.

All data analysis presented in this thesis is my original work, with the exception of the routines used to process the thermodynamic results, including heat release rates and fuel mass flow rates, which was developed by Jeremy Rochussen.

Simultaneous natural luminosity and OH* chemiluminescence imaging analysis of DIDF combustion discussed in Chapter 4 of this work has been presented and published as part of the 2016 Combustion Institute Canadian Section Conference and 2016 ASME-Internal Combustion Engine Conference. The enhancement to the two-color pyrometry algorithm, described in Chapter 5 has been published at the Journal of Automobile Engineering (Proceedings of the Institution of Mechanical Engineers, Part D). The Pyrometric imaging investigation of soot processes PIDING combustion, presented in Chapter 6, was ready for submission at the time of writing this document. I was the lead author for these works and performed all written and analytical work, while received input and assistance from co-authors Jeremy Rochussen, Jeff Yeo, Dr. Patrick Kirchen, and Drs. Gordon McTaggart-Cowan and Ning Wu:

- M. Khosravi, J. Rochussen, J. Yeo, and P. Kirchen, “Characterization of Diesel-Ignited Dual-Fuel Combustion in an Optical Engine – Part I: Effects of Fueling Parameters on Flame Structure”, *Proceedings of the CICS Conference*, 2016.
- M. Khosravi, J. Rochussen, J. Yeo, P. Kirchen, G. McTaggart-Cowan, and N. Wu, “Effect of Fuelling Control Parameters on Combustion Characteristics of Diesel-Ignited Natural Gas Dual-Fuel Combustion in an Optical Engine”, *ASME-Internal Combustion Engine Division Fall Technical Conference*, 2016.
- M. Khosravi, P. Kirchen, “Refinement of the Two-Color Method for Application in a Direct Injection Diesel and Natural Gas Compression Ignition Engine”, *Proc. Inst. Mech. Eng. D J. Automob. Eng.*, 2019.
- M. Khosravi, P. Kirchen, “Pyrometric Imaging of Soot Processes in a Pilot Ignited Direct Injected Natural Gas Engine”, under review.

In addition to the works listed above I co-authored the following papers, where my contribution was primarily in the form of rebuilding the optical engine and running optical tests with Jeremy Rochussen and Jeff Yeo, as well as capturing and post-processing the imaging data:

- J. Rochussen, J. Yeo, M. Khosravi, P. Kirchen, “Investigation of Pilot-Ignited Dual-Fuel Natural Gas Combustion in an Optically Accessible Engine”, *Proceedings of the CICS Conference*, 2015.
- J. Rochussen, M. Khosravi, J. Yeo, P. Kirchen, “Characterization of Diesel-Ignited Dual-Fuel Combustion in an Optical Engine – Part II: Optical and Thermodynamic Comparison”, *Proceedings of the CICS Conference*, 2016.
- J. Yeo, M. Khosravi, J. Rochussen, P. Kirchen, “Application of an In-Cylinder Line of Sight Two-Colour Pyrometry Probe in an Optical Pilot-Ignited Direct Injection Natural Gas Engine”, *Proceedings of the CICS Conference*, 2017.
- J. Rochussen, J. Son, J. Yeo, M. Khosravi, P. Kirchen, G. McTaggart-Cowan, “Development of a Research-Oriented Cylinder Head with Modular Injector Mounting and Access for Multiple In-Cylinder Diagnostics”, *SAE International Conference on Engines & Vehicles*; 2017-24-0044, 2017.

Contents

Abstract	iii
Lay Summary	v
Preface	vi
Contents	ix
List of Tables	xiii
List of Figures	xv
List of Symbols	xxi
List of Abbreviations	xxii
Acknowledgements	xxiv
1 Introduction	1
1.1 Role of Optical Diagnostics in IC Engine Development	1
1.1.1 Optical Diagnostics	1
1.1.2 Diesel Engines	4
1.1.3 Alternative Fuels for CI engines	6
1.1.4 Air Pollution	8
1.1.5 Developing Technologies	11
1.2 Objectives, Contributions, and Approaches	12

2	Background Information and Literature Review	15
2.1	Optical Diagnostics for Combustion In-Cylinder Processes	15
2.1.1	Optical Access to the Combustion Chamber	16
2.1.2	Natural Luminosity Imaging	20
2.1.3	Chemiluminescence Imaging	21
2.1.4	Two-Color Pyrometry	26
2.2	Modern Alternative Combustion Strategies	36
2.2.1	DIDF	36
2.2.2	PIDING	40
2.3	Summary and Literature Gap	43
3	Experimental Setup	47
3.1	Engine	47
3.1.1	Engine Facility Instrumentation	49
3.2	Imaging Systems	52
3.2.1	Natural Luminosity Imaging	54
3.2.2	Two-Color Pyrometry Imaging	54
3.2.3	OH* Chemiluminescence Imaging	59
3.2.4	Spectral Optics	61
3.2.5	Optical Probe	63
3.3	Integrated System Operating Protocols	66
3.3.1	Synchronization of optical diagnostics with the engine	67
3.3.2	Alignment and Calibration	69
3.3.3	Optical engine operation	71
4	Optical Investigation of DIDF combustion	73
4.1	Analysis Metrics and Engine Operating Conditions	73
4.2	Results and Discussion	78
4.2.1	Effect of the Pilot Fuel Injection Pressure	78
4.2.2	Effect of the PR and ϕ_{CH_4}	83
4.2.3	Influence of Diesel and Natural Gas on Each Other in Dual-Fuel Combustion Charge	88
4.3	Summary and Conclusions	89

5	Two-Color Pyrometry Method Improvement	92
5.1	Method Enhancement	92
5.1.1	Algorithm Selection	93
5.1.2	Experimental Considerations	98
5.1.3	System Calibration and Image Processing	100
5.2	Sample Results	111
5.3	Summary and Conclusions	115
6	Optical Investigation of PIDING Combustion	117
6.1	Engine Operating Conditions and Analysis Metrics	117
6.1.1	Analysis Metrics	120
6.2	Results and Discussion	122
6.2.1	Baseline Operating Condition	123
6.2.2	Fuel mass (injection Duration) Effect	129
6.2.3	Relative Injection Timing Effect	133
6.2.4	Injection Pressure Effect	139
6.2.5	Updated Understanding of Soot Processes during PIDING Combustion	141
6.3	Concluding Remarks	162
7	Optical Probe Signal Characterization	165
7.1	2D vs. 0D two-color pyrometry measurements	166
7.1.1	The FOV effects	168
7.1.2	Weighted function averaging	170
7.2	Thermodynamic vs. optical engine configurations	177
7.3	Concluding Remarks	182
8	Conclusions and Future Work	184
8.1	Summary of the Significant Findings	184
8.1.1	Optical Investigation of DIDF combustion	185
8.1.2	Two-Color Pyrometry Method Improvement	186
8.1.3	Optical Investigation of PIDING Combustion	188
8.1.4	Thermo-Optical Analysis Tool-Kit	188
8.1.5	Concluding Remarks	191

8.2	Future Work	192
8.2.1	2D optical DIDF combustion analysis	192
8.2.2	2D optical PIDING combustion analysis	193
8.2.3	Exhaust Gas recirculation (EGR)	194
8.2.4	Optical probe OD signal characterization	194
8.2.5	Linking in-cylinder to engine-out soot measurements	196
	Bibliography	198
A	High-Speed Imaging System Considerations	215
B	Ensemble Averaging of Results vs. Raw signal	217
C	PIDING Fuel Injection Profile	219
D	Optical and Thermodynamic Ignition Delays	221
E	NG Jet Momentum Reflection Effects	223
F	Mean Soot Cloud Growth Rate	225
G	Ensemble Averaging of Results vs. Raw signal	226
H	Radiation Heat Loss through Quartz Window	228

List of Tables

Table 1.1	Euro standards for heavy-duty vehicles	11
Table 2.1	Formation pathways and characteristic wavelengths of major chemiluminescence sources in combustion of hydrocarbon fuels	22
Table 2.2	Summary of reported two-color pyrometry uncertainties	32
Table 3.1	Optical engine specifications	48
Table 3.2	Engine sensors used in combustion analysis.	49
Table 3.3	Optical Imaging Equipment	53
Table 3.4	Imaging Systems Assemblies	54
Table 4.1	Operating points for investigation of DIDF combustion	75
Table 4.2	Simultaneous OH* and NL imaging system setting for optical investigation of DIDF combustion	76
Table 4.3	Ignition delay and combustion duration.	87
Table 5.1	Performance of considered numerical algorithms	96
Table 5.2	Optical engine and imaging system specifications for two-color pyrometry.	99
Table 5.3	Operating parameters for diesel and PIDING combustion.	100
Table 6.1	Operating points for investigation of PIDING combustion	118
Table 6.2	Imaging system specifications	119
Table 7.1	Operating points discussed in Figure 7.3; RIT = 8 CAD, P_{inj} =180 bar, speed=1000 rpm for all points.	169

Table 7.2	Operating conditions investigated under thermodynamic and optical engine configurations using OD optical probe measurements; Engine speed was 1000 rpm for all points.	178
Table D.1	Comparison of optical and thermodynamic ignition delays for operating points described in Table 6.1	222

List of Figures

Figure 2.1	Schematic of a sample optical probe light collection diagram . . .	17
Figure 2.2	Schematic of a sample endoscopic light collection diagram . . .	18
Figure 2.3	Schematic and photo of the optical configuration of the engine	19
Figure 2.4	Shadow and NL images of a single spray flame in a constant volume combustion chamber	33
Figure 2.5	$f_v L$, HRR, NL, soot volume, and NL images for high-temperature diesel operating condition	34
Figure 2.6	Sample 2D two-color pyrometry results and the corresponding filtered NL images	36
Figure 2.7	OH*-chemiluminescence image sequences for high-load and low-load DIDF operation in an RCEM	39
Figure 2.8	OH*-chemiluminescence image sequences for low-load and high-load DIDF operation with constant pilot mass	40
Figure 2.9	Combined 15-cycle ensemble averaged 2D images of OH* chemiluminescence and NL from PIDING combustion	42
Figure 3.1	Experimental facility process and instrumentation diagram for PIDING combustion experiments under optical configuration.	51
Figure 3.2	Ricardo Proteus engine schematic and imaging system setup on the optical engine	52
Figure 3.3	Image doubler design and two-color pyrometry system schematic.	55
Figure 3.4	Chemiluminescence Imaging system setup	56
Figure 3.5	The two-color pyrometry calibration setup	57
Figure 3.6	Response calibration with camera exposure vs. ND filters . . .	59

Figure 3.7	Chemiluminescence Imaging system setup	61
Figure 3.8	Transmission curves from the various optical filters used in this work	63
Figure 3.9	The engine head design for multiple in-cylinder diagnostics	64
Figure 3.10	Optical probe design used in this work	65
Figure 3.11	Optical probe assembly	66
Figure 3.12	Optical probe calibration system.	66
Figure 3.13	Simplified wiring diagram of the integrated optical systems.	69
Figure 3.14	Adjustable optical table design	70
Figure 3.15	Standard optical engine operation skip-firing scheme	71
Figure 3.16	Optical measurements protocol flowchart.	72
Figure 4.1	Schematic of the simultaneous OH* and NL imaging system used for optical investigation of DIDF combustion.	77
Figure 4.2	Sample image series of ensemble averaged NL and OH* chemiluminescence	79
Figure 4.3	Overlaid ensemble averaged OH* chemiluminescence and natural luminosity images	80
Figure 4.4	Overlaid ensemble averaged OH* chemiluminescence and natural luminosity images for dual fuel operating points	81
Figure 4.5	Conceptual effect of pilot fuel injection pressure on reaction zone growth mechanism on DF combustion mode	82
Figure 4.6	Comparison of spatially averaged NL, OH* chemiluminescence, and HRR results	85
Figure 4.7	OH* Chemiluminescence at the maximum bowl coverage.	86
Figure 4.8	Reaction zones in dual-fuel and diesel-only combustion	89
Figure 5.1	Soot cloud spectral emissivity vs. KL factor	94
Figure 5.2	Residual error behavior around the root of two-color pyrometry equation	94
Figure 5.3	Algorithm performance comparison and residual profile	97
Figure 5.4	Apparent temperature ratios map	98

Figure 5.5	Two-color pyrometry imaging system implementation on the optical engine.	99
Figure 5.6	Work flow to obtain temperature and <i>KL</i> distributions from recorded raw signal.	101
Figure 5.7	Influence of linearized extrapolation on two-color pyrometry results	103
Figure 5.8	Effect of spatial non-uniformities imaging system response . .	104
Figure 5.9	Increase in detection envelope by the imaging system dynamic range with matching aperture response.	105
Figure 5.10	Parallax calibration target images	106
Figure 5.11	Impact of static and dynamic parallax corrections to increase resolved pyrometric signal at different crank positions	107
Figure 5.12	Comparison of pixel binning and filtering on calculated temperature fields	109
Figure 5.13	Effects of individual and combined corrections on the resolved image data for the diesel operating mode	110
Figure 5.14	Temperature and <i>KL</i> distributions for diesel combustion using proposed refinements	112
Figure 5.15	Temperature and <i>KL</i> distributions for PIDING combustion using proposed refinements	113
Figure 5.16	Effects of individual and combined corrections on the resolved image data for PIDING combustion	114
Figure 6.1	Simultaneous two-color pyrometry and OH* chemiluminescence imaging system	120
Figure 6.2	Net soot formation and oxidation for baseline PIDING operating point	121
Figure 6.3	Baseline PIDING operating point; Ignition and early stage combustion	123
Figure 6.4	Baseline PIDING operating point; NG combustion and soot formation and oxidation	126

Figure 6.5	Area fraction distribution of two-color pyrometry soot temperatures and <i>KL</i> factors at each crank position for the baseline operating condition	128
Figure 6.6	Aggregate resolved temperature and <i>KL</i> factor cumulative distribution for the baseline operating condition after 10 CAD aTDC	129
Figure 6.7	NG fuel mass effects at constant injection pressure; 2D OH* chemiluminescence and two-color pyrometry results	130
Figure 6.8	NG fuel mass effects at constant injection pressure; Spatially averaged imaging and thermodynamic results	131
Figure 6.9	NG fuel mass effects at constant injection pressure; Two-color pyrometry soot temperature and <i>KL</i> factor area fraction coverage	132
Figure 6.10	Relative injection timing effect; 2D OH* chemiluminescence and two-color pyrometry results	134
Figure 6.11	Relative injection timing effect; Spatially averaged imaging and thermodynamic results	135
Figure 6.12	Relative injection timing effect on pilot combustion	136
Figure 6.13	High temporal resolution 2D OH* chemiluminescence and two-color pyrometry results for pilot combustion at RIT=2 CAD	136
Figure 6.14	Relative injection timing effects; Two-color pyrometry soot temperature and <i>KL</i> factor area fraction coverage	137
Figure 6.15	Fuel injection pressure effect; 2D OH* chemiluminescence and two-color pyrometry results	138
Figure 6.16	Fuel injection pressure effect; Spatially averaged imaging and thermodynamic results	140
Figure 6.17	Fuel injection pressure effects; Two-color pyrometry soot temperature and <i>KL</i> factor area fraction coverage	141
Figure 6.18	HRR and OH* chemiluminescence images of combustion reaction zones through a typical PIDING combustion event	143
Figure 6.19	Correlation between the peak HRR and detected onset of soot signal	144
Figure 6.20	Correlation between peak <i>KL</i> factor and NG EOI	145
Figure 6.21	Radial <i>KL</i> factor distribution time series for GPW=1.85 ms and P_{inj} = 140 bar operating conditions	148

Figure 6.22	Normalized net soot formation rates for GPW and P_{inj} sweeps	150
Figure 6.23	The influence of P_{inj} sweep on mean soot cloud growth rate	151
Figure 6.24	The effect of relative timing between onset of soot signal and cGSOI	153
Figure 6.25	The influence of considered parameter sweeps on mean net soot formation rates	155
Figure 6.26	Soot processes during a typical PIDING combustion event	157
Figure 6.27	Baseline PIDING vs. Diesel combustion; 2D imagin results	159
Figure 6.28	Aggregate resolved temperature and KL factor cumulative distribution for baseline PIDING and conventional diesel operating conditions	160
Figure 7.1	2D and 0D Two-color pyrometry measurement system on optical engine configuration.	166
Figure 7.2	Line-of-sight measurement effects in a partially transparent soot cloud	167
Figure 7.3	0D probe vs. mean 2D two-color pyrometry results	169
Figure 7.4	Generation of the weighted spatially averaged ROI for 2D two-color pyrometry	171
Figure 7.5	WSA ROI mask at three crank positions and the corresponding optical probe cone projection cross-sections	172
Figure 7.6	0D probe vs. WSA 2D two-color pyrometry results	174
Figure 7.7	Probe FOV geometry effect on WSA results	175
Figure 7.8	Two-color pyrometry temperature and KL factor population maps for the baseline operating condition at 5 and 8 CAD aTDC.	176
Figure 7.9	0D probe vs. WSA 2D two-color pyrometry results, and their corresponding apparent temperatures and 2D KL factor results vs. probe FOV coverage during soot oxidation stage in the baseline operating point	177
Figure 7.10	0D probe two-color pyrometry and HRR results for the baseline operating condition under optical and thermodynamic engine configurations	179

Figure 7.11	0D probe two-color pyrometry and HRR results for $P_{inj}=220$ bar, $P_{inj}=140$ bar, and long RIT operating conditions under optical and thermodynamic engine configurations	181
Figure 8.1	2D and 0D natural luminosity/two-color pyrometry and OH* chemiluminescence measurement system on optical engine configuration.	185
Figure 8.2	Conceptual effect of pilot fuel injection pressure on reaction zone growth mechanism on DF combustion mode	186
Figure 8.3	Two-color pyrometry method enhanced performance depicted as improvements in the resolved signal fraction throughout the ensemble averaged cycle and at a sample crank position for PIDING combustion	187
Figure 8.4	The four principal stages of soot processes during a typical PIDING combustion event	189
Figure 8.5	WSA mask at 25 CAD aTDC and comparison of the WSA 2D and 0D optical measurements for select operating points . . .	190
Figure B.1	Effect of ensemble averaging on the two-color pyrometry temperature distributions instead of using it as a SNR enhancement approach for the raw data	218
Figure C.1	Estimated PIDING fuel injection profile	220
Figure E.1	Soot cloud advection effects with reflected NG jet momentum after impingement onto the walls	224
Figure F.1	The influence of P_{inj} on 2D two-color pyrometry temperature distribution	225
Figure G.1	Alternative WSA procedures flowchart	227
Figure G.2	Alternative WSA procedures; sample results	227
Figure H.1	A simplified radiation heat loss model for comparison of the two engine configurations	228

List of Symbols

A_λ	soot volume fraction optical constant
α	Hottel & Broughton empirical soot constant
C_2	Diatomic carbon
CA_{50}	Crank angle corresponding to 50% heat release
C_6H_6	Benzene
CH	Methylidyne
CH_4	Methane
CHO	Formyl radical
CH_2O	Formaldehyde radical
CO	Carbon monoxide
CO_2	Carbon dioxide
CN	Cyanido radical
E_{input}	Total fuel energy input
f_v	Soot volume fraction
h	Planck's constant
$I\eta_{th}$	Indicated thermal efficiency
I_λ	Spectral radiant intensity
K	Absorption strength of the soot cloud
κ_λ	Absorption coefficient
L	Characteristic optical path length
λ	Wavelength
m_{diesel}	Diesel mass flow rate
NO_x	Nitrogen oxides
OH	Hydroxyl radical
OH^*	Electronically excited hydroxyl radical
OH^*-CL	OH^* Chemiluminescence
P_{inj}	fuel injection pressure
T_a	Apparent soot temperature
ϕ_{CH_4}	Methane equivalence ratio
ϕ_{global}	Global equivalence ratio
Θ_{Soot}	Onset of soot signal
$\tau_{ign,NG}$	NG optical ignition delay
$\tau_{ign,pi}$	Pilot optical ignition delay
τ_{Soot}	Onset of soot signal delay

List of Abbreviations

AFR	Air-Fuel-Ratio
aTDC	after Top Dead Centre
bTDC	before Top Dead Centre
CAD	Crank Angle Degree
CCD	Charged Couple Device
CHTS	Cumulative Histogram Time Series
CI	Compression Ignition
CMOS	Complementary Metal Oxide Sensor
cGSOI	command of Gas Start of Injection
cPSOI	command of Pilot Start of Injection
cSOI	command of Start of Injection
CR	Compression Ratio
CRP	Color-ratio pyrometry
CWL	Central Wavelength
DAQ	Data Acquisition
DRP	Diesel Rail Pressure
DIDF	Direct Injection Dual-Fuel
DISI	Direct Injection Spark-Ignited
ECU	Engine Control Unit
EGR	Exhaust gas recirculation
EOI	End of Injection
FOV	Field-of-View
FPGA	Field-Programmable Gate Array
fps	frames-per-second
FWHM	Full Width Half Maximum
GIMEP	Gross Mean Effective Pressure
GPW	Gas Pulse Width
HPDI	High Pressure Direct Injection
HRR	Heat Release Rate
HTC	high-temperature combustion
IC	Internal Combustion
IR	Infrared
IRO	Intensified relay optics
LHV	Lower Heating Value
LII	Light Induced Incandescence
LIF	Light Induced Fluorescence
LOS	Line of Sight
LTC	Low Temperature Combustion

NBP	Narrow Band-Pass
ND	Neutral Density
NIR	Near Infrared
NL	Natural Luminosity
NG	Natural Gas
OD	Optical Density
PIV	Particle Image Velocimetry
PIDING	Pilot-Ignited Direct-Injected Natural Gas
PR	Pilot Ratio
RIT	Relative Injection Timing
PM	Particulate matter
RCEM	Rapid Compression/Expansion Machine
SI	Spark Ignited
SNR	Signal to Noise Ratio
SOI	Start of Injection
TDC	Top Dead Center
tHC	Total Hydrocarbon
TTL	Transistor-Transistor Logic
uHC	Unburned Hydrocarbons
UV	Ultra-Violet
VOC	Volatile Organic Compounds
WSA	Weighted Spatially Averaging

Acknowledgements

The presented work would not have been possible without the financial support from Westport Fuel Systems and collaboration of its resourceful personnel, in particular Dr. Sandeep Munshi for his technical insight and encouraging remarks, Dr. James Saunders for sharing his experience in setting up an optical imaging setup, Dr. Gordon McTaggart-Cowan for his consistent involvement in progression of the work through our monthly meetings, and others including Drs. Ashish Singh, Ning Wu, and Jim Huang. In addition, I would like to acknowledge further financial support provided by the Natural Sciences and Engineering Research Council of Canada (NSERC) Collaborative Research and Development (CRD), the Canadian Foundation for Innovation (CFI), John Evans Leaders Fund (JELF), and the NSERC Discovery Grant Program. I would also like to thank Dr. Steven Rogak, whose scientific and engineering experience I always benefited from during our recurrent group meetings. I am also grateful to Oliver Terry for the design and fabrication of the optical table and to Bob Parry for his technical support.

I would like to express my most sincere gratitude to Dr. Patrick Kirchen, my supervisor, whose unfaltering oversight, mentorship, and evident passion for research was undoubtedly a principal driving force throughout my research. I could often perceive him also as a colleague when he would join us in late evening hunts for source of issues in the test cell, or spend hours discussing possible explanations for the perplexing problems.

Of the pleasant memories I will keep from my days at UBC for the rest of my life, are moments spent with my friends, in sharing happiness and laugh as well as in frustration and cursing programming scripts or equipment. Among these, I had the honor of being lab mates and working on the same test facility with

Jeremy Rochussen, Jeff Yeo, and Pooyan Kheirkhah, whose help and support I infinitely appreciate and find hard to be able to equally return. I would also like to thank David Sommer, Rene Zepeda, Aditya Prakash-Singh, Michael Karpinski-Leydier, Jeff Son, Jeff Meiklejohn, and Miayan Yeremi, my other colleagues at Clean Energy Research Center.

Finally, I would like to thank my family for everything they have made possible for me to achieve to this date, especially my mother, to whom I will always remain in debt for the sacrifices she made, and my beloved wife, Banafsheh, to whom I owe my prevailed sanity throughout my research, joy of today, and hope for a brighter future.

I dedicate this thesis to my mother and my wife, for everything I have...

Chapter 1

Introduction

The motivation for the presented work is elucidated in this chapter. The pressing need to further limit internal combustion (IC) engine emissions through modern alternative combustion strategies is discussed and a brief history around application of optical diagnostics for combustion in-cylinder soot characterization is presented. The major objectives of the current work and an overview of the approaches adapted to achieve those objectives are subsequently discussed.

1.1 Role of Optical Diagnostics in IC Engine Development

The major focus of the work presented herein was developing and implementing optical diagnostic tools to better understand combustion processes in reciprocating engines. As such, in what follows a brief overview of the application of optical diagnostics in engines is provided, along with some general background information regarding these applications. This is followed by an overview of compression engine operating strategies, with a focus on the associated pollutant emissions and the health and environmental effects thereof.

1.1.1 Optical Diagnostics

The scientific and technological advancements in imaging applications and manufacturing imaging systems have both come a long way since the earliest surviving

recording of an image in mid-1820s, where many hours or even days of exposure in the camera were required to successfully record the image of a bright landscape. Improvements of the optical diagnostic tools ever since has led to breakthroughs in health and cognitive sciences, with the likes of magnetic resonance imaging (MRI) and various computed tomography (CT) scan techniques and shaped our understanding of the universe through the likes of NASA's Great Observatories program series of telescopes (Hubble, Compton, Chandra, and Spitzer) and ESA's largest ever launched Herschel infrared telescope. Today, optical diagnostics has become an indispensable component of modern non-intrusive and nondestructive test methods and inspection techniques. Optical techniques play an extremely important role in wide variety of research and industrial applications, such as biomedical and biomechanical research, military applications and forensics, ballistics, astronomy, industrial inspection, analytical chemistry, fluid dynamics, and combustion.

The extensively developed optical techniques are today applied to institutional internal combustion engine development. On the research level, these methods aim at understanding the combustion event itself. These investigations can be outside the engine with various bench-top flame structures and geometries, inside constant volume chambers simulating the engine in-cylinder conditions, or actual in-situ optical measurements of combustion in an engine that offers optical access to the in-cylinder combustion processes. These analyses are often accompanied with reactive computational fluid dynamics simulations to compare and verify the findings and consolidate the method development tools. The developed methods and provided insights then lead to combustion system developments and new operation strategies, where certain component performance effects are investigated under the constraints of approaching more realistic and optimized final engine operating modes. These methods closely analyze a wide range of combustion in-cylinder phenomena, including but not limited to, flame kernel formation and flame propagation in spark ignited (SI) engines; diffusion flame formation, flame-wall interactions, and soot temperature and concentration in compression ignition (CI) engine; fuel spray propagation, droplet size, species concentration and temperature; and flow field velocity distribution.

Optical methods can be divided into major categories of 1: The passive techniques relying on the natural or spontaneous light emission from the source species

(no external light source) and 2: techniques focusing on the interactions between the species under investigation and an external light source illuminating these target species. These interactions can result in stimulated light emission from the targeted species or alterations in the illuminated light in the form of absorption, scattering, partial transmission, refraction, and interference.

Natural emission of light from combustion of hydrocarbon fuels can be divided into two categories of thermal radiation and spontaneous light emission. The solid soot particles, formed as a result of incomplete combustion of the hydrocarbon fuel and suspended in the high temperature flame emits a spectrum electromagnetic radiations. At combustion temperatures of typically much higher than the Draper's point threshold (~ 798 K), soot particles emit significant thermal radiation in the visible spectrum, referred to as incandescence. Spontaneous light emission stems in the quantum mechanics view of the light emission mechanisms and refers to the process during which a quantum in the form of a photon is released as a result of the transition of a quantum mechanical system (certain gaseous species within the flame in this case) from an excited energy state to a lower energy state, referred to as the ground energy state. In the case of combustion of hydrocarbon fuels, majority of spontaneous light emission comes from the molecular emissions from the diatomic carbon (C_2) radicals at a number of excited vibrational states in the visible spectrum, forming the Swan band [66], and weaker broadband emissions of CO_2^* radicals [50]. This phenomena is responsible for the blue flame associated with the more complete combustion of a hydrocarbon fuel. A more detailed discussion of combustion spontaneous light emission sources and the optical investigations thereof is presented in the next chapter.

A wide variety of optical diagnostic techniques rely on application of an external light source and investigation of the interactions the light rays make with certain species among the reactants, intermediate products, or final products and byproducts of the combustion process. Characteristics of such external sources are selected and designed depending on the physics of the process under investigation. This class of optical investigation can be as simple as illuminating the combustion chamber with a generic broadband white light source to visualize the injection process of the liquid diesel fuel through Mie scattering or require sophisticated and costly design and intricate post-processing such as in Coherent anti-Stokes Raman

spectroscopy temperature measurements for in-cylinder thermal boundary layer investigations [48].

From a different perspective, optical diagnostic techniques can be divided into qualitative and quantitative methods. Qualitative methods present valuable information such as the general shape of the flame kernel or diffusion flame formation, interactions with the walls, propagation of the liquid fuel spray, and relative distribution of signal intensities from various species. However, description of soot particles and gaseous species temperature and concentration distribution and the effects of wall impingement on these distributions, and droplet size and flow field velocity distributions are only possible through application of the quantitative methods. The latter measurement category, however, requires a calibrated or characterized light source specific to the technique under consideration, or a reference beam and/or higher fidelity combustion chamber illuminating system. These in-cylinder diagnostic techniques can also be categorized based on the geometry of the optical access provided into the combustion chamber. Creating a large access, in the order of the combustion chamber boundaries geometry (through the piston or walls), offers substantial depth of information and valuable insight into the in-cylinder processes, albeit at the expense significant geometric modifications and operational restrictions. Alternatively, a very small optical access can be introduced without major modifications to the engine design and alterations in standard operating conditions. Although this eliminates the challenges and restrictions of a large optical access, the information that could be extracted would be limited and lack spatial attributes. These two design approaches to optically access the combustion chamber were both utilized in this work; the large optical access is provided in the “optical engine configuration”, allowing 2D optical measurements, and the small optical access, leading to 0D measurements, can be implemented in the more realistic “thermodynamic engine configuration”. More details about these two designs is provided in §2.1.1.

1.1.2 Diesel Engines

In a similar way the invention of steam engines powered the industrial revolution, the compression ignition (CI) engine is regarded as a piece of technology that has

transformed the modern world and has been the driving force behind the globalization of today's economy. When fuelled with liquid diesel, CI engine approximately follows the thermodynamic Diesel cycle and presents many attractive characteristics. These systems are very robust and reliable, very versatile, more efficient than gasoline fuel engines, and deliver high torques at low speeds [20]. Vast majority of world's commercial, industrial, agricultural, and military machinery and vehicles are powered by CI engines burning diesel fuel (diesel engines).

When it was invented in 1890s, diesel engine was the most efficient heat engine ever made with nearly 20% higher efficiency than the gasoline engines and the prevalent labour-intensive steam engines. Soon, together with gasoline engines, they started to replace steam engines in mills and factories. During the first world war and European nations striving for improved submarine designs, the higher reliability of diesel engines was well recognized. After the world war, with innovations by Harry Ricardo, specifically the comet swirl chamber design and indirect diesel injection fuel delivery mechanism, diesel engines started to become the primary energy generation source for heavy-duty trucks, buses, trains, and the global sea trades transportation. Also, they proved to be a reliable source for stationary power generation in remote areas and emergency situations. During 1970s diesel engines won the race with gasoline engines on all forms of land transportation except for the important category of light-duty vehicles. During the same decade, the oil crisis in middle east and skyrocketed gasoline prices, became a motivation for improving diesel engines further so that they can compete with the higher performance gasoline engines. This led to the first direct injected diesel engine manufactured by Delphi. It was a turning point for diesel engine design and with further improvements of the direct injection process and introduction of high pressure common rails, today nearly half of the new light-duty vehicles in Europe are using diesel engines. Furthermore, the marine applications is perhaps where diesel engines have demonstrated their highest impact on modern global economy. Today's world intercontinental global trade depends on ocean transport to move billions of tones of resources every year, where marine diesel engines produce efficiencies of over 50%. Measured by the distance that goods have to travel from the manufacturing or collection source to the retail, more than 90% of the global trade is diesel powered making it the most indispensable engines of our era.

1.1.3 Alternative Fuels for CI engines

Diesel engines originally operated on peanut oil, but through early experiments a specific type of heavy hydro-carbon fuel, later called the Diesel fuel, became the standard fuel for the CI engine. This fuel was cheaper to refine from crude oil than gasoline, and it was less volatile and less likely to cause explosions. However, there are two major concerns associated with using conventional diesel fuel in the conventional diesel engine designs. First, heavily relying on this diminishing category of fossil fuels raises the concerns from the viewpoint of power generation stability policies. Despite the continuing percentage drop in oil products consumption since the beginning of the 21st century, it still constitutes the largest share in the global primary energy consumption at nearly 35%, followed by coal at 27%, primarily used in electricity generation sector. Furthermore, the average global oil production and consumption in 2017 both reached positive rates of 0.6 and 1.8%, respectively [49]. Secondly, and perhaps more importantly, these systems produce different levels of various air pollutants. Production of less greenhouse gas emissions in diesel engines compared to other in-use fossil fuel based power sources, as a result of their higher efficiency, has been a significant advantage from the environmental impacts point of view. However, these engines were soon realized to produce other unpleasant emissions due to the higher levels of sulfates and nitrates in the less refined long-carbon-chain diesel fuel and fundamental principles of CI engine operation. Common pollutants emitted from diesel engines are particulate matter (PM), nitrogen oxides (NO_x), unburned hydrocarbons (uHC), and carbon monoxide (CO), as well as toxics such as benzene (C₆H₆) and formaldehyde (CH₂O) in the form of volatile organic compounds (VOCs), which are significantly higher for diesel fuel combustion compared to other in-use transportation motive power sources [35, 97]. These emissions pose serious and complex risks to environment and have proven carcinogenic and dramatic respiratory system and cardiovascular health effects, leading to serious respiratory tract diseases such as bronchitis, pneumonia, asthma. Thus, they are all regulated in various emission standards, including US EPA, European Commission, and also regulations introduced by Environment Canada under the Canadian Environmental Protection Act, 1999 (CEPA 1999), to minimize the risks and undesirable consequences.

One feasible alternative fossil fuel that can diminish the two major concerns regarding the use of conventional diesel fuels in CI engines is natural gas (NG) [70]. It has lower NO_x emissions than diesel and gasoline as a result of burning at lower temperatures (having lower adiabatic flame temperatures). In addition, its low carbon-to-energy ratio combustion produces lower CO_2 emissions and less polycyclic aromatic hydrocarbon (PAH) and solid carbon (soot) and less PM is emitted [152]. Nevertheless, in comparison with diesel fuel, natural gas less readily self-ignites at standard pressures and temperatures and forced ignition systems are deemed necessary. The ignition system can be a spark plug, a glow plug as a hot surface, or a dual-fuel pilot ignition mechanism [1, 10, 13, 102, 116, 163]. In addition, plasma assisted and corona discharge ignition techniques are receiving more attention over the last few years [15, 138, 150]. Also in gasoline IC engines, inherent advantages of natural gas over gasoline fuel prompted its consideration as an alternative fuel [70]. Compared to gasoline fuel, it has higher Lower Heating Value (LHV) and stoichiometric air-fuel-ratio (AFR) its higher octane number allows higher compression ratios and, hence, higher efficiencies and boost in turbocharged engines, and lower knock sensitivity [19]. Nevertheless, air displacement by NG, slower flame propagation speed, and poor lean-burn capability of NG in gasoline engines result in performance loss, lower heat release rates and engine power output, and increase in the fuel consumption and, therefore, its implementation in these engines continue to be subject to research and improvement [19, 21].

Conventional diesel-ignited dual-fuel (DIDF) combustion strategy in CI engines ignites a compressed lean premixed homogeneous charge of air and natural gas by late cycle direct injection of pilot fuel. It produces efficiencies and brake mean effective pressures comparable to that of conventional diesel engines while emitting much less NO_x and PM. However, these systems have some drawbacks including high CO and unburned CH_4 emissions and some challenges associated with fuel efficiencies at light-load operation [153]. Furthermore, at high load operating conditions the premixed combustion of this homogeneous charge results in high cylinder pressure rise rates and engine knock [80], which can have undesirable consequences such as engine damage and excessive noise, and therefore restricts the operation limits of DIDF combustion compared to conventional CI combustion strategies.

Pilot-Ignited Direct-Injected Natural Gas (PIDING) combustion strategy is a more modern dual-fuel pilot ignition mechanism for natural gas, which was introduced by Westport Fuel Systems [112]. In this combustion strategy, typically a small amount of pilot diesel fuel is injected and self-ignite by the time the subsequent late cycle direct injection of natural gas happens and therefore acts as the forced ignition mechanism in the form of a number of combusted kernels. The direct injected natural gas in this case can be converted via a mixing controlled flame, depending on its injection timing, at locations close to the injector, similar to conventional diesel engines. The phasing of NG and pilot diesel injection can change in this method. This late cycle, direct injection approach resolves the high CO and CH₄ emission problem, harmful excessive pressure rise rates, and engine knock attributed to conventional dual fuel engines.

1.1.4 Air Pollution

Anthropogenic emissions of unregulated air pollutants has marked a number of catastrophes in human history. The most prominent example is certainly the great smog of London (the pea soup fog) in 1952 with 4000 casualties as the direct result of the smog and another nearly 6000 over the following months as a result of the incident [11]. Similar, not as deadly smogs formed in Kansai in Japan (1960s), Pennsylvania (1948) and California in US, where it has been a continuing challenge since its first reported dangerously high smog level (1943), and most recently Delhi in India (2016). The major culprits of smog formation are airborne particulate matter, sulphur dioxide, carbon monoxide, NO_x, VOCs, and unburned hydrocarbons, often aggravated by geographical properties of the region and atmospheric events such as temperature inversion.

The concurrent presence of sufficient concentrations of NO_x and VOCs in the atmosphere, with enough UV radiation energy from the sun, favors a photochemical reaction which yields airborne particles and ground-level ozone. Later another pathway from NO_x to ozone was found that predominantly occurs in coastal areas via formation of nitryl chloride when NO_x comes into contact with salt mist [120]. Through another chemical reaction, sulphur dioxide and nitrogen oxide react with the water molecules in the atmosphere to produce acids, lowering the PH in the

smog. Road transport is the largest contributor to urban NO_x emissions worldwide with approximately 40%, nearly double the share from the next big source, energy production and distribution sector. Diesel engines are responsible for about 85% of this share, primarily in the form of NO, which typically constitutes 85–95% of the total NO_x . With time, the colorless and odorless NO gradually converts to NO_2 , which is a brown-reddish gas with a pungent odor at normal temperatures and has a five times greater toxicity level [22, 56, 86, 151].

Particulate matter emission from coal and diesel power sources played a major role in the smog formation incidents and later realized to have significant health effects even at much lower concentrations. Particulate matter (PM) is the term used to refer to any airborne solid and liquid particulates. These particles can be directly emitted from a source or as a result of chemical reactions between certain gaseous species in the atmosphere. PM emission can be naturogenic or anthropogenic, it can comprise a wide variety of species, and its particle sizes vary depending on the circumstances under which they are formed. An aerodynamic or effective diameter is the typical metric to describe particle sizes. Coarse particles with a diameter greater than $2.5 \mu\text{m}$ have relatively high settling velocities and settle out of atmosphere in a matter of Hours or days. As the particles diameter decreases the settling velocity decreases. Ultrafine particles (sub 100 nm diameter) tend to agglomerate and form larger particles in the range of 0.1 to $1.0 \mu\text{m}$, which have low settling velocities and very long residence time [134]. PM emissions originating from combustion processes, such as in diesel engines, have size distributions within this range and lower, either directly as products or through condensation of VOCs in the exhaust stream [97, 132]. Diesel engine PM emission consists of three major components: soot, soluble organic fraction (SOF), and inorganic fraction (IF). Engine out soot, the amorphous black carbon shaped into a porous agglomerate structure through a complicated formation path, constitutes nearly 50 % of the total PM emissions. SOF consists of adsorbed or condensed heavy hydrocarbons on the soot surface, originating from the lubricating oil, uHC, and other byproduct of the combustion process [132, 144].

All of the compounds mentioned above have proven negative environmental and health effects. NO_2 exposures can lead to irritation in the lungs and affect respiratory tact immunity to infections such as influenza [56, 134]. The odorless

and colorless CO, when inhaled, binds to hemoglobin in bloodstream and inhibits its capacity to transfer oxygen. Depending on the concentration, this can cause impaired concentration, slow reflexes, dizziness, and ultimately asphyxiation leading to unconsciousness or death [149]. Ozone is a powerful oxidant that decreases lung function and produces toxic signals when reacts with the proteins and lipids within lung lining fluid compartment and, leading to inflammation and ultimately damage in pulmonary cells [103]. PM emissions have been the subject of numerous epidemiological studies and have shown strong correlations with impaired lung development, respiratory system irritation, cancers due to adsorbed or condensed VOCs such as benzene and formaldehyde, and overall increased cardiovascular and pulmonary system failure [31, 97]. Studies show that coarse particulates are unlikely to penetrate into the lungs and peak deposition occurs for particulates in the range of 0.01 to 0.1 μm . These smaller particles are also more likely to find their way to the bloodstream and a greater negative effect on the cardiovascular system [97]. Examination of diesel engine particulate diameters shows 90% of the size distribution below 1 μm [132]. There are also a variety of negative environmental effects associated with PM emissions, such as pollution of water and soil, soiling of buildings, reductions in visibility and agriculture productivity, and global climate change [35, 43].

Following the early high mortality incidents of dangerously high air pollutant levels, the Clean Air Act (CAA) legislation was enacted in UK in 1956 and US in 1963, followed by similar regulations in many other countries to avoid future occurrences of such incidents. Although the original regulations successfully prevented such severe cases, epidemiological studies later showed that exposures to pollutant levels much lower than those originally considered in the clean-air act regulations closely correlated to increased cases of serious health conditions and premature death [31, 35, 56]. As a result of these investigations and in response to the more in-depth understanding of the adverse effects of various emissions from heavy-duty vehicles governments have been consistently introducing more stringent regulations on permissible exhaust emission. This has been in the form of Euro I-VI standards by European Commission and Tier 1 to 3 EPA federal regulations in US, which has also adopted more strict regulation for the light-emission vehicle (LEV I-III), legislated by Air Resources Board in California (CARB) given

their continuous battle with higher air pollutant levels. Canada also closely aligns its emissions regulations with those of EPA's. As an example of evolution of these regulations over time, Table 1.1 shows European Union's Euro standards on four of the major emissions from the heavy-duty diesel engines [110].

Table 1.1: Euro standards for heavy-duty vehicles

	CO	uHC	NO _x	PM
	[g/kWh]	[g/kWh]	[g/kWh]	[g/kWh]
Euro I	4.5	1.1	8.0	0.61
Euro II	4	1.1	7.0	0.15
Euro III	2.1	0.66	5.0	0.13
Euro IV	1.5	0.46	3.5	0.02
Euro V	1.5	0.46	2.0	0.02
Euro VI	1.5	0.13	0.4	0.01

1.1.5 Developing Technologies

A comparison of the permissible pollutant levels between Euro I (implemented in 1993) and Euro VI (implemented in 2014) in Table 1.1 shows much tighter emission limits of 67% for CO, 88% for uHC, 95% for NO_x, and 98% for PM. The effectiveness of these corrective measures are conspicuous from the collected statistical emission data. In Europe, for instance, there has been a 60% drop in NO_x and non-methane VOC emission levels since 1990 and a 30% drop in PM emissions since 2000 [2]. However, despite the improvements made by introduction of new technologies to address the air pollution challenge, a significant role is still played by the exhaust stream aftertreatment procedures to meet the legislated standards. These effective techniques, in addition to design and operational complexities and capital costs, might require additional work output from the engine to expel the exhaust gas from the system. As such, further investigations and continuous improvements on these developing technologies are essential to increase engine efficiency and reduce the production of criteria emissions and the burden on the exhaust aftertreatment systems to meet the ever-increasing stringent emission regulations is of great value.

From the perspective of optical measurement techniques, however, the de-

scribed improvements to reduce formation of various pollutant species during the combustion in-cylinder processes can introduce challenges in terms of the signal-to-noise (SNR) ratio of the recorded data. This will limit the information provided by the qualitative measurements, but more importantly, it will directly affect the range of properties to be calculated in the quantitative measurements. Also, the low-SNR issue potentially can be more of a concern in the case of natural emission optical measurement techniques, where the collected data SNR is solely determined from the characteristics of the source species and there is no additional control factors such as the intensity of an external light source. As a consequence, specific considerations might be necessary to improve the performance of the imaging system so as to make it more suitable for these “low light” combustion strategies. The enhanced measurement techniques, along with introduction of novel analysis procedures, would present a valuable toolkit to better understand combustion in-cylinder processes within the existing and developing CI engine technologies. With reflection of the acquired insights from the likes of these investigations into the design of the next generation of these technologies and their operation protocols, the 19th century diesel engine invention can continue to evolve and adapt with the needs of our era and remain the the most important engine of the 21th century.

1.2 Objectives, Contributions, and Approaches

The motivation for more in-depth characterization of and further improvements to modern alternative CI engine strategies, and a brief overview of the current technologies was presented in the previous section. With this introduction, the major objectives and contributions of the current work can be listed as follows:

1. Development of standard high-speed imaging diagnostics, and the supporting analysis tools, to further study combustion strategies using NG in CI engines.
2. Enhancement of a quantitative in-cylinder soot concentration and temperature measurement technique (two-color pyrometry) for low-SNR signal situations associated with the these and any similar combustion strategies.
3. Implementation of the developed and enhanced techniques to multiple com-

bustion strategies to investigate various parameter effects and compare observed combustion trends with existing understanding of various combustion modes.

4. Facilitate and assess the correlations between 2D and 0D quantitative in-cylinder soot measurement techniques, as well as 0D measurements in optical vs. thermodynamic engines, as an attempt to extend the in-depth 2D optical results to 0D measurements under more realistic operating condition.

The approach adopted to achieve these objectives is detailed throughout the main body of this thesis. A literature review of the relevant optical diagnostic techniques and investigations of the DPDF and PIDING combustion strategies was performed and presented in Chapter 2 to establish current knowledge and elucidate the existing gap motivating the presented work. The standard high-speed imaging diagnostic systems developed in this work are described in Chapter 3, along with other experimental facilities used, as well as development of a simultaneous 2D optical measurement system to facilitate analysis of the results acquired from two optical methods. The spatially resolved (2D) measurements aimed at advancing interpretation of combustion analysis results obtained from other experimental measurement techniques as well as producing the baseline data required later in this work. As such, the commissioned simultaneous high-speed 2D optical measurements of DPDF combustion, as a case study, is discussed in Chapter 4. The two simultaneous optical diagnostics considered were both qualitative measurement techniques. As a prerequisite to performing the quantitative in-cylinder soot measurement technique in low-signal conditions of the combustion strategies considered for this work, Chapter 5 identified and assessed improvements to various stages of the standard technique. These included refinements to the measurement system calibration and configuration, image post-processing, and solution algorithm. The enhanced method was then implemented, simultaneously with measurement of spontaneous emissions characterizing high temperature reaction zones, for optical investigation of soot processes in PIDING combustion under a range of operating conditions. These results, presented in Chapter 6, also highlighted the major differences of PIDING, as an advanced natural gas ignition technology, in contrast to diesel and conventional DPDF strategies. The insight provided into the

influence of engine level control parameters on in-cylinder processes could help improve this combustion strategy; However, the anticipated changes in in-cylinder processes, imposed by the geometric modifications and restricted operational considerations in an optical engine, promotes application of the less processes-altering OD measurements in a less idealized engine environment. Therefore, a series of concurrent 2D and OD measurements of soot concentration and temperature was carried out in the optical engine configuration and presented in Chapter 7. An analysis methodology was developed for more meaningful comparison of the 2D and OD results and better assessment of the correlations between these two approaches. This was followed by implementation of the OD soot measurements in the thermodynamic engine configuration to investigate the different combustion environment effects as well as to better understand the 2D vs. OD measurement effects. The presented efforts to achieve a more characterized and reliable OD optical measurement tool to study combustion in-cylinder processes, is in fact an approach to assess the feasibility of extending the detailed optical diagnostics to engine operating conditions that are more representative of real-world on-road operation.

Chapter 2

Background Information and Literature Review

In this chapter, some background information and review of the relevant literature on the optical diagnostic techniques utilized in this work, as well as the combustion strategies these techniques were applied to, are presented. This will lay the groundwork for all the analysis results and interpretations made throughout the subsequent chapters of the current document.

2.1 Optical Diagnostics for Combustion In-Cylinder Processes

Optical diagnostics in nature is essentially the study of the energy exchange in the form of electromagnetic radiation and its interactions with matter. In the field of combustion research, these methods aim at understanding the fuel conversion process and providing insight into characteristics of the injected fuel (liquid droplets or gaseous cloud) and the produced particles and gaseous species. Parameters under investigation are majorly the instantaneous amounts and distributions of the reactants, intermediate, and product species, under various operating conditions; and the influence of different operational control parameters on these characteristics. Ultimately, in any combustion system, these findings are intended to optimize the system such that an operational space be described where the constituent oper-

ating points lead to lower undesired system-out emissions, while maintaining high efficiencies.

There is a wide range of optical methods applied in engine and combustion research, relying on thermal radiation from suspended particles; quantum emissions from gaseous combustion species or introduced seeding agents; or alterations in the characteristics of an external light source passing through the combustion chamber. In what follows an overview of prominent optical methods relevant to IC engine studies is presented, along with a brief overview of the involved background theory in each case.

2.1.1 Optical Access to the Combustion Chamber

In order to implement optical diagnostic methods to understand combustion in-cylinder processes, an optical access to the combustion chamber must be provided first. This, however, is a challenging task that induces various levels of complexity and changes in the combustion chamber geometry and conditions, depending on the type of optical access considered. In the absence of such an optical access to an engine, or in the case of more fundamental analysis of combustion, constant volume chambers (CVC) [62, 159] or rapid compression and expansion machines (RCEM) [133] have been used to mimic in-engine conditions and present valuable spatial information on combustion processes to complement traditional analyses results performed on the basis of calculated heat release rates (HRR) and engine-out emissions. However, being able to take optical measurements from the in-cylinder processes of an engine would undoubtedly provide more relevant information required to optimize operation or develop new combustion strategies under current designs, or improve future designs. optically accessible engines approaches can be divided into three major categories: optical probe design, endoscopic design, and Bowditch piston design [16].

Optical Probe Design

In optical probe designs, light is collected from a small control volume, defined by the field-of-view (FOV) of the probe optical lens, and the signal output, integrated over the control volume, is transmitted through fibre optic assemblies to

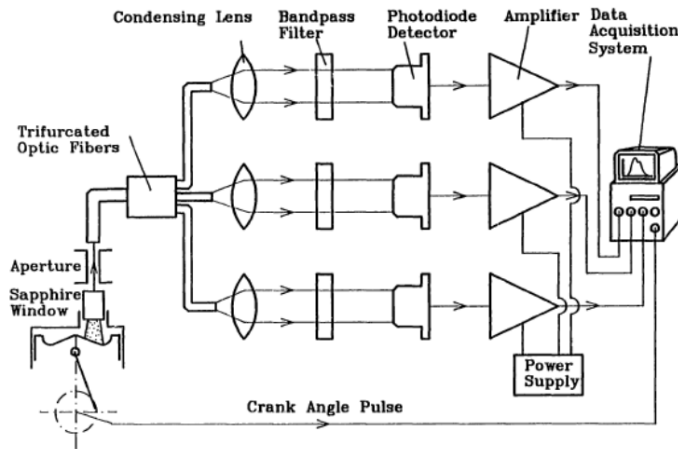


Figure 2.1: Schematic of a sample optical probe light collection diagram.
 Reprinted from [155] with permission from publisher

reach sensors. Today, these sensors are typically solid-state Silicon photodetectors or photomultiplier tube arrays, depending on the strength of the recording signals. The result would be single-value light intensities recorded with the temporal resolution of the sensors, possibly filtered around certain wavelengths depending on the phenomena under investigation. Figure 2.1 shows an schematic example of optical probe assembly.

Endoscopic Design

Endoscopic probe design is an extension to the optical probe design discussed in the previous section, where a coherent fibre bundle, maintaining the relative position of individual fibers in either end, transmits the high f-# collected light in the field-of-view. On the other side, a set of lenses are in-line mounted and focus on the fibre bundle exit port, magnifying the transmitted image to project onto a camera sensor. This will provide valuable 2D light measurements from in-cylinder combustion process, albeit within a limited field-of-view and from a small region within the combustion chamber. Figure 2.2 provides an schematic of such assembly and sample natural luminosity images taken from a diesel-ignited dual-fuel combustion case study.

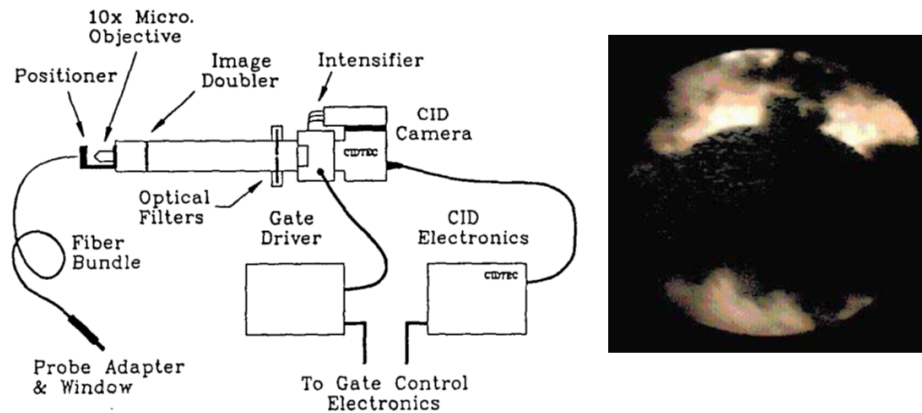


Figure 2.2: Schematic of a sample endoscopic light collection diagram, reprinted from [135] (left) and sample endoscopic image from DIDF combustion, adapted from [18] (right) with permission from publishers

Bowditch Design

The most common approach to gain a full optical access to the combustion chamber is a Bowditch optical piston extension design [16]. In this design, a relatively thick window (typically quartz or sapphire) is mounted inside a modified piston crown. A hollow engine block extension and an elongated hollow piston extension, with the window in its piston crown, are mounted on top of the main block and a dummy piston. A 45° mirror is then mounted on the block extension through the piston extension. With the long enough piston extension hollow area (stroke + mirror height + tolerance), the stationary mirror reflects the light from the combustion chamber, transmitting through the piston window, towards the imaging equipment, without interference from engine moving parts. Figure 2.3 shows the Bowditch optical engine design.

The modifications imposed by the optical engine configuration makes the processes no longer necessarily identical with those in the conventional “thermodynamic” configuration and impose a series of limitations on operating conditions, due to the optical parts mechanical properties. A thorough overview of the differences between thermodynamic and optical engine operations is presented by Kashdan *et al.* [72] and Aronsson *et al.* [5]. Among these are changes in the compression ratios as a result of altering the piston crown geometry and rings design,

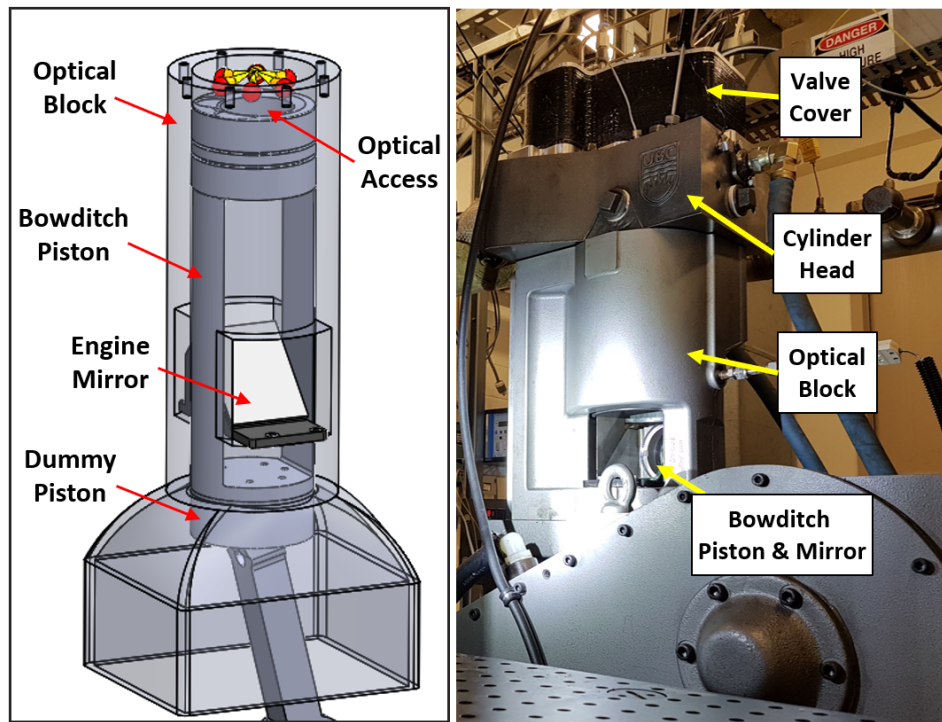


Figure 2.3: Schematic and photo of the optical configuration of the engine

lower heat losses through the walls due to the lower heat conductivity of optical parts and a less efficient cooling system [5], lower thermal conductivity of the glass compared to aluminum, which may promote the formation of hot spots, and the necessity of a skip-firing procedure to reduce window failure probability and cleaning requirements. Kashdan *et al.* also considered an “effective” compression ratio for the optical engine as a result of the dynamic and thermal loading of the extended piston-liner assembly [72]. The effects of these changes manifest both in the heat release and combustion phasing, and in the engine-out emissions [5, 72]. There are some practical approaches attempting to compensate for these differences. A common practice is to provide the engine with heated and pressurized air in order to compensate for the effects of the lower compression ratio in optical engines, as was done by Taschek *et al.* [142] and Dembinski [27], for instance, using an external boosting device. Intake air temperature and pressure is usually set based on estimations on the engine charge conditions at the top dead center (TDC)

for an equivalent thermodynamic engine. This estimation process becomes more challenging when heat transfer effects are to be considered as well or additional physics is involved, such as in exhaust gas recirculation (EGR) mode. Moreover, even if the thermodynamic conditions are matched at TDC, the total mass of the charge gas and its temperature and density away from TDC would be higher in optical engines [109].

2.1.2 Natural Luminosity Imaging

The natural luminosity (NL) imaging, as the name suggests, relies on the information that can be collected from the visible portion of the electromagnetic radiation spectrum from the self-radiating combustion products and scattered light (around 380-700 nm). This basic imaging technique attempts to qualitatively characterize the combustion in-cylinder processes by looking at the broadband emissions. The natural luminosity light from combustion of hydrocarbon fuels generally comprises a “blue” flame and a “yellow” flame [29]. The yellow flame attributed to the incandescence from glowing suspended particles, and the blue flame originates from chemiluminescence light from intermediate species, discussed in the next section [46]. During combustion, soot particles reach temperatures much higher than the Draper point and thermally radiate a broadband light, called incandescence and considered to be diffuse.

Natural luminosity imaging of the flame and the associated incandescent soot particles is the oldest optical diagnostic technique applied to better understand combustion in-cylinder processes. In an early CI engine optical investigation in 1934, Rothrock showed that the diesel flame first appears on the spray envelope and from there spreads to other parts of the combustion chamber; and that the course of combustion is highly dependent on the air pressure and temperature in the chamber between the injection and start of combustion [129].

When imaging the entire visible range, the chemiluminescence light is usually dominated by the incandescence generated from soot particles at elevated temperatures, when present concurrently. For typical diesel fuels and under typical CI engine operating conditions, natural luminosity from soot incandescence has been reported 4-5 orders of magnitude stronger than chemiluminescence [104]. Despite

the technological advancements and improved theoretical understandings of the details of in-cylinder processes, natural luminosity imaging remains a popular basic, easy-to-implement, technique to qualitatively characterize combustion, often used in conjunction with other optical methods [29, 104, 108, 136, 140, 142]. In addition to the interpretation of the broadband natural luminosity light, researchers have used the signal level disparity between the chemiluminescence and incandescence lights to segregate the blue and yellow flames. Taschek *et al.* [142], along with other optical diagnostic tools, adjusted camera exposure to discuss the soot cloud behavior and chemiluminescence from intermediate species separately in an optical CI engine, in order to study the effect injector nozzle holes geometry on spray formation, mixing, ignition, combustion, and soot formation. The high intensity soot incandescence required relatively much shorter camera sensor exposure time to record images with an acceptable dynamic range, while the low intensity chemiluminescence is expected to be negligible at such low exposure times. In contrast, high exposures required for imaging low intensity chemiluminescence light properly, would lead to sensor saturation in presence of intense soot incandescence. Alternatively, Singh *et al.* [136] and Musculus *et al.* [108] used Neutral Density (ND) filters in order to lower the transmitted spatially resolved natural luminosity signal level (without altering spectral information) and eliminate the weaker chemiluminescence light. The images of the stronger yellow flame were used to support the spatially-integrated quantitative measurements of in-cylinder soot. In two more recent studies by Khosravi *et al.* [75] and Hatzipanagiotou *et al.* [54] dichroic mirrors were used in the natural luminosity light path that blocked signals from lower wavelengths (350nm and 340nm, respectively), and thus, eliminated part of the chemiluminescence signal (spectral behavior of the chemiluminescence light from hydrocarbon fuels is discussed in the next section).

2.1.3 Chemiluminescence Imaging

Chemiluminescence is a sub-class of the spontaneous emission of light, where the atoms or molecules transition to an excited energy state by the energy released through chemical reactions and photons are released as they relax back to the ground energy state. In the case of combustion of hydrocarbon fuels, chemilumi-

chemiluminescence emitting molecules are mostly short-lived electronically excited intermediate species formed during the fuel pyrolysis chemical reactions and naturally emit photons in the UV and visible range [47]. The diatomic carbon (C_2^*), hydroxyl (OH^*), methylidyne (CH^*), and carbon dioxide (CO_2^*) radicals are the major sources of chemiluminescence emission from hydrocarbon fuel combustion, while chemiluminescence from formyl (CHO^*), formaldehyde (CH_2O^*), cyanido (CN^*), carbon monoxide (CO^*) can also be significant under certain operating conditions [6, 19, 46, 50, 53, 101, 140, 145]. Chemiluminescence from these species are often used as a quantitative diagnostic in combustion studies, e.g., for local equivalence ratio estimations in gaseous and liquid fueled systems [3, 51, 53, 106, 137], tracking locus of the flame front [61, 140], and analyzing heat release noise and instabilities in combustion dynamics investigations [6, 85]. Table 2.1 illustrates the formation reactions and emission peaks/bands for the major chemiluminescence sources in combustion of hydrocarbon fuels. In the listed chemical reactions in this table, M is a third-body chemical compound that participates in thermal deactivation of the excited molecules through inelastic collisions, a process referred to as “collisional quenching” [40, 46].

Table 2.1: Formation pathways and characteristic wavelengths of the major chemiluminescence sources in combustion of hydrocarbon fuels [9, 19, 46]; prominent peaks are printed in bold font.

Species	Reactions	Wavelengths [nm]
OH^*	$CH + O_2 \longrightarrow CO + OH^*$ $H + O + M \longrightarrow M + OH^*$ $OH + OH + H \longrightarrow H_2O + OH^*$	281, 307 , 342
CH^*	$C_2H + O_2 \longrightarrow CO_2 + CH^*$ $C_2H + O \longrightarrow CO + CH^*$ $C_2 + OH \longrightarrow CO + CH^*$	365, 389, 431.5
C_2^*	$CH_2 + C \longrightarrow H_2 + C_2^*$	474, 516 , 563, 655
CO_2^*	$CO + O + M \longrightarrow M + CO_2^*$	340-650

The spontaneous spectral emissions from these species can be in the form of

peaks of radiation at one or a few certain wavelengths with a relatively narrow bandwidth, as in the case of intermediate species such as OH*, CH* [46, 53]. Alternatively, these emissions might occur within a wider wavelength bandwidth at lower signal levels, as in the case of CO₂* [53] and CHO* and CH₂O* under certain operating conditions [145].

C₂* radicals chemiluminescence emission spectra comprises a number of excited vibrational states in the visible spectrum (473.7, 516.5, 563.5, and 655 nm [118]), making C₂* a major contributor to the blue flame [29, 66]. Among these peaks, the 516.5nm peak is the most prominent one and the target of C₂* chemiluminescence measurements [53, 137, 140, 145]. In one of the early studies in the search for a relationship between chemiluminescence and heat release rate, Price *et al.* [123] showed a linear relationship between the C₂* chemiluminescence and the mixture flow rate, independent from the conditions of turbulence. Langhorne [82] measured C₂* chemiluminescence emission to study reheat buzz, a combustion instability phenomenon that occurs in the afterburners of jet engines. C₂* chemiluminescence has often been used in conjunction with other chemiluminescence signals to quantitatively assess local heat release rates and equivalence ratios [53, 77, 131].

OH* and CH* radicals are two of the most significant chemiluminescence sources in combustion diagnostics. They are often used to locate flame fronts or to analyze local flame structure [19, 46, 61], as well as to study the heat release rate and equivalence ratio [6, 9, 46, 53]. De Leo *et al.* [89], for instance, observed high intensities of OH* and CH* chemiluminescence emitted in the reaction zone of opposed flow methane oxy-flames and concluded that their peak intensity is a good indicator of the flame front. The OH* radical shows a strong peak of naturally emitted chemiluminescence signal at a narrow wavelength band centered at 307 nm, which is the result of integration over multiple OH* (0, 0) bands at 306.4, 306.8, 307.8, and 309.0 nm and the OH* (1, 1) bands at 312.2, 312.6, 313.5, and 314.7 nm [77]. Besides this strong peak which is often the subject of chemiluminescence measurements, OH* spectra shows a weaker peak at 280 nm [101]. CH* spectra peak at 431.5 nm offers the stronger transition bands and is often used for chemiluminescence measurements [53, 140, 145].

In pollutant formation studies, CH is recognized to play a significant role in

NO_x formation through the prompt NO mechanism and oxidation of CH is one of the major pathways of producing chemically excited OH. It is very unstable and tends to chemically react with other species very quickly, and exists in a narrow spatial and temperature region within the flame, and can provide insight into the C2 reaction chain [19, 148]. The CH^* radical formation is a strong function of temperature [45] and high intensity CH^* chemiluminescence indicates high local temperatures. Since it is produced in a very narrow width region of the flame front, CH^* can be tracked to mark the locus of flame front, especially in turbulent flames [46, 101]. CH^* is also recognized as a marker for hydrocarbon fuel break-down into simpler molecules and high CH^* chemiluminescence emission was reported to indicate the continuing diesel fuel vaporization process [19].

OH^* chemiluminescence measurements has been widely used for combustion characterization. Investigation of the non-sooting flame or high temperature reaction zones is perhaps the most significant application of OH^* measurements [159]. The intensity of OH^* chemiluminescence depends on the local temperature and AFR [46]. Thus, high OH^* chemiluminescence intensities in a region can indicate near stoichiometric AFR and higher temperature [19, 142]. The ignition process in a diesel engine has been described to occur in three stages: starting with a cool flame reaction, followed by formation of chemiluminescent flame, and ending with the ignition of CO [105, 142]. During the simulation of ignition reaction mechanisms for n-heptane in a homogeneous reactor, OH^* appeared as one of the first species with significant concentrations [105], followed by CH^* shortly. This result was later confirmed by optical in-cylinder investigations of Bertsch [12] and Koyanagi *et al.* [79]. Based on this description, OH^* chemiluminescence was perceived as a good marker for the ignition process [142]. OH^* is also believed to be a good indicator for soot oxidation [94], and its presence has been used to define the flame area [25]. In addition, Ayoola *et al.* [6] compared spatially resolved OH^* and CH^* chemiluminescence and the flame surface density and heat release rate and demonstrated good correlations, which led them to the conclusion that both the OH^* chemiluminescence and flame surface density measurements reasonably estimate heat release rate. In gasoline engine studies, the described relation between OH^* chemiluminescence and local temperature and heat release has been used to distinguish between the unburned charge mixture and the burned gas re-

gions [101].

The ratio of various chemiluminescence peaks have been used to describe local equivalence ratios in engines [3, 19], given the dependence of these chemiluminescence intensities to the local AFR. OH* and CH* measurements of perfectly premixed flames showed a linear correlation between chemiluminescence intensities and charge mass flow rate and an exponential one between these intensities and the equivalence ratio [55]. Therefore, the ratio of two chemiluminescence peaks will be only a function of the equivalence ratio. Ratios of CH*/C₂*, CH*/OH*, and C₂*/OH* chemiluminescence demonstrated good estimates of local equivalence ratios [77].

The overlapping quantum emission bandwidths and signal interference, especially due to the existence of broadband emissions from certain species, should be considered during chemiluminescence measurements. Chemiluminescence from CH* radical at 431.5 nm, for instance, is identified to accompany background emission signal from CO₂* from 340-350 nm to somewhere between 500-650 nm [6, 9, 19]; convolution of the CH₂O* Vayda band from 250 nm to 410 nm, and CHO* Emeleus flame band from 330 to 523 nm [19, 46, 101]. Hardalupas and Orain [53] evaluated the magnitude of background intensity from CO₂* relative to the chemiluminescence signal from OH, CH, and C₂* radicals, using a Cassegrain optics system, in counter-flow natural gas flames with different equivalence ratios and strain rates. They observed that although at near stoichiometric and rich mixtures the ratio of the CO₂* background intensity over CH* and OH* chemiluminescence intensities are similar (~10%), the background/CH* ratio can be as high as 30% on the leaner mixture side. Another important source of signal interference for chemiluminescence measurements, especially when non-premixed flames are considered, is thermal radiation from generated soot particles. This effect is more significant for liquid fuels as they tend to produce more soot [161]. Background emission from incandescent soot particles is negligible in the UV range near the OH* chemiluminescence peak, but can be substantial around the peak of CH* radical emissions [63, 71].

2.1.4 Two-Color Pyrometry

As discussed in the previous chapter, characterization of the in-cylinder soot formation and oxidation processes is a valuable tool for reducing the engine out soot. However quantitative in-cylinder measurements are not trivial in light of the complex thermochemical processes and challenging access to the combustion chamber [147]. Several methods are available for characterization of the in-cylinder soot. Multi-color pyrometry is used to measure the soot concentration and temperature based on the radiation from a soot cloud, along with an empirical wavelength-dependent representation of the soot cloud emissivity [162]. The higher fidelity laser-based methods, such as Laser Induced Incandescence (LII) and light scattering methods, are also commonly used for quantitative in-cylinder soot characterization. In what follows, first a brief comparison between these two approaches are presented; the fundamentals of the two-color pyrometry measurement and analysis concepts are then reviewed and a few examples of its application for in-cylinder soot characterization is discussed.

Comparison with Laser-Based Methods

Laser Induced Incandescence (LII), light extinction method, Laser Induced Scattering (LIS), and Laser Induced Fluorescence (LIF) are the prominent laser based techniques used for quantitative in-cylinder soot characterization [88, 146, 147, 162]. LII provides planar distribution of the soot concentration on a laser sheet radiated to a soot cloud to increase soot particles temperature well above the surrounding gas. Light scattering can be divided into two groups of elastic and inelastic methods, depending on whether the energy exchange mechanism interferes with the irradiated/radiated frequencies. The light extinction method is an elastic technique based on measurements on the attenuation of emitted light (extinction) passing through a cloud of soot particles to calculate soot concentration [162]. LIS is another elastic scattering technique which uses simultaneous imaging of scattered light polarized in two directions to study spatial and temporal variations of soot based on interpretation of the polarized ratio [87]. LIF is perhaps the most important inelastic light scattering technique in soot formation and oxidation studies. In this technique, a species of interest is excited with a laser beam/sheet and

then emits light at wavelengths higher than that of the excitation laser used (de-excitation). Different species have been subjected to LIF investigation, based on the hypothesis of being precursors of either formation or oxidation of soot particles, e.g., formaldehyde [78], OH* [147], and PAH [88]. LIF and LII are often performed in conjunction to each other for comparison and cross-correlation purposes [78, 88, 147]. These elaborate techniques, however, are reported to have more limited maximum detection ranges, as the laser light must penetrate the soot cloud with sufficient intensity to produce an adequate signal, which then must penetrate through the soot cloud to reach the camera sensor [147]. Typical concentration limits for LII were reported to fall in the 0.1–0.3 ppm range by Pinson *et al.* [119], while higher soot volume fraction upper limits of ~20 ppm were identified in several two-color pyrometry studies [147]. Line of sight (LOS) extinction measurements by Tree and Dec [146] and Musculus *et al.* [107] also suggested that, under the operating conditions considered in their work, soot concentrations in diesel flames typically exceed the levels that can be measured using LII and LIS methods. In addition, the laser-based measurement techniques, such as the LII, LIS, and LOS extinction methods described above, require high capital investments, primarily for the laser, especially if high temporal resolution measurements are considered, as well as a second optical access to the combustion chamber to introduce the laser light. In comparison, a multi-color pyrometry system would be simpler and more cost-effective to setup, as it only requires one optical access to the engine and an imaging system, but no light source.

Fundamentals and Approach

The two-color pyrometry method considers the spectral radiant intensity at two wavelengths to evaluate the soot temperature and concentration. For this, the spectral emissivity of a soot cloud is assumed to be a function of the detected wavelength, soot concentration, optical path length, and optical properties of soot described by the complex refractive indices and soot particle size and shape (extent of agglomeration). The semi-empirical relationship proposed by Hottel and

Broughton [57], is commonly used to describe the soot cloud spectral emissivity:

$$\varepsilon_{\lambda} = 1 - e^{-KL/\lambda^{\alpha}} \quad (2.1)$$

where the KL factor, as shown in equation 2.2, is directly proportional to the soot volume fraction, f_v [147], and determines the amount of soot in the optical path of the captured light.

$$f_v L = \frac{KL}{A_{\lambda} \lambda^{\alpha-1}} \quad (2.2)$$

where L is the geometric optical path length and A_{λ} is an optical constant determined from the refractive indices of soot and was approximated by $6 + 0.27\lambda$ [μm] [41]. The parameter α is an empirical constant. It has been noted elsewhere that a constant value ($\alpha=1.39$) can be used for wavelengths in the visible range with negligible effect on the calculated temperature and KL [96, 162]. More recently, Kamimoto and Murayama [67], re-examined the value of α for diesel soot collected from the surface of a quartz window in an optical engine and obtained a close estimate of $\alpha=1.38$. They further examined this value theoretically through calculation of spectral extinction using the Rayleigh-Debye-Gans (RDG) theory of soot aggregate scattering with an assumption of constant refractive index and obtained a value of $\alpha=1.31$. Comparison of the acquired flame temperature and KL factor using their alternative description of the soot cloud emissivity with those of a conventional two-color pyrometry method showed an agreement of within 1-2%.

Equation 2.1 originates from the Kirchoff and Bouguer-Lambert laws for a homogeneous absorptive medium with no scattering resulting in:

$$I_{\lambda}(L) = I_{\lambda}(0) \exp(-\kappa_{\lambda} L) \quad (2.3)$$

where I_{λ} is the spectral radiant intensity and κ_{λ} is the absorption coefficient. κ_{λ} is a function of the detected wavelength, complex refractive indices, soot concentration, particles size and shape, As an approximation, Hottel and Broughton suggested the substitution $\kappa_{\lambda} = K/\lambda^{\alpha}$, where K is the absorption strength of the soot cloud [57], and is proportional to the number density of soot particles [162]. As a result, the effects of the wavelength, particle size and shape, and complex

refractive index on the emissivity are described by λ^α and the product KL characterizes the total soot volume [147]. The dimensionless product $\kappa_\lambda L$ (or equivalently KL/λ^α) is referred to as the optical thickness of the soot cloud. The recorded line of sight signal might originate from a thick cloud of low soot concentration, or a thin cloud of high soot concentration, while both scenarios represent the same soot cloud optical thickness. In the current work, a high KL factor signal will be attributed to an optically thick flame, and a low KL factor signal to an optically thin flame, regardless of the physical characteristic length.

Combining equation 2.1, the definition of emissivity, and Planck's distribution, and assuming that the KL factors at the two wavelengths are equal, result in a residual function f :

$$f(T, x_{i,j}, t) = \lambda_1^\alpha \ln \left[1 - \frac{e^{C_2/\lambda_1 T(x_{i,j}, t)} - 1}{e^{C_2/\lambda_1 T_{a,1}(x_{i,j}, t)} - 1} \right] - \lambda_2^\alpha \ln \left[1 - \frac{e^{C_2/\lambda_2 T(x_{i,j}, t)} - 1}{e^{C_2/\lambda_2 T_{a,2}(x_{i,j}, t)} - 1} \right] \quad (2.4)$$

where $C_2 = 1.43 \times 10^{-2}$ mK from Planck's Distribution, T is the soot cloud temperature, and $T_{a,1}$ and $T_{a,2}$ are the apparent temperatures at λ_1 and λ_2 , respectively. In a physical sense, apparent temperature at a certain wavelength, also referred to as the brightness temperature, is the temperature of a black body emitting the same spectral radiant intensity as the soot particles at that wavelength, as described in Equation.

$$I_{\lambda_b}(\lambda, T_a) = I_\lambda(\lambda, T) \quad (2.5)$$

Temporally and spatially resolved apparent temperatures are obtained using a calibrated high-speed imaging system (see §3.2.2). Equation 2.4 is solved iteratively for T at each image pixel $(x_{i,j})$ and time step t . The KL factor is then evaluated using:

$$KL(x_{i,j}, t) = \lambda^\alpha \ln \left[1 - \frac{e^{C_2/\lambda T(x_{i,j}, t)} - 1}{e^{C_2/\lambda T_a(x_{i,j}, t)} - 1} \right] \quad (2.6)$$

for either of the wavelengths. While the solution of equation 2.6 will pro-

vide the particle cloud temperature, Baker and Ryder,[8] have shown that equilibrium time constants for soot particles and surrounding gases are sufficiently small ($10^{-6} - 10^{-5}$ sec) that the soot particle temperature are indicative of the local gas temperature for engine relevant combustion processes.

The range of wavelengths considered for this method span from visible (0.38-0.7 μm) to Near-infrared (NIR, 0.75–1.4 μm). In the temperature ranges relevant to diesel combustion, which is approximately 1800-2800 K [117, 160], the electromagnetic radiation is dominated by the wavelengths in the NIR, which yields better signal-to-noise-ratio (SNR). However, shorter wavelengths in visible range are used in majority of the works for a number of reasons. In the visible range, the rate of change of spectral radiant intensity with respect to both the temperature and wavelength, dI_{λ}/dT and $dI_{\lambda}/d\lambda$, is larger [162]. Also, the effect of radiation from the wall is significant for the NIR and reflection of the soot particles radiation from the opposite walls significantly contributes to the total error [96]. Finally, the quantum efficiency of the sensor in majority of regular digital high speed cameras deteriorates starting from the end of the visible range (around 800nm) and also α can be considered to be constant in this range. For diesel combustion, wavelengths in the range of 550-750 nm are widely used [52, 62, 65, 117, 158, 160]. However, given the lower combustion temperature ranges for natural gas and less amount of soot expected to be produced, wavelengths around 700 nm and 800 nm were chosen in this work. For this selection, attention was paid to the relevant gaseous species spectra to ensure no interference from other species (notably CO_2 and H_2O).

The pyrometric method described above has been used for spatially integrated [108, 136, 162], as well as spatially resolved (imaging) measurements [62, 64, 92, 117, 158, 160]. For imaging purposes, two correlated images with known spectral intensities are required as inputs to equation 2.4. This has been achieved through using two calibrated monochrome cameras with a beam splitter [62], or an image doubler to project the filtered images on a single monochrome CCD or CMOS sensor [4, 117, 160]. As an alternative approach, Larsson [83], proposed extracting the required spectral information from the three color channels of a single color CCD camera using the Bayer filter mounted on the sensor (instead of the narrow band-pass filters); however, this method is susceptible to overlapping response of the colors bands, which results in an untraceable signal interference (cross-talk). This

technique is explained in detail by Svensson *et al.* [141], and has been applied by several researchers [29, 158]. As an extension to the described application of a color CCD camera, Ma *et al.* proposed a color-ratio pyrometry (CRP) technique using a color CCD camera, where ratios of the signals obtained at three visible wavelength channels (red, green, and blue) were used rather than the absolute signal values. This was done as an attempt to avoid the challenges associated with quantitative absolute intensity measurements, such as calibration errors, optical path variations, and window fouling [92]. It was found, however, that better temperature estimates could be achieved assuming a constant KL , rather than solving for KL . The calculated temperatures using this method were noted to be insensitive to the soot concentration as long as the signal ratios (red/green vs. red/blue) were adaptively selected based on temperature ranges being considered.

The uncertainties associated with pyrometry have been discussed in a comprehensive review by Zhao and Ladommatos [162], as well as other works considering the complex refractive index, and the shape of the soot agglomerates [30, 81, 95, 96, 147]. Furthermore, uncertainties due to wall reflections in the near infrared spectrum (NIR), soot deposition on the window, wavelength sensitivity [95, 96] and digitization errors [117, 160] have been reported. Payri *et al.* [117] discussed the effect of the intensity non-uniformity along the line of sight, as well as the effect of digitization uncertainty on a CCD sensor. Line-of-sight uncertainties are most significant for flames with optically thick regions ($KL_{\lambda} > 1$) [68], and higher gradients [108], particularly along the line of sight. Correspondingly, the uncertainties are lower for homogeneous combustion strategies, lower temperature combustion strategies (due to generally lower gradients) [108], or later in the combustion process when the soot is more uniformly mixed [68]. Table 2.2 summarizes the uncertainties relevant to two-color pyrometry as characterized in the literature. In general, the soot volume fraction and KL factor are more sensitive to uncertainties than the temperature. Furthermore, the uncertainties are more significant for lower soot concentrations.

In a recent study, Kamimoto *et al.* [68] also investigated the presence of soot outside the naturally luminous flame boundary, to identify soot cloud regions at temperatures below the detection limit. This was carried out using simultaneous natural luminosity and shadow images of a single diesel spray jet flame within

Table 2.2: Summary of reported two-color pyrometry uncertainties

Source of uncertainty	Error				Reference
	10 ppm; 700-800 nm range Temperature $f_v L^*$		0.1 ppm; 700-800 nm range Temperature $f_v L$		
Soot particle size distribution function	< 1%	2%	< 1%	2%	di Stasio (1994)
Complex refractive index	< 1%	8%	2%	12%	
Soot particle shape	< 1%	18%	2%	18%	
	High soot conc. Temperature KL		Low soot conc. Temperature KL		
Wall reflections (visible)	<< 1%	2%	<< 1%	10%	Matsui (1980)
Wall reflections (NIR)	5 – 8%	30%	5 – 8%	50%	
	High-T combustion Temperature $f_v L$		Low-T combustion Temperature $f_v L$		
Line-of-sight gradient effects	8%	50%	3%	20%	Musculus (2008)
	Temperature		KL		
Soot deposition on the window	1%		5%		Matsui (1980)
Pyrometry filter band-width	1%		2%		di Stasio (1994)
Digitization error	5%		20%		Payri (2007)

* $f_v L$: product of the mean soot volume fraction and line-of-sight path length. This is a measure of the mean optical thickness of the soot cloud [41, 147].

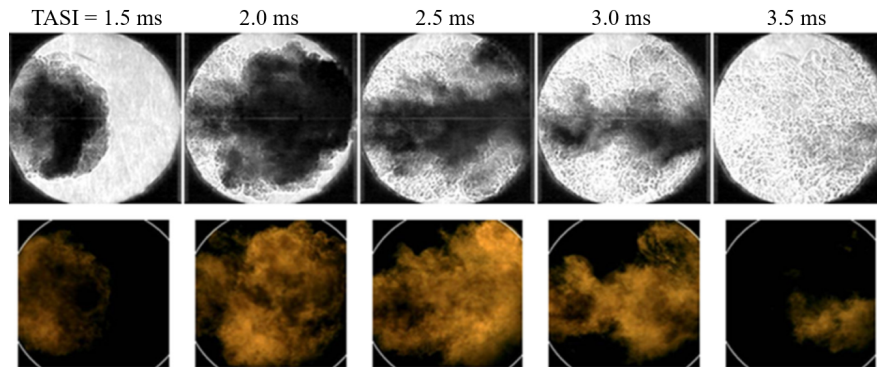


Figure 2.4: Shadow and NL images of a single spray flame in a constant volume combustion chamber (TASI: time after start of injection); operating conditions available in the reference. Adapted from [68] with permission from publisher

a constant volume combustion chamber, as shown in Figure 2.4. Generally, one can claim the natural luminosity and soot cloud shadow regions appear to coincide across the field-of-view. However, quantitative evaluation of the shadow images was not possible due to the significant background noise caused by the density fluctuations of the surrounding gaseous species at elevated temperatures [68].

Application in in-Cylinder Soot Characterization

Multi-color pyrometry has been used by numerous researchers to study soot processes in conventional and alternative combustion strategies. For instance, integrated light pyrometry was used in conjunction with high-speed spatially resolved natural luminosity imaging by Singh *et al.* to demonstrate lower amount of in-cylinder soot resulting from representative low-temperature diesel combustion (LTC) scenarios, compared to their conventional high-temperature combustion (HTC) strategies [136]. Also, it was inferred from the results that, during high-temperature operating conditions soot formation starts upstream in the jet, while for the low-temperature operating conditions, the start of soot formation appeared to occur further downstream, closer to the bowl edges. Two-color pyrometry results showed the onset of in-cylinder soot after the premixed burn and during the mixing controlled combustion phase. Figure 2.5 shows the calculated $f_v L$ factor

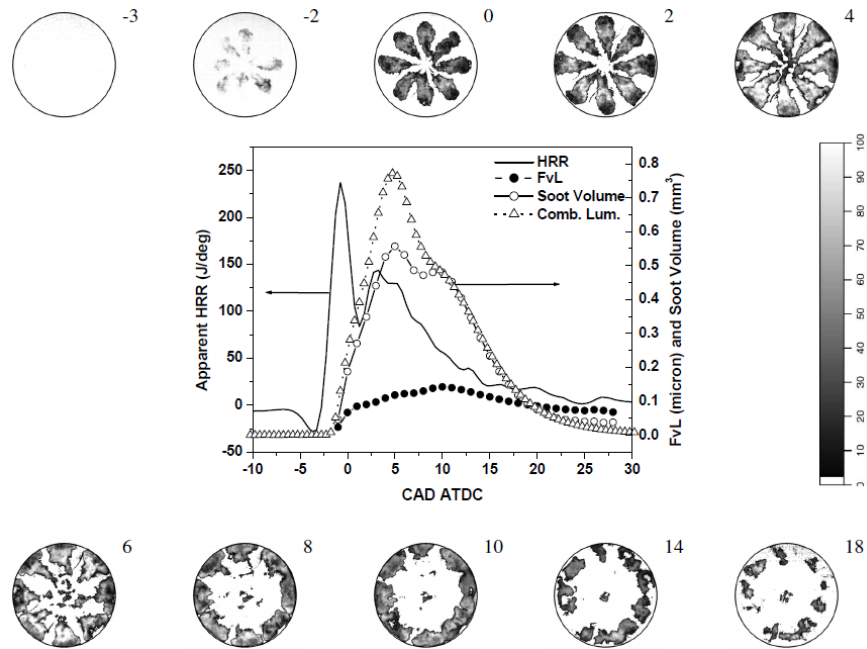


Figure 2.5: $f_v L$, HRR, NL, soot volume, and NL images for high-temperature diesel operating condition (the number to the upper right of each image is the crank angle aTDC). Adapted from [133] with permission from publisher

results for a high-temperature operating condition studied in [136]. Also shown in this figure are HRR, spatially averaged natural luminosity results, and a calculated “soot volume” parameter at each crank position, based on the soot cloud area indicated by the 2D natural luminosity images, as well as select instances of spatially resolved natural luminosity results. Although the detected onset of soot from NL and two-color pyrometry results are coincident, around peak HRR of the partially-premixed combustion phase, the peaks and trends in the two sets of results do not generally agree. The peak NL occurs closely after the peak HRR of the mixing-controlled combustion phase and end-of-injection (3 CAD aTDC), while the peak in the $f_v L$ factor was observed later during that phase.

In a direct injection spark ignited (DISI) engine, Ma *et al.* [92] used a variant of multi-color pyrometry technique to characterize soot and observed maximum in-cylinder temperature, based on spatially averaged soot temperature distri-

bution, and coincidentally maximum heat release rate just after TDC. In a different study, Zha *et al.* [158] used two-color pyrometry to compare the soot processes in biodiesel blend and diesel combustion in a CI engine. For biodiesel blends, they observed soot formation in low amounts over large areas between fuel jets, which was associated with more splashing in the fuel during wall impingement and rebounding fuel distribution over a thicker annual ring. Higher amounts of KL was formed on the jet axes and away from the bowl edge, which was attributed to the remnants of the fuel spray. Diesel combustion, in contrast, showed soot formation exclusively at the piston bowl regions through what was described as pool flames resulting from spray wall impingement. In comparison to the diesel fuel, the tested biodiesel showed earlier and significantly higher soot formation, but also higher soot oxidation rates, inferred from lower late-cycle KL values. In addition, similar to diesel combustion, application of higher fuel injection pressure for biodiesel showed to reduce late-cycle soot KL levels.

In a more recent study, Kamimoto *et al.* [68] used KL factor distributions from two-color pyrometry to study late-cycle soot oxidation in a heavy-duty diesel engine and an RCEM. In correlation with simulated soot mass traces, they specified a surface-specific soot oxidation rate in each case to comment on underlying oxidation mechanisms based on the Arrhenius diagram. They calculated a higher soot oxidation rate for combustion in the heavy-duty diesel engine than that of the RCEM, and, based on a soot oxidation model presented by Boba *et al.* [14], concluded that this higher soot oxidation rate could be attributed also to the well-mixed soot oxidizer structure in the flames, in addition to the higher soot temperatures. This was in contrast with the hypothesis proposed by Huestis *et al.* [60], which suggested in-cylinder soot temperature was more important than jet-induced turbulent mixing during the late-cycle soot oxidation processes. Figure 2.6 shows sample two-color pyrometry results from [158] and [68], as well as their filtered natural luminosity counterparts (raw images). The resolved distribution of temperature and KL factors presents valuable information regarding the relevant soot processes; however, there are regions in the raw data that have not been resolved into KL and temperature values, despite the available high soot signal.

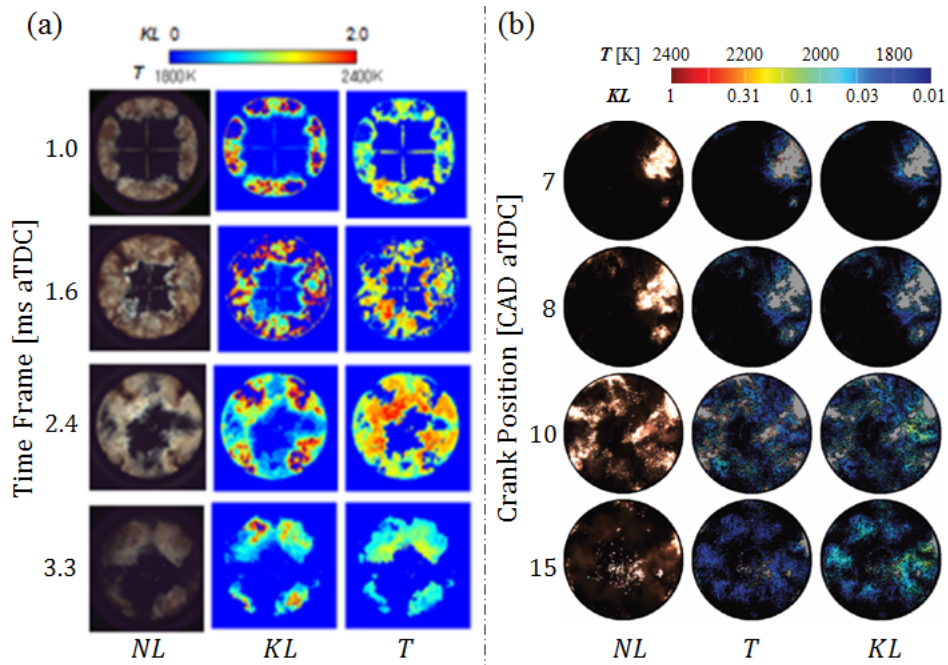


Figure 2.6: Sample 2D two-color pyrometry results and the corresponding filtered NL images from (a) diesel combustion in an RCEM [68] and (b) biodiesel combustion in a diesel engine [158]. Image sequences were adapted from references with permission from publishers

2.2 Modern Alternative Combustion Strategies

An overview of the alternative natural gas combustion strategies was presented in Chapter 1. Here, a review of the current understanding of these processes is provided and the areas with a potential for improvements are emphasized.

2.2.1 DIDF

DIDF engine operation is an attractive strategy for the application of natural gas in conventional CI engines because of the minimal modification to existing engine designs necessary and the relatively high efficiencies possible [130, 153, 154]. DIDF engine operation is characterized by premixing a high octane number fuel and then igniting it with a late-cycle direct injection of a high cetane number pilot fuel. Typically, the bulk of the energy is supplied by combustion of the premixed fuel.

Despite the significant reduction of the NO_x , CO_2 , and PM emissions, which originally made DIFD a promising combustion strategy, this technique poses a major deficiency by increased emission of unburned combustion species such as CO and CH_4 (when NG is used for the premixed charge), particularly at low engine loads. Higher CH_4 emission is particularly concerning, given it was shown to possess 21—72 times the greenhouse warming effect of CO_2 , and has made the low-load DIFD engine operation a more intense field of ongoing research [44, 124]. Emissions of unburned species can be related to the distinct combustion modes present throughout the dual-fuel combustion process [69, 127]. These combustion modes and the transitions between them are complex and not well understood. At the same time, the combustion behavior within dual-fuel engines have been shown to be highly dependent on the mass, timing, pressure, and fuel composition of the pilot injection, all of which can readily and predictably controlled [7, 127]. Karim introduced a model, where dual-fuel combustion was broken down into three distinctive stages: premixed combustion of the pilot fuel, immediately followed by combustion of the entrained premixed charge at the vicinity of the ignited pockets, and then conversion of the rest of the premixed charge through a turbulent flame propagation process [69]. In fact, Karim looked into the influence of premixed equivalence ratio on the shape of HRR curves to define different stages of combustion based on dominating fuel component in the charge in the proportion of released energy. With a similar approach although including ignition delay stages for both the pilot and primary fuels, Sahoo *et al.* [130] divided the DIFD combustion process into five stages: Pilot ignition delay followed by the premixed pilot fuel combustion, the NG ignition delay stage as a result of the higher auto-ignition temperature of methane, rapid combustion of the primary fuel, and finally, a late stage low-intensity diffusion combustion stage as a result of the decreasing combustion reactions rates with expanding cylinder volume and combustion diluents. In another work, Rochussen *et al.* [127] divided the dual-fuel combustion process into two main stages based on shape of HRR curves. The first stage was found to be dominated by auto-ignition and rapid combustion of pilot fuel and entrained CH_4 . This was then followed by the second stage, where conversion of premixed NG was regarded as the dominating process.

While such thermodynamic and emission based investigations can provide a

description of the combustion process, optical investigations of in-cylinder processes provide significantly more of these descriptions. There are a limited number of studies that have optically assessed DF combustion. These include visualization of the distribution of high temperature reaction zones and their correlation to unburned hydrocarbon emissions; spectroscopic analysis of the reactive charge, intermediate species and end products; visualization of soot particle production and oxidation [18, 33, 133].

Carlucci *et al.* [18] investigated the effect of inlet bulk flow, port-fuel injector positions, pressure and quantity of the diesel pilot injection on dual-fuel combustion at light load using single-shot endoscope natural luminosity imaging. The port-fuel injector positioning was modified to control charge mixture stratification and inlet port setup was modified to control swirl and tumble in the induced charge. Their analysis of the averaged NL curves showed a great influence from the injected diesel pilot properties under various conditions. In particular, lower pilot fuel injection pressure and higher injected mass, both led to higher recorded NL signal. Schlatter *et al.* [133] studied diesel pilot ignited dual-fuel in an RCEM by looking at spatially resolved OH*, and integrated OH*, CH*, C₂*. The focus of this work was to study the effect of sweep of methane equivalence ratios (0-0.65) and changes in the number of pilot jets (3 or 6) on the auto-ignition and combustion behavior, while the pilot injection pressure and timing was held constant (400 bar and 4.1 ms bTDC). Under both high and low load operating conditions ($\phi_{\text{CH}_4} = 0.37$ and $\phi_{\text{CH}_4} = 0.67$), the high temperature reactions were localized on the pilot jet axes, denoted by the high intensity OH* chemiluminescence in these regions, for both pilot injectors. Figure 2.7, reprinted from [133], illustrates this process. In this work, authors also observed an increase in ignition delays, as indicated by first measurable OH* signal, with increasing amounts of premixed methane.

Dronniou *et al.* [33] focused on the effect of the premixed charge equivalence ratio using time-resolved natural luminosity and single-shot OH* chemiluminescence imaging in an optically-accessible 0.5L single-cylinder engine. Single-shot PLIF-tracer¹ imaging under equivalent motored conditions was also considered to

¹Planar Laser Induced Fluorescence of a tracer species added to pure nitrogen instead of air

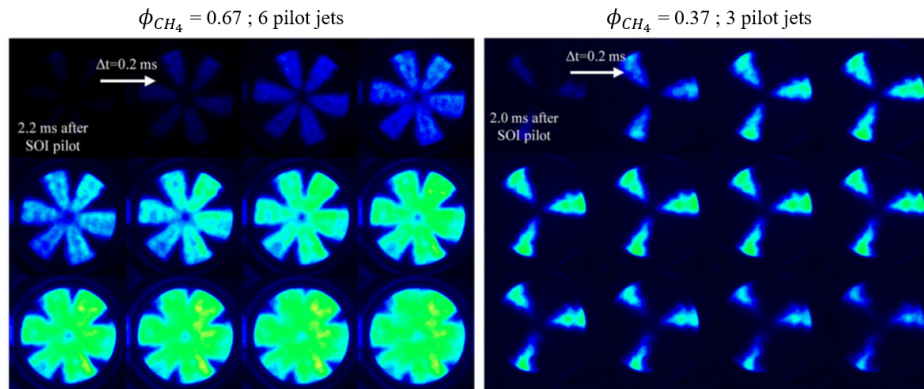


Figure 2.7: OH*-chemiluminescence image sequences for high-load (left) and low-load (right) DIFD operation in an RCEM, with 6 and 3 pilot jets, respectively. Adapted from [133] with permission from publisher.

characterize spatial distribution of the pilot fuel and provide complimentary information during the ignition process. The major goal of the work was to identify principal combustion regimes characterizing the dual-fuel combustion processes. More specifically, whether the DIFD combustion can be described by auto-ignition or sequential auto-ignition, flame propagation, diffusion, or a combination of these combustion modes. NL and OH* chemiluminescence results showed that the ignition consistently occurred in the bowl periphery throughout a sweep of global equivalence ratios (ϕ_{global}) in the range 0.33-0.94, while the injected pilot mass was held constant. From there, the high temperature reactions show increasingly more intense OH* chemiluminescence and develop further towards the central bowl region. Although it was acknowledged that differentiating sequential auto-ignition from flame propagation would be challenging, the reaction zone growth was interpreted as flame propagation based on experimental and numerical laminar flame speed analyses for methane-air mixtures [32] and repeating experiments with a lower octane fuel (iso-octane) [33]. The extent of reaction zone growth towards the center was observed to correlate with the equivalence ratio. Full growth and homogeneous high intensity OH* chemiluminescence was recorded at $\phi_{\text{global}} = 0.94$, while a notable part of the bowl area was left with no OH* signal detected at $\phi_{\text{global}} = 0.56$. The described reaction zone growth comparison is shown in Figure 2.8, reprinted from [33]. It was concluded that the observed higher unburned

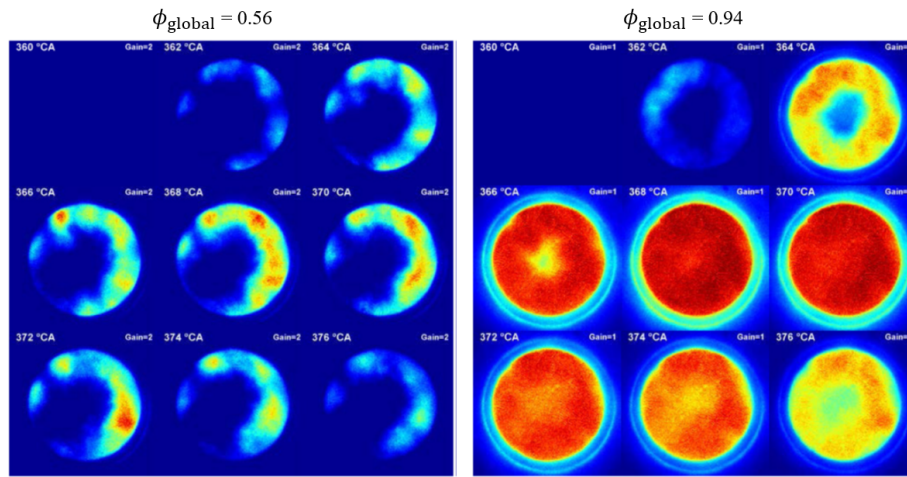


Figure 2.8: OH*-chemiluminescence image sequences for low-load (left) and high-load (right) DIDF operation with constant pilot mass. Adapted from [33] with permission from publisher

hydrocarbon emissions during fuel-lean DIDF operating conditions, is to a great extent, an artifact of the reaction zone not being able to propagate further through the globally leaner mixture and reach the central bowl regions.

The DIDF combustion mode illustrated in Figure 2.8 significantly differ from those described by Schlatter *et al.* in Figure 2.7, where the flame propagation appears to initiate around the injected pilot jets, despite the similar injection pressures and injected masses. This discrepancy is further discussed later in Chapter 4. In addition to the more conventional DIDF operations, optical investigations on alternative dual-fuel applications are available. Florea investigated ethanol and n-heptane dual-fuel partially-premixed combustion using time-resolved NL and single-shot OH* measurements [42] and Mancaruso *et al.* studied bio-ethanol and diesel dual-fuel using single-shot spectroscopic measurements [93].

2.2.2 PIDING

The Pilot Ignited Direct Injected Natural Gas (PIDING) combustion strategy, is a commercially viable technology that addresses the common problems associated with conventional dual-fuel combustion[33, 75, 80, 153], while matching perfor-

mance of conventional diesel combustion. The PIDING injector uses concentric, hydraulic-servo actuated needles to control both natural gas and diesel injection and enables diesel pilot ignited, direct injected natural gas combustion. Near top dead center, high pressure natural gas (NG), which constitutes approximately 95% of the total energy, is injected and ignited by the combustion of a small amount of direct injected diesel. In a typical operating condition, the diesel pilot injection and ignition precede the NG injection. This combustion approach has been commercialized by Westport Fuel Systems Inc. as High-pressure direct-injection (HPDI) of NG [112].

Previous understanding of the impacts of the pilot ignition and subsequent fuel-air mixing and combustion process of the gas jets have depended on experiments [34, 38, 97, 99, 100], or CFD simulations [54, 90, 114]. PIDING experimental investigations have been based on conventional thermodynamic analyses using in-cylinder pressure traces and engine boundary conditions, or engine-out emissions measurements of soot and various gaseous species. Based on these extensive surveys, the PIDING strategy is perceived as being predominantly governed by non-premixed NG combustion, preceded by a fraction of premixed NG combustion before transition to the non-premixed stage, similar to conventional diesel combustion [38, 99]. Fraction and mode of the premixed NG combustion phase [38], determined by engine control parameters such as combustion timing and relative delay between the pilot and NG injection [99, 100], and fuel rail pressure and combustion duration [34, 98], have been characterized as the major factors that could be “tailored” to control engine-out PM emissions, while also affecting CO, tHC and NO_x emissions during PIDING combustion. The relative pilot and NG injection timing, and the interlace angle between the pilot and NG nozzle holes, was reported to determine the state and locus of the ignited pilot kernels and the corresponding interaction with the NG jets, significantly impacting the NG ignition processes [97]. Ultimately, the variations to the ignition processes impact soot formation, oxidation, and engine-out emissions [34, 38, 90]. Advancing the gas injection relative to the diesel ignition can lead to a more premixed combustion strategy, especially at lower engine loads, reducing PM and CO emissions substantially at the expense of increased tHC and NO_x emissions [34, 99, 100]. As in conventional diesel engines, high thermal efficiencies can be achieved through increasing the fuel rail

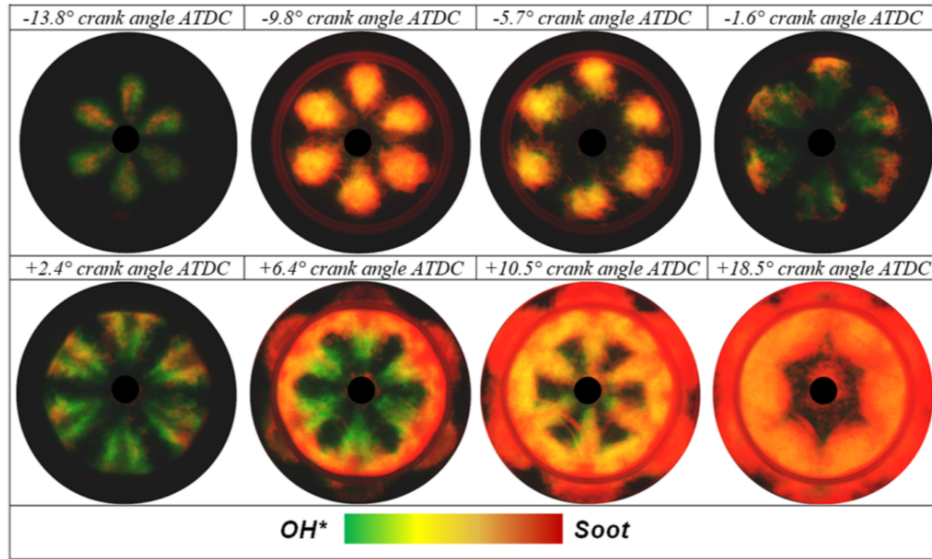


Figure 2.9: Combined 15-cycle ensemble averaged 2D images of OH* chemiluminescence and NL from PIDING combustion. Adapted from [54] with permission from publisher

pressure, which results in higher NG injection rates and more rapid combustion processes [34]. Higher fuel rail pressure is reported to substantially improve fuel conversion efficiency and particulate oxidation through enhanced mixing after the end of the injection event, leading to improved efficiency and reduced PM emissions [98]. However, the more rapid non-premixed burning rates will also produce higher flame temperatures and was observed to increase NO_x emissions [34].

To date, only one optical investigation of PIDING combustion has been published [54]. In this work, simultaneous 2D OH* chemiluminescence and filtered natural luminosity measurements were used to analyze the mixture formation and ignition of the gas jets, and to validate numerical simulation of these processes. A 2.13 L single-cylinder engine with a 17.3 compression ratio, available in both thermodynamic “all-metal” and optical configurations with an omega-shaped quartz glass piston window, was used in this work. PIDING combustion was broken down into four combustion phases of diesel pilot combustion (1), ignition of gas jets at diesel pilot zones (2), main combustion of natural gas with main heat release (3), and soot post-oxidation (4). Figure 2.9 shows an image sequence of PIDING

combustion produced based on combined 2D ensemble averaged images (from 15 cycles) of the OH* chemiluminescence and natural luminosity. More detailed discussion of these results, in conjunction with the findings of the work presented herein, is presented in Chapter 6. After validating their simulation methodology against thermodynamic engine measurements of the pressure traces, heat release rates, and “end of engine” soot, Hatzipanagiotou *et al.* compared local combustion features and observed a good agreement between optical measurements and simulations.

2.3 Summary and Literature Gap

The complexities and intricacies of the phenomena involved in diesel-ignited dual-fuel combustion strategies go well beyond the already analytically challenging physical and chemical processes occurring in conventional diesel engines. The port fuel injection of NG during DDF, for instance, significantly changes the compression processes and the properties of the premixed charge and, consequently, the combustion chamber conditions at the time of direct injection of the diesel fuel. This has been shown to influence the pilot fuel ignition processes [91, 115], which, as a result, significantly affects the combustion of the premixed charge itself and the resulting gaseous and PM emissions [69, 115, 154]. Also, while the PIDING combustion strategy is generally perceived to have similarities with diesel engine operation characteristics and can achieve diesel-like efficiency with lower PM and greenhouse gas emissions [34, 112], significant differences in the soot processes are expected to result from replacing the liquid diesel sprays with non-premixed gaseous jets.

The highly complex and interrelated chemical and physical processes occurring during these combustion processes demands for application of a wide range of experimental and numerical investigations in order to provide more insight into and better characterize these seemingly perplexing mechanisms. This better understanding would be imperative for making improvements to the current designs with the goal of surpassing the performance of existing technologies and replacing them with more efficient technologies with less pollutant emissions. The conventional thermodynamic analysis of in-cylinder pressure traces and engine boundary condi-

tions, analysis of engine-out emissions measurements, and CFD simulations, have already provided invaluable information regarding DIDF and PIDING combustion strategies, as reviewed in §2.2. In the case of PIDING combustion, these experimental investigations and numerical simulations highlighted some of its fundamental characteristics differing from those of conventional diesel and DIDF combustion strategies.

As also elucidated in §2.2, optical measurements of the combustion in-cylinder phenomena offer a unique perspective into the problem, providing a more in-depth analysis of the information that is otherwise inaccessible. Nevertheless, limited number of optical investigations of these combustion processes and their control parameter effects are reported in literature (discussed later in this chapter), and many aspects of their conceptual behavior are yet to be studied and characterized. As an example, discrepancies were observed in the ignition processes and reaction zone growth behavior of the DIDF combustion in optical measurements by Droniou *et al.* and Schlatter *et al.*, which is not explained [33, 133]. As such, a section of the current work has focused on addressing some of these unanswered questions. More importantly, however, none of the available optical studies have implemented detailed spatially resolved quantitative measurements of soot concentration and temperature distributions, using techniques such as the two-color pyrometry, to study in-cylinder conditions of NG combustion in diesel engines. Diagnostic techniques are of great significance for better characterization of the hypothesized combustion mechanisms developed based on prior experimental investigations and would allow further optimization of the existing CFD tools.

The examples reviewed in §2.1.4 illustrated the utility of multi-color pyrometry for in-cylinder soot analysis in conventional diesel engines. Closer examination of the calculated soot temperature and KL factor distributions presented across these studies partly reveals its challenges, appearing occasionally in the form of regions with unresolved data, as shown in §2.1.4. Majorly contributing to the lack of such quantitative optical investigations for diesel-ignited dual-fuel operation to date is the additional challenges associated with the low-SNR optical signal available from these and other low-sooting combustion strategies. Essentially, since the two-color pyrometry method is an unstimulated emission technique, its implementation becomes more challenging at lower soot concentrations and temperatures

where the SNR decreases. This can be particularly problematic for strategies such as Low Temperature Combustion (LTC), or PIDING combustion [112], where exhaust stream soot is relevant but in-cylinder concentrations and temperatures are lower than in conventional diesel combustion. Some studies have applied the integrated light two-color pyrometry technique to low-sooting, low-temperature applications. Singh *et al.* [136] used this technique, along with high-speed spatially resolved natural luminosity imaging to characterize the lower soot concentrations representative of low-temperature diesel combustion (LTC). In a more recent study, Hatzipanagiotou *et al.* [54] used integrated light two-color pyrometry for analysis of PIDING combustion. Both of these works attempted to use 2D natural luminosity as a means to roughly describe soot distributions. However, comparison of the integrated combustion light intensities at three wavelengths, where two were used for two-color pyrometry and the third was used as a reference soot luminosity signal, in general, did not show a close correlation between natural luminosity and pyrometry soot signal trends [108, 136], as can be seen in Figure 2.5 ($f_v L$ vs. combustion luminosity curves). Spatially resolved two-color pyrometry measurements of these lower-soot combustion methods, however, is more challenging and has not been reported in the literature. As a major contribution, this work will demonstrate improvements to the two-color pyrometry method to facilitate its application for low-sooting combustion conditions. The improved method is then implemented to PIDING combustion and a conceptual understanding of the in-cylinder soot formation and oxidation processes is presented.

The undeniable advantages and valuable information the spatially resolved optical measurements of combustion in-cylinder processes offer, however, is only possible at the expense of alterations to the engine operating conditions. As discussed in §2.1.1, these changes are imposed by the necessary major modifications to the combustion chamber geometry and measures are adopted to compensate for them primarily through manipulation of intake air conditions and fuel injection parameters to match charge conditions at TDC, combustion phasing, and the shape of the HRR profile. Nevertheless, a remaining valid concern is the discrepancies these intrinsically different engine operations might cause for in-cylinder optical measurements and the extent that the optical measurements findings would be relevant to more realistic and less idealized conditions of a thermodynamic en-

gine operation. Several studies have been performed on highlighting the need to characterise the differences between optical and all-metal engine measurements [5, 23, 72]. These include investigating the effects of piston surface temperature differences, using cycle-resolved thermocouples in DISI engine [139] and material properties of optical components (windows), and the differing heat transfer characteristics [5], as well as simplified flat bowl vs. more representative toroidal bowl design [79] and implementing (simulated/synthetic) EGR, on in-cylinder phenomena in the two engines. Study of implications of the described differences, and additional factors such as dynamic loading of the Bowditch piston, on charge mixing, combustion, and emissions under LTC diesel operating conditions indicated significant discrepancies and several necessary measures for valid comparison of the results [72]. The described complexities associated with spatially resolved optical measurements from in-cylinder combustion phenomena, motivates OD optical diagnostics of these processes under all-metal engine configurations. The major deficiency of such measurements is the lack of spatial attributes in the spatially integrated light from a control volume whose geometry changes with piston movement. Thus, as another novel contribution, the current work focuses on characterizing the integrated light measurement signal from an optical probe design (see §2.1.1) through comparisons with simultaneously recorded spatially resolved measurements. The better characterized optical probe is then used for comparison of the pyrometric measurements of in-cylinder soot processes in optical and thermodynamic engines, which has not been reported in literature.

The characterized rugged optical probe, together with thermodynamic analysis metrics (e.g., HRR and fuel flow rates), and exhaust stream measurement tools, would provide a valuable “Thermo-Optical” analysis toolkit to study combustion in-cylinder processes. Such analysis toolkit could help optimize the operating protocols and improve future designs of various combustion strategies.

Chapter 3

Experimental Setup

In this chapter, a description of the experimental facilities and measurements systems developed and utilized in this work are presented. These details elucidate the measurement capabilities of the integrated diagnostics system as well as the operational restrictions, the range of possible measurements, and limitations imposed to the interpretation of the results.

3.1 Engine

The experimental facility used in this work is a single-cylinder optical research engine (Ricardo Proteus) with a Bowditch design. The geometry is representative of a 2.0 Litre heavy-duty compression ignition engine. The core feature of the facility is the ability to convert between two distinct configurations:

1. Thermodynamic Configuration; which has a geometry similar to a conventional IC engine, also referred to as the “all metal” engine configuration.
2. Optical Configuration; which provides large optical access into the combustion chamber, affording 2-D visualization of the combustion processes in the piston bowl, at the expense of engine and bowl geometry modifications.

Relevant specifications of the engine are provided in Table 3.1 and are compared to a typical heavy-duty engine.

Table 3.1: Optical engine specifications

	Ricardo Proteus	Typical HD Diesel/NG
Type	4-stroke, compression ignition	
Number of cylinders	1	6
Displacement	1998 cm^3	2500 cm^3
Bore	130 mm	135 mm
Stroke	152 mm	170 mm
Max. cylinder pressure	170 bar (thermodynamic) 117 bar (optical)	180 bar
Compression Ratio	13.9:1 (thermodynamic) 12.9:1 (optical)	17:1
Max. speed	2050 rpm (thermodynamic) 1200 rpm (optical)	2050 rpm
Max. charge pressure	3 bar	turbocharger limited
Visible bore	83 mm; ~40% of bore area	N/A

The Ricardo Proteus engine design is based on the Volvo TD120-family of engines. These were 12-litre, in-inline 6-cylinder (I6), overhead valve, heavy-duty CI engines, originally designed for on-highway applications. Designed as a research-oriented single-cylinder engine (single head, cylinder, piston, and valve train assembly from the stock Volvo engine), with the capability to transition between the two described configurations, the Ricardo Proteus engine provides a platform for combustion diagnostics focusing on the in cylinder processes of a heavy-duty CI engine. Under the “all metal” thermodynamic configuration, an eccentric toroidal bowl design is used and there is no major modifications to that of a conventional CI engine, except for small diagnostic ports to allow in-cylinder measurements of certain combustion characteristics. As such, more realistic operating conditions, resembling those on-road applications, can be investigated. Under the optical con-

figuration the engine, a large optical access to the combustion chamber is afforded through use of a Bowditch piston design (see §2.1.1). This results in a square bowl design as a result of the installed flat quartz window. Although this optical access opens up extensive opportunities for acquiring more insight into combustion in-cylinder processes through spatially and temporally resolved optical diagnostics, the necessary major modifications to the engine geometry inevitably introduces restrictions to the range of operating conditions, operating protocols, and interpretations to be made through the analysis of the results. This is discussed in further detail in §3.3 and §2.1.1.

3.1.1 Engine Facility Instrumentation

The described research engine and the test-cell it is operated in are equipped with many auxiliary systems and diagnostic tools. Many of these sensors are responsible for monitoring engine health and test-cell safety and not utilized combustion analysis (e.g, thermocouples, pressure sensors, dyno speed sensors, and chemical alarms). Sensors that were crucial in the collection of combustion related engine data are listed in Table 3.2 and details of how they are connected to and controlled by data acquisition and engine control unit systems are available in [156].

Table 3.2: Engine sensors used in combustion analysis.

Measurement	Sensor Description
Methane mass flow rate	Endress & Hauser Promass 80A Coriolis Meter
Diesel mass flow rate	Mettler Toledo Viper Ex MB SM12 Gravitric Scale
Intake mass airflow rate	Bosch OEM Hot Film Sensor
Intake manifold absolute pressure transducer	Kistler 4005B Piezo-resistive Pressure Sensor; Kistler 4618A Amplifier
In-cylinder pressure transducer	Kistler 6125C Piezo-electric Pressure Sensor; Kistler 5010B Charge Amplifier
Engine position and crank-synchronous timing	BEI H25 Incremental Quadrature Optical Encoder; Hamlin 55505 Hall Effect Sensor mounted on flywheel; Hamlin 55505 Hall Effect Sensor mounted on cam-gear

As discussed in the previous chapter, the developed optical diagnostics in the work presented herein were designed for and implemented to DIDF and PIDING combustion strategies (see §2.2). For DIDF combustion experiments, port injection of methane was executed via a Bosch NGI2 injector and pilot diesel fuel was directly injected using a Bosch CRIN2 injector. For PIDING combustion experiments, a research-level High-Pressure Direct Injection (HPDI) injector was used for direct injection of Natural Gas (NG) and diesel (separate internal fuel lines). This injector was supplied by Westport Fuel Systems and is derived from their production first-generation HPDI fuel system. More details regarding this injector design and operation was presented in §2.2.

National Instrument's Powertrain Control hardware was used to control the fuel injection system. The control hardware is based on a field-programmable gate array (FPGA) and uses the NI cRIO-9068 (CompactRIO) chassis with selected Powertrain Control modules as hardware drivers for the various sensors and actuators on the engine. A simplified process and instrumentation diagram for the PIDING combustion experiments under optical configuration of the engine is presented in Figure 3.1.

The commissioning of the Ricardo Proteus engine under thermodynamic configuration and the first major research investigations conducted using this engine facility was performed prior to this work and recently reported by other group members [124, 156]. A complete description of the facility can be found in [124]. This work focused on the development of the spatially and temporally resolved optical measurement (i.e., high-speed imaging) systems.

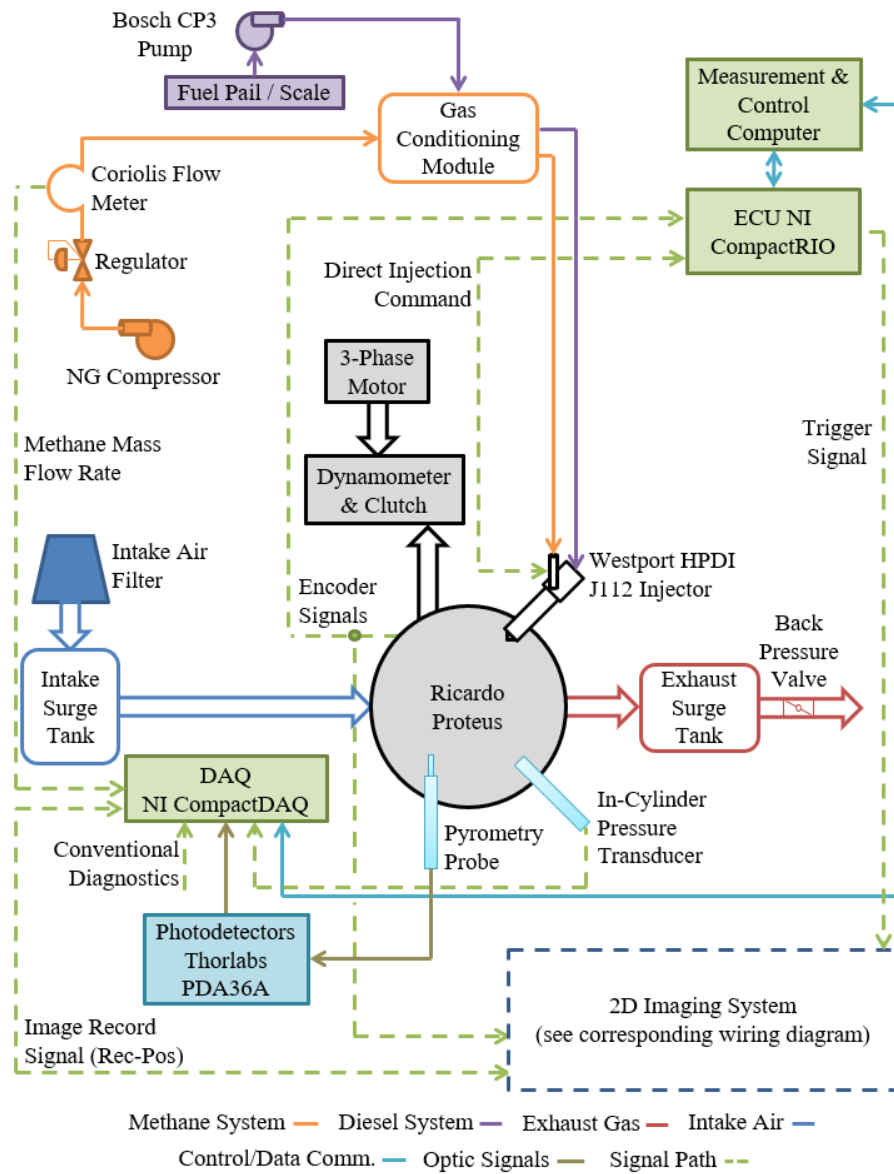


Figure 3.1: Experimental facility process and instrumentation diagram for PIDING combustion experiments under optical configuration.

3.2 Imaging Systems

A major focus of this work was to develop spatially and temporally resolved optical diagnostics, integrate them with the existing engine facility, and discuss the measurement results in conjunction with the thermodynamic and spatially-integrated optical measurement results. As such, preparations for three different classes of spatially resolved optical measurement techniques, namely natural luminosity, chemiluminescence, and two-color pyrometry, were considered. This was followed by the calibration of the optical probe in order to better characterize its spatially-integrated signal through comparisons with the spatially resolved measurements. Ultimately, these comparisons would help extend the interpretations that can be made from the results obtained through restricted optical access available under thermodynamic configuration of the engine.

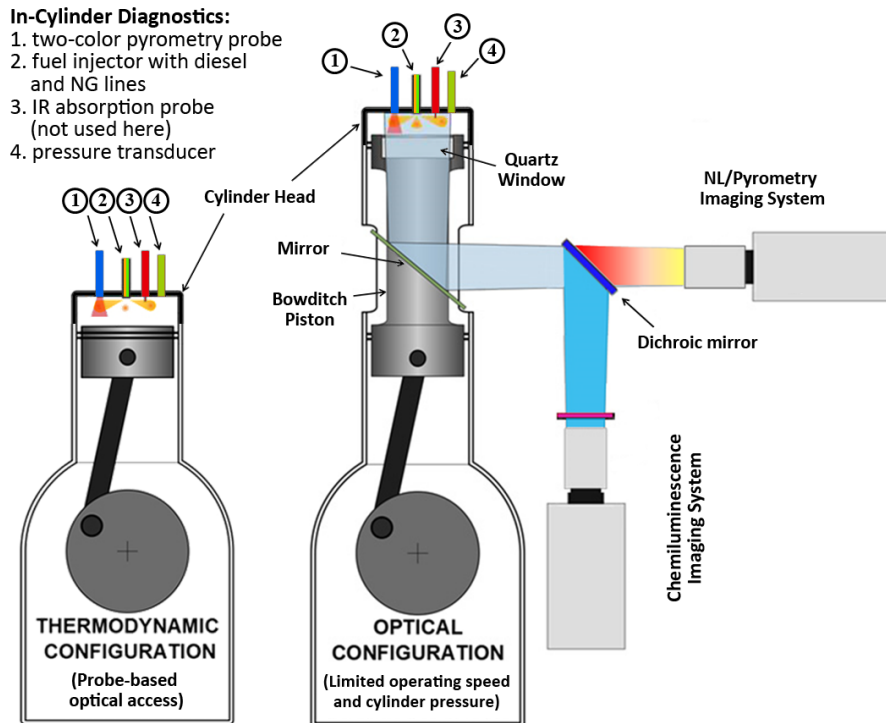


Figure 3.2: Schematic of thermodynamic and optical configuration of the Ricardo Proteus engine and imaging system setup on the optical engine.

Table 3.3: Optical Imaging Equipment

High-Speed Cameras		
Camera	Phantom V7.1	Photron SA-1
Sensor design	CMOS	CMOS
Sensor ISO	4,800	10,000
Bit-depth	12	12
Max. resolution	800×600 pix ²	1024×1024 pix ²
Pixel size	22 μm	20 μm
Max. frame rate (full res.)	4,500 fps	5,400 fps
Min. exposure duration	2 μsec	1 μsec
Spectral response	200 nm - 1,100 nm	200 nm - 1,100 nm
Paired objective lens	60 mm-f/2.8 Micro-Nikkor	98 mm-f/2.8 Cerco UV
Trigger signal input	TTL	TTL
Digital interface	Gigabit Ethernet	Gigabit Ethernet
Primary lens mount		F-mount
Image Intensifier		
Design	LaVision two-stage high-speed IRO	
Spectral response	200-900 nm	
Min. gate	100 ns	
Max. operation frequency	2 MHz	
Max. MCP amplification	1000×	
Image size	25 mm	
Camera Coupling	1:1 optical lens coupling	
Photocathode	S20	
Phosphor screen	P46	

The thermodynamic and optical configuration of the Ricardo Proteus engine, together with simultaneous imaging equipment setup, are schematically shown in Figure 3.2 and imaging system general specifications are presented in Tables 3.3 and 3.4. Details of individual components of the imaging equipment and the integrated optical measurement systems are discussed in the next section.

Table 3.4: Imaging Systems Assemblies

Imaging technique	Sensing Optics	Light Collection Optics	Optical Filters
2D natural luminosity	Phantom camera	Nikon lens	optional HP filter
2D two-color pyrometry	Phantom camera	Nikon lens and doubler	700 & 800 nm CWL; 10 nm FWHM
2D OH* CL	Photron & IRO	Cerco UV lens	307nm CWL & 20nm FWHM (compound)
0D two-color pyrometry	PDA36a	Sapphire rod lens, fibre optics and collimators	700 & 800 nm CWL; 10 nm FWHM

3.2.1 Natural Luminosity Imaging

Details of the NL imaging technique was discussed in §2.1.2. A Phantom V7.1 high-speed camera, equipped with a 60 mm $f/2.8$ Nikon objective lens (Micro-Nikkor AF-D), was used for NL measurements in this work. The camera has a 12-bit monochrome CMOS sensor with 800×600 pixel resolution and $22 \times 22 \mu m^2$ pixel area. Details of high-speed camera setup considerations are provided in Appendix A.

3.2.2 Two-Color Pyrometry Imaging

The two-color pyrometry technique fundamentals were discussed in §2.1.4. The same camera and objective lens system used for NL imaging was also used for two-color pyrometry measurements. An image doubler design and an integrating sphere are the other two essential elements of the two-color pyrometry imaging system. In what follows details of these two pieces of equipment are discussed.

Image Doubler

The two-color pyrometry measurement principles discussed in §2.1.4 elucidated that in order to perform two-color pyrometry measurements using a single monochrome camera, two simultaneous images of an instantaneous combustion event should be projected onto the camera sensor. This was carried out in the current study using

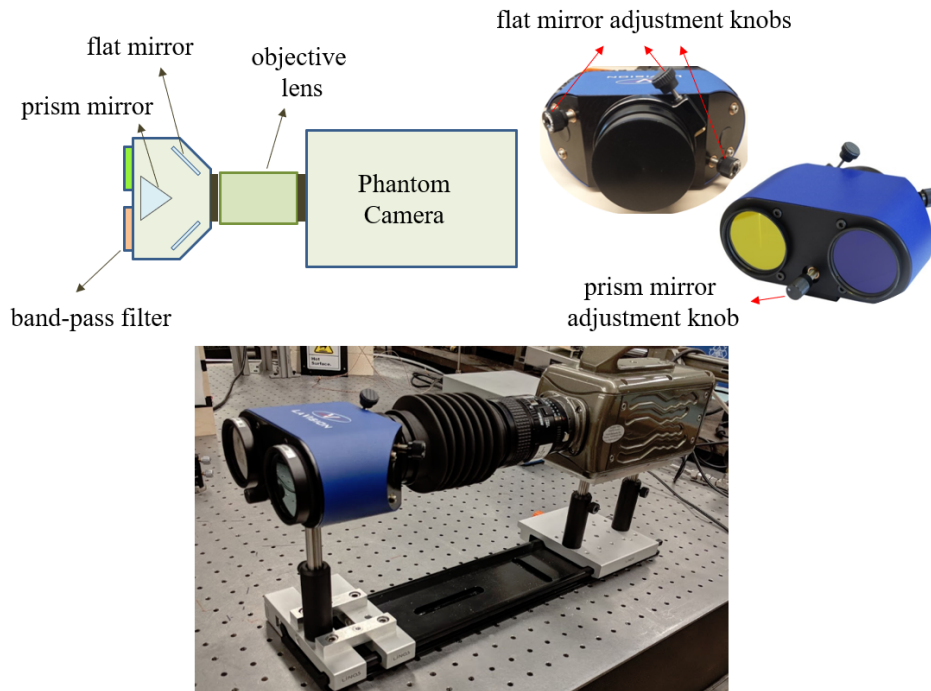


Figure 3.3: Image doubler design and two-color pyrometry system schematic.

a LaVision image doubler, mounted with a stand-off distance in front of the Phantom V7.1 camera, equipped with the 60 mm f/2.8 Nikon objective lens. The image doubler is an optical assembly that duplicates the original image and projects them onto the sensor side by side using adjustable flat and prism mirrors. Figure 3.3 shows a schematic diagram and a photo of the optical assembly for the two-color pyrometry imaging system. The pair of flat mirrors can be horizontally and vertically adjusted for proper projection of the individual duplicated images. The prism mirror sits on a rail parallel to the optical axis, which allows for controlling the light interference from one channel to the other (referred to as the cross-talk between channels). A pair of narrow band-pass filters are mounted onto the channel light input ports, to view each image within a different bandwidth.

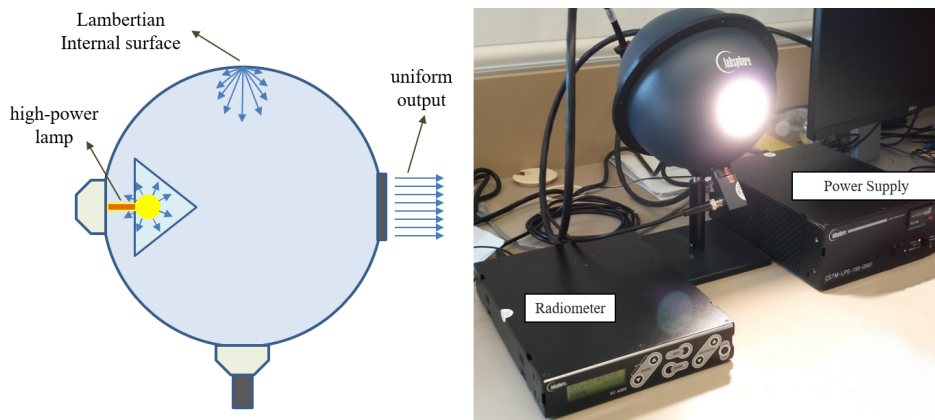


Figure 3.4: Chemiluminescence Imaging system setup

Integrating Sphere

The purpose of the two-color pyrometry imaging system is providing instantaneous measurements of the apparent temperatures of the combustion at the two wavelengths being considered. This is executed through quantifying the spectral radiant intensity radiated from the combustion flames. Thus, it is necessary to calibrate the response of the sensor to the incident spectral radiant intensity. The instantaneous spectral radiant intensity $I_{\lambda}(x_{i,j}, t)$, which is the required input to the two-color pyrometry equation 2.4 (see §2.1.4), is evaluated from the recorded images using a reference characterized light source. A high-intensity integrating sphere setup, custom design by LabSphere, comprising a 150W NIST traceable calibrated tungsten halogen lamp controlled by a precision regulated DC current power supply and a 200 mm diameter integrating sphere with a 50 mm light port is used as the calibration light source in this work. The calibration system output is monitored by a radiometer during calibration. A schematic diagram and photo of the integrating sphere are shown in Figure 3.4.

The cone baffle and the internal Lambertian surface design of the integrating sphere provides a uniform light output, with 98% uniformity across its exit port. The large light port provides illumination of a large part of the sensor area at once and enables the sensor response uniformity to be characterized.

During the calibration process the integrating sphere is mounted on the op-

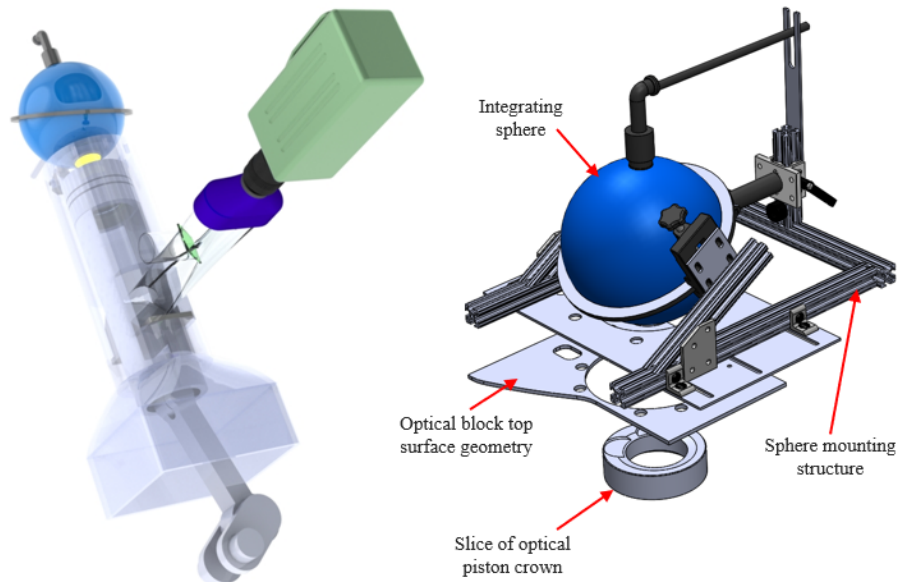


Figure 3.5: The two-color pyrometry calibration setup (left) and the integrating sphere mounting structure (right).

tical engine block in place of the cylinder head and the response calibration is determined with all relevant optical components in the light path. The integrating sphere and the mounting structure are shown in Figure 3.5, along with the two-color pyrometry calibration setup. To assess the sensor non-uniformity, the integrating sphere is translated such that the entire field-of-view of the two-color pyrometry measurement system is illuminated. At each position, an average of 30 images is considered to eliminate the effect of shot noise and is spatially averaged over a smaller area at the center of the sphere target image to avoid potential pixel bias.

The integrating sphere was selected over commonly used tungsten-ribbon lamps [64, 117], as the latter provides a small calibration target ($1.6 \times 20 \text{ mm}^2$ [117]), with only slightly higher spectral radiant intensity levels ($\sim 5e3$ vs. $8e3 \text{ W/m}^2 \cdot \text{sr} \cdot \mu\text{m}$). Other lower intensity light sources have also been used, including tungsten light sources [52, 92, 160] and low intensity blackbody sources [158, 160]. These sources consequently require more significant extrapolation to combustion intensi-

ties under consideration.

Despite using a high intensity light source for calibration, the maximum spectral radiant intensity provided by the integrating sphere was still lower than that of the combustion process (e.g., $9.5e4 \text{ W/m}^2\cdot\text{sr}\cdot\mu\text{m}$ maximum intensity was detected in this work), as is typically the case with two-color pyrometry system calibration [52, 64, 92, 117, 158, 160]. During preliminary engine combustion imaging, optimum objective lens aperture to be used for both the calibration and combustion imaging was identified and sensor exposure duration was adjusted to properly record higher intensity combustion images with minimal saturation. Although the lens aperture setting (f-number) can be incorporated into the signal calibration process, bench top measurements showed that the factor of two estimation in light intensity change due to light-stop increments is an approximation that introduces small, yet preventable errors in the calculated results. The ratio of the sensor exposure durations for calibrating integrating sphere signal and the experiment was used as the scaling factor for the spectral radiant intensity extrapolation in the calibration curves (X_τ).

In order to calibrate the camera sensor response, measurements from a sweep of characterized spectral radiant intensities are required to obtain calibration curves at the two pyrometry channels. This can be achieved through selective attenuation of the integrating sphere signal using neutral density filters with a range of optical densities, without altering the spectral information of the incident light (see §3.2.4). However, bench top measurements suggest that exposure duration time can be used to mimic physically attenuated integrating sphere signal through use of neutral density filters. This would significantly expedite the sensor response calibration process, typically performed prior to a two-color pyrometry measurement campaign. Figure 3.6 shows an example of a response calibration curve acquired using the integrating sphere and also compares the two different approaches to perform the required reference intensity sweep as described above. As can be seen here, the use of camera exposure for sensor response calibration also allows for a high resolution calibration curve, which can be used to examine the linearity of the correlation between the illuminating light and recorded charge on the CMOS sensor. The final stage in the sensor response calibration process is attributing the recorded intensity values to characterized spectral radiant intensity values of the

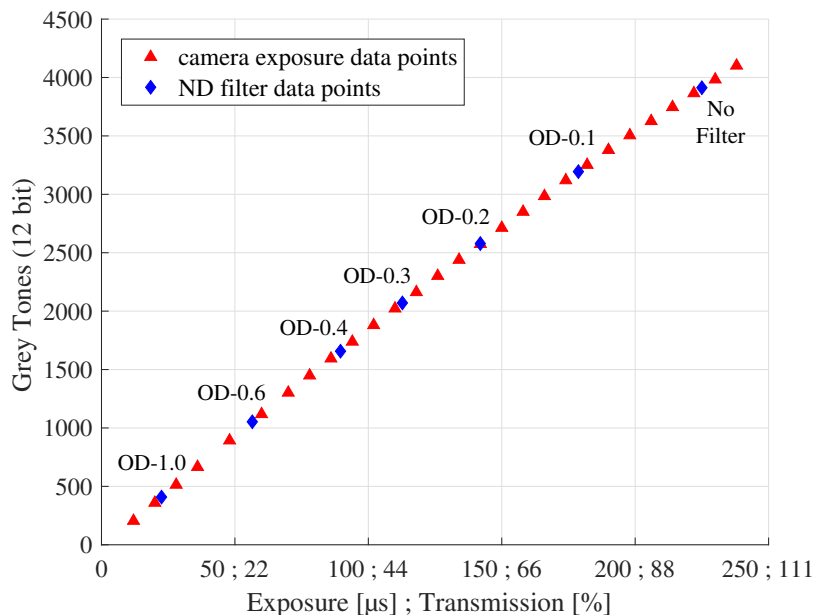


Figure 3.6: Sample response calibration data points obtained for 800 nm two-color pyrometry channel from sweep of camera exposure as well as using a set of ND filters. The “no filter” data point was recorded at 225 μ sec camera exposure.

integrating sphere (see Chapter 5).

3.2.3 OH* Chemiluminescence Imaging

Details of the chemiluminescence imaging technique was discussed in §2.1.3. In this work, OH* chemiluminescence measurements were carried using a Photron SA-1 high-speed camera, equipped with a high-speed image intensifier and a 100 mm f/2.8 Cerco® UV objective lens. This camera holds a 12-bit monochrome CMOS sensor with 1024×1024 pixel resolution and 20×20 μm^2 pixel area.

As discussed in §2.1.3, chemiluminescence imaging of the combustion intermediate species targets relatively low intensity signals within small spectral bandwidths around certain wavelength peaks. A fraction of the already weak signal is also lost to attenuation in the optical path in the processes of guiding it towards the imaging sensor (engine window and mirror) and restricting the incoming light

to the desired spectral range (see §3.2.4). This necessitates a significant increase in the SNR and a shift the target wavelength before the signal can be recorded at the spectral and ISO ranges of the high-speed CMOS sensors. Image intensifier designs, also referred to as the intensified relay optics (IRO), can fulfill this task. These are electro-optical devices, which in a conventional design comprise three main stages:

1. A photocathode plane, which when illuminated, transfers the incident photon quanta to the electrons and, as such, converts the light rays into electron beams.
2. A micro channel plate (MCP); which amplifies the signal as the electrons pass through its numerous microscopic high-voltage semi-conductor channels, acting as photomultipliers.
3. A phosphor screen, which re-converts the amplified electron beams back to light, after accelerating them using a high potential applied to it.

For this setup, the objective lens focuses the image onto the photocathode plane. The photocathode, in addition to photon-electron conversion, serves as a very fast global electronic shutter as it is connected to a high-voltage pulser, affording exposure duration values (referred to as “the gating”) in the order of a few nanoseconds. The electron beams are then amplified traversing the high-voltage MCP, where the magnitude of electron amplification is controlled by the adjustable potential across the MCP (referred to as “the intensifier gain”). The electrons leaving MCP are accelerated towards the phosphor screen by a fixed bias voltage of several kV, to increase electron-photon conversion efficiency.

In this work, a LaVision high-speed two-stage IRO, capable of relaying intensified images at high rates of 2 MHz, was used. The output image from the IRO was guided to the Photron SA-1 sensor for OH* chemiluminescence measurements. Given the complexities involved in the photocathode-intensive two-stage focusing process of the chemiluminescence imaging system, the camera and IRO were fixed on a designed adjustable base after calibrated for the best intensified image focus. A schematic diagram and a photo of assembled chemiluminescence imaging system are shown in Figure 3.7

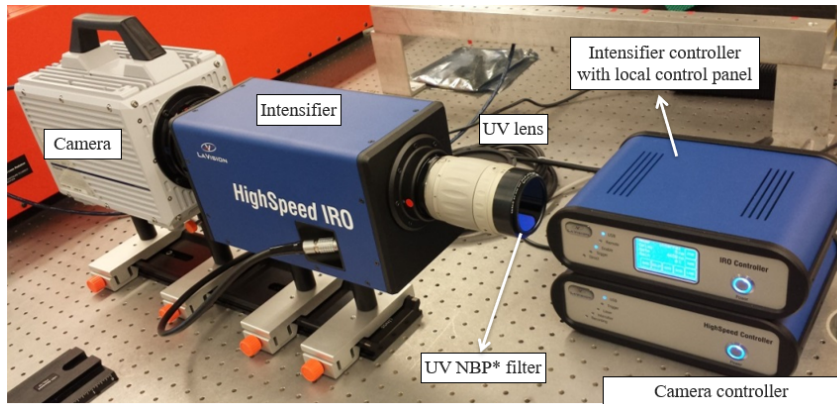
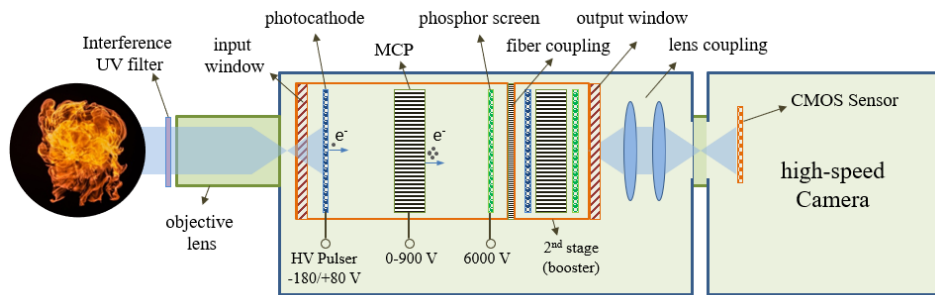


Figure 3.7: Chemiluminescence Imaging system setup

3.2.4 Spectral Optics

As discussed in §2.1.3 and §2.1.4, depending on the considered application, the broadband light from the combustion event often is required to be restitched to a certain spectral bandwidth. This is achieved through spectral filtering of the incoming combustion light before it reaches the camera sensor, through use of short-pass, long-pass, and narrow band-pass (NBP) filters. These filters have special coatings that would selectively transmit, absorb, and reflect wavelengths of incident light. For natural luminosity measurements, depending on the case under consideration, either the broad-band unfiltered light was recorded or a long-pass filter with 575 nm edge wavelength (Omega Optical-575HLP) was considered. The latter would focus the measurements on the incandescent soot particles and eliminate the majority of the chemiluminescence signal (e.g., from OH*, CH*, CN, Swan bands; see §2.1.3). In the case of two-color pyrometry, a pair of hard coated narrow band-pass filters with 700 nm and 800 nm central wavelength (CWL) and 10 nm FWHM bandwidth

(Edmund Optics) were used. These filters have optical density of more than 4 (OD-4) for out-of-band rejection (200-1200 nm range) to avoid signal interference from outside the pass-band. Equation 3.1 describes the relation between filter optical density (OD) and transmission ($T_{\text{filter}}[\%]$).

$$OD = -\log_{10} \frac{T_{\text{filter}}}{100} \quad (3.1)$$

For OH* chemiluminescence measurements, a compound filter set comprising a narrow band-pass filter with 310 nm CWL and 20 nm FWHM (Chroma; CT31020 UV NBP) and a custom band-pass filter with 330 nm CWL and 80 nm FWHM was used (Omega Optical; based on 330WB80 with higher transmissivity at 307 nm). The narrow band-pass OH* filter (Chroma) provides excellent transmissivity in the pass-band and OD-6 out-of-band rejection in the 200-390 nm range, but suffers from interference after 400 nm (low out-of-band rejection); in order to block this spectral interference region, the band-pass filter (Omega Optical) was considered since its pass-band overlaps that of the primary NBP filter, with a relatively high transmissivity, and it provides OD-6 rejection in 380-700 nm and OD-5 in 700-1200 nm range. As such, the filter combination offers a high transmission of ~70% in the overlapping pass-band, while effectively rejecting out-of-band signal interference. In addition, a UV enhanced long-pass dichroic mirror, with 350 nm edge wavelength (Chroma-ZT325DCLPXT), was used for simultaneous OH* chemiluminescence and natural luminosity/two-color pyrometry measurements. The mirror reflects the UV light towards the chemiluminescence imaging system, with a 98% reflectivity at 307 nm and adds another OD-3 rejection to the higher wavelengths in the visible range, expected from high intensity incandescence signals from particles at elevated temperatures.

In all cases discussed above, the significant drop in the CMOS sensor and the photocathode quantum efficiency to nearly zero beyond 1,100 and 900 nm, respectively, defines the upper range for the out-of-band rejection limit considerations. Figure 3.8 shows the transmission curves for all optical filters used in this work.

In addition to the interference filters discussed above, a series of metallic neutral density (ND) filters, available in a range of optical densities, were also used in this work. These filters have metallic coatings on crown-glass substrates and, as

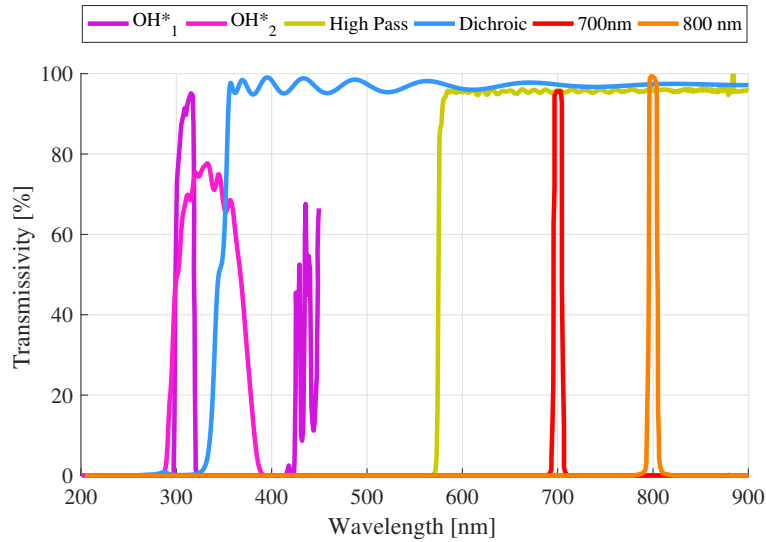


Figure 3.8: Transmission curves from the various optical filters used in this work

the name suggests, are neutral to spectral information and uniformly attenuate the incoming light, mostly through reflection, given their OD value (see equation 3.1).

3.2.5 Optical Probe

In addition to the development of the spatially resolved optical diagnostics described above, a custom cylinder head, designed concurrent to this work [128] to enable mounting a wide range of fuel injectors and in-cylinder diagnostics, was used to investigate the effect of spatially integrated measurements of similar phenomena. The spatially-integrated in-cylinder diagnostic tool of interest to this work was a custom optical probe design, also designed and commissioned concurrent to this work [156]. Simultaneous measurements and comparisons with the imaging results would allow for better characterization of the spatially integrated measurements and extension of the optical diagnostics capabilities to more realistic higher load operating conditions. Figure 3.9 shows the engine head design with the in-cylinder diagnostic tools installed.

The optical probe design utilized in this work comprises a trifurcated fiber

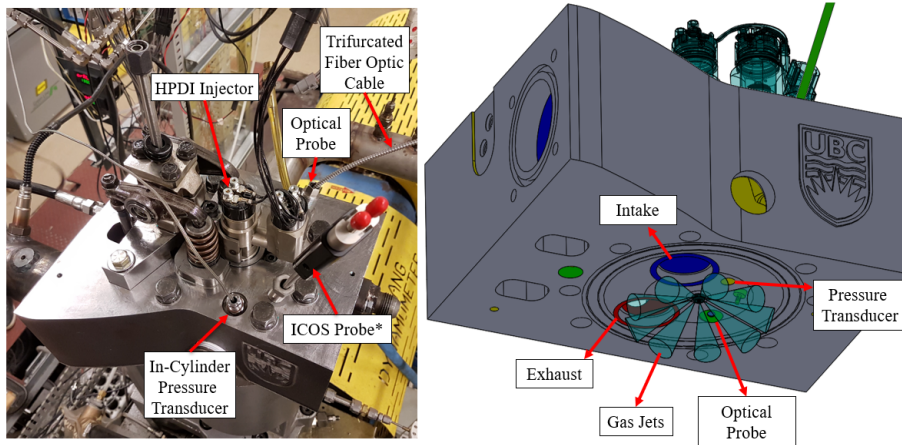


Figure 3.9: The engine head design with multiple in-cylinder diagnostics installed [128]. The ICOS sensor uses infrared absorption for local fuel concentration measurements (see [156] for more details)

optical bundle and sapphire rod lens to collect the combustion light from inside the combustion chamber. An interesting feature of the probe design was its self-cleaning capability [155, 156]. Considering the constraining effects of optics contamination and signal degradation, the self-cleaning feature was a significant design characteristic as it would allow for longer operation durations, with the collection lens remaining clean under steady-state full load conditions. Figure 3.10 shows the optical probe designed in the group [156] alongside the original design it was based on [155]. Further details of the optical probe design used in this work and the lens self-cleaning processes are available in [156].

In this work, the optical probe was used for two-color pyrometry measurements to provide estimations of in-cylinder temperature and soot concentration using the spatially integrated light collected from its conical field-of-view. As such, similar narrow band-pass filters to those used in the spatially resolved two-color pyrometry setup were mounted in the optical path of two of the optical fibers. The filters were positioned after the collimating lens and before recording the signal using silicon switchable photodetectors (Thorlabs). A schematic diagram of the optical probe two-color pyrometry measurements and a photo of the optical probe assembly are presented in Figure 3.11

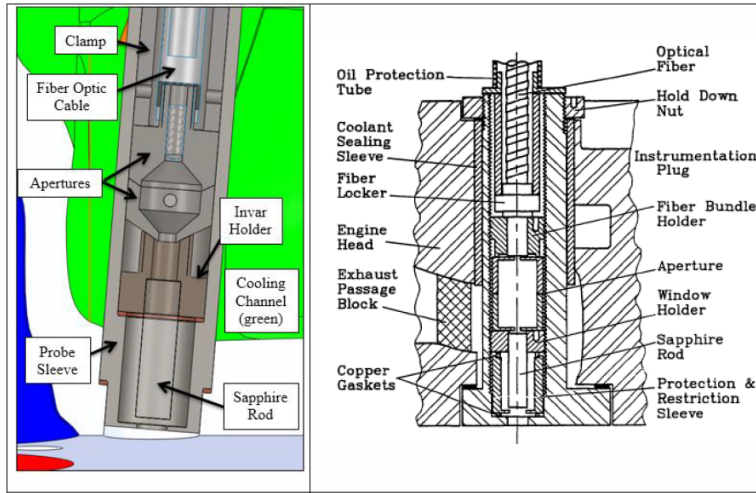


Figure 3.10: Optical probe designs. Left: by Yeo [156] (used in this work), Right: by Yan and Borman [155].

Similar to the spatially resolved two-color pyrometry imaging system, the optical probe requires calibration for sensor response in order to convert the recorded voltage into spectral radiant intensity and, ultimately, apparent temperature values. Following this step, the temperature and KL values are estimated using the two-color pyrometry equation 2.4. Therefore, the integrating sphere also serves as the characterized calibration light source for the optical probe, although setup with a different layout to address probe measurement principles. Figure 3.12 shows the optical probe calibration setup for two-color pyrometry measurements. In the absence of a linear exposure duration setting used in the imaging system, neutral density filters (see §3.2.2) of a range of optical densities (0.1-0.6) were mounted in the filter to attenuate the sphere intensity. A calibration curve is obtained from these intensity measurements, which can be used to reach high intensities of combustion through extrapolation.

The self-cleaning performance of the optical probe was evaluated through implementation of the calibration curves obtained for clean and dirty sapphire rod lenses, after nearly three hours of thermodynamic engine operation, on a sample operating condition [156]. This investigation showed an overestimation of 0.3% for temperature and 8% for the KL factor.

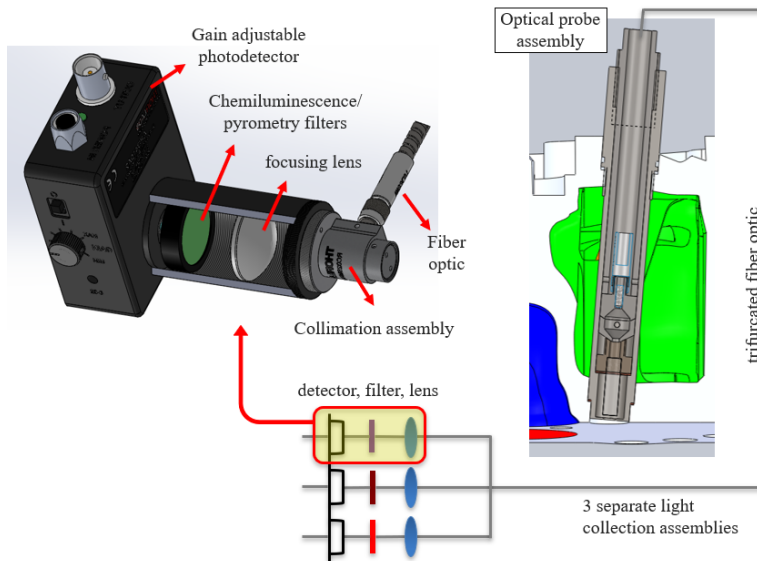


Figure 3.11: Optical probe assembly: Sensor assembly (Left) and probe assembly installed in the engine head, adapted from [156] (right)

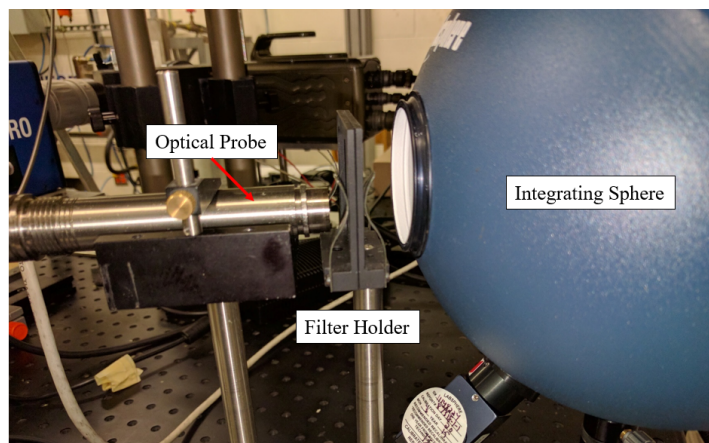


Figure 3.12: Optical probe calibration system.

3.3 Integrated System Operating Protocols

Under both engine configurations, the engine and camera systems are controlled using the in-house developed data acquisition (DAQ) and engine control unit (ECU) systems, primarily using National Instrument's LabView programming environ-

ment and FPGA. The intricate details of the designed engine control and DAQ system, and sensors and actuators involved in the successful and safe operation of engine, can be found in [156]. The work presented here only focused on integration of the optical diagnostics to the developed engine control and DAQ systems. In what follows the major details of imaging systems integration to the engine, calibration, and setup are presented.

3.3.1 Synchronization of optical diagnostics with the engine

An optical encoder was used to synchronize the engine and the imaging systems, through determination of camera trigger TTL signal timings and/or individual image frame capture synchronous to engine rotation, as well as synchronized sensor data logging onto the DAQ. A 1440 pulses/revolution optical encoder (BEI) was the central electro-mechanical piece for the imaging system integration task.

The engine synchronous sensor data logging with this encoder provides quarter crank-angle degree (CAD) temporally resolved optical probe and HRR (pressure) results. In the case of spatially resolved optical measurements, there are two synchronization factors involved: 1- The start of an image recording sequence, controlled by a TTL signal, setup *a priori* at a crank-position offset from the engine top-dead-center (TDC), and 2- individual image frame capture timing. The latter can be executed at a constant frequency, determined as the recording frame rate in the camera software. In this case, the camera sets its internal crystal clock at this constant frequency and starts the imaging sequence on the first clock tick after the detection of the trigger signal rising edge (under normal settings). However, given the concentrated power delivery to the shaft of the single cylinder engine setup, the system does not operate under a constant frequency and instead periodically undergoes acceleration and deceleration in each cycle. As such, alternatively the individual encoder pulses might be used to control the timing of the electronic shutter on the camera sensor chip and capture the individual image frames so as to accurately match the timing with the engine synchronous data. However, the camera system capability to operate under a variable frame capture frequency needs to be supported by the designed camera firmware, which was only the case for the Phantom V7.1 camera used in this work.

In addition to the high-speed cameras, the high-speed image intensifier is also required to be synchronized with its paired camera (i.e., the Photron SA-1). The image intensifier is operated by a control unit, which in addition to the MCP gain and photocathode gate settings, manages system triggering and frequency. Triggering the intensifier has a slightly different concept from the high-speed cameras. An arming/disarming port at the intensifier controller back panel accepts a Boolean to energize the photocathode and start the photon-electron conversion. This signal is provided by the Photron camera signal output bundle, during an image recording sequence (RecPos signal). Another output signal from the camera to the intensifier is the camera internal clock pulses, which provides the synchronization of individual image frames between the two. The frame exposure duration of the assembled chemiluminescence measurement system is determined by the smaller of two values: Photron camera exposure or intensifier gate settings. To avoid unnecessary burden on the photocathode, the exposure of system is controlled by the intensifier gate settings. As such, the Photron camera exposure must be set to a longer duration, yet not too long to unnecessarily record the background noise (a few microseconds longer than the intensifier gate).

A simplified wiring diagram of the integrated optical diagnostics are presented in Figure 3.13. In this configuration, the images recorded by the Phantom camera (NL and pyrometry images) are synchronous with the HRR and optical probe results, while the images recorded by the Photron camera (OH^* chemiluminescence images), captured with a constant frequency, are not necessarily synchronous with other measurements. As such, the time stamps from the engine encoder and Photron camera internal clock, recorded on the DAQ, were compared and interpolated to attribute OH^* chemiluminescence image frames to the closest encoder time stamps. It is worth noting that this process occasionally leads to repeated OH^* chemiluminescence image frames for two consecutive registered encoder timings, given the higher than nominal frequency of engine rotation after TDC of combustion cycle, and appears as “frozen frames” in the phasing-adjusted sequence.

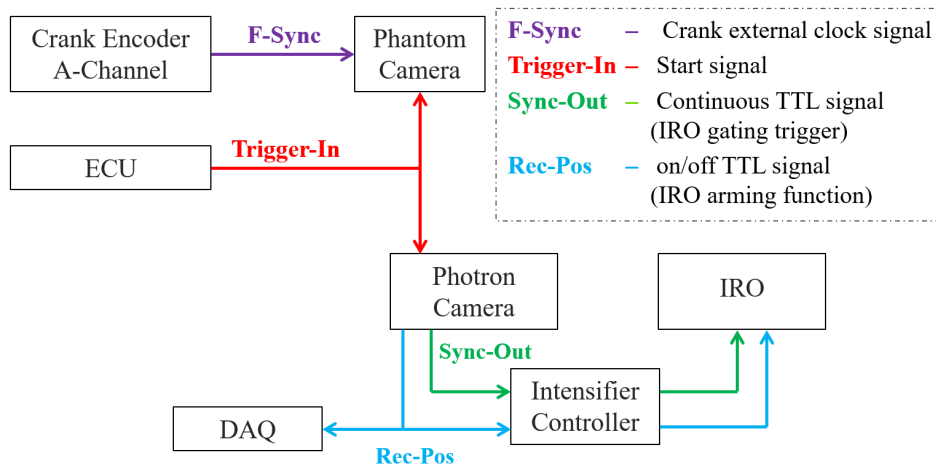


Figure 3.13: Simplified wiring diagram of the integrated optical systems.

3.3.2 Alignment and Calibration

Several preparation steps are required before each new set of spatially resolved optical measurements of combustion in an IC engine. This procedure makes such measurements relatively time-consuming and labour-intensive to setup. For a fresh set of optical measurements, engine window, optical probe lens, and if necessary, the engine head are removed and cleaned, and certain mechanical parts are replaced, if needed. After engine reassembly, the imaging systems should be positioned at the suitable stand-off distance (see Appendix A) and be aligned and focused, and in the case of two-color pyrometry, calibrated (see §3.2.2). It is worth noting that in the case of chemiluminescence measurement setup, choosing a higher intensifier gain setting and the lowest frame-rate setting on the controlling camera (see §3.3.1) would reduce the photocathode use overhead during system alignment and focusing process.

Continuous optical in-cylinder soot measurements is challenging to maintain due to mechanical and instrument-related limitations and the preparation protocols described above should be repeated often. Window contamination is typically the primary source of disruption in continuous measurements. Optical rings and window gaskets also need to be replaced due to wear occasionally during optical engine maintenance, albeit less frequently under normal operation. In order

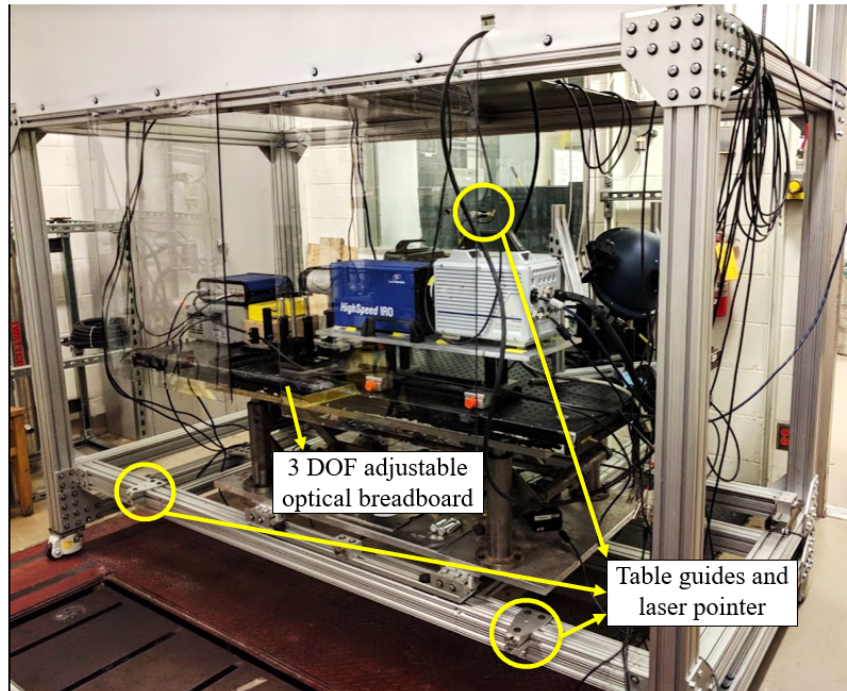


Figure 3.14: Adjustable optical table system to facilitate higher throughput and repeatable optical measurements.

to improve optical measurements system throughput and repeatability, a portable optical table was used with three DOF¹ optical breadboard control. The breadboard can be fine-tuned for elevation, stand-off distance and lateral positioning, and the table structure, sitting on casters, can be rolled close to or away from the engine. Once the imaging systems and all the relevant optical elements were properly mounted and locked in position on the breadboard, the entire imaging system can be conveniently removed and then put back in position for a new set of optical measurements. A pair of mechanical table guides and a laser pointer aiming at a target affixed to the optical engine block allow for accurate re-positioning of the optical table in front of the optical engine mirror. The mechanical table guides are removable to prevent table movements during engine operation. Figure 3.14 shows the optical table structure and mounted imaging system setup.

¹Degree of freedom

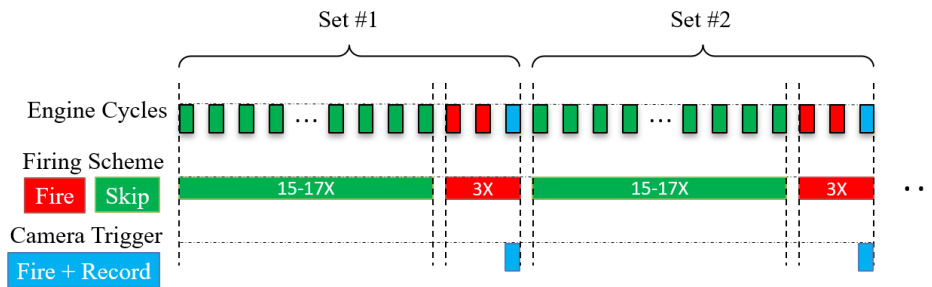


Figure 3.15: Standard optical engine operation skip-firing scheme. 15 repetitions of the skip-firing sequence sets are performed during each optical engine run.

3.3.3 Optical engine operation

As discussed in §2.1.1, continuous firing should be avoided in order to allow for the cooling of the quartz engine window between cycles. As such, to facilitate the in-cylinder imaging of a more representative combustion event, a skip-firing procedure was used in which three fired cycles followed by a certain number of motored cycles (15-17). Only the final of the three fired cycles was used for imaging purposes, as the first and second cycles were noted to be transitory while the third cycle was observed to reach a steady state [124]. The described skip-firing set was repeated for 15 times, restricted by the partitions limit of the Phantom camera. The ensemble average of these 15 cycles were considered to limit the cycle-to-cycle variability effects. A schematic illustration of the skip-firing procedure is presented in Figure 3.15.

Also as discussed in §2.1.1, the geometric modifications to afford the spatially resolved optical access into the combustion chamber usually results in a lower compression ratio and necessitates measures to compensate for the discrepancy. In the current optical engine setup, this was addressed through heating of the intake air (to 50-80°C, depending on the operating conditions) and boosting intake air pressure (~1 bar-gauge) to compensate for air density change. These adjustments would create similar conditions at TDC and result in close combustion phasing, characterized by the 50% integrated heat release (CA50), to that of an equivalent thermodynamic operating condition. Further fine-tuning of the combustion phasing is then executed through adjustments in fuel injection timings [124]. A summary flowchart of the

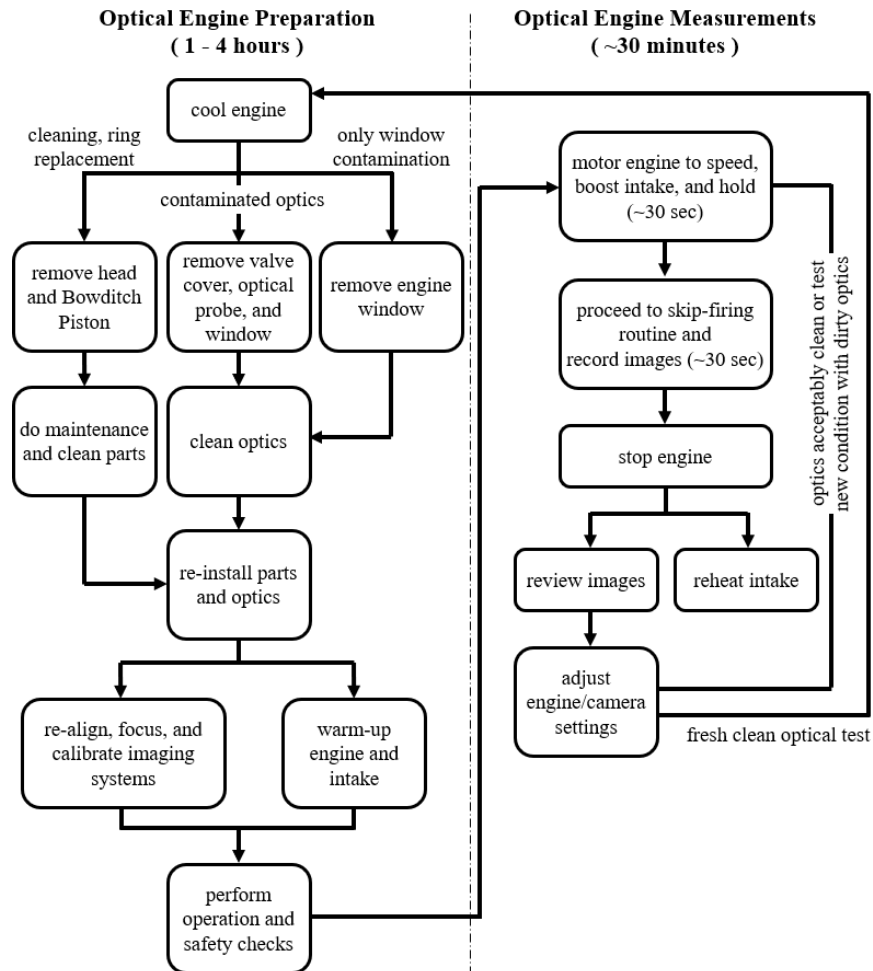


Figure 3.16: Optical measurements protocol flowchart.

optical measurement protocol is provided in Figure 3.16. As illustrated here, the optical engine preparation stage constitutes the majority of the operation time for a set of optical engine measurements. Depending on engine and optics conditions, engine preparation can take anything between one hour, with only engine window cleaning required, to 4 hours, due to engine disassembly for required cleaning and regular maintenance of optical and engine parts and re-calibrating and re-aligning the imaging systems.

Chapter 4

Optical Investigation of DIDF combustion

Following the commissioning of the simultaneous spatially and temporally resolved OH* chemiluminescence and natural luminosity measurement system, a study on the effects of fueling control parameters on combustion characteristics of DIDF combustion of methane was carried out, as a case study [75]. The current chapter presents the findings of this investigation.

4.1 Analysis Metrics and Engine Operating Conditions

The metrics used to identify operating points in the current work are pilot fuel injection pressure, the global equivalence ratio (ϕ_{global}) and pilot ratio (PR). The latter two are described through equations 4.1 and 4.2 [127]:

$$\phi_{\text{global}} = \frac{\dot{m}_{\text{diesel}} \cdot \frac{A}{F_{\text{diesel,stoich}}} + \dot{m}_{\text{CH}_4} \cdot \frac{A}{F_{\text{CH}_4,\text{stoich}}}}{\dot{m}_{\text{air}}} \quad (4.1)$$

$$PR = \frac{\dot{m}_{\text{diesel}} \cdot LHV_{\text{diesel}}}{\dot{m}_{\text{diesel}} \cdot LHV_{\text{diesel}} + \dot{m}_{\text{CH}_4} \cdot LHV_{\text{CH}_4}} \quad (4.2)$$

where \dot{m} is the mass flow rate and LHV is the lower heating value of each fuel. The thermodynamic results in [127] indicated that increasing pilot injection pres-

sure increased the fraction of fuel converted in the first stage of DIDF combustion. Up to a certain limit, increasing PR increases the proportion of energy released in the first stage. Conversely, increasing methane equivalence ratio (ϕ_{CH_4}) increased the energy fraction released in the second stage. The observed effects of the injection pressure and PR on dual fuel combustion can be further supported using optical measurements. In addition, lowering pilot injection pressure was observed to result in higher methane emissions. This observation, combined with the toroid combustion behavior reported by Dronniou *et al.* [33], which suggests the possible origin of the increased unburned methane emissions might be the central region premixed charge, can be another motivation to see how manipulation of pilot injection pressure will affect the combustion behavior. This investigation presented in this chapter examines the effects on dual fuel combustion incurred by changing the pilot fuel injection pressure and the pilot ratio. These effects are studied optically through use of simultaneous spatially and temporally resolved OH^* and NL imaging.

A combination of testing in thermodynamic and optical configurations was employed for this investigation. The first round of testing was performed with the engine in thermodynamic configuration and detailed thermodynamic analysis results were presented by Rochussen *et al.* [127]. The primary goals of the thermodynamic testing, relevant to the discussion presented in this chapter, was to define the operating points of interest (e.g., pilot injection parameters), and to characterize metrics which are not readily measured during short optical measurements (e.g., fuel and air flow rates, emissions, etc.).

Thermodynamic measurements presented in [127] identified distinct regimes of dual-fuel combustion. A representative operating point from each combustion regime was selected for further investigation through optical measurements in this study. After defining the operating points to be optically studied, the engine is converted into the optical configuration to more closely investigate the effects observed in the thermodynamic measurements. The selected operating points are presented in Table 4.1 and will be discussed in detail below.

The operating points outlined in Table 4.1 were selected because they demonstrated significantly different combustion characteristics such as the energy release fraction in different stages of combustion, shape of HRR curves, occurrence of

Table 4.1: Operating points specifications. Mass of diesel was set based on the injection duration determined in thermodynamic configuration. E_{input} is the total fuel energy input to the system and $I\eta_{th}$ is the indicated thermal efficiency.

Point	ϕ_{global} [-]	ϕ_{CH_4} [-]	PR [-]	m_{diesel} [mg/cyc]	E_{input} [kJ/cyc]	$GIMEP$ [bar]	$I\eta_{th}$ [%]	CSOI [bTDC]
A-1300	0.8	0.75	0.1	7.2	4.5	7.4	32	4
A-300	0.8	0.75	0.1	7.2	4.5	6.2	27	8
B-1300	0.7	0.60	0.14	15.6	4.1	6.4	31	6
B-300	0.7	0.60	0.14	15.6	4.1	5.1	25	10
C-1300	0.7	0.45	0.35	31.7	4.0	6.0	30	4

flame propagation, and dependence of emissions and HRR curve on pilot fueling parameters [127]. In the naming convention used here for each operating point, the letter corresponds to the fueling parameters (ϕ_{CH_4} , ϕ_{global} , and PR), while the number indicates the injection pressure in bars.

As discussed in §3.3.3, due to the mechanical limitations of optical engine operation, a skip-fire operating protocol was used. To maintain a consistent heat release rate, this protocol consisted of three consecutive fired cycles, with images being recorded on the final cycle. This was then followed by 12 motored cycles. For each test point, a total of 15 fired cycles were recorded, as limited by the camera buffer capacity. Also, as discussed in §2.1.1 and listed in Table 3.1, the optical and thermodynamic configurations have different compression ratios and, therefore, the intake air temperature was adjusted using electric heaters prior to running each optical test in order to compensate for this discrepancy and approximately match the combustion phasing to previous thermodynamic measurements. The combustion phasing was characterized by the crank position at which 50% of energy is released (CA50). For this study, the engine was naturally aspirated and intake air was heated up to $80 \pm 5^\circ\text{C}$. The simultaneous OH* and NL imaging system and general engine specifications were presented previously in Table 3.3 and 3.1; Table 4.2 here specifies the imaging and optical engine settings used for the

current investigation. A schematic of the simultaneous measurement system used is shown in Figure 4.1.

Table 4.2: Simultaneous OH* and NL imaging system setting for optical investigation of DIDF combustion

Optical Engine	
Direct Injector	Bosch CRIN2
Port Injector	Bosch NG12
Pilot fuel	pump diesel
Premixed fuel	pure methane
Intake air condition	naturally aspirated; heated to $80 \pm 5^\circ\text{C}$
Speed	600 rpm
NL Imaging System	
Frame Rate	Variable (Externally triggered)
Resolution	320×240
Exposure	$8 \mu\text{sec}$
Aperture	f/2.8
OH* Chemiluminescence Imaging System	
Frame Rate	12,000 fps (Internal Clock)
Resolution	640×640
Exposure	$84 \mu\text{sec}$
Aperture	f/5.6
IRO Gating	$10 \mu\text{sec}$
IRO Gain	70%
Interference Filter	20 nm FWHM band-pass; 307 nm CWL

Here, the Phantom v7.1 camera was synchronized with the thermodynamic data using the crank-shaft encoder signal (0.25 CAD resolution), while the OH* chemiluminescence images were captured at a constant frequency 12,000 frames/second. This frame rate corresponded to ~ 0.3 CAD resolution at the 600 rpm engine speed used for this study.

The recorded images were processed for image enhancement, as well as to spatially and temporally align the images from the two imaging systems. The 12-

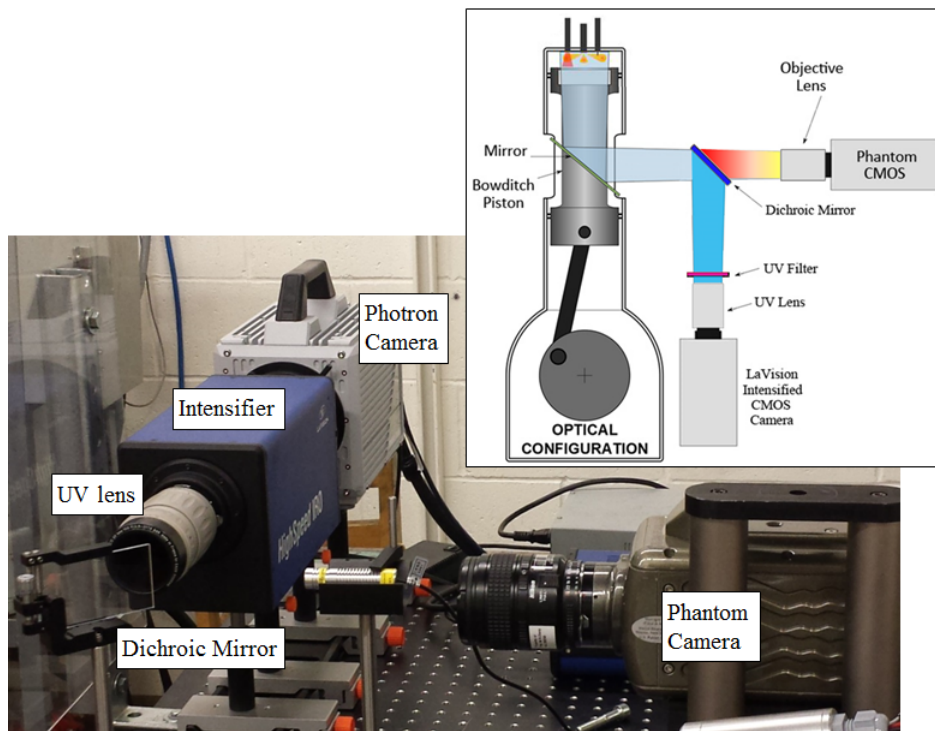


Figure 4.1: Schematic of the simultaneous OH* and NL imaging system used for optical investigation of DIDF combustion.

bit raw images captured by the two cameras had the following post-processing steps applied:

1. Temporal synchronization of the image series from the two cameras.
2. Image registration: adjustment of image size, scale, and positioning to be consistent between the two series.
3. Background and noise removal, intensity adjustments and image enhancements (gain, brightness, and gamma corrections).
4. Ensemble averaging, morphological operations and edge detection, image thresholding, preparation of compatible color maps, alpha blending, and image overlay.

4.2 Results and Discussion

For the A and B operating points two P_{inj} are compared to illustrate the effect of pilot fuel injection pressure on dual-fuel combustion with similar fuelling parameters. Points A, B, and C, on the other hand, can be studied at constant P_{inj} (1300 bar) to consider the effect of PR and ϕ_{CH_4} .

In addition to the injection pressure and relative fuel quantities, the influence of the premixed methane on combustion of diesel was studied by comparing the dual-fuel operation with representative “diesel-only” points. For these points, the diesel injection parameters are the same, but no CH_4 is inducted into the combustion chamber. Such comparisons were carried out for B-1300, B-300 and C-1300.

4.2.1 Effect of the Pilot Fuel Injection Pressure

This section discusses the effects of different pilot fuel injection pressures on dual-fuel combustion behavior. In order to elucidate the approach taken to discuss optical data in this study, two sample operating points are presented in Figure 4.2. This figure presents two series of images for each of the two sample operating points, where OH^* and NL processed signals can be compared at each crank position. This illustrates evolution of combustion at each operating point and affords comparison of this process among different operating points. However, it is more useful to present and discuss the information provided through both OH^* and NL at each crank position on a single image. This will provide a more compact presentation of data and also enables comparison of spatial distribution of high temperature reaction zones, characterized by OH^* , and high intensity NL regions, usually attributed to incandescent soot particles. The combined presentation of OH^* and NL images is illustrated in Figure 4.3 for B-1300 operating point at 14.5 CAD after command-of-start-of-injection (aCSOI). In this context, Figure 4.2 is a reference to facilitate interpretation of overlaid blended images in Figure 4.3. Here, the NL data is false colored with shades of yellow to dark red, as in figure 2. Thresholding is applied to the OH^* chemiluminescence data to reduce clutter in the overlaid images. The three regions, delimited by contours in dark blue (solid), cyan (dashed), and green (dotted) color, show the boundary of upper 75, 50, and 25% chemiluminescence, respectively. False coloring (shades of green) is used to indicate the highest OH^*

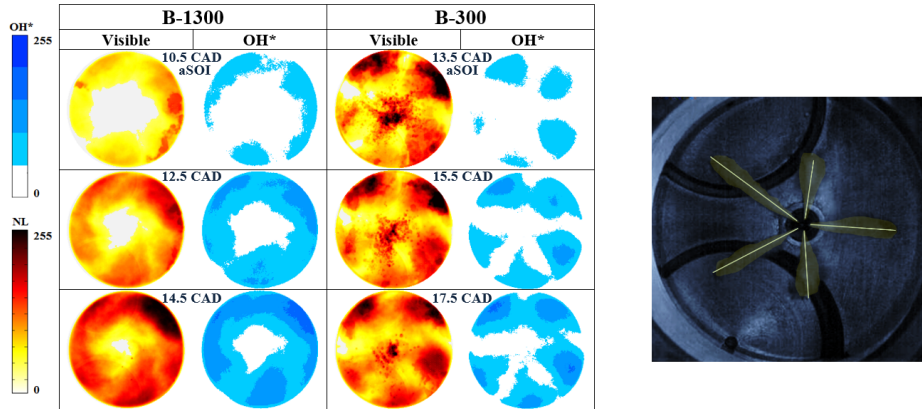


Figure 4.2: Sample image series of ensemble averaged NL and OH* chemiluminescence (left); and jet orientations from a split injection diesel test with external illumination (right).

intensities ($>75\%$). A different OH* color map from Figure 4.2 was used in Figure 4.3 in order to enhance the visualization of OH* signal in the overlapping regions.

Figure 4.2 also shows the five diesel jets produced by the injector nozzle and their orientation. This sample back-scattering image was obtained from a diesel-only combustion test (no NG), where the combustion chamber was illuminated via an external light source for spray visualization. Due to the CCW swirl motion of the charge (swirl number ≈ 3.2) and ignition delays, the jet structures in A-300 and B-300 points are rotated relative to the original sprays.

Following the procedure described in Figure 4.3, the combined OH* and NL images for all operating points in Table 4.1 are shown in Figure 4.4. 15 fired cycles were imaged for each operating point and Figures 4.2-4.4 present the ensemble averaged results. Each image series in Figure 4.4 starts at approximately 5% gross integrated heat release (IHR) and for the sake of brevity, only images at 2 CAD intervals are presented. The crank positions reported on each frame in these figures are relative to the CSOI.

For the pilot injection pressure comparison (points A and B), the pilot injection duration was adjusted for equal pilot injection masses. The required durations at each pilot pressure were determined during thermodynamic engine tests [127]. The penetration of the pilot fuel and distribution of ignition sites were significantly

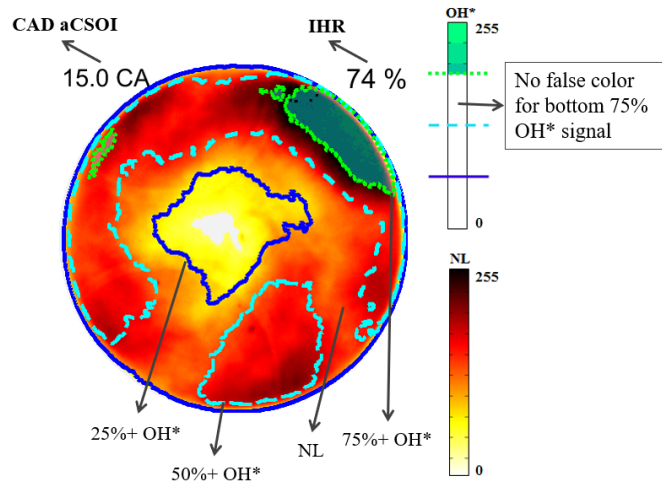


Figure 4.3: Overlaid presentation of ensemble averaged OH* chemiluminescence and natural luminosity images for B-1300 at 14.5 CAD aCSOI. The gross IHR value up to this instance is presented at the top-right of the image frame.

affected by the injection pressure. Comparisons of ignition site locations and reaction zone growth mechanisms between high injection pressure points (A-1300 and B-1300) with their corresponding low pressure cases (A-300 and B-300), demonstrate how the dual-fuel combustion mode can be manipulated by controlling the injection pressure of the diesel pilot fuel.

For the higher injection pressure, the liquid diesel atomizes better, entrains and mixes faster with charge gas, and penetrates further into the combustion chamber. This results in auto-ignition of a partially-premixed diesel mixture at the bowl periphery (the first three columns in Figure 4.4). The reaction zone then propagates towards the center, via what is commonly accepted to be turbulent flame propagation, as was also observed by Dronniou et al. [33]. The dual-fuel combustion in these cases produces fewer high intensity localized NL regions when compared to the lower injection pressure, which, for instance, depicts multiple black pockets at 13 CAD aCSOI in A-300 case. Since these high intensity regions are associated with radiation from soot in locally rich regions, their absence can be indicative of combustion initiation in lean, well-mixed regions.

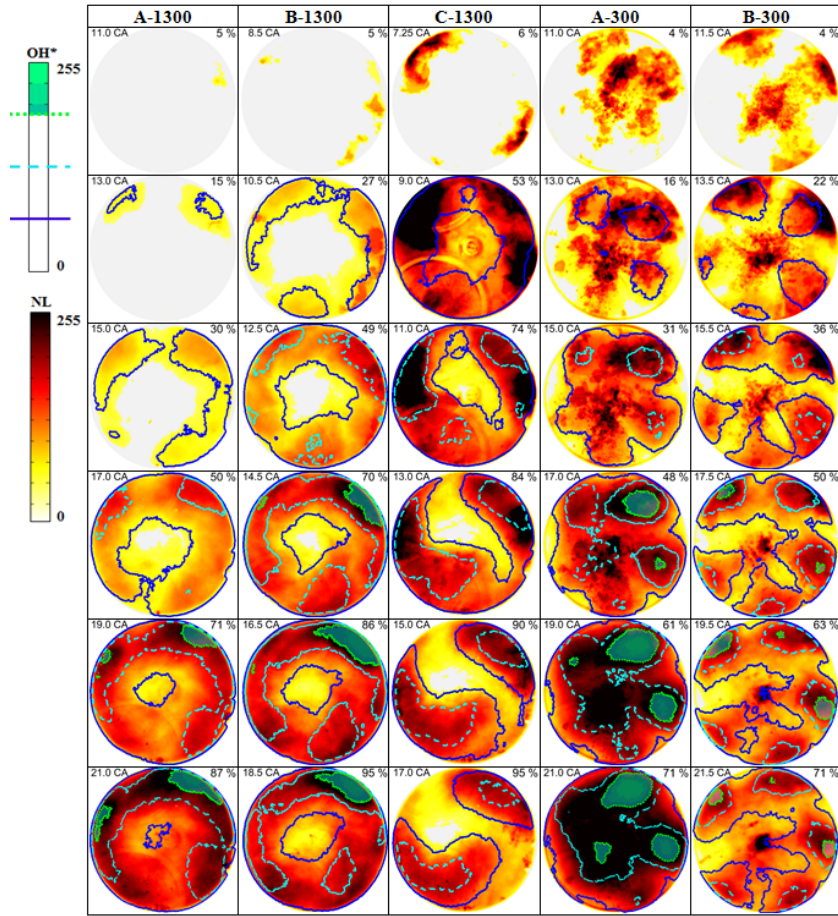


Figure 4.4: Overlaid ensemble averaged OH* chemiluminescence and natural luminosity images for dual fuel operating points described in Table 4.1. Crank positions are relative to CSOI and gross IHR values are presented at the top of each frame.

It should be noted, however, that high-intensity NL regions that show high spatial gradients (i.e., are more localized) and emerge at earlier crank positions and closer to CSOI are more likely to indicate production of incandescent soot. This should not be confused with high-intensity NL regions appearing later in the cycle which may be from soot or natural luminosity from gas phase products such as CO₂, HCO, CH₂O, and C₂* [93].

For the lower injection pressure (points A-300 and B-300), the diesel jet does

not penetrate as far or mix as well. As a result, the ignition sites are localized around the vicinity of the pilot fuel jets and a more heterogeneous auto-ignition of the charge was observed. The auto-ignition in these cases occurs after the end of injection (EOI) and the “jet” refers to the region in which the injected fuel has increased the local equivalence ratio, rather than the actual liquid pilot fuel jet. In these auto-ignition regions, intense luminosity was observed, attributed here to the presence of soot particles and indicative of a locally rich mixture (the last two columns in Figure 4.4). The jet structures can also be recognized in OH* images from pilot fuel ignition towards later in the combustion cycle. Ignition of the premixed natural gas occurs at the proximity of the ignited pockets around the jet structures, observed across the entire chamber.

Thus, the pilot fuel injection pressure and consequent effects on fuel mixing rates greatly affect the distribution of equivalence ratios and formation of fuel-rich regions, potentially producing more soot and stronger NL intensities in some regions. This confirms the results of Carlucci *et al.* [18], where higher total time integrated and peak luminosity was observed for lower pilot fuel injection pressures.

The conceptual representation of the described behaviors as the result of changing P_{inj} is presented in Figure 4.5, which is based on OH* images from representative high and low pilot injection pressure operating points.

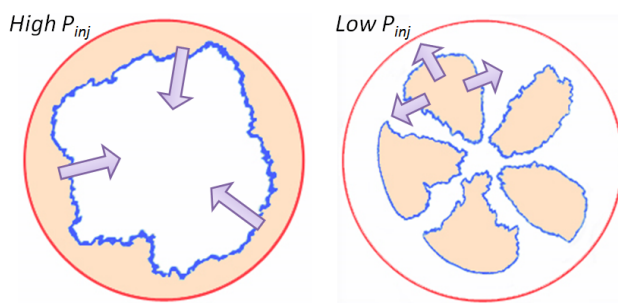


Figure 4.5: Conceptual effect of pilot fuel injection pressure on reaction zone growth mechanism (left: high pressure; right: low pressure) on DF combustion mode

The conceptual description of the effect of pilot injection pressure may also provide an explanation for lower unburned methane emission with high P_{inj} , as

observed in thermodynamic investigations [127]. Concentration of auto-ignition and high temperature reaction zones around the edges enhances the fuel conversion in these critical, wall-influenced regions. The propagation of reaction zone towards the center consumes the rest of the charge in the higher temperature, central regions. For low injection pressures, the scattered auto-ignition and localized reaction zones, not necessarily close to the walls, leaves more premixed pockets behind.

Another observation made from Figure 4.4 was that the high temperature reaction zones (characterized by OH* chemiluminescence) are coincident with mid to high level broad-band light emitting regions (high intensity NL), except for earlier stages in low P_{inj} points when intense luminosity is observed and suggestive of early soot production in poorly mixed fuel-rich regions. This was consistent among all operating points studied in this work. According to Karim's thermodynamic analysis results [69], the pilot diesel fuel is assumed to be almost completely consumed in the first stage. This is in contrast with optical results acquired in this work, where, for the lower pilot injection pressure cases, the pilot jet structures are present in the later combustion stages. These jet structures are suggestive of higher local equivalence ratios and higher reactivity in those regions probably due to the conversion of the remaining diesel fuel.

4.2.2 Effect of the PR and ϕ_{CH_4}

The other important fueling parameters investigated in this work were diesel pilot ratio and methane equivalence ratio. Points A-1300, B-1300, and C-1300 have the same pilot injection pressure, as do the points A-300 and B-300. They also have a similar ϕ_{global} and, therefore, can be used to investigate the combined effect of different PR and ϕ_{CH_4} values. Point A has the smallest PR value, while C has the largest PR value. Because they have similar global equivalence ratios, this also requires that C have a lower ϕ_{CH_4} . From the OH* images (Figure 4.4), C-1300 demonstrates high temperature reaction zone propagation from the periphery to the center, similar to the other high injection pressure points (A-1300 and B-1300). However, the fuel conversion rate is more rapid for this higher PR point (C-1300).

From natural luminosity images, C-1300 shows a more heterogeneous combus-

tion event than the other high injection pressure points, and high intensity incandescent soot regions as a result of increasing PR . Observation of soot regions at this increased pilot ratio suggests that the otherwise effective charge mixing (atomization at 1300 bar injection, available turbulence and dwell time) are not sufficiently effective anymore to handle the increased diesel in the charge. This can also be inferred from Figure 4.6-a, where spatially averaged NL histories are compared for all operating points ($\Sigma I_{x,y}/N$, where I and N are pixel intensity and number of pixels, respectively). Point C-1300 looks different from the bell shape curves of A-1300 and B-1300, and shows a sharp peak of natural luminosity shortly after ignition. The optical data in Figure 4.6 were not subjected to any non-linear intensity adjustments or histogram shifts; however, they are all normalized with the maximum signal intensity in point A-1300 to facilitate direct comparison.

Although points A-1300, B-1300, and C-1300 show similar high-temperature reaction zone propagation mechanism in the OH^* chemiluminescence images, the extent and rate at which this growth takes place correlates with ϕ_{CH_4} (and therefore PR). The results presented in Figure 4.4 (first 3 rows for these 3 points) and Figure 4.6-b, show that a higher initial rate of reaction zone growth can be observed for higher PR . Comparison of the slope of rising spatially averaged OH^* signals amongst A-1300, B-1300, and C-1300 points in Figure 4.6-b expresses this increased growth rate for a higher PR .

Figure 4.7 shows the 20% thresholded OH^* chemiluminescence for each operating point at its maximum bowl coverage (i.e., the pixels registering intensities less than 20% of the dynamic range are set to zero). This thresholding technique facilitates comparison of the extent of spatial progression of the high temperature reaction zones for different operating points. From Figure 4.7, it is evident that reducing ϕ_{CH_4} restricts the extent of reaction zone propagation in high P_{inj} operating points (A-1300, B-1300, and C-1300). The reduced extent of reaction zones can be linked to increased unburned CH_4 emissions observed for decreasing ϕ_{CH_4} in thermodynamic engine configuration [127], suggesting a less complete fuel conversion process.

A similar conclusion can be inferred from points A-300 and B-300 (Figure 4.7). Less heterogeneity is observed in the OH^* signal from point A-300 (having larger ϕ_{CH_4}), which also appears to cover the whole chamber later in the combus-

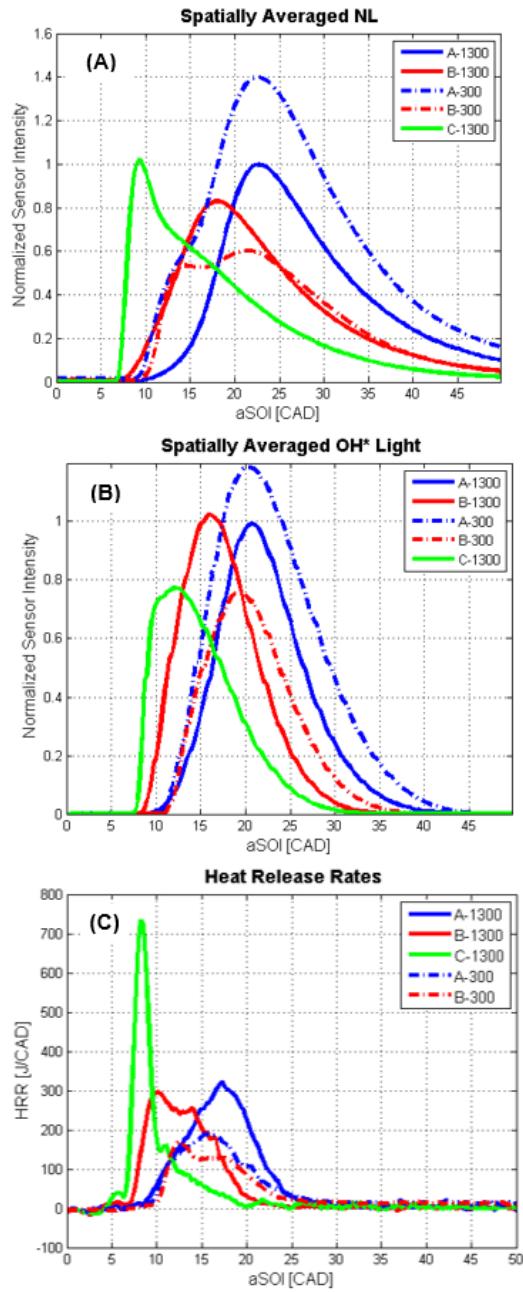


Figure 4.6: Comparison of spatially averaged NL (a) and OH* chemiluminescence (b) determined by $\Sigma I_{x,y}/N$, where I and N are pixel intensity and number of pixels, respectively, and HRR (c).

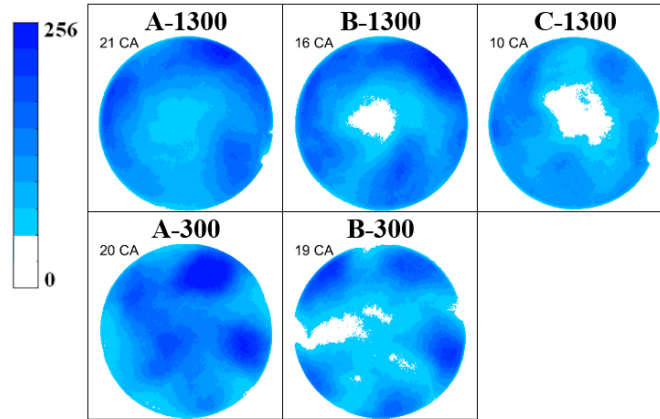


Figure 4.7: OH* Chemiluminescence at the maximum bowl coverage.

tion cycle. Similar to what was discussed above, this slower rate of reaction zone propagation can be attributed to smaller PR in A-300. Point B-300 appears to be more dominated by the diesel fuel in the charge and follows the pilot fuel jet structures till later in the cycle (Figure 4.4 and Figure 4.7).

Variation of pilot injection pressure and pilot ratio has a marked impact on the ignition delay. From a thermodynamic analysis perspective this is conventionally characterized by CA5. From the optical point of view of this work, the ignition delay can be characterized by the detection of the earliest OH* chemiluminescence after CSOI, which is indicative of the onset of high temperature reactions with respect to CSOI. It should be noted that these two ignition delays are not the same. Figure 4.6 also describes these effects, where lower ϕ_{CH_4} (higher PR) results in an earlier rise of the OH* and NL signal among the high P_{inj} points. The ignition delay defined by the crank position when the spatially averaged OH* and NL signals exceed 5% of their maximum value are listed in Table 4.3. It is worth noting that a 2 CAD advanced CSOI for B-1300, relative to A-1300 and C-1300, does not affect the ignition delay behavior among these three points. These observations are consistent with results presented by Schlatter *et al.* [133], where higher values of ϕ_{CH_4} promoted propagation of the premixed flame, as was seen in this work from the comparison of points A-1300 and B-1300, but delayed the auto-ignition of the pilot spray considerably.

Table 4.3: Ignition delay and combustion duration.

	A-1300	B-1300	C-1300	A-300	B-300
Ignition delay (OH*) [CAD aSOI]	7.75	5.5	4.25	7.75	8.25
Ignition delay (NL) [CAD aSOI]	8.75	5.0	3.5	6.0	6.75
Ignition delay (CA5) [CAD aSOI]	11	8.5	7.2	11.1	11.6
Combustion phasing (CA50) [CAD aSOI]	17	12.5	9	17	17.5
Combustion duration (CA90-CA5) [CAD]	21.6	17.2	15	37.5	41.2
CSOI [CAD bTDC]	4	6	4	8	10

As the injection pressure is decreased, a longer delay is observed, except for point A-1300. This is most likely a result of a more advanced CSOI for A-300 and B-300, coupled with a very low diesel mass quantity in the dual-fuel charge of A-1300. The enhanced mixing at this high P_{inj} resulted in a diluted pilot mixture, whereas at the low P_{inj} , the slower mixing and stratification in the charge made for more reactive regions for auto-ignition across the chamber.

Figure 4.4 also presents gross IHR fractions corresponding to each image frame (top right at each frame). The heat release rates information also indicates increased fuel conversion rates and more aggressive combustion events for increased pilot ratio. The IHR values in figure 3 show that in the first 8 CAD after start-of-combustion (aSOC), 84%, 69%, and 66% of the total apparent energy release occurs for C-1300, B-1300, and A-1300, respectively. 47% of the total apparent energy is released over only 1 CAD for the C-1300 operating point, which makes it the most aggressive point presented in this work and was observed as substantial oscillation of the flame structures in the single cycle image sequences (not discernible in ensemble averaged results). This can also be inferred from the heat release rates presented in Figure 4.6-c, where larger slopes are observed for higher PR points.

For lower pilot injection pressures, the energy is released at a slower rate of

around 57-59% of the total apparent energy release over the first 8 CAD aSOC. Thermodynamic analysis results do not reveal other effects discussed based on the optical data. This investigation suggests that the shape of the heat release rate curves are most strongly influenced by the pilot ratio. A transition from bell-shaped heat release rate, to one weighted more heavily towards earlier crank positions, regardless of the pilot fuel injection pressure, is observed with increasing *PR*. The B and C HRR curves show the same two-stage combustion process discussed in [69].

The deviation from a bell shape in the spatially averaged NL curve pointed out for C-1300, was also observed for A-300 and B-300 (10-15 CAD) in Figure 4.6-a. The shape of these curves appears to have some correlation with HRR curves and will be the focus of a future work. This can be important since, according to Karim's conceptual model [69], deformations in HRR curves and presence of multiple peaks are indicative of different stages of combustion. The first deformation/peak can be associated with the partially-premixed pilot fuel and entrained premixed NG heat release, followed by the conversion of natural gas plus the rest of diesel from the pilot. From this perspective, the sharp peak in spatially averaged NL and HRR curves of C-1300 is a result of a more profound first stage due to its higher *PR*.

4.2.3 Influence of Diesel and Natural Gas on Each Other in Dual-Fuel Combustion Charge

The optical results presented in the previous sections demonstrated that, as expected, there is a strong interaction between the premixed methane and the diesel pilot. To further consider this, "diesel-only" cases were also considered for operating points B-1300, B-300, and C-1300. These points have the same total diesel mass and mass flow rate as their corresponding dual-fuel point. Thus, each of the corresponding diesel-only and dual-fuel point pairs can be studied to compare the effect of presence air vs. premixed NG on the combustion process. Figure 4.8 shows an image series comparing OH* chemiluminescence from dual-fuel and diesel-only combustion of these three points at 2° CAD increments. The crank positions are relative to CSOI. The imaging system settings were identical for all of points; however, the image gain was doubled for the diesel points to better visualize

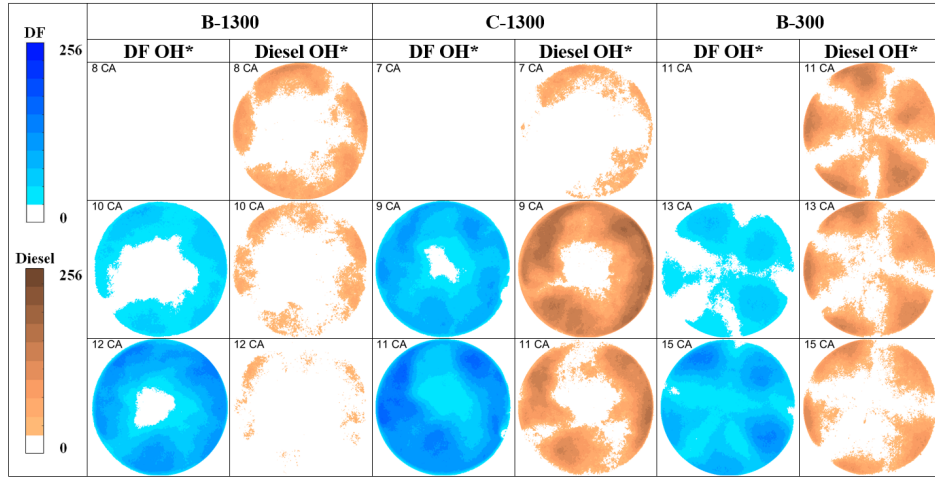


Figure 4.8: Reaction zones (OH* images) in dual-fuel and diesel-only combustion. Crank positions are relative to CSOI and the image gain was doubled for diesel points for better visualization.

the phenomena.

All the diesel-only cases agree with the conclusions made for their equivalent dual-fuel case. That is, point B-300 shows the pilot fuel jet structures, whereas points B-1300 and C-1300, once again, show the start of the process at the periphery of the bowl and propagation directed inwards. Also, the larger total mass of diesel fuel injected in operating point C-1300 manifests as larger high temperature reaction zone areas relative to B-1300 and more rapid growth of these regions.

The comparison of these points also demonstrates the increased ignition delay due to the premixed natural gas. In all instances presented here, the diesel-only case shows the start of reaction zone growth at an earlier time than the dual fuel case. These observations are consistent with results presented by Schlatter *et al.* [133], where injection of diesel pilot in pure air advanced the auto-ignition considerably.

4.3 Summary and Conclusions

The work presented in this chapter, for the first time, has utilized simultaneous spatially and temporally resolved OH* chemiluminescence and NL imaging to investigate effects of fueling control parameters on direct-injected diesel and premixed

natural gas dual-fuel combustion. The effects of pilot fuel injection pressure and ratio on dual-fuel combustion were investigated. The results demonstrate the potential to manipulate combustion of premixed natural gas (ignition sites locations and reaction zone growth mechanisms) through the fuelling strategy (P_{inj} , PR and ϕ_{CH_4}).

At high pilot injection pressures, the high temperature reaction zones and luminous ignition sites emerge around the edges of the piston bowl and propagate towards the center. This observation is in agreement with previous results [33] despite the fact that a light-duty optical engine with a much smaller displacement (499 cm³) and bore size (85 mm) was used in that work. It was also noted that the extent and rate at which the growth occurs correlates with the equivalence ratio of the premixed CH₄ charge (which is inversely proportional to the diesel pilot ratio for a given ϕ_{global} , i.e., load). Increasing the pilot ratio, while keeping the global equivalence ratio constant, resulted in a more rapid fuel conversion but limited the reaction zone propagation towards the center. This has the potential to be related to the emission of unburned species, which will be discussed in a future investigation. The possibility of increasing flame propagation to reach the central region by increasing ϕ_{CH_4} was also observed in [33].

Lower pilot injection pressures resulted in a more heterogeneous combustion event and locally fuel rich zones producing highly luminous soot particles. In general, the reaction zone initiated at the diesel pilot sprays and propagated outwards from there. This is a significantly different mechanism than noted for the higher injection pressures. Similar flame propagation mechanism was noted by Schlatter *et al.* in an RCEM with an 84 mm bore diameter with 400 bar injection pressure [133].

The comparison of investigated dual-fuel operating points to their corresponding diesel-only cases indicated similar trends in the reaction zone growth mechanism. This indicates that the premixed methane conversion mode is strongly impacted by the diesel pilot injection strategy.

The combustion modes observed at the different injection pressures are consistent with those proposed in previous thermodynamic studies [69, 127] and can significantly impact emissions and indicated efficiency. In addition, the diesel-only investigation indicated the hindering effect of presence of natural gas in the cham-

ber on the ignition of the charge, which has been noted elsewhere [133]. Further investigations are still required to assess the sensitivity of these observations to other engine operating speeds, loads and operation with EGR.

Chapter 5

Two-Color Pyrometry Method Improvement

In Chapter 2, the concept, fundamentals, and a review of the literature on implementation of two-color pyrometry technique, to obtain spatially resolved distribution of soot cloud temperature and concentration, was presented. Later in that chapter (see §2.3), it was discussed that the implementation of this method becomes more challenging at lower soot concentrations and temperatures, as the two-color pyrometry is an unstimulated emission technique relying on the naturally emitted incandescence from particles at elevated temperatures and the signal-to-noise (SNR) ratio significantly drops at those low concentration and temperature scenarios. Thus, this chapter has focused on identifying and assessing improvements to two-color pyrometry in order to facilitate its application to conditions with lower light intensities, such as LTC, PIDING, or late cycle soot characterization. These improvements were then applied to conventional diesel combustion as well as the low-soot conditions for PIDING combustion.

5.1 Method Enhancement

Several stages were considered to improve the overall performance of the two-color pyrometry method. In particular, improvements are identified through refinements to the solution algorithm, pyrometry system configuration, calibration, and image

processing. A detailed discussion of the individual steps are presented in what follows.

5.1.1 Algorithm Selection

The solution of equation 2.4 provides the KL factor and temperature for each pixel of each image recorded during a measurement; however, the efficacy and efficiency with which this is done varies significantly between various algorithms. Not all pairs of apparent temperatures will result in a solution for equation 2.4, with feasible temperature and KL values and thus the method is susceptible to signal noise. As such, the applied solution methodology can have a significant impact on the total calculation time and robustness. The performance of several solution methodologies was compared on the basis of their accuracy and computation requirements. To elucidate these influences, the behavior of the pyrometry equations are examined over the parameter ranges relevant to combustion studies, and several solution methodologies are compared.

The range of KL values which may be evaluated using the pyrometry method depends on the considered wavelengths (700 and 800 nm in this work, see §2.1.4). As shown in Figure 5.1, for $KL > 3$ the emissivity is approximately unity and the soot cloud acts like a blackbody and changes in KL are too difficult to assess as it becomes very sensitive to any noise in the data. Thus, KL factors in the range of [0.01 3] were considered to assess algorithm performance.

The solution of equation 2.4 can be achieved using a range of numerical root finding algorithms. To demonstrate the challenges associated with the solution of this equation, Figure 5.2 shows the residual (f , see equation 2.4) for a representative apparent temperature pair at 700 nm and 800 nm ($T = 2708$ K and $KL = 0.796$). Near the root (i.e. $f = 0$, $T = 2708$ K) the residual changes rapidly, which typically facilitates a rapid and robust solution. However, if a poor initial estimate for T is used (e.g., > 3000 K), the root may not be found. Furthermore, as the apparent temperatures change, due to changes in T and KL , the shape of the residual will also change.

The characteristics of three classes of root-detecting algorithms were evaluated: Newton-Raphson, Brent-Decker, and non-linear least square optimization al-

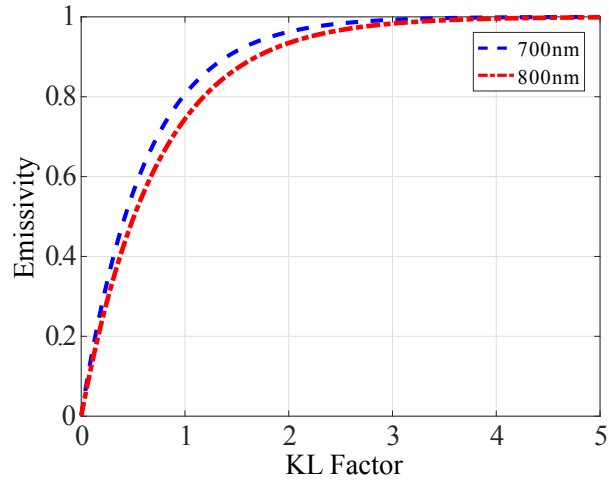


Figure 5.1: Soot cloud spectral emissivity vs. KL factor based on Hottel-Broughton’s empirical relationship (Equation 2.1) for typical engine relevant KL factor range.

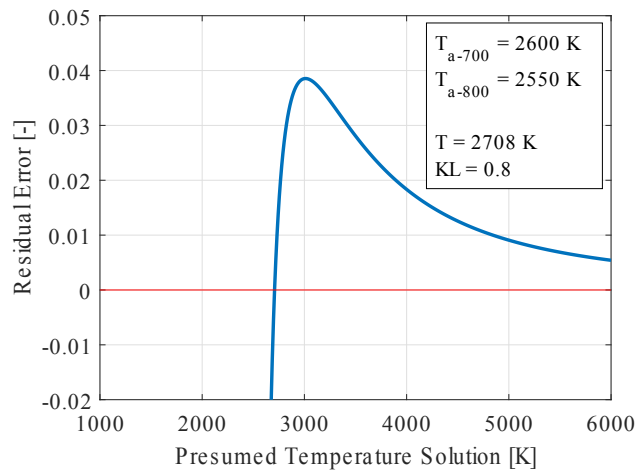


Figure 5.2: Residual error behavior around the root of equation 2.4. Temperature and KL were calculated using the non-linear least square trust-region dogleg algorithm (explained below). Solution: $KL=0.8$, $T=2708$ K.

gorithms. The Newton-Raphson method is relatively efficient but often encounters difficulties, such as overshoot due to inflection points or failure at stationary points. It is also susceptible to poor initial estimates of the root. It is therefore common to place limits on the number of iterations, bound the solution to an interval known to contain the root, and combine the method with a more robust root-detection algorithm.

The Brent-Dekker algorithm [17, 26] is a hybrid method which combines three different methods: 1) the Secant method, which is a finite difference approximation of the Newton-Raphson method with a slower but still super-linear convergence if the function meets certain criteria [122]; 2) the well-known bisection method, which is a relatively slow, yet robust method; and 3) inverse quadratic interpolation, which uses a recurrence relation based on Lagrange interpolation formula to find a quadratic approximation of the inverse of the function [36]. A secant method or inverse quadratic interpolation is used for fast convergence or, alternatively, bisection method will be used if a more robust approach is necessary. The detailed procedure on how the technique determines the suitable method for each iteration is described in [17].

As an alternative to conventional root-finding algorithms, equation 2.4 can be treated as an optimization problem where the objective is to minimize f with a non-linear constraint applied to $T(x_{i,j}, t)$. For this, the trust-region dogleg method was considered, in which f is approximated using a simpler function (\bar{f}) that has similar behavior near the point $T(x_{i,j})$ (trust-region). The next iteration is evaluated by minimizing \bar{f} in the trust-region using Powell dogleg procedure [111, 121].

The performance of each of the selected algorithms was evaluated over a range of temperatures and KL factors representative of engine combustion ($T=1500-3000$ K; $KL=0.01-3$). The apparent temperatures for this $T-KL$ space were used as inputs to equation 2.4 to assess the ability of each algorithm to evaluate the corresponding T and KL , as well as the computational time. The Newton-Raphson method is susceptible to poor initial estimates and an initial guess of the form of $T_{\text{initial}} = T_{a,700nm} + g(T_{a,700nm}/T_{a,800nm})$ was used and improved its performance notably (“assisted Newton-Raphson”).

Table 5.1 summarizes the convergence time of the different methods for a representative condition ($T = 2300$ K and $KL = 0.4$). The reported calculation time for

Table 5.1: Performance of considered algorithms (Core i5 3.2 GHz processor, 16 GB RAM). NLS: non-linear least squares.

Algorithm	Convergence time [ms] ($KL = 0.4, T = 2300K$)	Fraction of $T-KL$ space with $< 1\%$
Newton-Raphson	118.6 (11 iterations)	80%; Increased error for
Assisted Newton-Raphson	63.8 (6 iterations)	$0.5 < KL < 1$ and $KL > 2$, $T < 2200$
Brent-Dekker	2.9	60%; No convergence for $T_{a,700nm}/T_{a,800nm} > 0.994$
NLS optimization	5.5	99%
Hybrid Algorithm	3.9	99%

each method is for a single pixel, but it should be noted that a two-color pyrometry imaging analysis of a complete combustion process will require significantly more evaluations (on the order of 10^7). The Newton-Raphson method is slower from the remaining algorithms by an order of magnitude.

Also indicated in Table 5.1 are regions of the $T-KL$ space where the algorithms failed (Brent-Dekker) or had reduced performance, as well as the fraction of the $T-KL$ space that was resolved with $< 1\%$ error by each method. This is illustrated more clearly in Figure 5.3, where the performance over the complete range of temperatures and KL factors is considered. Here, it is noted that the assisted Newton-Raphson and Brent-Dekker methods result in significant errors and unresolved regions, respectively. The empty spaces in the error maps in each case show the areas where a high accuracy solution was achieved. In comparison, the trust-region dogleg algorithm, with an error tolerance of $1e-8$, successfully resolved all regions except those with $KL < 0.05$ (hence the mostly blank map in Figure 5.3). Lowering the error tolerance improves this limit at the expense of CPU cost. Also shown in Figure 5.3 are the residual errors for representative $T-KL$ combinations within the unresolved and high error regions. In these cases, the residual asymptotically decreases with increasing temperature, resulting in a false solution being returned.

Further investigation of the Brent-Dekker algorithm failure mode revealed that

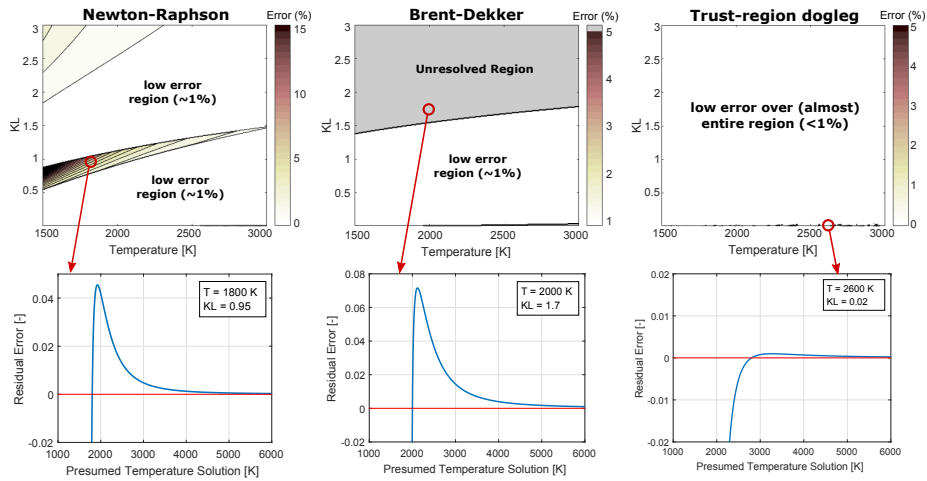


Figure 5.3: Algorithm performance comparison (temperatures) and representative solution residual profile: Assisted Newton-Raphson (left), Brent-Dekker (center), and trust-region dogleg with $1e-8$ error tolerance (right).

the regions which could not be resolved coincide with apparent temperature ratios ($T_{a,700}/T_{a,800} > 0.994$) greater than 0.994 (Figure 5.4), which cause a very sharp overshoot of the residual close to the root, followed by the asymptote. Thus, a hybrid algorithms comprising the Brent-Dekker and NLS optimization (trust region dogleg) was selected. This hybrid algorithm utilizes the faster convergence time of the Brent-Dekker and the robustness of NLS optimization (trust region dogleg). The Brent-Dekker algorithm is used for $T_{a,700}/T_{a,800} < 0.994$, and the NLS optimization is used elsewhere. The improved efficiency and increased robustness of this hybrid algorithm provides faster processing of images or can be used for the efficient generation of look-up-tables for image post-processing. Processing of combustion images from a single test in this work led to around 12 hours of total computation time.

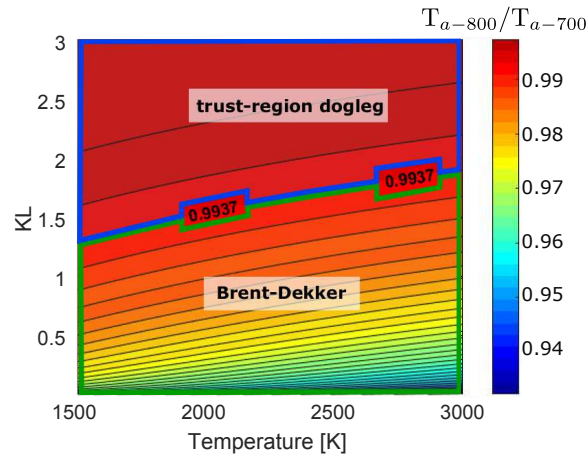


Figure 5.4: Apparent temperature ratios map shows correlation with unresolved regions in Brent-Dekker and Newton-Raphson temperature map and sets a criterion to switch between Brent-Dekker and trust-region dogleg with $1e-8$ error tolerance

5.1.2 Experimental Considerations

Accurate, correlated apparent temperature measurements are required as inputs to equation 2.4, though these measurements are affected by numerous experimental factors. To assess these, high speed two-color pyrometry imaging was applied to the optical engine configuration described in §3.1 and the effects of parallax, calibration, sensor response uniformity, and SNR improvement strategies were evaluated. The engine and imaging system setup specifications used for the presented analysis are listed in Table 5.2 and the optical engine configuration for two-color pyrometry is shown in Figure 5.5.

The HPDI injector design described in §3.1 was used for direct injection of Natural Gas (NG) and diesel. More details regarding the injector design and operation was presented in §2.2. The PIDING strategy presented here is not an optimized operating condition calibrated for on-road use. Rather, it was selected for the purpose of pyrometry method evaluation and development. Similarly, the diesel operating point, carried out using the same HPDI injector, is utilized to demonstrate the sensitivity of two-color pyrometry system to imaging parameters and data post-processing procedure. As such, the presented diesel operating point is

Table 5.2: Optical engine and imaging system specifications for two-color pyrometry.

Engine	Ricardo Proteus in optical configuration
Direct injector	Westport 1 st Gen. HPDI*
Fuel	Pump diesel, Natural Gas
Speed	600-1000 rpm
Imaging assembly	Phantom + Doubler (See § 3.2)
Exposure	8-32 μ sec at f/5.6
Frame rate	7,200-12,000 fps (0.5 CAD resolution)
Spatial resolution	624×304 pixels, 0.47 mm/pixel
Narrow band-pass filters	700 and 800 nm CWL; 10 nm FWHM

* High Pressure Direct Injection (See § 2.2)

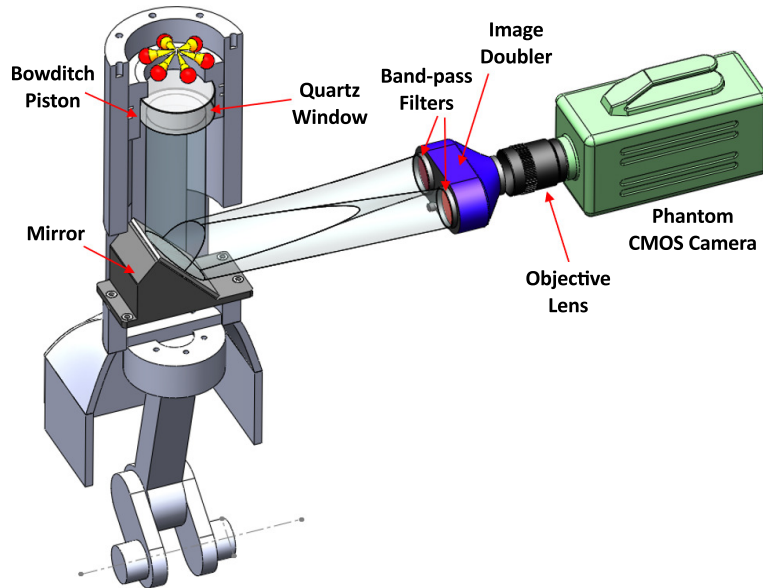


Figure 5.5: Two-color pyrometry imaging system implementation on the optical engine.

not representative of modern common-rail diesel injection systems, operating at much higher rail pressures. Table 5.3 lists the specification of the considered fueling and imaging parameters.

Table 5.3: Operating parameters for diesel and PIDING combustion.

Combustion Mode	Pilot Fuel	Main Fuel	Speed [rpm]	GIMEP [bar]	P_{inj} [bar]	Exposure [μsec]
Diesel	Diesel	Diesel	600	1.8	200	8 at f/5.6
PIDING	Diesel	NG	1000	10.5	180	32 at f/5.6

As described in §3.3.3, a skip-firing procedure was used and the final fired cycle from each repetition was imaged. Here, 3 fired cycles are followed by 15 motored cycles, and this set is repeated 15 times (restricted by camera buffer). In-take air heating ($\approx 80^\circ C$) was used to ensure ignition of the pilot diesel fuel. The flat piston bowl and lower compression ratio are expected to lead to more pre-mixing for the PIDING operation, especially at the loads considered here. Such partially-premixed NG strategies have been noted elsewhere to result in significant reductions in engine-out PM [38, 99]. This represents an even more challenging condition for pyrometric imaging, as the corresponding lower in-cylinder soot concentrations will result in lower imaging signal intensities.

Images were captured using the high-speed Phantom camera and the 60 mm lens coupled to the image doubler. Details of these components are presented in Chapter 3 and the layout is illustrated in Figure 5.5. The use of flat and prism mirrors in the image doubler design to project two combustion images onto the sensor provides a compact and robust method to capture two images with one sensor. This results in a lower signal attenuation compared to approaches using a beam splitter; however, it will introduce a parallax error, which must be addressed to ensure correlated apparent temperatures are considered.

5.1.3 System Calibration and Image Processing

The imaging system response was calibrated to relate the measured pixel intensities, D (i.e., “counts”) to the apparent temperature in equation 2.4. Furthermore, as two spectral intensities are required for each pixel position, a geometric calibration

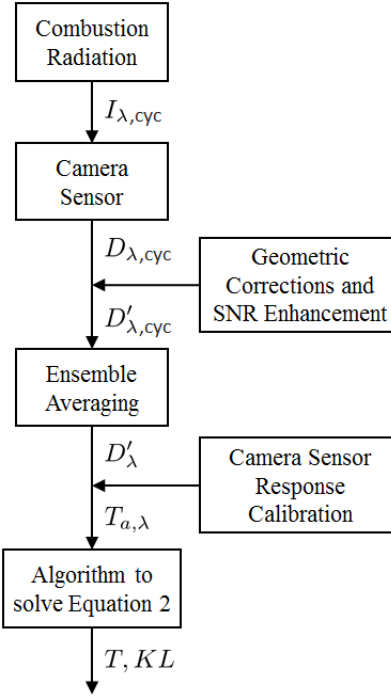


Figure 5.6: Work flow to obtain temperature and KL distributions from recorded raw signal.

was also implemented to ensure that the pixel spectral intensities are correlated between the two images. This geometric calibration includes an affine transformation, as well as static and dynamic parallax corrections. Finally, the SNR of the images was improved through image filtering. Figure 5.6 shows work flow to evaluate the temperature and KL for each image pair, beginning with the combustion radiation. The geometric corrections are applied to the recorded pixel intensities from individual cycles $D_{\lambda, cyc}$ prior to ensemble averaging to improve the SNR. Ensemble averaging to reduce noise was selected over ensemble averaging of T and KL , as solutions (T , KL) are not available for each pixel for each image and can result in unrepresentative mean values (see Appendix B). The sensor response calibration is applied to the ensemble averaged pixel intensities D'_{λ} to evaluate the apparent temperature, after which KL and T are calculated for each pixel. In the following, the effect of each of the geometric and sensor response calibration op-

erations are evaluated based on their impact on the calculated temperature and KL factors for the diesel operating mode (see Table 5.3).

Camera Sensor Response Calibration

The instantaneous spectral apparent temperature $T_{a,\lambda}(x_{i,j},t)$ is correlated to the imaging system output using the integrating sphere described in §3.2.2, where details of camera sensor response calibration using the integrating sphere is also presented. As discussed, extrapolation to combustion relevant intensities is still required in spite of the high intensity light source selected in this work. A high resolution calibration of the CMOS sensor showed that the camera chip does not provide a linear response between the illuminating light and the detected charge, as has been noted in literature [28, 59]. This effect was quantified and compensated for during the sensor response calibration process. An extrapolation approach similar to Jakob *et al.* is used [64], whereby the sensor response is linearized to facilitate extrapolation. In addition to the non-linearities at high intensities noticed and considered in their work, non-linearities at lower intensities were captured and accounted for. The geometrically corrected pixel intensities D' are linearized using a fourth order polynomial, based on the intensity calibration. The apparent temperature of the combustion radiation is then:

$$T_{a,\lambda} = \beta \times (X_{\tau} \times D'_{lin,\lambda}) + \gamma \quad (5.1)$$

where $D'_{lin,\lambda}$ is the linearized, ensemble averaged, corrected pixel intensity, β and γ are calibration coefficients, obtained from the sensor response calibration process, correlating the pixel intensity and apparent temperature, and X_{τ} is the ratio of the exposure time used during the combustion imaging to the exposure time for calibration. The exposure times are different during calibration and combustion imaging to ensure that the camera sensor is not saturated.

Application of the response linearization affected both the calculated temperature and KL factor, as shown in Figure 5.7. A more significant effect was noted for the KL factor than for T . Both the temperature and the KL factor were most affected along the flame boundaries, where mean temperature and KL factor differences of $> 8\%$ (200 K) and $> 60\%$ are present, respectively, relative to an analysis without

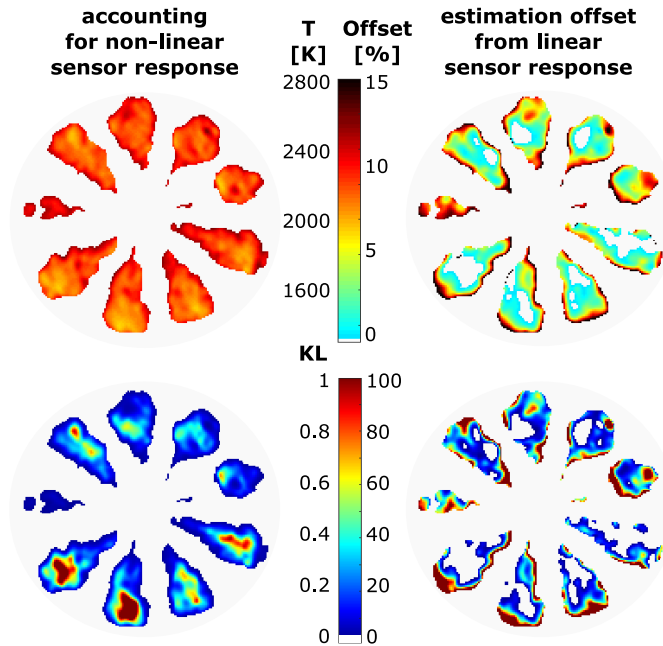


Figure 5.7: Influence of linearized extrapolation on two-color pyrometry results. Images shown for 9 CAD aTDC, diesel combustion. Geometric calibrations were implemented, and temperature and KL were calculated using the hybrid algorithm.

linearized extrapolation. The high relative differences for the KL factor around the edges of the flame is, in part, caused by the low absolute KL factor values resolved when response linearization is used.

Spatial non-uniformities in the intensity calibration can affect the local temperature and KL factors and may be caused by vignetting from optical components (e.g., image doubler, lens) and non-uniform CMOS sensor response [143]. To characterize these, the integrating sphere was translated while mounted on the engine, and the response was evaluated at several positions and used to correct the nominal intensity calibration. The effect of the non-uniform response on the temperature and KL fields is shown in Figure 5.8, where a significant difference is noted at the bottom of the images. The average error over the entire region was 4% for temperature and 20% for KL factor. A later crank position image is considered here to show the sensor response inhomogeneity near the piston bowl perimeter.

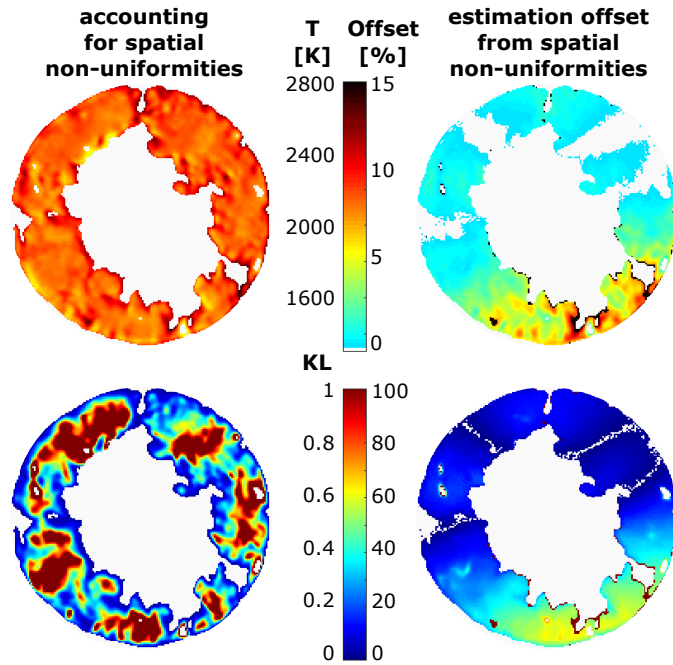


Figure 5.8: Effect of spatial non-uniformities imaging system response (caused by sensor, optical elements, and vignetting). T and KL were calculated using the hybrid algorithm. Images are for diesel combustion at 21 CAD aTDC.

To maximize the detection envelope of the system, it was configured such that the camera sensor saturation limit is the same for both wavelengths. This is affected by the spectral response of the camera, spectral transmissivity of the optical components, and the spectral emissivity of the soot cloud. A neutral density filter (0.2 OD) was used to attenuate the 700 nm light, which resulted in sensor saturation for both wavelengths at approximately the same apparent temperature. Figure 5.9 illustrates the detection envelope for the imaging system with and without matched dynamic ranges. The detection envelope is bounded at lower temperatures by background noise and at higher temperatures by saturation of the imaging sensor. By matching the dynamic ranges of the two wavelengths, the temperature detection envelope is increased by $\approx 25\%$ for temperatures at $0.5 < KL < 3$ and by $\approx 30\%$ for KL (at 2600 K). With the extended detection envelope, soot particles in the 1720-2300 K temperature range at higher soot concentrations ($KL = 3$) and

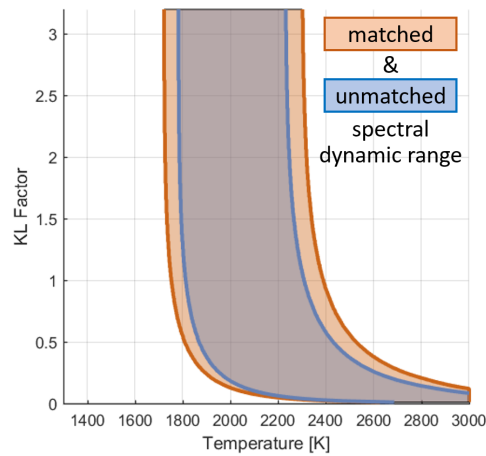


Figure 5.9: Increase in detection envelope by the imaging system dynamic range with matching aperture response.

the 2050-3000 K temperature range at low soot concentrations ($KL = 0.1$). Lower temperature soot particles (to the left of the marked region in Figure 5.9) cannot be resolved due to the pyrometry signal being too low for the current settings.

Geometric Corrections and SNR Enhancement

To ensure that the apparent temperature (pixel) pairs correspond to the same physical position in the cylinder, the recorded images are corrected using an image transformation based on the system geometry and parallax caused by the image doubler. To account for imperfect image corrections, filtering was implemented to improve SNR.

Parallax : To correct for parallax caused by the doubler, as well as other geometric differences between the images, a calibration target was positioned at the firedeck plane (with cylinder head removed) and used to develop an image transformation matrix. Images of the parallax calibration target were acquired with all relevant optical components (window, mirror, doubler, and lens) in the light path. Equation 5.2 describes the transformation matrix used to apply the affine and pro-

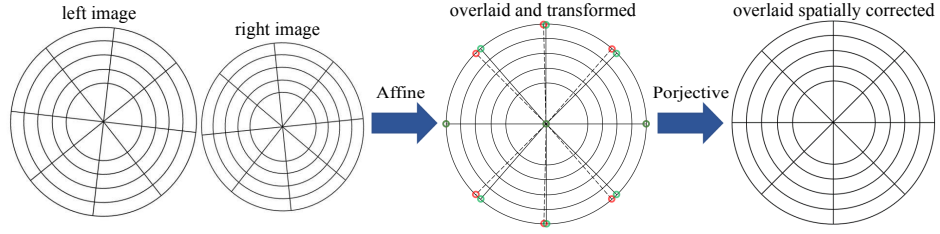


Figure 5.10: Parallax calibration target doubled image on the sensor (left), offset after affine transformation and the control point locations (center), and the fully registered doubled images (right).

jective transformations:

$$[u, v, w] = [x, y, 1] \cdot \begin{bmatrix} s_x \cos \theta & \sin \theta & p_x \\ -\sin \theta & s_y \cos \theta & p_y \\ t_x & t_y & 1 \end{bmatrix} \quad (5.2)$$

where $s_{(x,y)}$, $t_{(x,y)}$, $p_{(x,y)}$ are scaling, translation, and projective elements in x and y directions, respectively and θ is the rotation angle. After applying affine transformations (translation, rotation, and scaling), nine control points on each parallax calibration target (at 45° intervals and the center) were used to create eight corresponding regions on the two images. The vertices of these regions, expressed in homogeneous coordinates (u, v, w) , were used to fit a projective transformation matrix mapping each region to its corresponding pair. The projective image transformation was performed on all eight regions independently and the image pieces were then concatenated. The transformation matrix identified using this method was applied to every frame of a recorded image sequence. Figure 5.10 illustrates different stages of the image registration process using schematic images of the parallax calibration target with exaggerated effects for more clarity. Affine transformation of the two distorted aperture images results in a doubled image and a successful registration of the two images is achieved through elimination of the perspective error using a projective transformation.

Through the parallax correction, a significantly larger fraction of the image data could be resolved into T and KL , as shown in Figure 5.11. In addition, this figure also indicates the regions where no solution for equation 2.4 could be found, which

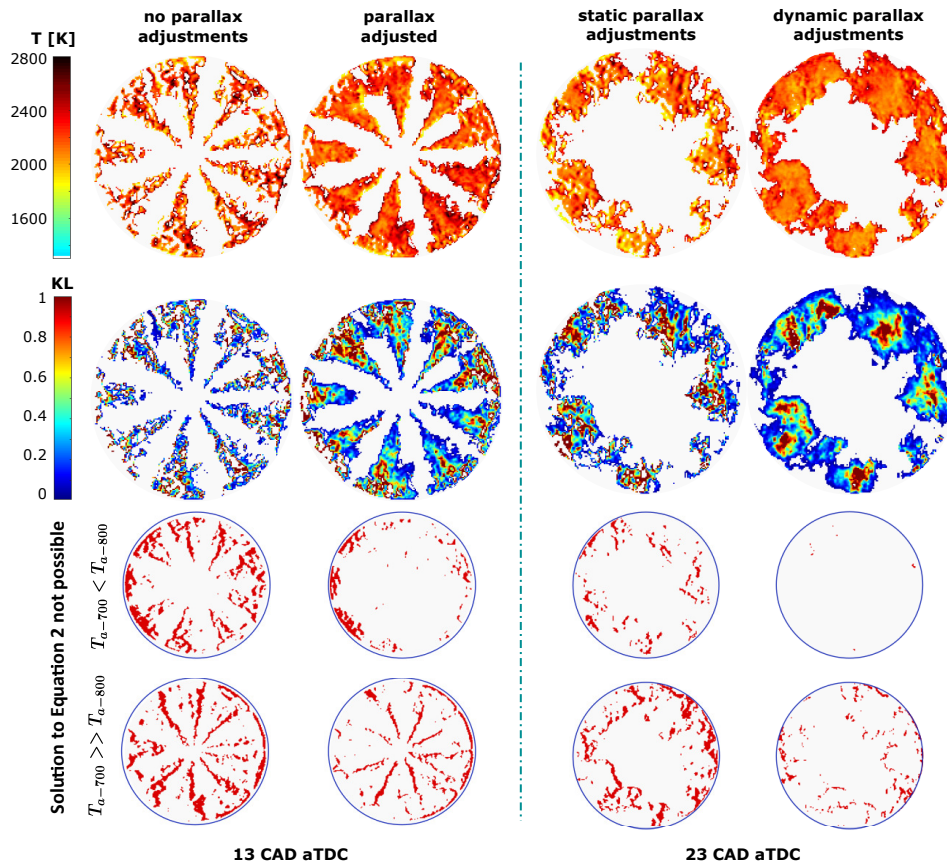


Figure 5.11: Impact of static and dynamic parallax corrections to increase resolved pyrometric signal at different crank positions. Unresolved regions are either due to $T_{a,700nm} < T_{a,800nm}$ or $T_{a,700nm} \gg T_{a,800nm}$. Linearized calibration extrapolation was implemented, and T and KL were calculated using the hybrid algorithm.

were found to coincide with conditions where: 1) $T_{a,700nm} < T_{a,800nm}$, which is not possible based on Planck's distribution, and 2) the difference between $T_{a,700nm}$ and $T_{a,800nm}$ was too large and resulted in calculated temperatures higher than the adiabatic flame temperature. Both of these conditions can be caused by imperfect image registration or response calibration, as well as signal attenuation and wall reflections.

Despite the improvements made by considering the parallax, there are still sig-

nificant unresolved regions, particularly late in the cycle. Consideration of parallax effects caused by the moving soot cloud, termed here dynamic parallax, enabled a significant increase in the resolved T - KL space later in the cycle, as shown in Figure 5.11 (right). Dynamic parallax was corrected using an image transformation matrix generated using the calibration target at firedeck (i.e., as above), as well as at the piston crown position later in the cycle (23 CAD aTDC). For each crank position the applied transformation matrix was an interpolation between the two reference matrices, on the basis of the piston displacement.

Binning/filtering : Pixel binning and spatial filtering can be used to improve the SNR of the unprocessed images [62], as well as to compensate for imperfect image registration and parallax correction. When binning is applied, the SNR is improved by averaging the intensity of several pixels, at the expense of reduced resolution. Filtering (as opposed to binning) is a preferred approach for SNR improvement as it has less significant resolution impacts. Image filtering is applied through convolution of the image with a filter kernel, H . Figure 5.12 compares the temperature fields evaluated using images with no SNR enhancement, 4×4 binning, a 4×4 box-filter kernel, and a Gaussian filter kernel ($\gamma = 1.5$). The latter is commonly referred to as a Weierstrass transformation [157]. The total number of pixels with a recorded signal are indicated in Figure 5.12 to provide a characterization of the resolution. Also given is the fraction of the pixels for which a solution to equation 2.4 was possible. The Weierstrass transformation resulted in the largest resolved signal fraction and was thus applied for the remainder of this work. For both filtering techniques (c and d), an increase in resolution is indicated, though this is, in part, due to pixels originally without a signal being assigned an intensity based on neighboring pixels or having their unsolvable intensity pairs altered through filtering into resolvable values.

The impacts of the individual refinements are presented above; however, their combined effect is much more significant, particularly with regard to increases in the fraction of the image data for which a solution to equation 2.4 is possible. The fraction of the imaged data for which a solution could be evaluated is shown in Figure 5.13 for each of the proposed corrections individually, as well as the use of all corrections and without any corrections. The uncorrected signal represents any

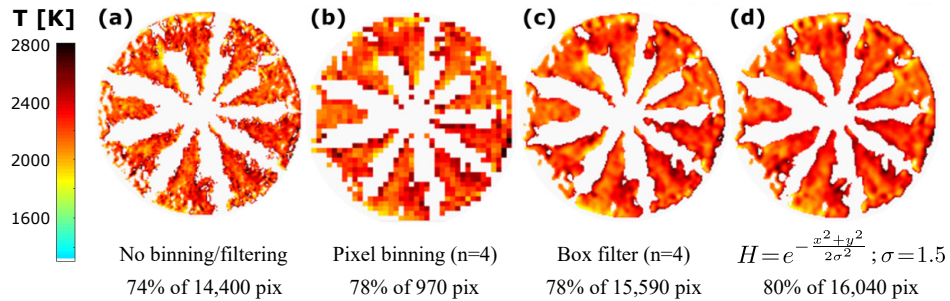


Figure 5.12: Comparison of pixel binning and filtering on calculated temperature fields. Image registration and non-linear response calibration are implemented, and T and KL were calculated using the hybrid algorithm. Images shown for diesel combustion at 13 CAD aTDC.

pixel with a recorded signal for both wavelengths, for which equation 2.4 could be solved, without applying any of the corrections. In this configuration, an average of 38% of the pixels could be evaluated to give T and KL values. With the exception of the parallax correction (55% resolved), other refinements do not result in significant increases in the resolved signal area (hybrid algorithm 44%, linearized response calibration 41%, and Weierstrass filtering 45% resolved). When these corrections are combined, a much more significant increase in the resolved signal is possible (38% vs. 85% signal resolved). For the diesel operating condition considered here, nearly all of the late-cycle signal is resolved which is relevant for relating in-cylinder soot to exhaust stream measurements. Figure 5.13 also shows the percentage difference in the spatially averaged two-color pyrometry temperature and KL factor calculations with and without all the refinements. As shown in this figure, while the temperature estimation difference remains within the $\pm 10\%$ band, differences of up to 80% was observed for KL factor estimations.

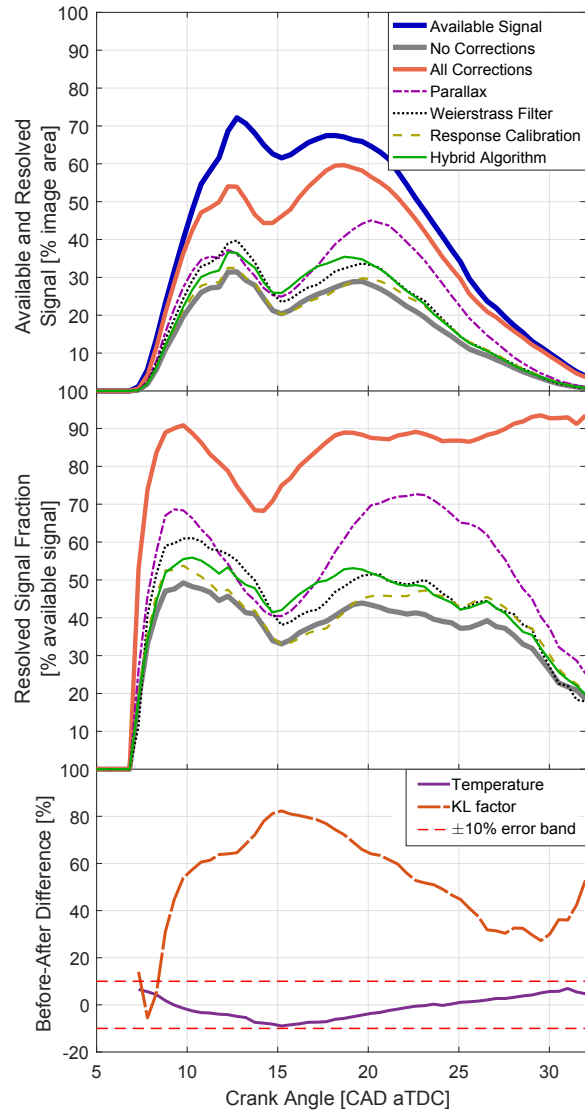


Figure 5.13: Effects of individual and combined corrections on the resolved image data, resolved data fraction, and spatially averaged T and KL factor estimations for the diesel operating mode.

5.2 Sample Results

The imaging system and proposed refinements were evaluated using two combustion strategies: direct injected diesel and Pilot Ignited Direct Injection Natural Gas (PIDING) combustion (see Table 5.3). While numerous works have applied two-color pyrometry to diesel combustion, PIDING has only been evaluated using an integral pyrometry system (i.e., not spatially resolved) [54]. As discussed in Chapter 2, PIDING is expected to be a challenging application for pyrometry in light of the lower PM concentrations and lower combustion temperatures associated with partially-premixed natural gas combustion. Furthermore, the relatively low-load and non-EGR conditions conserved here are expected to result in relatively low soot concentrations, even by PIDING standards, and thus add to the difficulty of pyrometry measurement. To demonstrate the efficacy of the proposed corrections, temperature and KL images are shown for diesel and PIDING combustion in Figures 5.14 and 5.15, respectively, with all corrections and with only affine geometric corrections and matched dynamic ranges. Through the additional corrections (static and dynamic parallax, response non-uniformity, and spatial non-uniformities), a larger portion of the soot cloud could be resolved. The diesel and PIDING combustion modes are only discussed briefly below to demonstrate the utility of pyrometry enhancements and a much more thorough evaluation of the soot processes is presented in the next chapter.

The diesel combustion shown in Figure 5.14 is in agreement with the conceptual mixing controlled combustion model presented by Dec [24], as well as two-color pyrometry results reported by Payri *et al.* [117]. In particular, a significant portion of the soot is generated through a mixing controlled flame established by the fuel spray. During later stages of the cycle, the KL signal decreases in both magnitude and area due to soot oxidation and advection of the tail of the reacting jet. The net result is a ring-shaped soot cloud that remains at the bowl periphery for the rest of the cycle, in part due to the low swirl in the considered engine. Although the uncorrected two-color pyrometry image sequence indicates a similar behavior, the refinements result in a significantly higher fraction of the signal being resolved (see Figure 5.13), generally for regions with higher KL factors. This effect is of particular significance later in the cycle (e.g., after 20 CAD aTDC) where the re-

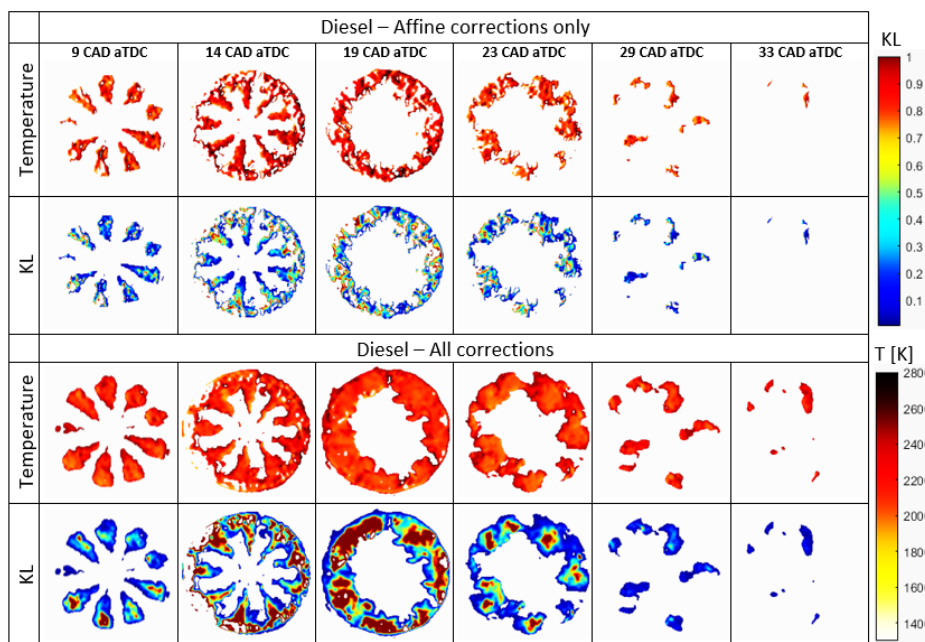


Figure 5.14: Temperature and KL distributions for diesel combustion (see Table 5.3) using proposed refinements developed in this work. Images with only affine corrections and matched dynamic ranges are shown to indicate the improvements due to the refinements.

finements can increase robustness of the pyrometric method for weak signals and provide insight into the late-cycle KL and temperature values, which are closely related to the exhaust stream emissions [76].

For PIDING combustion, shown in Figure 5.15, the KL factor is generally lower, relative to diesel combustion, as expected with natural gas as the primary fuel. The high methane content and the low load, which leads to premixing of the natural gas before ignition, results in lower temperatures and less potential for soot due to the low aromatic content of the fuel. In contrast to diesel combustion, the soot cloud is first detected at the piston bowl periphery and then propagates inwards to form a more uniform region. This is followed by a reduction in the soot area due to soot oxidation. While the uncorrected two-color pyrometry results for PIDING combustion indicate the location and timing of detectable soot, neither the soot cloud size, nor its growth rate could be resolved when the corrections are not

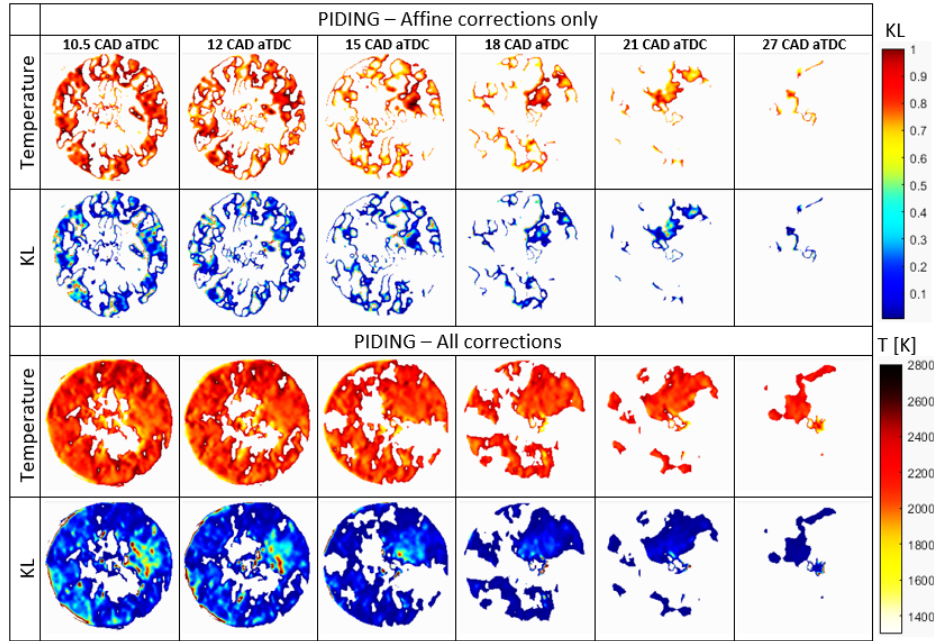


Figure 5.15: Temperature and KL distributions for PIDING combustion (see Table 5.3) using proposed refinements developed in this work. Images with only affine corrections and matched dynamic ranges are shown to indicate the improvements due to the refinements.

applied.

To quantify the impact of the corrections for PIDING, the resolved signal area and resolved signal fraction are shown in Figure 5.16. This improvement is of particular significance in the case of PIDING combustion, where the light intensity was 75% lower than for diesel operation, based on the required camera sensor exposure to provide suitable dynamic range (see Table 5.3). For the majority of the cycle the resolved signal fraction is approximately doubled. While the late cycle performance was increased, the low resolved fraction does indicate that this is a challenging application. It should be noted that there is little signal available after ≈ 24 CAD. The percentage difference in the spatially averaged T and KL factor calculations, with and without the proposed corrections, are also shown in Figure 5.16, which indicates up to 50% error in KL factor estimations, while the temperature estimation still remains within the $\pm 10\%$ difference band.

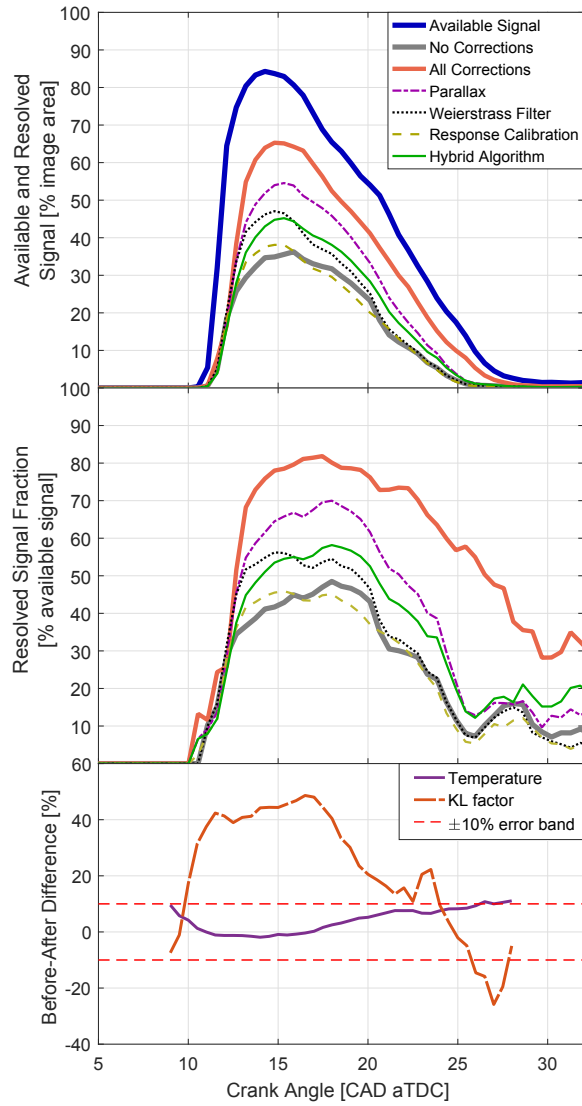


Figure 5.16: Effects of individual and combined corrections on the resolved image data, resolved data fraction, and spatially averaged T and KL factor estimations for PIDING combustion.

5.3 Summary and Conclusions

This chapter focused on identifying and assessing measures towards improved high speed, two dimensional pyrometric imaging in a compression ignition engine. This was carried out through revisiting implementation procedure, algorithm selection, imaging system calibration, and image post-processing. The refined technique was used to consider direct injection diesel combustion and natural gas combustion in an optically accessible engine. It should be noted that the enhancements proposed in this work will not overcome the short-comings of the two-color pyrometry method inherent with line-of-sight methods, nor will they address uncertainties due to window contamination or wall reflections.

Several improvements to the two-color pyrometry method were characterized:

1. Use of a combined non-linear least square optimization algorithm (for high apparent temperature ratios) and Brent-Decker method (for lower apparent temperature ratios) reduced the computation time by 95% relative to a Newton-Raphson method, and resolved 99% of the measurement space with $< 1\%$ error ($\approx 80\%$ for Newton Raphson). The total computation time for a single test ($\approx 10^7$ analysis points) was close to 12 hours with the operating system used in this work. In addition, use of this combined approach resulted in a more robust algorithm which allowed equation 2.4 to be solved for a greater range of apparent temperatures. This algorithm can be used for evaluation of images, or for the generation of look-up tables for subsequent processing of images.
2. Static and dynamic parallax correction resulted in an increased fraction of the image being resolved ($\approx 1.3 - 2\times$ increase). The former is a result of the imaging system used, and the latter due to the piston motion. Utilizing these corrections, it is possible to utilize a compact and robust image doubler, simplifying the hardware and avoiding the SNR penalty associated with a beam splitter.
3. Weierstrass spatial filtering improved the SNR and provided increased image resolution and resolved signal fraction, relative to pixel binning and box filtering, respectively. The increase in resolved signal fraction is attributed

to the increased signal to noise ratio for individual pixel, resulting in better correlation between the two images.

4. By matching the imaging dynamic range for each considered wavelength, the dynamic range of the camera is fully utilized for both wavelengths. This increased the KL and T detection envelopes by $\approx 25\%$ and $\approx 30\%$, respectively.

Application of all of the refinements resulted in an increased resolved signal fraction for diesel and PIDING combustion strategies. For diesel combustion, a temperature and KL could be evaluated for $> 80\%$ of the image data, while for PIDING 40-80% of the image data could be resolved. It should be noted that 100% of the data cannot be resolved due to line-of-sight integration, wall reflections, and ensemble averaging resulting in unrepresentative pixel intensities. The refinements enabled the pyrometric method to be applied to PIDING combustion, which had a 75% lower signal intensity than the considered diesel combustion. In the next chapter, the refinements presented here are used to assess the soot formation and oxidation in the low sooting PIDING combustion strategy under a wide range of operating conditions.

Chapter 6

Optical Investigation of PIDING Combustion

The improved two-color pyrometry method, as concluded in Chapter 5, can be implemented to study soot processes in low soot signal combustion strategies. The pilot-ignited direct-injection natural gas combustion is a good example of such low soot signal combustion scenarios. As such, this chapter focuses on utilizing simultaneous spatially and temporally resolved two-color pyrometry and OH* chemiluminescence measurements to better understand soot formation and oxidation processes of PIDING combustion.

6.1 Engine Operating Conditions and Analysis Metrics

In order to better understand the underlying fuel conversion mechanisms and identify the soot formation and oxidation modes during typical PIDING combustion operation, a range of engine operating conditions were considered. A “baseline” operating point, representative of a medium-load engine operating condition, was selected at the center of the operating space. The pilot fuel and NG injection timing for this operating point was selected such that NG ignition happens during NG fuel injection, with the goal to examine whether a quasi-steady, non-premixed jet flame corresponding to mid- and high-load diesel combustion operation can be achieved [126]. The baseline operating condition selected as such, served as a datum to

study the influence of the major fueling control parameters. Sweeps of three different control parameters, namely the NG injection pulse width (GPW), the relative timing between the pilot diesel and NG injections (RIT), and the fuel injection pressure (P_{inj}) was considered.

The investigated parameter space was selected through measurements under thermodynamic engine configuration with steady state operating conditions. These measurements were used to identify the appropriate optical engine control settings, including pilot fuel and NG injection timing and duration and intake air conditions, as well as to evaluate air and fuel flow rates. Table 6.1 lists the operating conditions investigated in this work. The selected operating conditions listed in this table were not derived from or representative of any specific engine calibration.

Table 6.1: Operating points specifications. cPSOI: commanded Pilot Start of Injection; cGSOI: commanded Gas Start of Injection; PPW: Pilot Pulse Width; GPW: Gas Pulse Width; P_{inj} : fuel injection pressure; RIT: Relative Injection Timing. The fuel system controls the natural gas rail pressure to a level ~ 10 bar below that of the diesel rail pressure.

Point	cPSOI [° aTDC]	cGSOI [° aTDC]	PPW [ms]	GPW [ms]	P_{inj} [bar]	RIT [°]	GIMEP [bar]
Baseline	-18	-10	0.7	1.45	180	8	11.5
Short GPW	-18	-10	0.7	1.05	180	8	5.3
Long GPW	-18	-10	0.7	1.85	180	8	14.2
Short RIT	-11	-9	0.7	1.45	180	2	11.85
Long RIT	-24	-10	0.7	1.45	180	14	11.3
Negative RIT	-16	-22	0.7	1.45	180	-6	11.82
High P_{inj}	-16	-8	0.6	1.2	220	8	12.8
Low P_{inj}	-22	-14	1.0	2.1	140	8	11.2
Diesel	-18	-10	0.7	1.75	180	8	2.2

As discussed in Chapter 2 (§ 2.1.3) OH* chemiluminescence signal can be used to identify the non-sooting flame area and high temperature reaction zones (local heat release), and it is also believed to be a good marker for soot oxidation [25, 94, 159]. Simultaneous two-color pyrometry and OH* chemiluminescence measurements provides more insight into in-cylinder soot analysis by consideration of these high temperature reaction zones and local heat release information in conjunction with soot formation and oxidation processes. The configuration of the

engine and the measurement setup is shown in Figure 6.1 and the imaging system settings are presented in Table 6.2. Additional details on the imaging system and test facility is available in Chapter 3.

To facilitate the imaging, the skip-firing procedure was used in which 3 fired cycles followed 17 motored cycles and only the final of the three fired cycles was used for imaging purposes (see §3.3). The combustion images presented below are ensemble averages of 15 cycles obtained using this skip-firing method. The low compression ratio (CR) required that the intake air be heated (~50-60°C) to ensure ignition of the pilot diesel fuel. Intake air pressure was adjusted to compensate for the air density change due to the change in temperature.

Table 6.2: Imaging system specifications

	Two-color Pyrometry	OH* Chemiluminescence
Camera	Phantom v7.1 CMOS	Photron SA1 CMOS
Intensifier	-	LaVision high-speed IRO
Image doubler	LaVision	-
Gain	-	70%
Exposure/Gate	8-64 μ sec @ f/5.6	10 μ sec @ f/5.6
Bit-depth	12	12
Lens	60mm-f/2.8 Micro-Nikkor	98mm-f/2.8 Cerco UV
Camera Resolution	624x304	640x640
Physical Resolution	0.47 mm/pixel	0.19 mm/pixel
Narrow band-pass filters	700 & 800 nm CWL	307 nm CWL
filter bandwidth	10 nm FWHM	20 nm FWHM
Frame rate		12,000 fps
Engine Window		83 mm unblocked

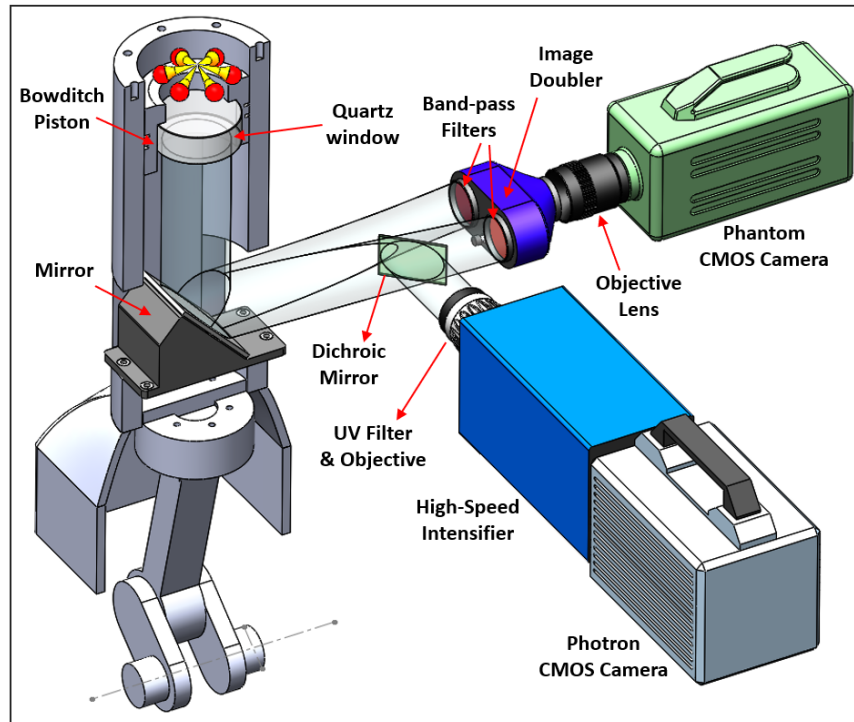


Figure 6.1: Simultaneous two-color pyrometry and OH* chemiluminescence imaging system

6.1.1 Analysis Metrics

The analyses presented on in-cylinder soot processes in this chapter are based on 2D and spatially averaged temporally resolved two-color pyrometry and OH* chemiluminescence, as well as HRR results, and also in correlation with pilot and NG injection pulses, presented in terms of estimated mass flow rates normalized by the baseline value (more details in Appendix C). Mechanical injection delay was estimated through illuminated combustion chamber optical measurements and needle ramp-up and ramp-down timings were estimated in a previous work [37].

The extent and mode of soot cloud development and combustion chamber coverage, temperature and KL factor levels, and late-cycle oxidation rates are the major factors that determine the engine-out soot. In order to better understand the processes controlling these determining factors, the rate of soot formation and oxida-

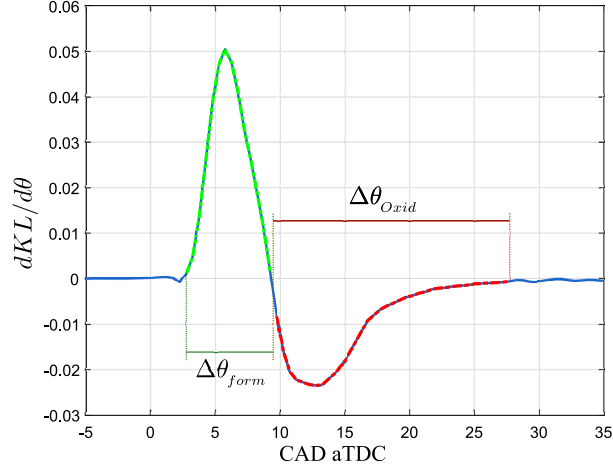


Figure 6.2: Net soot formation and oxidation for baseline PIDING operating point and the corresponding detected soot formation and oxidation durations.

tion, as well as its correlation with instantaneous distribution of soot temperatures and KL factors was investigated in the current analysis. A normalized net value for the rate of soot formation was considered, which is described in equation 6.1. This process is illustrated for the pyrometry results from baseline operating condition in Figure 6.2.

$$\dot{KL}_n = \left[\frac{\overline{dKL/d\theta}}{\Delta\theta} \right]_{form} \quad (6.1)$$

where $\Delta\theta_{form}$ is the crank position range from the first detected soot until the peak KL and $\overline{dKL/d\theta}$ is the mean production rate within $\Delta\theta_{form}$ range. The mean production rate was normalized by the formation duration in equation 6.1 in order to isolate that effect in comparison of the results.

To supplement the possible interpretations from pyrometric imaging results, the temperature and KL area fraction distributions, A_T and A_{KL} , were considered. At each crank position, the area fraction distribution is described using a “set”

(denoted by $\{\}$):

$$A_{\xi}(\theta) = \left\{ n_j = \frac{1}{N_{pix,tot}} \sum_{i=1}^{N_{pix,tot}} (pix_i | \xi_{pix_i} > \xi_j) \right\} \quad ; \quad j = 1, \dots, m; \quad (6.2)$$

where ξ is the metric of interest (T or KL), $N_{pix,tot}$ is the total number of pixels within the bowl area, subscript j denotes the T or KL bin and m is the total number of bins, and n_j is the fraction of $N_{pix,tot}$ falling in bin j . The fractional area distributions for all crank positions can be shown in a Cumulative Histogram Time Series (CHTS) diagram [125]. Figure 6.5, discussed in §6.2.1, shows an example of the area fraction CHTS diagrams for the baseline operating condition. Area fraction distributions were calculated for individual cycles and then ensemble averaged at each crank position.

6.2 Results and Discussion

The focus of the current work was on the optical investigation of the described parameter sweeps, specifically soot formation and oxidation processes. The study of the pilot and NG ignition and fuel conversion modes, using high-speed OH* chemiluminescence and natural-luminosity imaging, was the focus of a parallel work in the group [126]. This investigation provided an updated conceptual understanding of the governing mechanisms controlling the PIDING combustion.

In order to facilitate the interpretation of the two-color pyrometry and OH* chemiluminescence results, in conjunction with the hypothesized processes, this section first focuses on describing typical soot formation and oxidation trends for the baseline operating point. This is followed by highlighting the effects of considered parameter sweeps on the described trends and the correlations between various diagnostics during each parameter sweep. Based on these results, the next section attempts to make the link between the various parameter sweeps and help understand the soot formation and oxidation processes in accordance with the current conceptual description of PIDING combustion modes.

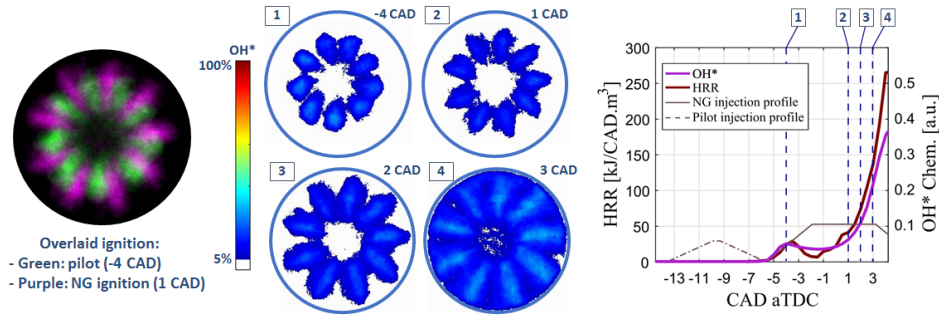


Figure 6.3: Baseline PIDING operating point; Ignition and early stage combustion. Left: Overlaid OH* images of pilot and NG ignition from their corresponding crank positions showing their spatial correlation; Center: OH* images of pilot ignition and NG ignition and ignited reaction zone growth; Right: HRR and spatially averaged OH* results

6.2.1 Baseline Operating Condition

The baseline operating condition was designed based on comparisons with typical HRR response in a production engine. In order to achieve this, the combustion control parameters, namely the fuel rail and intake boost pressure, commanded start of pilot and NG injections and the relative injection timing between these two were adjusted. The absolute value of these control parameters will not match those of a production engine due to the differences in the compression ratios, bowl geometries and intake air temperatures. As a standard PIDING operating point, a small amount of pilot diesel fuel is injected at 18 CAD bTDC, prior to injection of the primary natural gas fuel (10 CAD bTDC), to ignite and provide the activation energy required to ignite the lower cetane natural gas. Figure 6.3 shows the OH* chemiluminescence images of the pilot and NG ignition as well as early combustion processes.

The optical ignition timing and delay (θ_{ign} and τ_{ign} , respectively) were characterized based on the first indication of the OH*-CL signal, for pilot and NG fuels. Comparison of optical and thermodynamic ignition delay values for operating points in Table 6.1 are available in Appendix D. OH* images of the baseline PIDING ignition phase shows that the pilot diesel fuel is ignited after estimated pilot end-of-injection (EOI), with 12.5° optical ignition delay. At 4 CAD bTDC, the

OH* chemiluminescence images in Figure 6.3 shows that pilot combustion creates a ring of “high reactivity” approximately half-way through the combustion chamber, i.e., a ring shaped high temperature reaction zone comprising ignited pilot fuel combustion products and radicals, which matches the pilot HRR peak in phasing. The HPDI injector used in this work had 9 pilot and NG fuel injection holes, with 20° interlace angle between each pair of holes. Thus, the natural gas is injected in the space between ignited pilot kernels where it ignites on the jet axis along the sides of the quasi-steady gas jet as it passes through the high energy ring. This process is illustrated in the overlaid OH* chemiluminescence images from pilot and NG ignition in Figure 6.3 (-4 and 1 CAD aTDC, respectively), and was also predicted by numerical simulations [90]. Using a 0° interlace angle, as OH* imaging of NG ignition process showed [54], would cause the ignited pilot kernels to engulf the NG jet and ignite it at the head of the jets.

After ignition, high temperature reaction zones develop in predominantly radial directions on the NG jet axes (OH* chemiluminescence in Figure 6.3, 1-3 CAD aTDC), with a calculated average reaction zone growth rate of approximately 10 m/s [126]. No soot was resolved within the detection limit of the current imaging setup during the diesel pilot and primary NG combustion prior to the peak HRR. This is evident from Figure 6.4, which shows the process of soot formation, soot cloud growth and oxidation for the baseline operating condition, through spatially resolved and averaged pyrometry and OH* chemiluminescence, as well as HRR results. This suggests combustion of a sufficiently mixed charge of pilot diesel and NG during this phase. During this early stage of combustion, the mean OH* chemiluminescence signal follows HRR trend very closely and OH* signal is concentrated on the NG jet axes for NG ignition and early primary combustion. Filtered NL measurements ($\lambda > 340$ nm) of the NG ignition and early combustion before the peak HRR by Hatzipanagiotou *et al.* [54], also show low NL signal, originated from the chemiluminescence emitted by CH*, C₂*, CN* and CO₂* radicals present in the same range of the spectrum, in addition to the soot luminescence [88].

The mean imaging parameters ($\overline{OH^*}$, \overline{KL} , and \overline{T}) in Figure 6.4, and all subsequent figures in this chapter are evaluated from the OH* images and calculated KL and T distributions as follows:

$$\overline{OH^*} = \frac{1}{N_{pix,tot}} \sum_{pix} OH_i^* \quad (6.3)$$

$$\overline{KL} = \frac{1}{N_{pix,tot}} \sum_{pix} KL_i \quad (6.4)$$

$$\overline{T} = \frac{1}{N_{pix,res}} \sum_{pix,res} T_i \quad (6.5)$$

where subscript i denotes each pixel in processed images, $N_{pix,tot}$ is the total number of pixels. For \overline{T} only pixels for which a temperature can be solved ($N_{pix,res}$) are considered. For $\overline{OH^*}$ and \overline{KL} all pixels are considered. \overline{T} is plotted for crank positions where $\overline{KL} > 0.01$, which is ~5% of the peak KL for the baseline operating condition, given the low SNR and growing error bars outside this region (shaded area around \overline{T} and \overline{KL} curves).

As natural gas fuel conversion continues, the high temperature reaction zones, localized along the gas jets, reach the bowl wall region and PIDING combustion proceeds to the primary phase exerting heat at higher rates (Figure 6.3, 3 CAD aTDC). This is followed by the onset of soot signal detected at the points of NG jet impingement on the wall, forming small soot “pockets” on individual NG jet axes around the periphery of the bowl wall. The detected onset of soot signal (6.4, 4 CAD aTDC) temporally coincides with formation of toroidal shaped zone of higher temperature reactions from OH^* chemiluminescence, with higher signal levels than off-axis area between NG jets.

During the rest of NG injection, each initial soot pocket grows and merges into neighbor pockets, forming a toroid adjacent to the wall (4-6.5 CAD aTDC). The soot cloud toroid then expands and progresses towards the center, as a result of continued soot formation and reflected momentum of the NG jets impinging on the bowl wall. The latter process was discerned through tracking small high intensity soot pockets at higher temporal resolution in the range of 7.5-12 CAD aTDC, presented in Appendix E, and also through comparison of parameter sweep effects as discussed later in this chapter.

Comparison of the temporal changes in intensity gradients of the 2D OH^* chemiluminescence signal and KL factor distributions in Figure 6.4 (4-8.5 CAD aTDC),

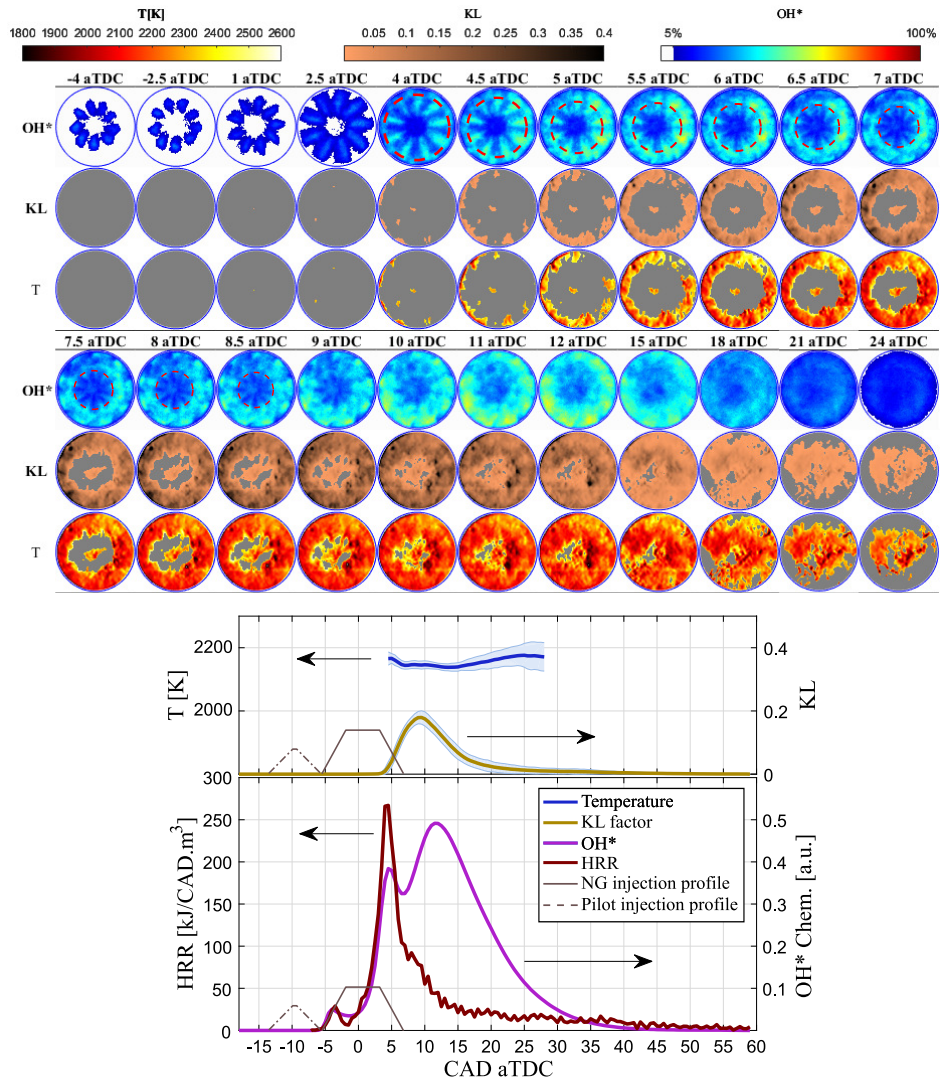


Figure 6.4: Baseline PIDING operating point; NG combustion and soot formation and oxidation. Results are ensemble averaged from 15 cycles (see §3.3.3).

depicts signal interference for measurable OH* signals. This is shown more clearly by the dash-line rings on OH* image frames within this range, marking the leading edge of the growing soot cloud. During this process, the OH* signal on NG jets outside the expanding soot cloud toroid remains undisturbed, while portions of the OH* signal within the soot cloud are partially attenuated by this optically thicker medium. The higher OH* signal zones on the NG jet axes then partially recover later in the cycle (Figure 6.4, 10-12 CAD aTDC), as parts of the soot cloud become optically thinner through soot oxidation, before the final decay in the OH* signal through the late-cycle soot oxidation stage. Alternatively, the recovery of the OH* signal might be due to production of more OH* radicals and stronger chemiluminescence signal, or a combination of these two processes. On the spatially averaged results, this results in a local minimum, followed by a 2nd OH* peak due to partial signal recovery. The OH* chemiluminescence signal attenuation by the optically thick soot cloud should be accounted for during interpretation of the OH* imaging results and, in some cases, explains discrepancies in spatially averaged results, as discussed later in this work.

High temperature reactions on the NG jet axes, producing higher intensity OH* chemiluminescence relative to off-axis space between jets, are visible until shortly after NG EOI ([1 8.5] CAD aTDC in Figures 6.3 and 6.4). This is not overlapped by any detected soot particles (lie within the described dash-line rings zone), which suggests during PIDING baseline operating condition a portion of the direct injected natural gas undergoes a low-sooting non-premixed combustion mechanism localized along the gas jets.

Following the soot processes later in the cycle, the pyrometry signal starts to decay and disappear after the mean *KL* peak, starting from the wall regions (Figure 6.4, 18 CAD aTDC). This process is accompanied by higher intensity OH* signal on the periphery of the visible bowl area, denoting overlapping high temperature reactions and late-cycle soot oxidation process. This is followed by a more homogeneous OH* signal distribution and soot signal decay at a slower rate in the central bowl regions, suggesting a more uniform soot oxidation process towards the end of the cycle. The soot oxidation process at different concentration levels from after the peak *KL* factor through the late-cycle stage is also evident from the CHTS diagrams of the baseline operating condition shown in Figure 6.5. Here,

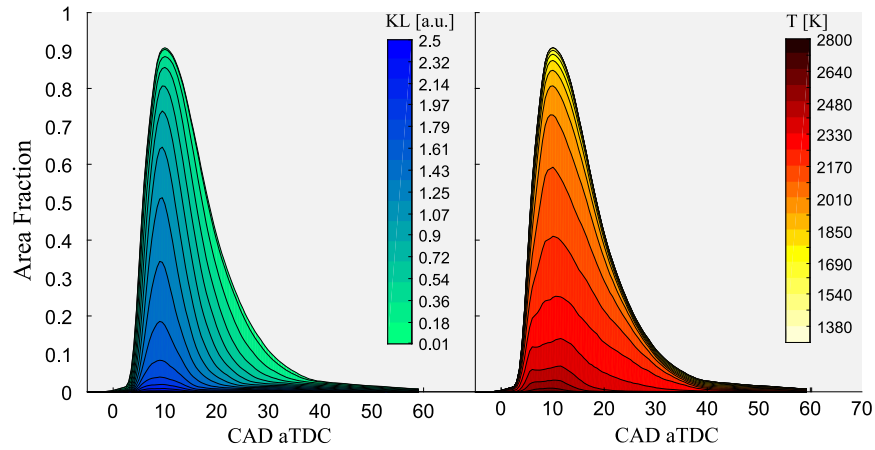


Figure 6.5: Area fraction distribution of two-color pyrometry soot temperatures and KL factors at each crank position (CHTS diagram) for the baseline operating condition. Results are ensemble averaged from 15 cycles (see §3.3.3).

there is notably higher decay rates in KL factor levels compared to more steady temperature levels denoting consistent exothermic reaction of oxidizing the diminishing soot particles. The comparison of KL factor peaks at different levels in this figure and the mean KL factor curve in Figure 6.4 shows matched phasing as expected. However, focusing on the processes after 20 CAD aTDC shows low mean KL factor values during the late-cycle oxidation stage and large resolved areas with predominantly low KL factor values.

It is worth noting that the soot cloud signal disappearance, in addition to the late-cycle oxidation processes, could in-part be due to the soot particles cooling later in the cycle during expansion and transitioning below the current two-color pyrometry detection limit. The two-color pyrometry system detection envelope and its optimized adjustments were discussed in §5.1.3. Figure 6.6 shows T - KL cumulative distribution from all optically recorded combustion cycles after 10 CAD aTDC. The enclosing red lines in this figure shows the pyrometry detection limits, determined by the dynamic range of the camera (12 bits) and the calibration range. Here, the pyrometry system detection range was optimized to avoid sensor saturation at higher intensities. High number of resolved values can be observed across the lower detection limit at $KL < 0.25$ and temperatures in the

range of 1700-2600 K, whereas limited number of higher KL points were observed at the lower temperature limit (~ 1600 K). This is an indication of oxidation being a significant contributor to pyrometry signal decay, compared to the cooling effects, especially during the late cycle oxidation stage.

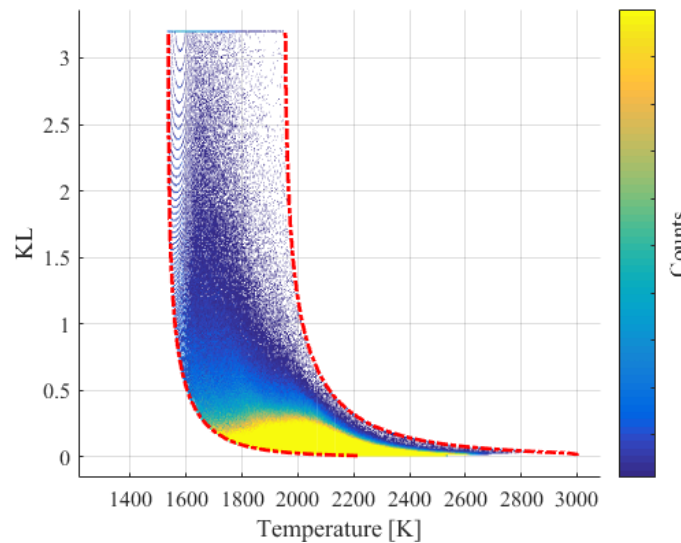


Figure 6.6: Aggregate resolved temperature and KL factor cumulative distribution for the baseline operating condition after 10 CAD aTDC. Results are ensemble averaged from 15 cycles (see §3.3.3).

6.2.2 Fuel mass (injection Duration) Effect

The primary fuel (i.e., natural gas) injection pulse width, GPW, is used in combination with the fuel injection pressure to control the injected fuel mass and the engine load, similar to diesel engines. Injection of more natural gas is expected to increase the engine load at the expense of higher soot formation. The imaging and integrated measurement results illustrated in Figures 6.7 and 6.8, respectively, show the effect of extending GPW on PIDING combustion. The commanded start of pilot and NG injection, pilot injection duration, and the fuel injection pressure are kept constant to facilitate assessment of the GPW sweep effects. As a result, optical pilot and NG ignition timings and delays remain the same among GPW sweep operating points

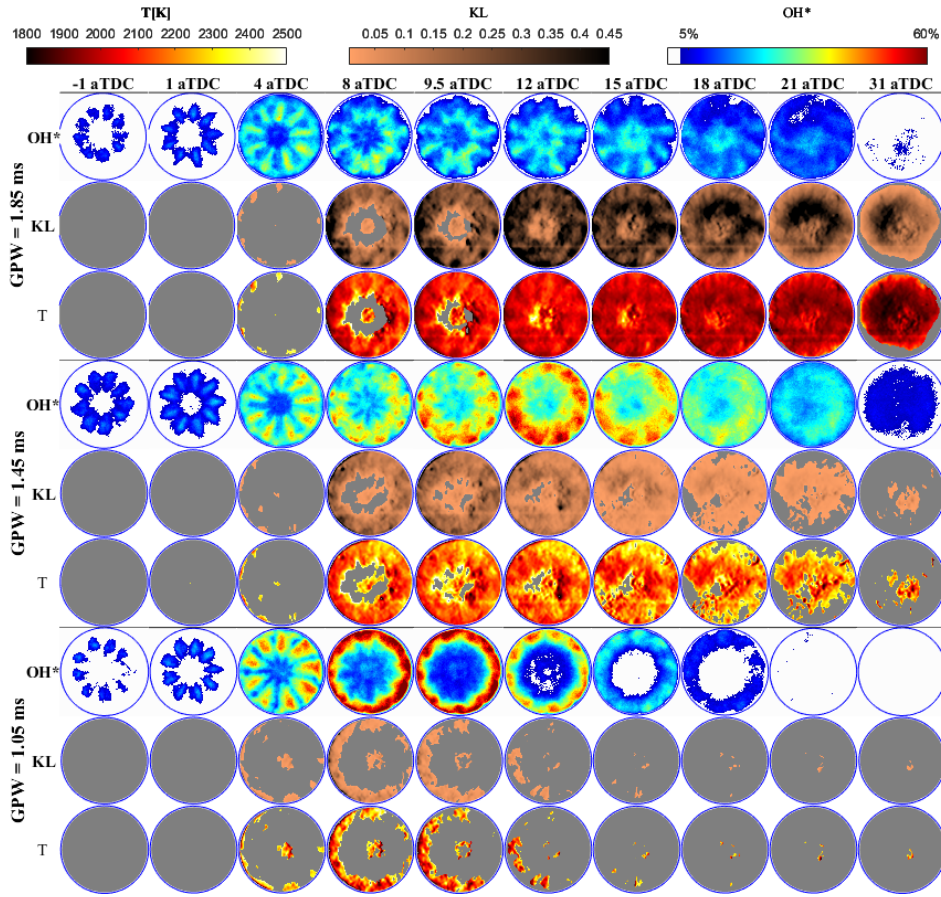


Figure 6.7: NG fuel mass effects at constant injection pressure; 2D OH* chemiluminescence and two-color pyrometry results. Results are ensemble averaged from 15 cycles (see §3.3.3).

(Figure 6.7, $\Theta_{ign,pi} = -1$ and $\Theta_{ign,NG} = 1$ CAD aTDC, respectively), as do other processes described by the OH*, pyrometry, and HRR results, until the NG EOI in the shortest GPW operating point (~ 4 CAD aTDC). The overall processes as inferred from the evolution of OH* and soot distributions and the HRR shapes are similar although, as expected, more soot was produced in response to increasing the NG injection duration.

For the shortest injection duration (GPW=1.05 ms), NG EOI occurs before the onset of soot signal was detected at the wall region. The soot cloud does not

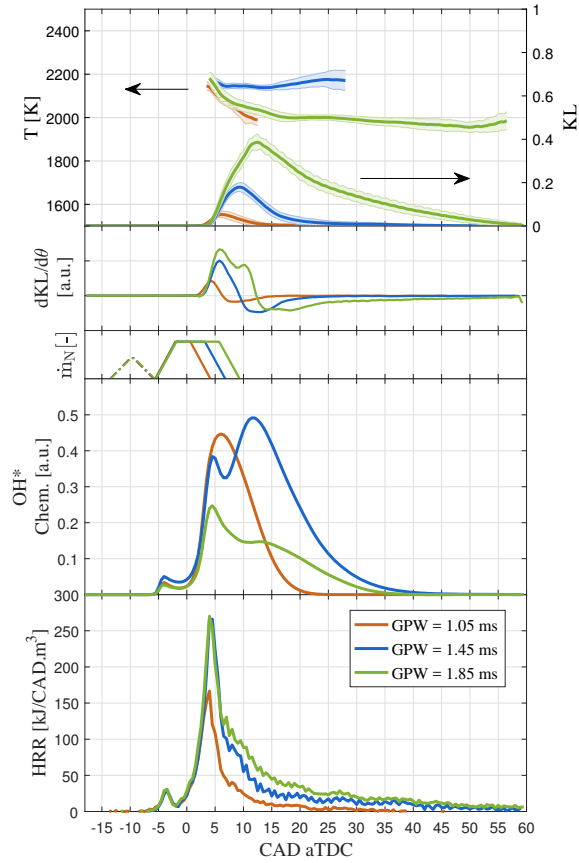


Figure 6.8: NG fuel mass effects at constant injection pressure; Spatially averaged OH^* chemiluminescence and two-color pyrometry, net soot formation and oxidation rates, estimated normalized fuel flow rates (\dot{m}_N), and HRR. More window contamination and ensemble averaging effects (15 cycles) are responsible for the lower peak OH^* at GPW = 1.85 ms (before NG EOI for GPW = 1.45 ms)

progress towards the center and soot oxidation takes over soon after formation of the soot cloud toroid. High temperature reactions also remain concentrated at the wall region after NG EOI during the late-cycle oxidation phase. Compared to the baseline, this operating point resulted in a lower peak HRR and lower average temperature in the combustion chamber (Figure 6.8) and lower soot production as well as higher OH* signal with minimal soot cloud attenuation (Figures 6.7 and 6.8).

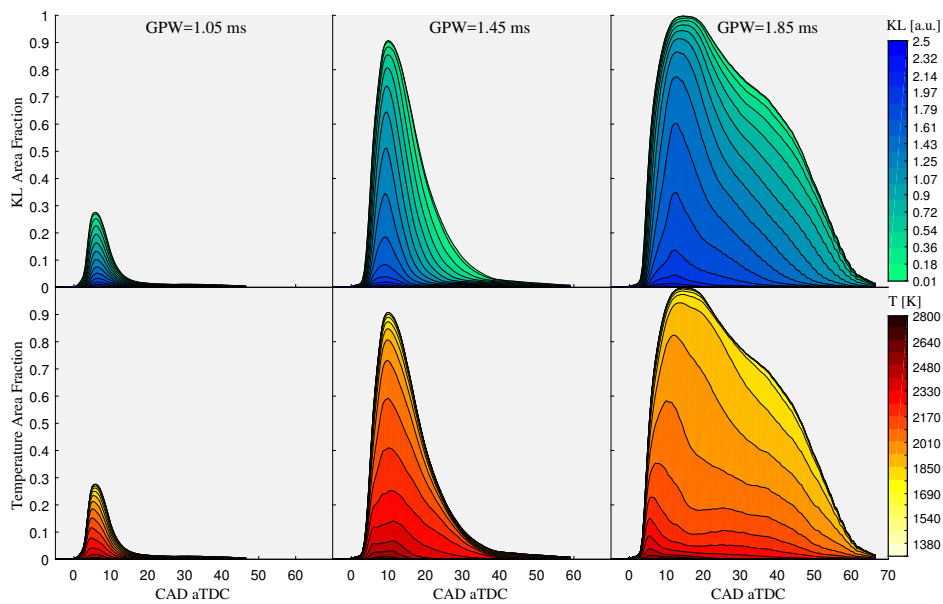


Figure 6.9: NG fuel mass effects at constant injection pressure; Two-color pyrometry soot temperature and KL factor area fraction coverage at short GPW (left), baseline (center), and long GPW (right). Results are ensemble averaged from 15 cycles (see §3.3.3).

For $GPW = 1.85$ ms, the soot cloud eventually covers the entire bowl area and a more homogeneous temperature distribution is resolved during the late-cycle stage, which is also shown in Figure 6.9. More soot formation and higher optical thickness with longer injection duration is observed in the larger area fractions with high KL values in this figure, as well as the high KL peaks in the spatially averaged results (Figure 6.8), in addition to the 2D results (Figure 6.7). More significant OH*

signal attenuation with increasing GPW manifests in lower spatially averaged OH* signal after 7 CAD aTDC (Figure 6.8), leading to no signal recovery and 2nd peak for GPW = 1.85 ms. Before 7 CAD aTDC (baseline NG EOI), however, the lower OH* peak for GPW = 1.85 ms in Figure 6.8 is due to window fouling and is an artifact of ensemble averaging.

6.2.3 Relative Injection Timing Effect

The relative timing between the commanded start of pilot and NG injections is another important PENDING combustion control parameter that impacts the degree of NG premixing [99] and consequently, affects the soot formation and oxidation processes. Figures 6.10 and 6.11 show the spatially resolved and averaged results on the effect of changing relative injection timing (RIT) from the baseline value. The PPW and GPW values are held constant and combustion phasing approximately matches for all these operating points.

As the imaging and HRR results in Figures 6.10 and 6.11 reveals, the sweep of RIT has a notable impact on the combustion mode and soot processes, although these points lead to roughly the same engine load (see Table 6.1). There is no soot signal in the negative RIT case (i.e., injection of NG prior to the pilot fuel injection) and less developed soot cloud with lower peak *KL* is observed for both short and long RIT operating conditions. Higher 2D OH* signal levels and peaks are recorded and HRR curves are significantly different (Figures 6.10 and 6.11).

The retarded cPSOI for the shortest RIT (RIT=2 CAD), closer to TDC than the baseline case, leads to a shorter pilot ignition delay and less jet penetration before ignition, and consequently formation of a smaller high reactivity ignited pilot kernel ring (Figure 6.12-a), which is soon quenched by the concurrent NG injection before growing further (Figure 6.10, 1-4 CAD aTDC). Throughout the measurement campaign, the RIT=2 operating point is unique in that it is the only case where soot signal is detected during the pilot fuel combustion phase. This is illustrated more clearly in 2D pyrometry results at a higher temporal resolution within the 1-4 CAD aTDC range in Figure 6.13. Despite the small area fractions covered by the pilot soot pockets, as shown in Figure 6.14, zooming into these regions shows a rather uniform distribution of resolved temperatures and *KL* factor

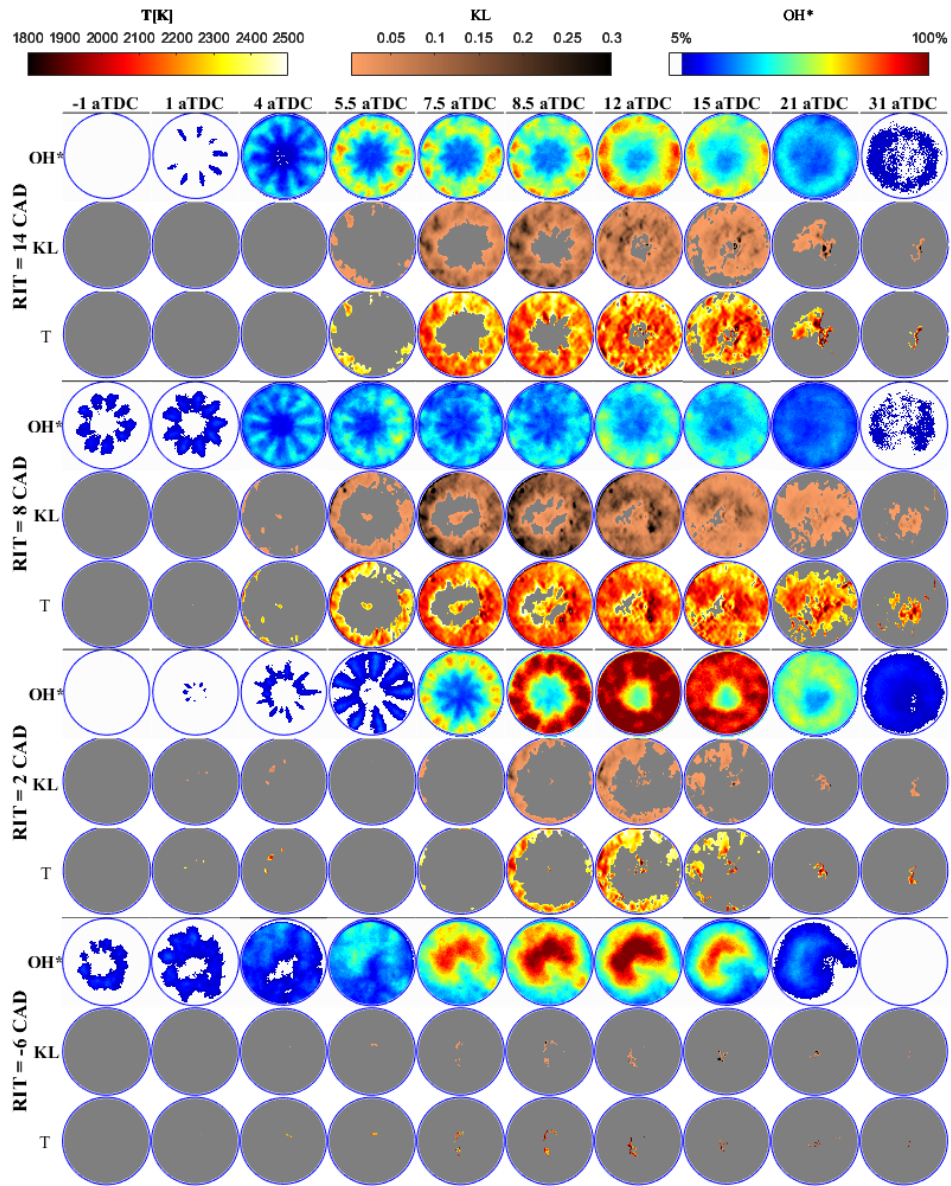


Figure 6.10: Relative injection timing effect; 2D OH* chemiluminescence and two-color pyrometry results. Results are ensemble averaged from 15 cycles (see §3.3.3).

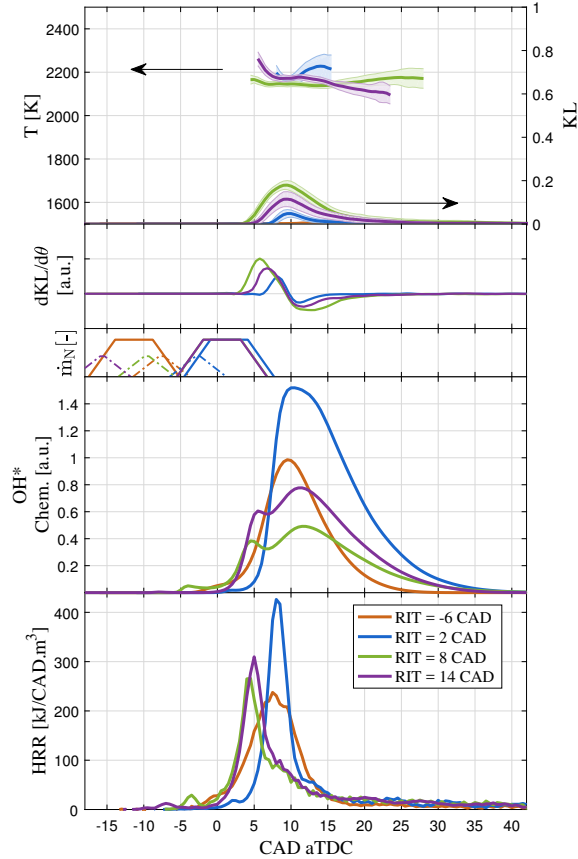


Figure 6.11: Relative injection timing effect; Spatially averaged OH* chemiluminescence and two-color pyrometry, net soot formation and oxidation rates, estimated normalized fuel flow rates (\dot{m}_N), and HRR. Results are ensemble averaged from 15 cycles (see §3.3.3).

levels, indicating consistent signal with sufficient SNR in the ensemble averaged results. The shorter pilot ignition delay and less pilot diesel mixing, as a result of injecting into a hotter chamber environment, and concurrent injection of NG, displacing the air, are the probable causes for a locally richer pilot fuel conversion and detectable soot signal during the pilot combustion. Filtered NL images of pilot combustion during PIDING under higher compression ratio of 17:1 (Figure 2.9, -9.8 and -5.7 CAD aTDC) also show signal levels comparable to those of the

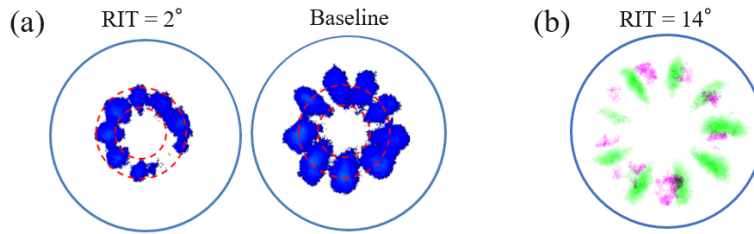


Figure 6.12: Relative injection timing effect on pilot combustion (OH^* chemiluminescence images); (a) smaller high reactivity ignited pilot kernel ring at $\text{RIT}=2^\circ$ relative to baseline as a result of retarded cP-SOI, closer to TDC, and less jet penetration before ignition, and (b) Overlaid NG ignition (1.5° aTDC) and gamma enhanced ignited pilot kernels (-8° aTDC). Results are ensemble averaged from 15 cycles (see §3.3.3).

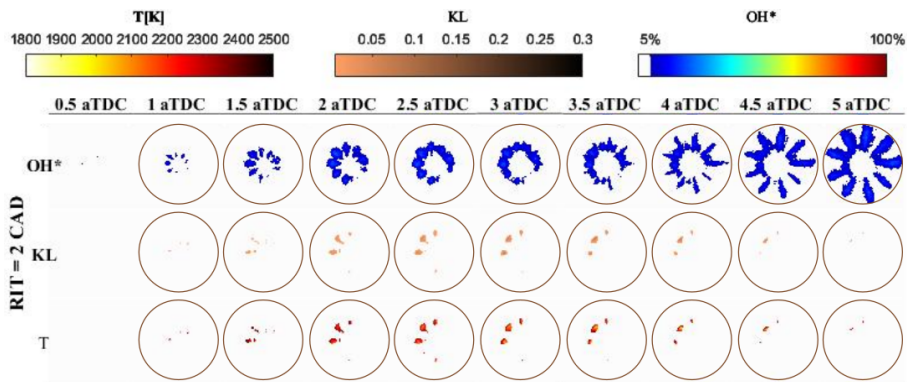


Figure 6.13: High temporal resolution 2D OH^* chemiluminescence and two-color pyrometry results for pilot combustion at $\text{RIT}=2$ CAD. Results are ensemble averaged from 15 cycles (see §3.3.3).

primary combustion stage (>6.4 CAD aTDC), which suggests non-negligible soot signal [54].

Despite the shorter pilot ignition delay for $\text{RIT}=2$ CAD, optical NG ignition delay is longer than that of the baseline ($\tau_{ign,NG} = 12.5$ vs. 10 CAD), as a result of the retarded pilot injection. This is followed by a higher peak HRR and higher intensity OH^* chemiluminescence ring close to the walls and mean OH^* chemiluminescence peak, compared to the baseline (Figures 6.10 and 6.11). Despite the same NG injection duration, $\text{RIT}=2$ CAD leads to less soot cloud formation and

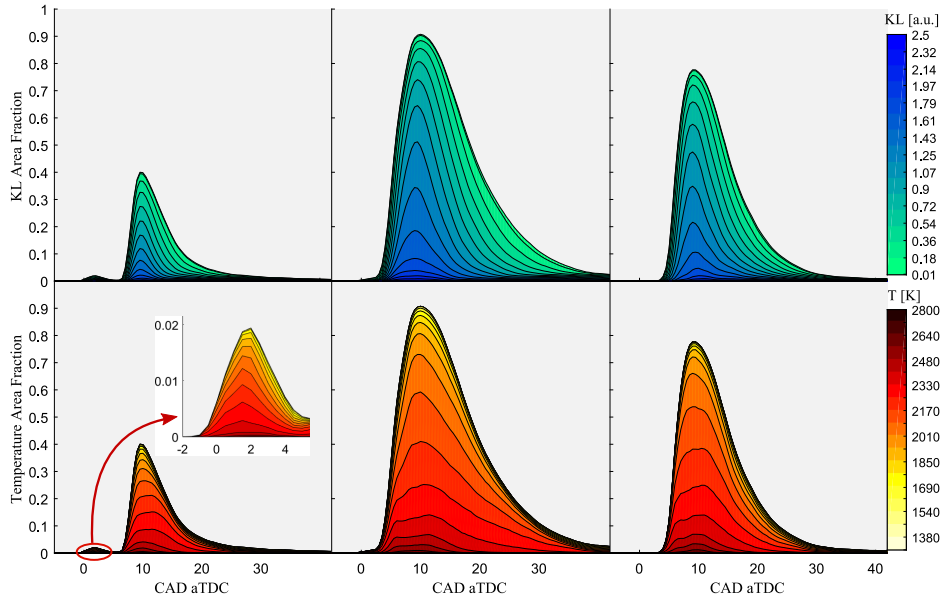


Figure 6.14: Relative injection timing effects; Two-color pyrometry soot temperature and KL factor area fraction coverage at short RIT (left), baseline (center), and long RIT (right). Results are ensemble averaged from 15 cycles (see §3.3.3).

growth, with lower KL factor values, and minimal attenuation of the stronger OH^* signal. Similar to the $\text{GPW}=1.05$ ms operating point, the OH^* signal peak matches in phasing with the peak KL factor.

The pilot ignition delay is longer for the $\text{RIT}=14$ CAD operating condition relative to baseline ($\tau_{\text{ign},pi} = 17$ vs. 13 CAD) and is followed by a lower pilot peak HRR and weak OH^* chemiluminescence signal, which was only visible through image gamma corrections at the current settings (Figure 6.12-b). The extended $\tau_{\text{ign},pi}$ did not appear to affect the $\tau_{\text{ign},NG}$; nevertheless, NG ignition was more localized on the gas jet axes. Overall, similar to the short RIT, this operating point leads to a higher peak HRR, OH^* signal at the wall region, and lower KL factor levels and peak mean value. The comparison of area fraction distributions shown in Figure 6.14, however, shows more dominating higher temperature regions later in the cycle as the RIT is decreased.

Early timing of the NG commanded start of injection for the negative RIT operating point (RIT=-6 CAD) results in a significantly longer NG ignition delay of $\tau_{ign,NG} = 20$ CAD. HRR curve is broadened and negligible soot signal was recorded throughout the cycle rendering the soot temperature calculations not possible due to the SNR being too low.

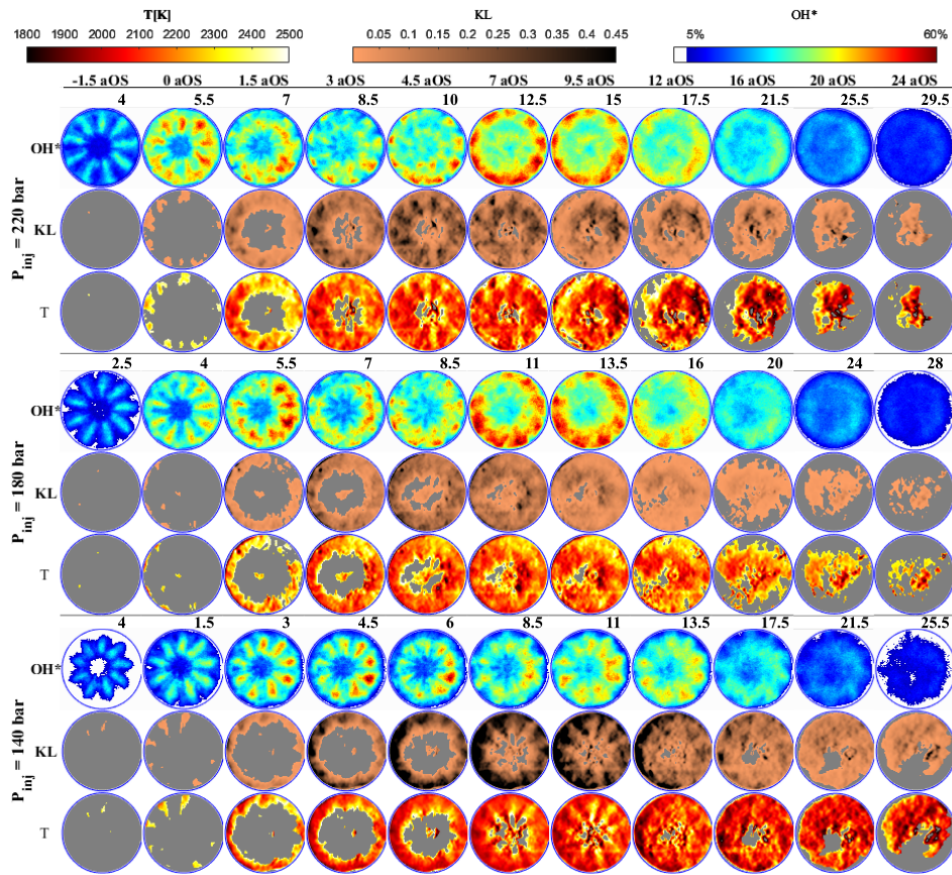


Figure 6.15: Fuel injection pressure effect; 2D OH* chemiluminescence and two-color pyrometry results. Crank positions are synced relative to the onset of soot (aOS) signal and crank position aTDC for each operating point is reported at the top-right of the OH* images. Results are ensemble averaged from 15 cycles (see §3.3.3).

6.2.4 Injection Pressure Effect

The fuel injection pressure (P_{inj}), similar to diesel engines, is another key control parameter to modify engine load and fundamental combustion processes in PIDING combustion and, thus, has been a major focus in the PIDING combustion studies to date [34, 98, 99]. The density of the injected fuel and its mass and momentum flow rate increases with the upstream fuel rail pressure. The fuel system controls the natural gas rail pressure (GRP) to a level ~ 10 bar below that of the diesel rail pressure (DRP). Figures 6.15 and 6.16 show the spatially resolved and averaged results on the influence of a $\sim 20\%$ increase and decrease in the P_{inj} . Duration and timing of the injection pulses were adjusted to maintain similar injected fuel mass and combustion phasing for the considered P_{inj} sweep operating points. As such, in order to facilitate the comparison, the crank positions in the 2D results presented in Figure 6.15 are relative to the onset of soot signal (aOS).

Decreasing P_{inj} to 140 bar spread the onset of soot signal region upstream on the NG jets to also include regions away from points of impingement on the bowl wall. This is in contrast with other operating points listed in Table 6.1. This onset of soot signal is followed by a higher KL factor distributions at the bowl wall and along the gas jets (Figure 6.15, 3-9.5 CAD aOS), higher mean KL peak and a lower peak HRR and mean soot temperature (6.16). In contrast to the long injection case (GPW=1.85 ms, Figure 6.7), the high KL factor region for the low P_{inj} operating point in Figure 6.15 remains concentrated at the proximity of the bowl wall throughout the cycle.

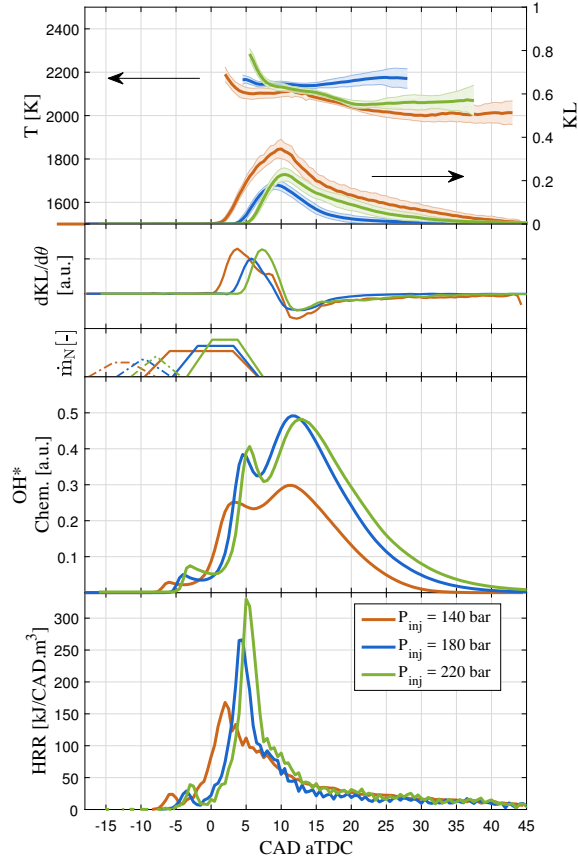


Figure 6.16: Fuel injection pressure effect; Spatially averaged OH* chemiluminescence and two-color pyrometry, net soot formation and oxidation rates, estimated normalized fuel flow rates (\dot{m}_N), and HRR. Results are ensemble averaged from 15 cycles (see §3.3.3).

Similar to the $P_{inj}=140$ bar operating point, increasing P_{inj} to 220 bar also led to higher peak KL factor than the baseline case with traces of higher soot signal along the NG jet axes (Figure 6.15, 4.5-7 CAD aOS). However, the $P_{inj}=220$ bar also increased the peaks for HRR and corresponding OH*, for both pilot and NG combustion (Figure 6.16, -3 and 5 CAD aTDC, respectively), relative to the baseline condition, and resulted in higher engine load. High P_{inj} and baseline points otherwise show similar onset of soot signal locus, estimated temperature at the peak KL , and OH* chemiluminescence signal levels and attenuation from soot cloud.

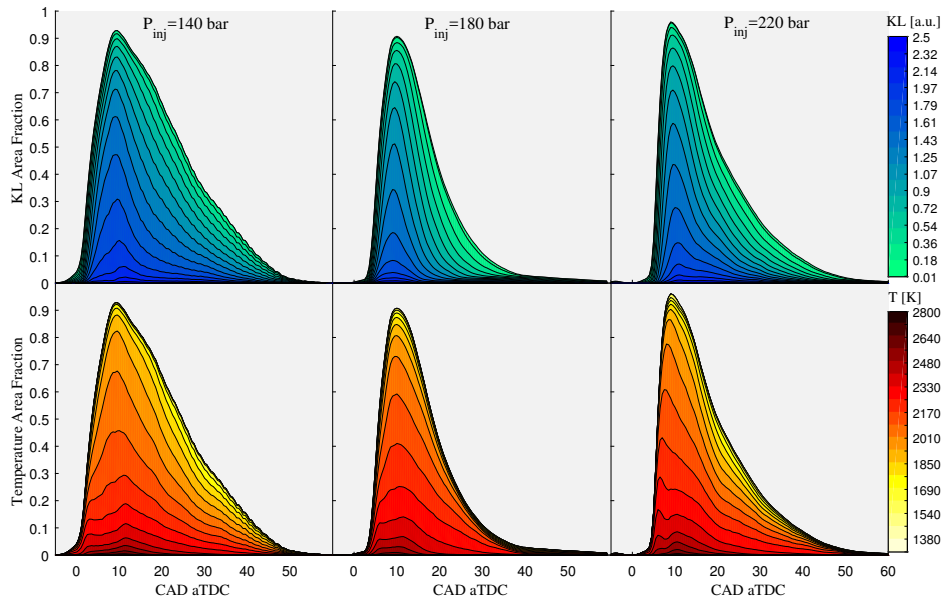


Figure 6.17: Fuel injection pressure effects; Two-color pyrometry soot temperature and KL factor area fraction coverage at low P_{inj} (left), baseline (center), and high P_{inj} (right). Results are ensemble averaged from 15 cycles (see §3.3.3).

6.2.5 Updated Understanding of Soot Processes during PIDING Combustion

Combustion mode analysis of the current investigation campaign identified five major stages to provide a conceptual description for the PIDING combustion processes, for a positive RIT value [126]. Figure 6.18 illustrates these through representative OH^* chemiluminescence snapshots linked to corresponding sections of the HRR history for the baseline operating point described in Table 6.1. According to the proposed conceptual description, PIDING combustion comprises (in chronological order): 1- Auto-ignition of a low-momentum pilot diesel “puff” jets away from the bowl wall; 2- ignition of the NG jets passing through the pilot reaction zones containing high temperature combustion products and radicals; 3- combustion of the partially-premixed NG at the wall region; 4- Non-premixed combustion with continuation of NG injection during and after the partially-premixed

fuel conversion stage; and 5: late-cycle oxidation of the remaining reactants and incomplete combustion products, after NG EOI.

The reaction zone growth in a predominantly radial direction during the NG ignition stage (Figure 6.18, stage 2) was attributed to NG fuel conversion along the gas jets, with a low HRR, and momentum of the fuel jets. In a previous work, local fuel concentration measurements showed evidence of methane concentration increase at the wall region before fuel was oxidized [156]. This suggests that an unreacted fraction of the injected NG penetrates beyond the ignited pilot kernels and reaches the wall region, where it partially premixes with air while impinging on the bowl walls. Numerical simulation of equivalence ratio distributions during PIDING NG injection also showed NG jet wall impingement, under similar operating conditions [54]. Once the reacting NG reaches the bowl wall, the partially-premixed charge is converted rapidly, which leads to a sharp rise in the heat release rate and formation of a toroid of higher temperature reactions at the wall region. The transition to the partially-premixed combustion was also characterized by reaction zone growth rates of more than 40 m/s [126]. Presence of a transitional combustion regime between stages 3 and 4 was acknowledged, where distinguishing between the simultaneous combustion modes was not possible.

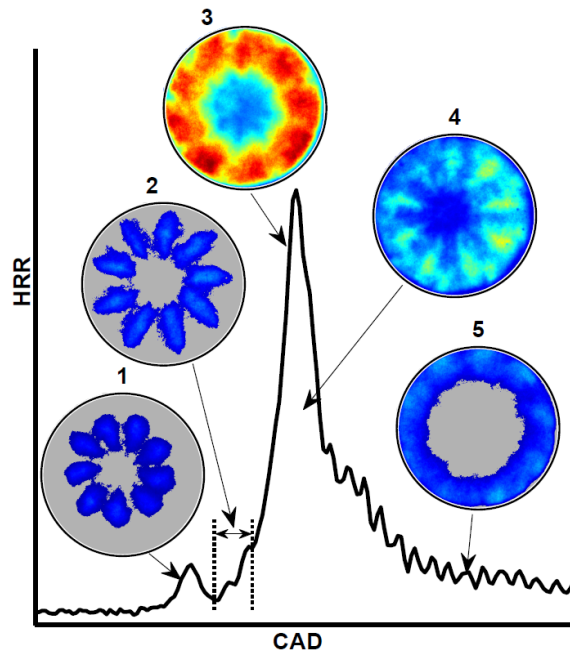


Figure 6.18: HRR and OH* chemiluminescence images of combustion reaction zones through a typical PIDING combustion event. Reprinted from Rochussen *et al.*[126], with the permission from publisher

Throughout the parameter sweep campaign presented in this work, there appears to be a consistent correlation between the partially-premixed HRR peak and onset of soot signal detected at the points of NG jet impingement on the wall. Figure 6.19 illustrates the correlation between the peak HRR and onset of detectable soot signal crank positions. As pointed out before, the $P_{inj}=140$ bar operating point showed an earlier onset of soot signal, detected along the gas jets, and before the HRR peak and was an exception to this trend. Combustion of the partially-premixed charge at the wall region brings about higher fuel conversion and oxidation (oxidizer combustion) rates. Furthermore, continued injection of NG into these high temperature reaction zones and air displacement also contribute to make the wall regions locally richer zones. This is often accompanied by accumulation of low concentration soot formed on the NG jets, which are below the detection limit, especially for longer injection durations. Altogether, these processes result

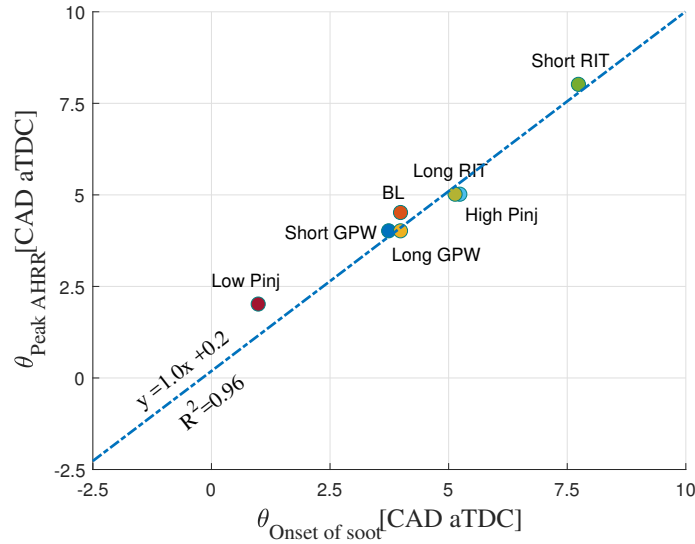


Figure 6.19: Correlation between the peak HRR and detected onset of soot signal

in higher local soot formation rates and explain the matched phasing with the onset of soot signal detected at the points of NG jet impingement on the wall. A similar correlation was reported in a diesel engine study by Bobba *et al.* [14], where the soot mass in the cylinder started to become significant enough to be captured optically roughly at the peak premixed HRR. Prior to the described onset of soot signal at the wall region, ignition and combustion of the low carbon:energy ratio gaseous NG on the free injected jets, does not lead to enough soot production to the detection limits of the current imaging system.

The peak KL factor timing for all operating conditions investigated in this work shows a correlation with the NG EOI and the resulting abrupt change in the rate of available mixture, i.e., converted vs. introduced NG in the reaction zone. Figure 6.20 illustrates this correlation across all operating points in the current campaign. During the GPW sweep, in each case the peak crank position is retarded with increasing injection duration, such that it still lies at a consistent shift from NG EOI. The RIT or P_{inj} effects did not affect the correlation between KL peak and NG EOI, despite altering fuel conversion and soot formation and oxidation trends, as

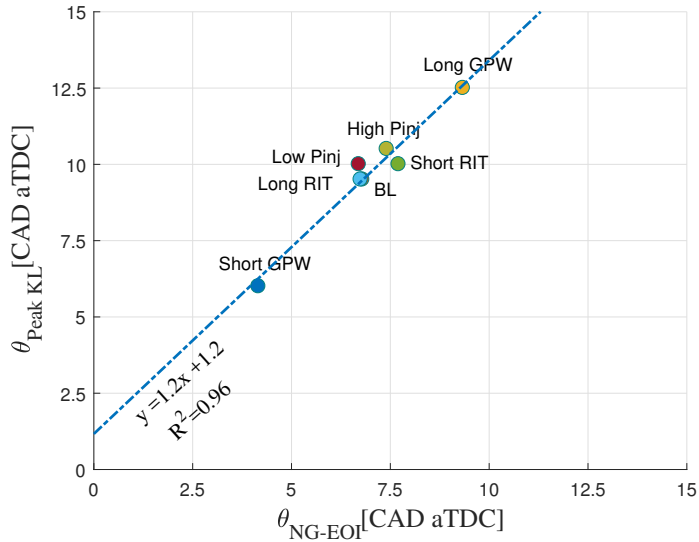


Figure 6.20: Correlation between peak *KL* factor and NG EOI

highlighted in the previous section. These observations suggest that the NG EOI is the determining factor in establishing the extent of soot formation and the peak *KL* phasing. As such, this crank position marks the end of high soot formation rates and the dominance of the soot oxidation processes, in response to the end of NG supply into the reaction zone.

The peak HRR and onset of soot signal also corresponds to the 1st OH* chemiluminescence peak, from the combustion of the partially-premixed charge, where there is a temporary drop in the signal, supporting the hypothesis presented on OH* signal attenuation from the developing optically thick soot cloud. For cases with minimal OH* signal attenuation, such as the GPW=1.05 ms and the RIT=2 CAD operating points, the undisturbed OH* curve peak matches the peak *KL* factor instead. This further supports the discussion on transition to oxidation dominated stage and more clearly marks the peak of the soot oxidation process followed by rapid decrease in *KL* factor values at more steady temperature levels (e.g. Figure 6.14, first column).

These results reveal that there is an important correlation between PIDING soot formation and oxidation processes and the relative timing between the fuel

injection profile and the peak HRR. Based on these correlations, the extension of the NG injection beyond the peak HRR and into the reaction zones leads to increasingly mixing-rate limited fuel conversion [126], and higher soot formation, optically thicker soot cloud development, and higher peak KL factors. The $GPW=1.85$ ms and $P_{inj}=140$ bar operating points in Figures 6.8 and 6.16, respectively, illustrate these phenomena. Operating points with the lowest KL factor peaks and distributions ($RIT=-6$ and 2 CAD in Figure 6.11 and $GPW=1.05$ ms in Figure 6.8), have their NG EOI advanced relative to the HRR peak. This revelation was also the basis for choosing the normalized net rates as described in §6.1.1. Since by extension of NG injection beyond the peak HRR, soot formation rate would continuously increase, normalizing the net rates with the formation/oxidation duration could isolate this effect and help assess the influence of the considered parameter sweeps more independently.

Continuation of NG injection during and beyond the partially-premixed HRR peak, in addition to increasing local soot formation at the bowl wall, contributes to the soot cloud growth and progression towards the center through the reflected momentum of the NG jets impinging on the bowl wall. This phenomenon can be inferred from examining injection duration effects and also comparison of the $GPW=1.85$ ms vs. $P_{inj}=140$ bar operating points (discussed in the next section), in addition to tracing small high intensity soot pocket trajectories, as described before. In what follows the influence of considered parameter sweeps are analyzed in accordance with the soot formation and oxidation mechanisms described above.

NG Fuel Mass (Injection Duration)

With the extended NG injection duration in $GPW=1.85$ ms operating point, while the commanded injection settings and P_{inj} are held constant, the described soot cloud growth mechanisms are extended. As a result, soot cloud develops further towards the center and covers a higher percentage of the combustion chamber, and the soot signal is extended until later in the cycle. While the mean KL factor peaks and trends are similar between this and the $P_{inj}=140$ bar operating points (Figures 6.8 and 6.16), the soot cloud toroid in $P_{inj}=140$ bar remains more concentrated at the bowl wall region throughout the cycle (Figure 6.21), despite the longer injection

duration (GPW=2.1 ms), as a result of the lower momentum of injected NG jets. This is illustrated more clearly in Figure 6.21, which shows time series of the radial distribution of the soot KL factor values. At each radial position, the mean KL factor value over a thin ring element ($KL_{mean,R}$) was considered to generate the radial distribution vector. In this figure, GPW=1.85 ms operating condition, after formation of high KL factor values at the bowl wall region (5-10 CAD aOS), shows high KL factor concentrations half-way into the bowl (10-25 CAD aOS). $P_{inj}=140$ bar case, in comparison, shows high KL factor values at R_{bowl} earlier after onset of soot signal and the KL factor concentration region remains at the wall region.

The distribution contours of Figure 6.21 are overlaid by the concentration centroid radius histories, described in equation 6.6. Here, GPW=1.85 ms case shows transition of the centroid radius back to half-way into the bowl at 15 CAD aOS, while at $P_{inj}=140$ bar the centroid radius tends to remain further away from the center and shows a plateau around 15 CAD aOS.

$$R_C = \frac{\sum_{i=0}^{R_{bowl}} (KL_{mean,R_i} \times R_i)}{\sum_{i=0}^{R_{bowl}} (KL_{mean,R_i})} \quad (6.6)$$

Conversely, for GPW=1.05 ms, with the early end of injection and lack of the described reflected NG jet momentum effects, soot cloud does not progress towards the center. Here, NG EOI is notably advanced relative to the partially-premixed HRR peak and fuel is majorly injected during $\tau_{ign,NG}$ (needle closing starts at ~ 0.5 , $\Theta_{ign,NG} = 1$, and $\Theta_{peakHRR} = 4$ CAD aTDC). As a result, this operating point leads to predominantly partially-premixed fuel conversion, with higher OH* signal and less soot formation at the wall and lower peak KL factor. The lower NG input before ignition of the partially-premixed charge also led to a lower HRR peak and mean soot temperature for GPW=1.05 ms operating point.

The mean soot temperature for GPW=1.85 ms is also lower than that of the baseline. The lower rate energy release within the rich mixture with injection of more fuel into the reaction zone causes an extended combustion phasing, smaller area fractions at high temperatures and larger low temperature regions (Figure 6.9), and a lower averaged temperature estimation. As previously reported elsewhere [108, 162], it is possible that the decreased area fraction of the high temperature

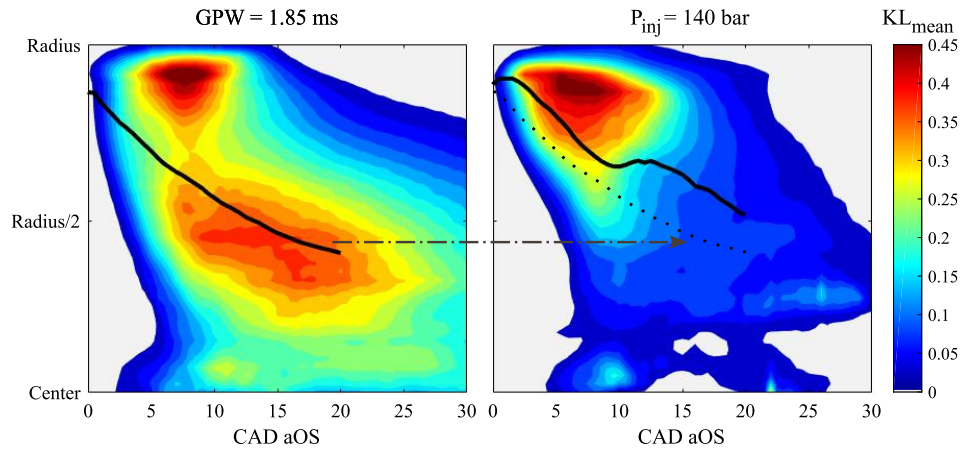


Figure 6.21: Radial KL factor distribution time series for $GPW=1.85$ ms and $P_{inj}=140$ bar operating conditions (see Table 6.1); the overlaid solid black lines mark the corresponding concentration centroid radius (see equation 6.6). The dotted line on $P_{inj}=140$ bar contour map is the projection of $GPW=1.85$ ms concentration centroid radii for comparison

regions is due to the shrouding from the high optical thickness, low temperature soot cloud, which introduces a bias in pyrometry temperature estimates.

Compared to the fraction distributions for the baseline GPW , the longer injection duration results in Figure 6.9 (right column) show a smaller difference in the decay rates for KL and temperature levels of 2000 K and below, after the mean KL peak (12.5 CAD aTDC, 6.8). Although there is an even steadier temperature distribution evolution at the high temperature levels (>2100 K) compared to the baseline case, these regions only constitute a small fraction of the more developed soot cloud (Figure 6.9, bottom-right, 20-40 CAD aTDC). This ultimately leads to a lower soot oxidation rates, supported by early disappearance of OH^* signal relative to the soot cloud signal (Figure 6.7, 21-31 CAD aTDC), and higher ranges of KL factors within the larger soot cloud and extended soot signal (Figures 6.7 and 6.9).

Fuel injection pressure

The increase in P_{inj} of NG and the consequent increased fuel jet momentum flow rate was shown elsewhere to increase the NG jet penetration and mixing rates for a given charge density [113]. Also, higher rates of heat release during the mix-

ing controlled combustion stage of PIDING with higher P_{inj} was attributed to the increased fuel-oxidizer mixing rates [126].

For $P_{inj}=140$ bar operating point, the lower fuel jet momentum flow rate and the consequent lower mixing rates result in richer charge mixture around jet axes. The resulting richer zone at the bowl wall region makes NG conversion more bound by mixing, leading to a broadened HRR curve with a lower peak [126]. This leads to higher soot formation and onset of soot being detected also on the NG jet axes and before reaching the bowl wall, unlike any other cases studied in the current campaign. Followed by more soot formation at the wall with the continued fuel injection after the peak HRR, and with accumulation of more soot formed on the jet axes, a higher optical thickness soot cloud toroid was produced (2D KL). The poor charge mixing at the wall region and lower rate of heat release also results in a lower two-color pyrometry temperature. Study of fuel injection pressure effects in multi-cylinder PIDING engines suggested that insufficient injection pressure resulted in “under-penetration” of the NG jets in the combustion chamber and poor mixing of the gas with air, slow combustion and ultimately low thermal efficiency and higher soot emissions [34, 98].

At $P_{inj}=220$ bar, the higher peak HRR relative to the baseline, caused by the higher fuel jet momentum and enhanced mixing, is also followed by a higher KL factor peak. The higher KL values recorded along the gas jets (Figure 6.15, 10-12 CAD aTDC), mark the higher mass flow rate and higher local net soot formation rates. The effect of injected fuel mass flow rate on soot formation becomes more clear through comparison of the normalized net soot formation rates at different injection pressures in Figure 6.22. Here, the combined effects of the increased rate of reactions, due to enhanced mixing, and increased mass flow rate at a higher P_{inj} lead to a higher normalized net formation rate. As illustrated in Figure 6.22, the net soot formation rate, normalized over the entire span of the formation process, decreases with reducing P_{inj} , despite the higher peak KL factor. Comparison of area fraction distributions in Figure 6.17 shows a shift in the peaks of temperature levels towards the rising edge and onset of detectable soot signal with increasing P_{inj} from 140 to 220 bar, which is consistent with expected higher rate of reactions as discussed above. A similar normalized net soot formation rate was estimated by increasing injection duration from 1.45 (baseline) to 1.85 ms (GPW sweep) as

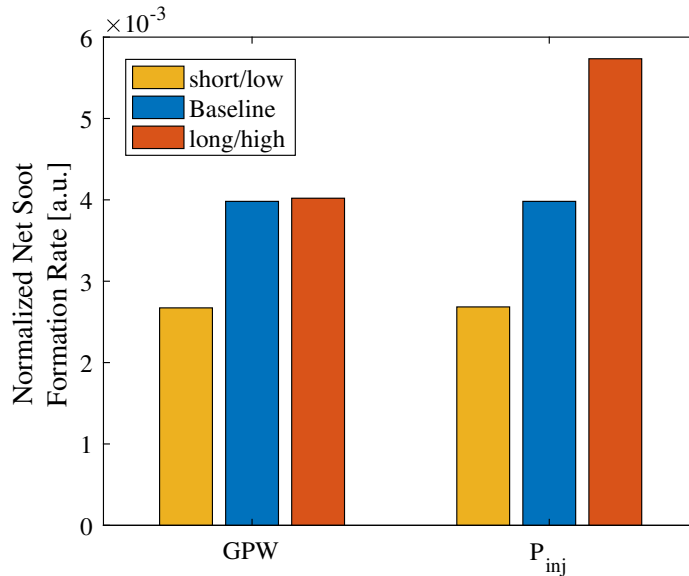


Figure 6.22: Normalized net soot formation rates for GPW and P_{inj} sweeps. A similar normalized net soot formation rate is estimated at GPW=1.85 ms with extending soot cloud growth mechanisms under similar P_{inj} and injection timing. Increasing P_{inj} , and the consequent mass and momentum flow rates lead to higher normalized net soot formation rates.

similar soot cloud growth mechanisms are extended.

In addition to the normalized net formation rates, reducing the P_{inj} from 220 to 140 bar, also decreases soot cloud growth rates towards the center. The mean soot cloud growth rate was evaluated based on the crank position range from onset of soot signal at the wall until soot cloud growth to $\sim 30\%$ of the visible bowl radius. Comparison of mean soot cloud growth rates at different injection pressures are illustrated in Figure 6.23 and more details regarding the analysis metric is available in Appendix F. At $P_{inj}=140$ bar, mean growth rate is reduced to 48 m/s (less than half the rate at $P_{inj}=220$ bar), and the higher optical thickness region as a result remains concentrated at the proximity of the wall, which leads to more heterogeneity in distribution of KL factors over the bowl area. This phenomenon confirms the described reflected jet momentum effects after impinging on the bowl walls (see

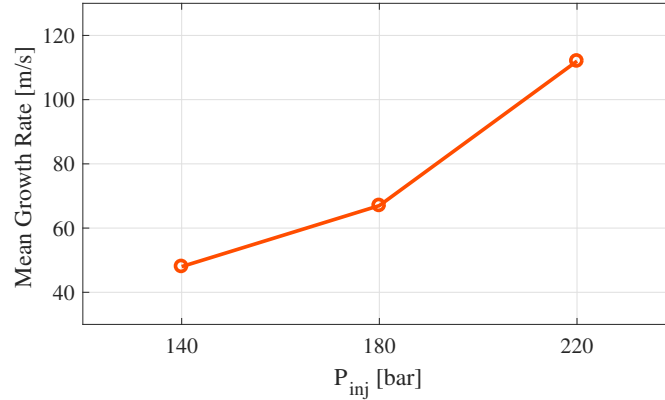


Figure 6.23: The influence of P_{inj} sweep on mean soot cloud growth rate. The rates are evaluated based on 2D pyrometry results (See Appendix F for details of analysis metric).

Figure 6.21). At $P_{inj}=220$ bar, the initial soot pockets quickly merge and form the soot cloud toroid, and develop towards the center at a higher rate. The higher momentum flow rate causes more rapid cloud development following reflection off the wall as well as further progression of the soot cloud towards the bowl center, despite the shorter relative timing between the NG EOI and peak HRR with P_{inj} .

During the soot oxidation phase, the lower momentum flow rate and higher peak KL factor of the $P_{inj}=140$ bar point lead to a lower oxidation rate compared to the baseline. Despite the enhanced mixing at 220 bar P_{inj} , the normalized net soot oxidation rate is similar to that of the $P_{inj}=140$ bar case. This phenomenon can also be inferred from the comparison of the CHTS diagrams in Figure 6.17, where after ~ 20 CAD aTDC temperature and KL levels decay with similar rates for the low and high P_{inj} cases, unlike the baseline operating point. In addition, noticeable low temperature area fractions for these two cases also indicate lower soot oxidation rate compared to the baseline point.

Relative Injection Timing

The longer NG ignition delay for RIT=2CAD allows for more charge mixing, especially close to the walls, and creates a more partially-premixed NG combustion

[126]. The delayed combustion of the partially-premixed charge led to NG EOI prior to the peak HRR, similar to the GPW=1.05 ms operating point. Combined with the combustion of the remainder of the diesel fuel, this results in the highest peak HRR and OH* chemiluminescence signal in the current campaign. The high intensity OH* chemiluminescence ring indicates higher temperature reactions, and presumably higher NO_x formation [34, 100]. As a result of the more premixed nature of this operating point, and despite the same injection duration, it leads to significantly less soot cloud formation and growth with lower *KL* factor values. Thus, there is minimal attenuation in the stronger OH* chemiluminescence signal and no temporary drop in the OH* chemiluminescence curve (8.5-15 CAD aTDC in Figures 6.10 and 6.11), whose peak matches in phasing with the peak *KL* factor instead. This is similar to GPW=1.05 ms case, as the other predominantly partially-premixed operating point.

Contrary to the RIT=2 CAD case, the advanced commanded pilot injection for RIT=14 CAD and injecting into a colder environment, resulted in a more homogeneous reactive region from lean dispersed pilot diesel combustion with a longer $\tau_{ign,pi}$, a lower pilot peak HRR and OH* signal. Despite the unaffected $\tau_{ign,NG}$, in the absence of stratified pilot kernels the NG ignition was more localized on the jet axes and showed a slower growth, especially in peripheral directions from the jets. The less peripherally expanding high temperature reactions on the jet axes consequently lead to more partial premixing. Ultimately, similar to the RIT=2 CAD, this creates a higher partially-premixed peak HRR, higher temperature reactions and higher OH* signal ring at the wall, and retarded onset of soot signal with lower *KL* factor values and peak, compared to the baseline.

The influence of premixing on the *KL* formation can also be elucidated by considering the soot formation delay, i.e., the time from the start of NG injection until soot is first detected ($\tau_{soot} = \Theta_{soot} - cGSOI$). The retarded onset of soot signal relative to cGSOI (increased τ_{soot}) as a result of moving RIT in either direction from the baseline value and higher fraction of the partially-premixed charge, is shown in Figure 6.24. As can be seen in this figure, despite the same NG injection durations and pressures and similar engine loads, manipulation of the RIT towards a more partially-premixed charge, delays the onset of soot formation processes (and peak HRR as described above), which in turn leads to a lower peak *KL* factor. As dis-

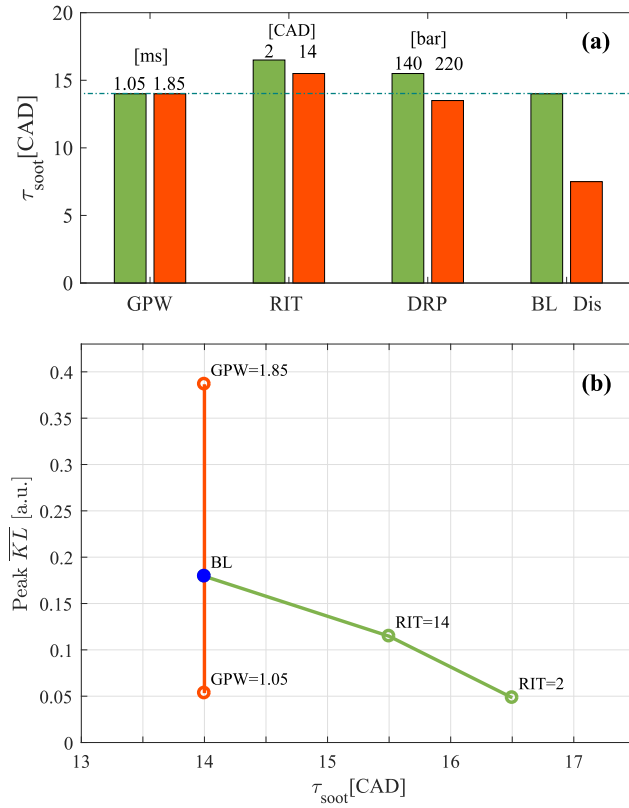


Figure 6.24: The effect of relative timing between onset of soot signal and cGSOI ($\tau_{soot} = \Theta_{soot} - cGSOI$): (a) τ_{soot} comparison for all operating points in Table 6.1. “BL” and “Dis” labels denote baseline and diesel operating points, respectively; (b) lower KL factor peak at longer τ_{soot} as a result of more partial premixing with RIT sweep and increasing KL factor peak at consistent τ_{soot} for GPW sweep.

cussed before, modifications in duration of NG injection changes peak KL , without affecting the onset of soot signal, and hence τ_{soot} . However, it is evident from Figure 6.24-a that discussed correlation does not hold for the P_{inj} sweep points, due to the changes in mixing rates as a result of concurrent changes in injection timings, durations, and mass and momentum flow rates. At $P_{inj}=220$ bar, despite the similar τ_{soot} to the baseline, a higher KL peak is obtained with the higher mass flow rate and at $P_{inj}=220$ bar the combination of poor mixing and low rates of heat release,

and earlier cGSOI led to a high KL peak with an extended τ_{soot} relative to baseline. As expected, the τ_{soot} in diesel operating condition is much shorter (Figure 6.24-a). This is discussed in more detail later in this chapter.

In comparison with RIT=2 CAD, however, the NG injection profile for RIT=14 CAD is closer to the peak HRR, which as described above, could explain the similar 2D soot cloud evolution, KL factor peaks, and OH* chemiluminescence curves (Figures 6.10 and 6.11). The higher oxidation rates can also be inferred from the area fraction distributions shown in Figure 6.14, where more high temperature regions are evident through the late-cycle stages as the RIT is decreased. In this figure, CHTS diagrams for the baseline and long RIT are only different at the lower temperatures, given the overall higher soot formation in the baseline.

Comparison of the net soot formation and oxidation rates in Figures 6.8, 6.11, and 6.16 supports the HRR-injection pulse timing correlations and extent of partial-premixing effects discussed above. To facilitate the comparison, the mean net production rates were evaluated within the $\Delta\theta_{form}$ range (i.e., $[\overline{dKL/d\theta}]_{form}$) for the considered parameter sweeps and is shown in Figure 6.25. RIT=2 and 14 CAD points, similar to the KL factor peaks, both lead to a lower mean net soot formation rate as a result of more partial-premixing. Increasing NG injection duration and injecting into a successively richer reaction zone consistently increases the net formation rate and results in a non-linearly increasing KL factor peak (Figure 6.24-b). Comparison of the net soot formation rates from the P_{inj} sweep, unlike the normalized net soot formation results, shows a higher rate for P_{inj} =140 and 220 bar operating points.

By transitioning to negative RIT values, a different combustion mode, qualitatively similar to classic dual-fuel combustion, is achieved [126]. Significantly advanced NG injection, before injection of the pilot fuel, results in a longer NG ignition delay ($\tau_{ign,NG}$ =20 CAD). As a result of the more homogeneous charge distribution, leaner NG auto-ignition sites, and flame propagation, NG conversion energy release increases (and decays) at a slower rate, leading to a broadened HRR curve (extended heat release at a lower rate). The locally leaner NG combustion process and delayed energy release and high temperature reactions relative to EOI result in negligible soot signal throughout the cycle. As a result, the mean soot temperature and KL calculations have significant uncertainty due to the weak py-

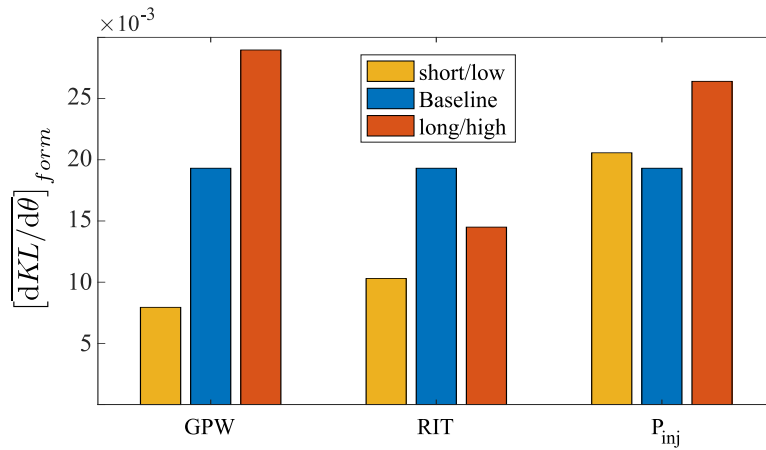


Figure 6.25: The influence of considered parameter sweeps on mean net soot formation rates. Lower soot formation rates are obtained as a result of more premixing at RIT=2 and 14 CAD and increasing GPW consistently increases the formation rates.

rometry signal and low SNR.

Summary of PIDING in-cylinder soot processes

Based on the discussed correlations and investigated parameter sweep effects, in-cylinder soot processes during a typical PIDING combustion event can be described through four stages as follows. The summary of these processes is illustrated in Figure 6.26 through HRR and mean *KL* factor results from the baseline and representative *KL* factor distributions.

1. **Pilot combustion and NG ignition (no detectable soot):** Combustion of a small mass diesel pilot “puff” jet, sufficiently mixed with air during the pilot ignition delay, creates a high reactivity ring approximately half way through the combustion chamber, without soot formation to detectable levels. This is followed by ignition of the injected NG along the gas jets passing through the high reactivity pilot ring. Lower soot production characteristics of the NG as the primary fuel result in negligible soot signal during this stage, below the detection limits. Retarded injection timing of the pilot diesel fuel and injecting into a hotter combustion chamber closer to TDC resulted in

detection of soot also during pilot combustion 6.13.

2. **Partially-premixed NG combustion and soot formation:** Some unreacted fraction of the injected NG penetrates past the pilot high reactivity ring and to the bowl wall, where it mixes with air. Ignition of this partially-premixed charge around the periphery and the corresponding peak HRR coincides with the onset of soot signal at the points of NG jet impingement on the bowl wall, forming small “pockets” of soot. The higher fuel conversion and oxidation rates within and continued injection of NG into the reaction zone and air displacement, as well as accumulation of low concentration soot formed on the NG jets are the contributing factors for the timing and locus of the onset of soot signal. Manipulation of relative pilot and NG injection timings towards a more partially-premixed combustion increased the onset of soot signal delay relative to the start of NG injection and led to a lower KL factor peak and less soot cloud growth. The locus of the detected onset of soot moves upstream along the gas jets at lower P_{inj} , due to the lower jet momentum and poor mixing.
3. **Soot cloud growth:** With continuation of soot formation mechanisms, initially formed soot pockets grow and merge to form a toroidal soot cloud. The soot cloud toroid grows towards the center of the bowl following more soot formation and advection from NG jet momentum reflected off the wall. The extent of soot cloud growth towards the center and soot concentrations closely depend on the relative timing between the NG injection profile and partially-premixed HRR peak, as well as P_{inj} . Further NG injection beyond the peak HRR and higher P_{inj} lead to increased peak KL factors and bowl area coverage. Combination of a lower P_{inj} and extended NG injection beyond HRR, however, still leads to high KL factors and soot cloud growth, but with a more heterogeneous KL factor distribution. The normalized net rates of soot formation also increase with P_{inj} . Numerical simulations by Hatzipanagiotou *et al.* showed high equivalence ratios on the NG jets and suggested mixture formations resembling that of a classic diesel injection with rich zones ($\lambda \ll 0.5$). Nevertheless, during this stage, high temperature reactions on quasi-steady lifted jet flames outside the growing soot

cloud indicates low-sooting non-premixed combustion on the NG jets, given the lower soot production propensity of NG.

4. **End of Injection and soot oxidation:** After NG EOI and the peak KL factor, with higher oxidation rates more concentrated around the periphery of the bowl, soot oxidation becomes the dominating process. As such, the soot cloud starts diminishing around the edges and disappears latest in the central region of the bowl. This is followed by the diminishing of the more homogeneous OH^* chemiluminescence signal during the late-cycle oxidation stage. The soot oxidation rates majorly depended on the KL factor peak and distribution. The longest injection duration showed the lowest normalized net soot formation rates and more soot cloud signal throughout the late-cycle oxidation stage, followed by $P_{inj}=140$ and 220 bar operating points. Increased momentum flow rates at $P_{inj}=220$ bar did not show signs of enhanced soot oxidation after NG EOI.

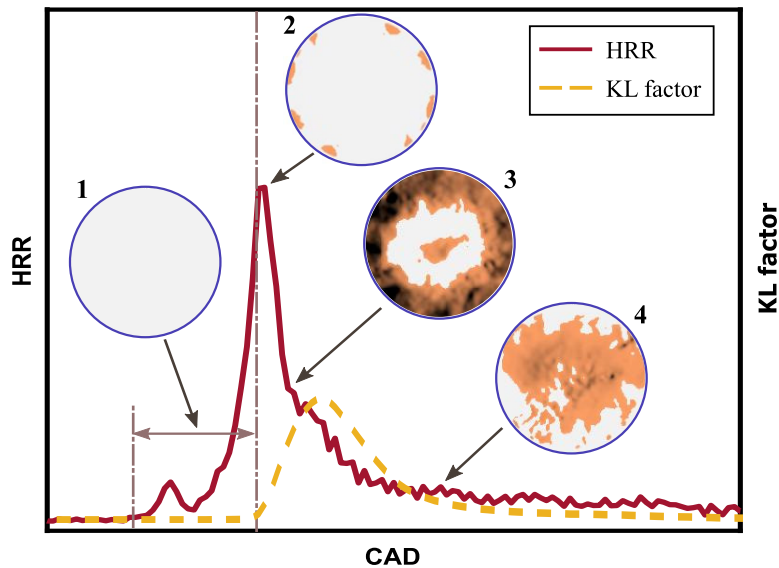


Figure 6.26: Soot processes during a typical PIDING combustion event. The illustration is based on the baseline operating condition and images show KL distribution at select crank positions.

It is worth noting that the above describes the statistically representative in-cylinder soot formation and oxidation processes, based on the ensemble averaged results. Deviations from these general behaviors in individual cycles, e.g., sporadically detected soot signal during pilot combustion or extended signal later in the cycle than described above, has been noted.

PIDING vs. Conventional Diesel Combustion

The typical PIDING combustion soot formation and oxidation behavior described above is substantially different from that of the conventional diesel combustion, although both ultimately lead to similar efficiencies [112]. Figure 6.27 presents a comparison between the baseline PIDING combustion and examples of diesel combustion NL and two-color pyrometry imaging results. The NL images by Singh *et al.* [136] were captured using a 10-bit CMOS camera with exposures set to higher intensities of diesel soot particles. Figure 6.27 also illustrates the results from a low pressure, double pulse (pilot and primary injections, both through the diesel holes), diesel operating condition, which was carried out using the current HPDI injector (see Table 6.1). The HPDI injector is designed to inject only enough diesel to provide pilot ignition and is not meant to be used for conventional diesel-only combustion. Furthermore, the injection pressure is much lower than modern common-rail diesel engines, which will impact the results. It is worth noting that, although consistent trends are observed among the cases illustrated in Figure 6.27, the engine specifications and fueling settings are different and the absolute results are not directly comparable. Despite the varying operating conditions, the diesel combustion in all cases similarly show higher temperature sooty mixing-controlled standing primary diesel flames. Soot formation and oxidation is observed on injected diesel jets, showing higher KL levels/incandescence signal with the localized fuel conversion process, consistent with Dec's conceptual model [24].

When compared to NG ignition in PIDING, primary diesel ignition occurs with a much shorter optical ignition delay and closer to the injector, well within the pilot high reactivity ring. This is accompanied by much earlier soot detection along the gas jets, with the current imaging system settings. The high temperature reaction zones (OH^* signal) and strong soot cloud signal (KL distributions) continue to

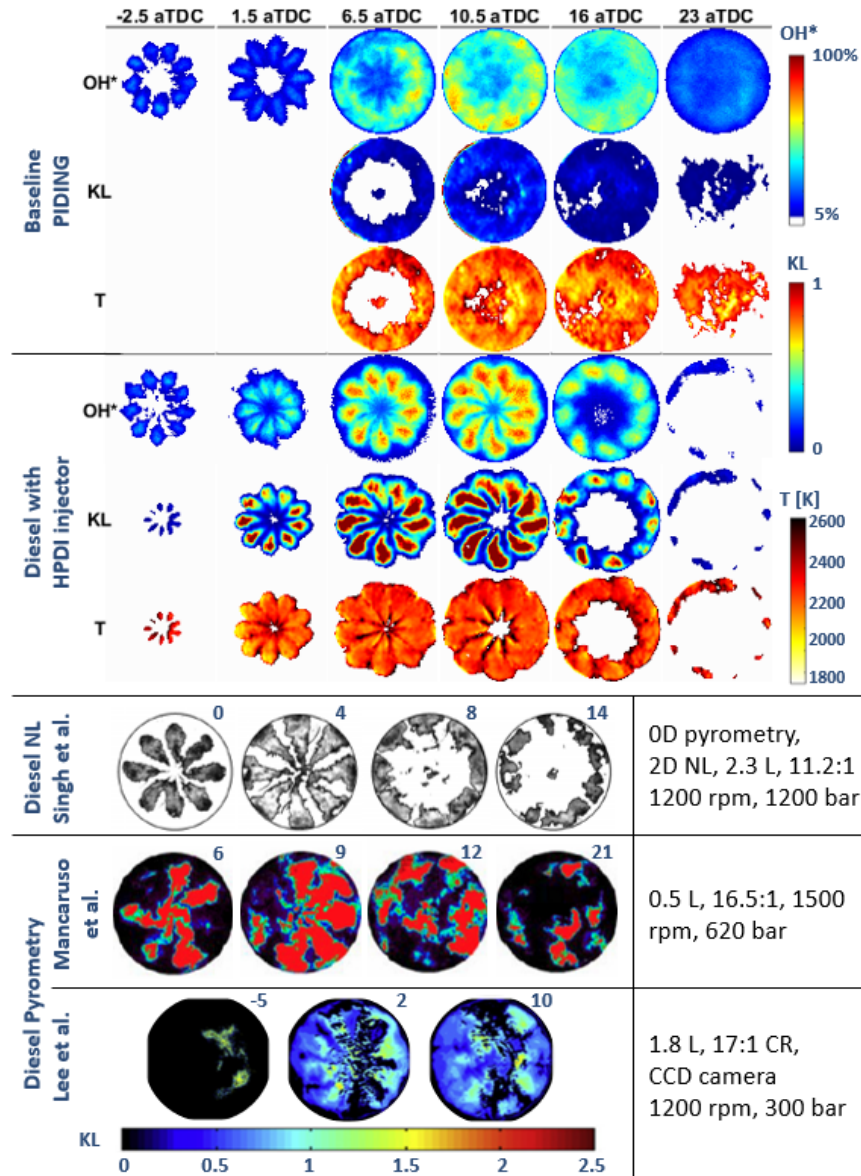


Figure 6.27: Baseline PIDING vs. Diesel combustion; 2D OH* chemiluminescence and two-color pyrometry results from this work, NL imaging results from Singh *et al.* [136], and two-color pyrometry results from Mancaruso *et al.*[94] and Lee *et al.* [84]. Numbers at the top-right of image frames indicate CAD aTDC.

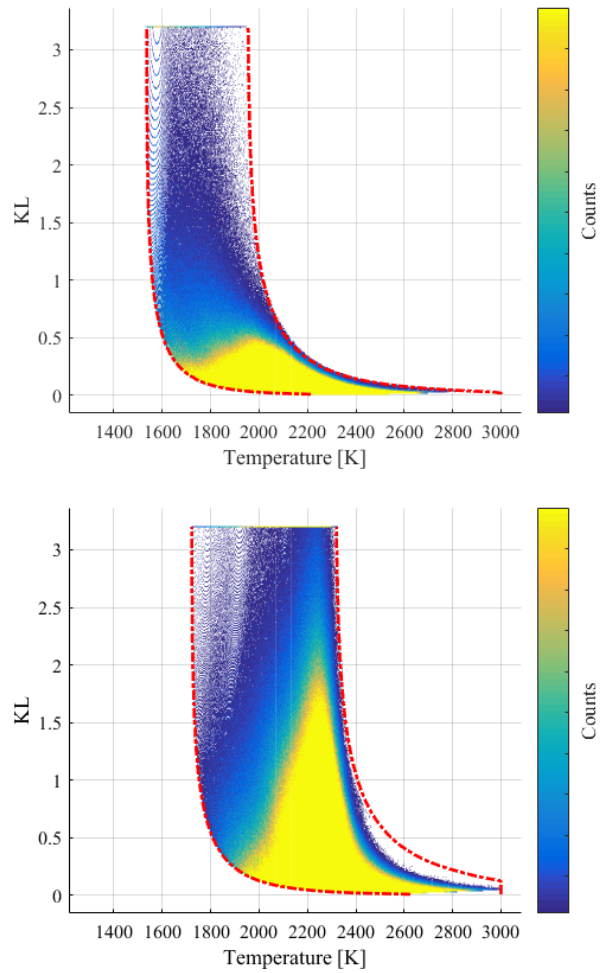


Figure 6.28: Aggregate resolved temperature and KL factor cumulative distribution for baseline PIDING (top) and conventional diesel (bottom) operating conditions

overlap throughout the entire cycle, remaining localized on the jet axis, consistent with Dec's description of OH* radicals creating an envelope around the mixing controlled flame. The close matching between OH* signal and soot clouds is still observed during late-cycle oxidation process in diesel combustion, concentrated around the bowl walls. This emphasizes the much more localized phenomena, differing significantly from that of the PIDING combustion, where soot signal is not detected until the combustion of the partially-premixed charge close to the wall and the peak HRR timing. The processes remain substantially different after the detected soot signal in PIDING, as low-sooting non-premixed NG conversion along the gas jets continues, while a toroidal soot cloud is formed at the wall region. The soot cloud growth stage, however, is in part mixing-rate limited [126], similar to the diesel combustion processes. Finally, a more uniform late-cycle oxidation stage is observed for the PIDING combustion across the bowl area, unlike the overlapping soot oxidation regions (OH* and *KL* regions) in diesel combustion.

These two fundamentally different engine operating conditions ultimately lead to substantially different soot concentration distributions. This is illustrated in Figure 6.28, which shows *T-KL* cumulative distribution throughout the cycle from all optically recorded combustion cycles in each case. The enclosing red lines in each case shows the two-color pyrometry detection limits, determined by the dynamic range of the camera and the calibration range. As discussed in the previous chapter, particular attention was paid to maximizing the detection limit in consideration of the expected limited pyrometry signal in PIDING combustion[74]. The imaging system in both cases was optimized for the primary combustion stage, specifically to capture majority of the signal while avoiding saturation and data loss. As such, the high population area for both combustion strategies is located well within the detection limit. Comparison of the baseline PIDING and diesel combustion temperature and *KL* factor distributions in Figure 6.28 shows significantly less soot formation and slightly lower temperature combustion for PIDING operation strategy, relative to the very low load diesel point considered in this work.

6.3 Concluding Remarks

Optical investigation of in-cylinder soot processes during the PIDING CI engine operating strategy was executed for the first time, using simultaneous spatially and temporally resolved two-color pyrometry and OH* chemiluminescence measurements. Typical soot formation and oxidation processes under a standard baseline operating condition were analyzed. This was followed by parameter sweeps of NG injection pulse width, relative injection timing between pilot and NG fuels, and fuel injection pressure.

Throughout the investigated campaign, consistent correlations were observed between the partially-premixed HRR peak and onset of detectable soot signal. Peak *KL* factor also demonstrated a close correlation with an offset from NG EOI across the campaign, regardless of the commanded start of injection settings and injection durations, the consequent degree of partial premixing, or NG jet momentum flow rates. These correlations suggest that the relative timing between the injection profile and peak HRR play a significant role in the soot processes during PIDING combustion. Extending NG injection beyond the partially-premixed peak HRR and introducing more NG into the reaction zone results in increasingly mixing-rate limited combustion mode and substantially increases soot formation and peak *KL* factor levels. The principal conclusions on the analysis results can be listed as follows:

- No soot signal was detected for a typical PIDING combustion prior to the peak HRR, due to sufficiently mixed pilot diesel combustion and ignition of the lower soot production propensity NG. Once the ignited charge reaches the bowl wall, NG is converted through both low-sooting non-premixed combustion along the gas jets and partially-premixed combustion of the fuel injected during the NG ignition delay. Coincident with combustion of the partially-premixed charge, soot was formed in the reaction zone at the points of NG jet impingement on the wall. From there, soot pockets then form a toroid and grow towards the center following more soot formation and advection from reactive NG jets reflected off the wall. With oxidation happening more extensively on the periphery, the soot cloud starts diminishing around the edges and disappears latest in the central region of the bowl. This

is followed by the diminishing of the more homogeneous OH* chemiluminescence signal during the late-cycle oxidation stage.

- Increasing NG injection duration resulted in further soot cloud growth with higher optical thickness and extended soot signal and more significant OH* signal attenuation. Minimal net soot formation during the short GPW operating point showed negligible OH* signal attenuation and strong OH* chemiluminescence was recorded at the wall region. Although the onset of the detectable soot signal and peak HRR timing remained the same, the high amount of soot formed within a rich mixture for the long GPW operating condition led to a much slower normalized net soot oxidation rate.
- Reducing or increasing the relative injection timing value from the baseline resulted in more partial premixing, higher peak HRR and OH* chemiluminescence signal at the wall region and lower peak KL factor. The short RIT in particular led to much higher partially-premixed peak HRR and OH* chemiluminescence signal peak, with no sign of attenuation from the less developed optically thin soot cloud.
- Increasing fuel injection pressure introduced a trade off between higher momentum flow rate effects, i.e., enhanced mixing during injection and due to stronger reflected momentum off the walls after impingement, and higher mass flow rate effects, i.e., richer NG jets and higher local soot formation rates. As such, a higher P_{inj} increased the rate of reactions and soot cloud growth, peak HRR, and also the normalized net soot formation rate, leading to a slightly higher KL factor peak, as a result of enhanced mixing, but higher mass flow rate. With the lower injection pressure, the lower momentum flow rate and mixing leads to earlier onset of detectable soot signal on the NG jet axes before they reach the bowl wall, followed by more soot formation within the rich mixture with the extended NG injection duration. These effects combine to produce a much higher KL peak in the soot cloud that is formed at a lower normalized net formation rate and remains more concentrated at the wall region due to the weaker advection forces in reflection after jet impingement.

The presented optical investigation of PIDING combustion in this chapter provided insight into the typical soot formation and oxidation modes, and the effect of GPW, P_{inj} , and RIT control parameters on these processes. Most significantly, as described by the effects of the relative timing between NG injection profile and peak HRR, these control parameters alter the fraction of partially-premixed versus mixing-controlled energy release. This in turn, determines the rate and extent of soot formation and oxidation and, ultimately, is expected to affect engine out soot, through manipulation of injected fuel mass, momentum flow rate, and residence time.

This survey, however, was conducted using a limited number of PIDING operating space points, within inherent restrictions of an optical engine, with a lower compression ratio, and line-of-sight two-color pyrometry measurements. Designed based on the current findings, a more comprehensive investigation of the aforementioned control parameter effects in a thermodynamic engine is introduced and discussed in the next chapter.

Chapter 7

Optical Probe Signal Characterization

The study of in-cylinder processes through spatially resolved optical measurements offers a substantial depth of information on the involved combustion mechanisms and soot formation and oxidation modes, as demonstrated in the previous chapter. However, as discussed in §2.1.1, the optical engine configuration necessities modifications to the combustion chamber geometry and engine operating conditions, which could alter the in-cylinder processes relative to a thermodynamic “all-metal” engine. As a less processes-altering approach, the optical probe design described in §3.2.5 can be used for optical measurements from the combustion chamber of an all-metal engine, without imposing optical engine restrictions, albeit without providing spatial attributes of the collected signal.

Therefore, in order to extend the understating afforded by the 2D measurements, and to study the in-cylinder processes under more realistic conditions of the all-metal engine, this chapter focuses on simultaneous 2D and 0D optical measurements of the PIDING combustion, performed under the optical engine configuration. This is then followed by discussion of 0D two-color pyrometry measurements in thermodynamic engine, to analyze the effects of different engine configurations. Better characterized optical probe measurements of in-cylinder soot temperature and concentrations, and chemiluminescence, in conjunction with HRR results, would set the framework to develop a thermo-optical analysis tool-kit, to

study combustion in-cylinder processes under more realistic operating conditions.

7.1 2D vs. 0D two-color pyrometry measurements

The measurement characteristics of the optical probe and 2D measurement systems were described in Chapter 3. To facilitate characterization of the optical probe signal, the analysis of in-cylinder soot processes based on 0D optical probe measurements was considered in correlation with spatially resolved and averaged 2D two-color pyrometry. Figure 7.1 shows the optical engine and measurement system layout used for this analysis.

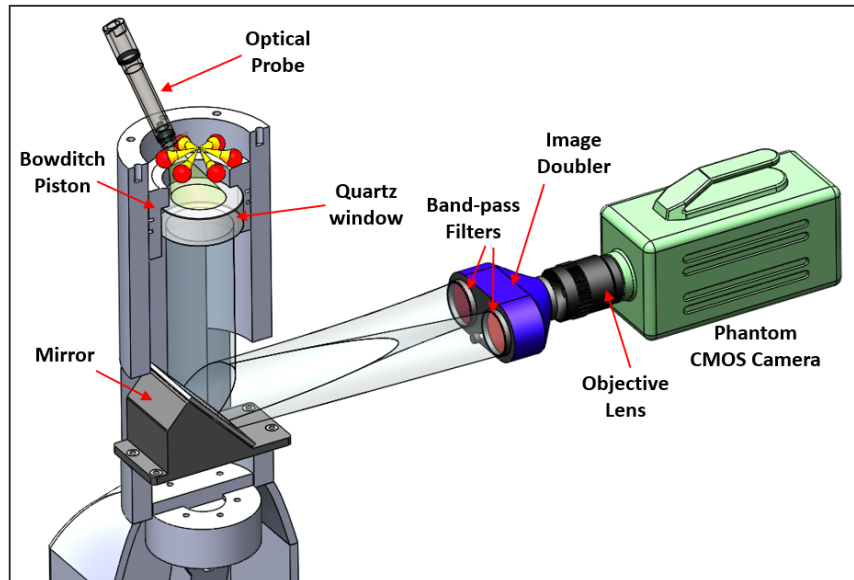


Figure 7.1: 2D and 0D Two-color pyrometry measurement system on optical engine configuration.

The two-color pyrometry method described in Chapter 2 is a line-of-sight measurement technique. As described by the Radiative Transfer Equation (equation 7.1), the incremental changes and ultimately recorded spectral radiant intensity signal on any directional pathway (line-of-sight) is the aggregate result of the combination of light emission from hot soot parcels at each point, and partial attenuation of the light from previous points on the pathway through absorption and scatter-

ing, and light scattered into the considered pathway from any incoming directional pathways.

$$\frac{dI_\lambda(S,t)}{dS} = \kappa_\lambda I_{\lambda,b}(S,t) - \kappa_\lambda I_\lambda(S,t) - \sigma_{S,\lambda} I_\lambda(S,t) + \frac{1}{4\pi} \int_{\Gamma_i=4\pi} \sigma_{S,\lambda} I_\lambda(S,t) \Phi_\lambda(\Gamma_i) d\Gamma_i \quad (7.1)$$

where S is the line-of-sight path, κ_λ is the absorption coefficient (see §2.1.4), $\sigma_{S,\lambda}$ is the scattering coefficient, and Φ_λ is the scattering phase function, and Γ is the solid angle. The RTE is the conservation of radiative energy through an absorbing, emitting, and scattering medium along a path (S) for a given wavelength. The scattering effects are assumed negligible for the size of particles pertinent to two-color pyrometry measurements of soot clouds [58] (3rd and 4th terms on right-hand-side of equation 7.1). The light emission and absorption effects are illustrated in Figure 7.2.

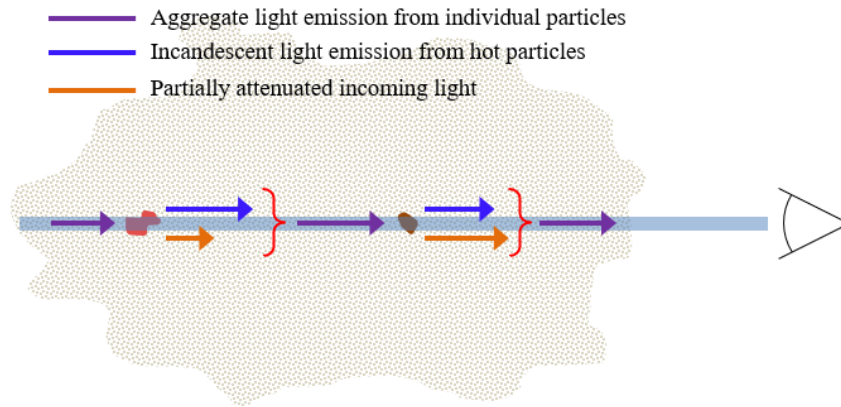


Figure 7.2: Line-of-sight measurement effects in a partially transparent soot cloud. The incandescent light emission and illuminating light rays from and to individual particles occur at all directions and here shown only on the optical path for simplicity.

Therefore, changing the point of view to the soot cloud in the combustion chamber might affect the detected light intensity (i.e., two-color pyrometry raw signal), due to the asymmetries in the soot particle distributions in the soot cloud.

In addition to the described point of view effects, the field-of-view (FOV) in the considered optical measurement systems in this analysis, as illustrated in Figure 7.1, also have significantly different geometries. The cylindrical FOV of the 2D measurement system collects an array of (approximately¹) parallel directional spectral radiant intensities on the CMOS sensor of the high-speed camera. The optical probe, conversely, collects the incoming light within its conical FOV, using its sapphire rod lens, onto a small surface area of an optical fiber, which leads to a single value spectral radiant intensity reading.

In what follows, the influence of this inherently different measurement characteristic is examined and an approach to reflect it into comparison of the results is introduced. The introduced method is then evaluated through analysis of a range of PIDING combustion operating conditions.

7.1.1 The FOV effects

The differences in measurement principles of the optical probe and 2D measurement systems can render the direct comparison of the results more challenging. Figure 7.3 compares probe 0D two-color pyrometry results and the mean temperature and KL factor values over the bowl area from the 2D measurements (described by equation 6.3). Here, the baseline and long GPW PIDING operating conditions are shown (see Table 6.1), as is a double NG pulse PIDING operating condition, with high amount of soot production (here referred to as the long split GPW operating condition). Table 7.1 presents the specifications for these operating conditions. The long split GPW operating point is not to be mistaken for the late post injection (LPI) strategy, which uses a smaller mass second injection of NG later in the cycle, calibrated (relative timing and duration) to enhance late cycle soot oxidation and reduce engine-out soot [39]. The dwell between EOI of the 1st and the GSOI of the 2nd NG injection result in significant soot and ample two-color pyrometry signal, which makes it suitable for the purpose of the current analysis.

Comparison of the results in Figure 7.3, in general, shows a close estimation of the temperature and KL factor values and trends, considering the differences in FOV geometries and dimensional differences. In both set of measurements, the

¹In the case of two-color pyrometry measurements via image doubler the collected columns of light make a $\sim 3^\circ$ angle

Table 7.1: Operating points discussed in Figure 7.3; RIT = 8 CAD, P_{inj} = 180 bar, speed=1000 rpm for all points.

Point	cPSOI [° aTDC]	cGSOI ₁ [° aTDC]	cGSOI ₂ [° aTDC]	PPW [ms]	GPW ₁ [ms]	GPW ₂ [ms]	GIMEP [bar]
Baseline	-18	-10	-	0.7	1.45	-	11.5
Long GPW	-18	-10	-	0.7	1.85	-	14.2
Long split GPW	-20	-12	3	0.7	1.25	0.85	14.1

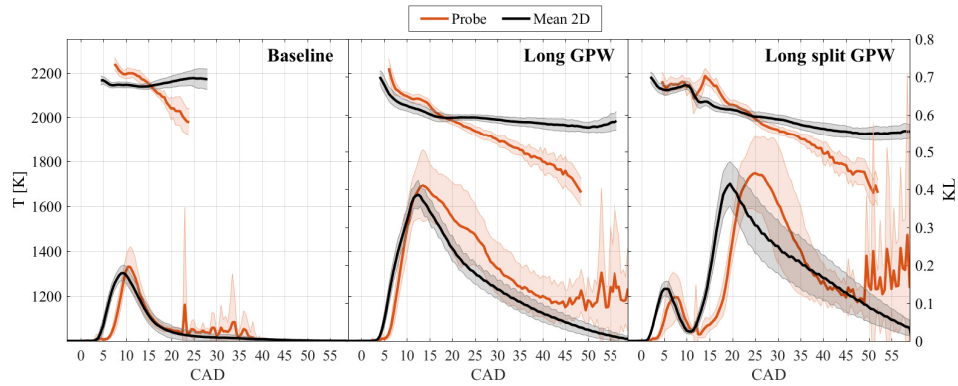


Figure 7.3: 0D probe vs. mean 2D two-color pyrometry results (equation 6.3) for the operating points listed in Table 7.1.

two KL factor peaks at long split GPW, resulting from the two closely coupled NG injection pulses [39], are resolved. The 0D and mean 2D measurements both captured the higher KL factor peaks for the long split GPW and long GPW operating conditions, and the value of the peaks in all the cases are in close agreement between the two set of measurements. Furthermore, the crank positions of the KL factor peaks and the rising edge of the curves, between the optical and 2D measurements, are relatively close (<5 CAD offset).

The 0D probe results in Figure 7.3 indicate more significant cycle-to-cycle variability, as marked by the shaded regions, especially for the baseline and long GPW cases. This is explained by the more localized measurements within the probe FOV, compared to the entire bowl area available for spatial averaging in the mean 2D results, and is relevant for heterogeneous combustion processes under

consideration.

Despite the general agreement between the 2D and 0D results, consistent discrepancies are noticed in Figure 7.3. The mean temperature estimates from the 2D measurements are up to 50 K lower than those from the 0D probe measurements, before the KL factor peaks. Furthermore, the rising edge of KL curves and the peaks are delayed in 0D results and more fluctuations are observed in the tail-end of those results. The 2nd NG injection in long split GPW is not as clearly captured in mean 2D temperature results and there is a rather consistent decay in calculated temperature results from the optical probe measurements.

7.1.2 Weighted function averaging

The observed discrepancies described above, are in part an artifact of the more localized nature of the optical probe measurements. Accounting for the FOV differences will allow more direct comparison of the 2D and 0D results. While, this is not completely achievable solely based on the available optical results, an approach is proposed towards this goal and to provide a closer comparison between the two methods.

The approach is based on generation of a dynamic weighted averaging function for the 2D results, as illustrated in 7.4, knowing the relative distances and cosine angles between the probe sapphire lens and the window normal vectors. The optical probe FOV ($F(\mathbf{u})$) is modelled using a general 3D right circular cone equation:

$$F(\mathbf{u}) = (\mathbf{u} \cdot \mathbf{d})^2 - (\mathbf{d} \cdot \mathbf{d})(\mathbf{u} \cdot \mathbf{u}) \cos^2 \theta \quad (7.2)$$

Where θ is half of the aperture angle (25°), $\mathbf{u} = (x, y, z)$ is the position vector, apex is at the origin, and axis is parallel to the unit vector $\mathbf{d} = (d_x, d_y, d_z)$. At each crank position, the intersection of the window surface and the probe FOV forms an ellipse whose boundary is described by equation 7.3, where h_{wf} denotes the instantaneous distance between window surface and the firedeck. As such, a region-of-interest (ROI) mask is created at each crank position, which focuses the averaging on the instantaneous projection of the conical FOV of the probe onto the quartz window. At each pixel coordinate within the ROI mask, the fraction of the column height above it (window to firedeck) that lies within the angled conical

FOV is used as a weight factor for that pixel coordinate, at that crank position (Figure 7.4 and equation 7.4). Repeating the described procedure for every pixel within the ROI mask, results in the final dynamic weighted averaging function matrix. The weighted spatially averaged (WSA) 2D results as such, could eliminate some of the discussed localized measurement effects.

$$A_y y^2 + 2d_y(h_{wf}d_z + d_x x)y + A_z h_{wf}^2 + 2h_{wf}d_z d_x x + A_x x^2$$

$$A_{(x,y,z)} = (d_{(x,y,z)}^2 - \cos^2 \theta) \quad (7.3)$$

$$WSA(x,y,\theta) = \frac{h_{FOV}(x,y,\theta)}{h_{wf}(\theta)} \quad (7.4)$$

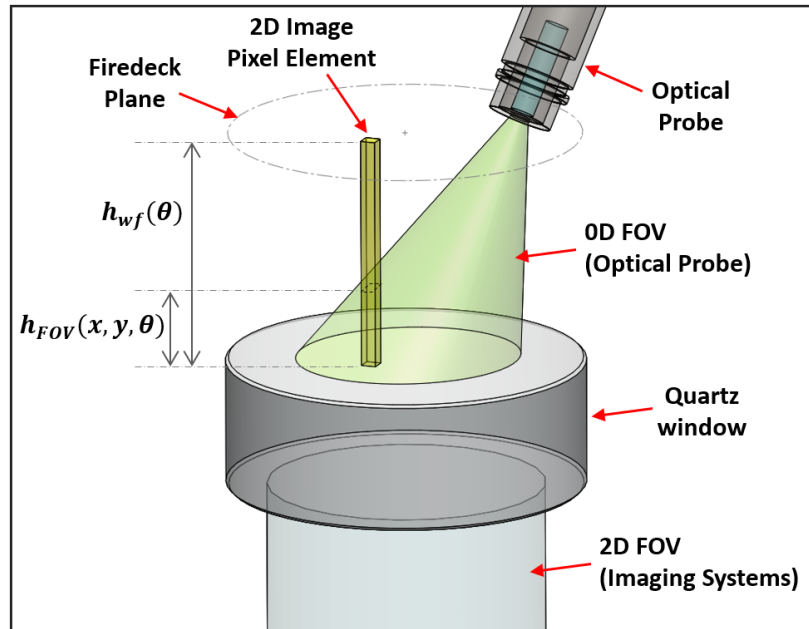


Figure 7.4: Generation of the weighted spatially averaged ROI for 2D two-color pyrometry results based and projection of optical probe conical FOV onto the quartz window surface. The fraction of column within the inclined probe FOV at each coordinate is used as the weight factor for the ROI mask. The ROI mask geometry changes corresponding to optical piston movement within the cycle.

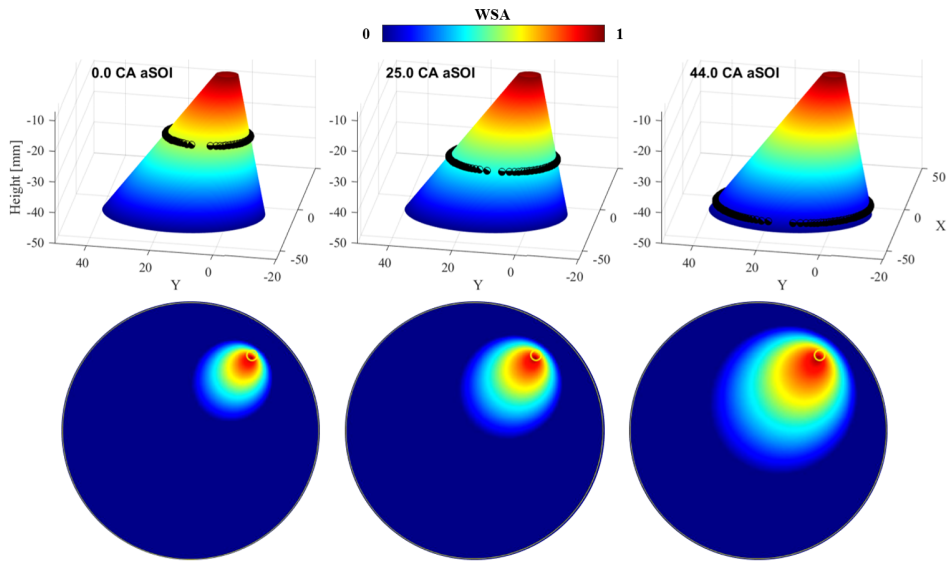


Figure 7.5: WSA ROI mask at three crank positions and the corresponding optical probe cone projection cross-sections. The surrounding ring on the WSA cones depicts the intersection with the quartz window surface at each crank position.

Figure 7.5 shows snapshots of the dynamic weighted averaging function at sample crank positions. The WSA 2D results, however, rely on a rather homogeneous angular distribution of the soot cloud signal, at least within the FOV of the two measurement systems, in order to provide a good agreement with the 0D probe measurements. This premise is not necessarily always true, especially under certain engine operating conditions which lead to high heterogeneity in the results, as will be discussed later in this chapter.

With the optical test repeatability measures put in place (see §3.3.2), the stand-off distance between the 2D imaging systems and the firedeck is constant among different measurements. However, there is slight variations in the injector coordinates on the image sensor, which is recorded during two-color pyrometry calibration. Therefore, once the dynamic weighted averaging function matrix was generated for the baseline operating condition, translation of the matrix by the center-to-center distance vector (injector position between the baseline and operating point under consideration) makes it applicable to the new 2D results.

The order in which the image processing stages, from the individual cycles of the raw image sequences to the WSA curves, is implemented can also affect the results. The major stages involved are the ensemble averaging of the recorded cycles, the two-color pyrometry algorithm (see Chapter 5), and weighted spatially averaging procedure described here. Different permutations of these stages are discussed in more detail in Appendix G. Based on that analysis, this chapter presents WSA results from two different approaches: 1) Application of the WSA to the pyrometry results, and 2) Ensemble average of the single cycle WSA KL and T results. The former approach is spatially averaging of the pyrometry results as presented in Chapter 6 and here is referred to as the WSA_{SNR} , while the latter provides a conventional ensemble average for comparison with OD probe results and is referred to as the WSA_{Ens} .

The WSA_{SNR} and WSA_{Ens} approaches are implemented on the operating conditions listed in Table 7.1 and the results are compared to their OD probe counterparts in Figure 7.6. The WSA results show better agreement with the probe temperature measurements, compared to the mean 2D results. In all cases, the WSA temperature trends closely follow OD results during the soot formation stage (before peak KL) until shortly after the peak KL factor. Also similar to the probe results, the 2nd NG injection effects in long split GPW are evident in WSA results (KL and T in 7-22 CAD aTDC range). Later in the cycle and during the soot oxidation stage, the WSA results stabilize and deviate from those of the optical probe, which continue to decay. In addition, WSA KL factor results more closely follow the OD results, especially during the soot oxidation stage (after KL factor peak) for the GPW=1.85 ms and long split GPW operating points. The onset of soot signal and soot formation rates, identified by the rising edge of the KL factor results, more closely match in phasing between the WSA and probe results (<1.5 CAD).

The comparison of the WSA_{SNR} and WSA_{Ens} results in Figure 7.6 suggests that the ensemble averaging of the raw signal for the WSA_{SNR} approach leads to lower KL factor values, relative to the WSA_{Ens} approach.

Thus, the observed improvements in correlations between the WSA and OD results demonstrates the influence of accounting for FOV geometry differences. The rising edge of the KL factor and detected onset of soot is delayed for OD probe due to delay in the soot cloud growth until it reaches the probe FOV. This can be

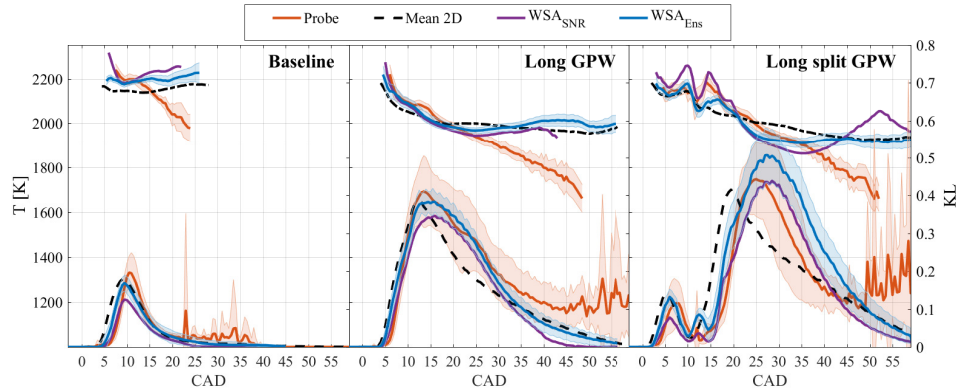


Figure 7.6: 0D probe vs. WSA 2D two-color pyrometry results for the operating points listed in Table 7.1.

inferred from the comparison of the overlay of weighted mask on KL factor distributions for the baseline condition in Figure 7.7-a with KL curves in Figure 7.6 (5.5-6.5 aTDC). In addition, the positioning of the probe closer to the wall region, where higher temperature reactions from combustion of the partially-premixed charge occur and remain concentrated until late in the cycle (see §6.2.5), explains the closer temperature estimations with the WSA results (OH* results in Figure 7.7-a; note that the ROI is more heavily weighted here).

Similarly, crank positions after the KL factor peak in the GPW=1.85 ms operating condition reveals that with transition of the higher optical thickness region towards the center (reflected momentum effects, see §6.2.5), the mean 2D results show a more rapid decay in the KL signal, while the 0D and WSA results capture more soot within the “FOV” (Figure 7.7-b and middle column in Figure 7.6).

Soot formation in the high temperature reaction zone during the mixing-rate limited fuel conversion processes after the peak HRR [128] and formation of higher KL factor, lower temperature soot pockets, results in a decay in estimated temperature values starting from onset of soot signal (coinciding the peak HRR) until shortly after the peak KL factor. This phenomenon is illustrated more clearly in comparison of the T - KL cumulative distribution diagrams² in the range of 5-10 CAD aTDC for the baseline operating condition, shown in Figure 7.8. The high

²See §6.2.1 for details regarding the metric

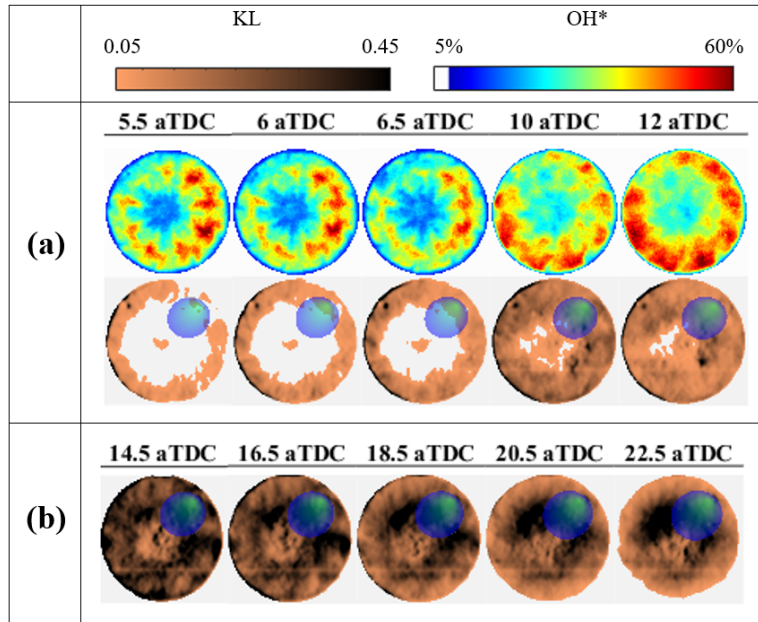


Figure 7.7: Probe FOV geometry effect on WSA results: (a) 2D OH* chemiluminescence and *KL* factor results for the baseline, (b) 2D *KL* factor results for the GPW = 1.85 ms operating point.

temperature region (yellow color denotes highest counts) moves from 2300-2500 K at 5 CAD aTDC to 2100-2300 K at 8 CAD aTDC with notable population at around 2000-2200 K. Consequently, the spatially averaged temperature values will decrease between 5 to 8 CAD aTDC. This, however, does not explain the discrepancy between temperature estimates from WSA and 0D results later in the cycle, which is investigated later in this section.

As discussed above, the WSA results explains the 0D pyrometry temperature decay before and shortly after the *KL* factor. In order to investigate the continued temperature decay in probe results and the discrepancy between 2D and 0D temperature estimations later in the cycle, the apparent temperature data for the two measurement techniques and the ideal gas temperature histories are considered. For the WSA results, the weighted function was applied to each pair of instantaneous apparent temperature images from individual cycles and the results were ensemble averaged for each wavelength ($T_{a,WSA}$ at 700 and 800 nm). The results

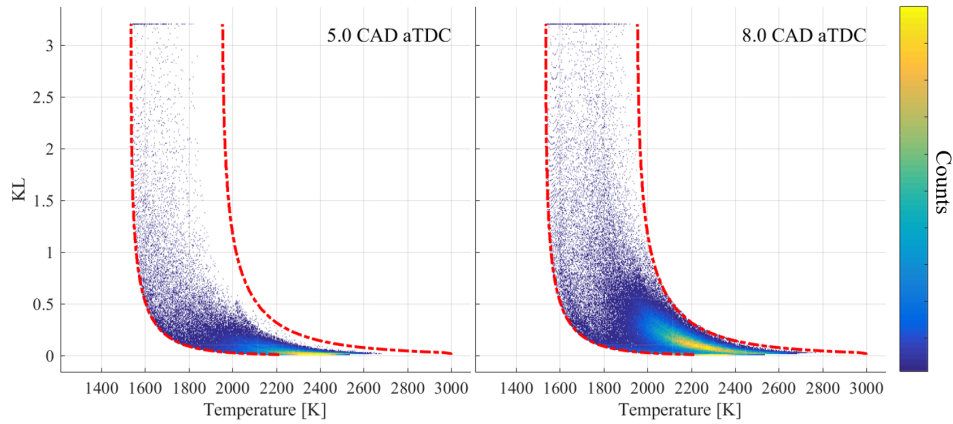


Figure 7.8: Two-color pyrometry temperature and KL factor population maps for the baseline operating condition at 5 and 8 CAD aTDC.

are shown in Figure 7.9.

Comparison of the apparent temperatures in Figure 7.9-a, similarly to the calculated temperature results, shows a departure in the WSA and OD results later in the cycle. The timing at which this deviation in temperature estimations occurs appears close to the peak of the ideal gas temperature estimation, especially for the baseline and long GPW operating conditions. Therefore, it can be inferred that the continuous decay in probe temperature results, in part, originates from the sufficiently optically thick soot cloud moving away and out of the probe FOV, with downward piston motion, and is not entirely an artifact of the solution algorithm and low SNR later in the cycle. The low SNR however, ultimately causes the higher uncertainty temperature and KL calculations later in the cycle (after 22 and 45 CAD aTDC for baseline and GPW=1.85 ms cases, respectively, in Figure 7.9, with widening error-band probe apparent temperatures). Although the hypothesized cloud movement away from the firedeck cannot be illustrated via the available imaging system, the diminishing probe FOV coverage in Figure 7.9-b supports the loss of signal in the conical FOV. The OD two-color pyrometry KL factor calculations of PIDING combustion by Hatzipanagiotou *et al.*[54], under similar operating conditions, also shows the similar late-cycle KL behavior, i.e., decreasing oxidation slope with higher fluctuations in the results (peremptory temperature results was not reported). Similar temperature decay behavior was observed for

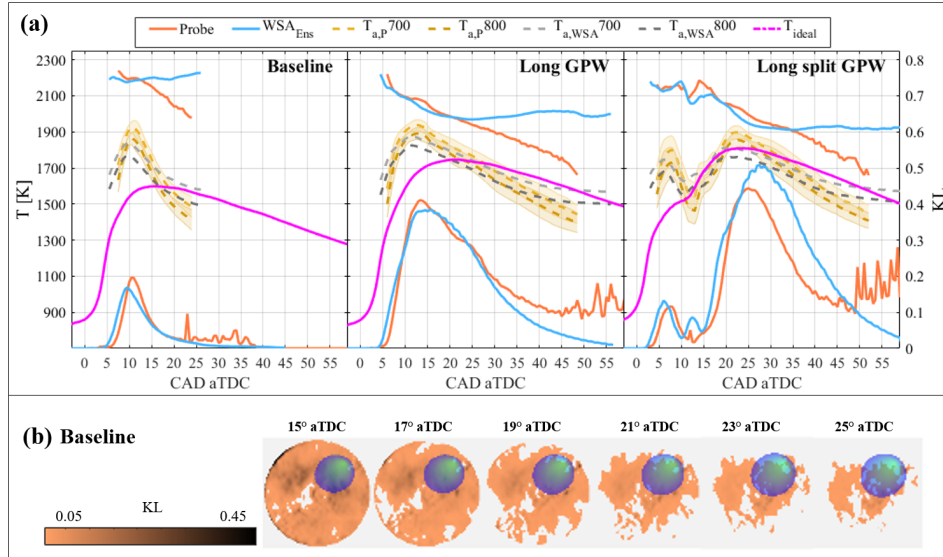


Figure 7.9: (a) 0D probe vs. WSA 2D two-color pyrometry results, and their corresponding apparent temperatures (T_a), for the operating points listed in Table 7.1, (b) 2D KL factor results vs. probe FOV coverage during soot oxidation stage in the baseline operating point.

alternative weighted spatially averaging approaches later during the low-SNR late-cycle soot oxidation stage (WEP and WPE results in Appendix G).

7.2 Thermodynamic vs. optical engine configurations

Following the characterization measures described in the previous section, the optical probe was used for 0D two-color pyrometry measurements of PIDING combustion in thermodynamic engine configuration. The primary goal of these measurements was to compare the in-cylinder processes in the thermodynamic engine with the toroidal bowl design (as opposed to the transparent flat cylindrical bowl of the optical engine) and without constraints of optical measurements (e.g., skip-firing and load limits), as inferred from the optical measurements. In the process, the possibility of extending the spatially resolved measurements findings to the processes occurring in a thermodynamic engine was assessed. Table 7.2 provides the specifications for the operating conditions considered for this investigation.

Table 7.2: Operating conditions investigated under thermodynamic and optical engine configurations using OD optical probe measurements; Engine speed was 1000 rpm for all points.

Point	Configuration	cPSOI [° aTDC]	cGSOI [° aTDC]	PPW [ms]	GPW [ms]	GIMEP [bar]	CA50 [° aTDC]
Baseline*	Thermo.	-16	-10	0.55	1.45	11.8	6.7
	Optical	-18	-10	0.7	1.45	10.8	7.9
Long RIT	Thermo.	-22	-10	0.55	1.55	12.3	6.6
	Optical	-24	-10	0.7	1.45	11.3	7.4
$P_{inj}=220$ bar	Thermo.	-15	-8.5	0.45	1.25	13.1	6.8
	Optical	-16	-8	0.6	1.2	12.8	9.0
$P_{inj}=140$ bar	Thermo.	-21	-13.5	0.7	2.2	12.3	7.2
	Optical	-22	-14	1.0	2.1	11.2	7.9

* $P_{inj}=180$ bar; RIT= 8°

It should be noted that due to technical difficulties in the available engine facility, performing optimized replicas (based on CA₅₀, load, HRR shape) of the optical campaign operating points discussed in the previous chapter (see Table 6.1), under the thermodynamic engine configuration was not possible in the time frame of this work. Nevertheless, the presented available pairs of operating conditions in Table 7.2 suggest relatively similar in-cylinder phenomena, inferred from general HRR shapes, engine loads and combustion phasing, and therefore, still could be used to compare the OD two-color pyrometry results under the two engine configurations. Figure 7.10 illustrates this comparison for the baseline operating condition. The HRR and two-color pyrometry results for the thermodynamic measurements in this and all subsequent figures are the ensemble average of 110 cycles, and the temperatures are plotted only in the range where the cycle-to-cycle standard deviation is less than 150 K (for both engine configuration results).

Here, with the toroidal bowl design and higher compression ratio in the thermodynamic configuration, a lower HRR peak is observed for the thermodynamic configuration, which suggests less partially premixing at the bowl wall (shorter ignition delay and lower injection rate). The combustion chamber reaches a higher

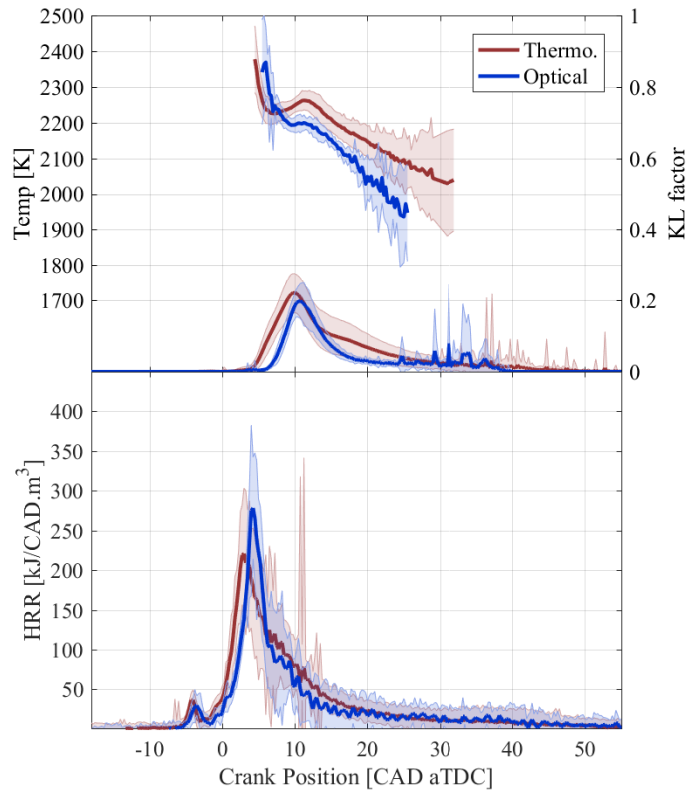


Figure 7.10: OD probe two-color pyrometry results (top), and HRR results (bottom) for the baseline operating condition under optical and thermodynamic engine configurations.

temperature in the thermodynamic engine, due to the higher compression ratio as well as continuous firing (no skip-firing cycles) and different heat transfer characteristics of the two engine configurations (further discussed below). This results in higher pyrometry temperatures and advanced NG ignition (shorter τ_{NG}), inferred from the advanced rising edge of HRR at ~ 0 CAD aTDC and advanced peak. An earlier rise in the KL curve (and first appearance of temperature signal) is observed as a result. The strong correlation between the onset of KL and peak HRR timing was shown in Figure 6.19. A higher fraction of the NG mass being converted through a more mixing-rate limited process leads to a slightly higher peak KL , as well as later in the cycle (figure 7.10, 15-25 CAD aTDC). However, the higher py-

rometry temperature within the same range suggests higher soot oxidation rates, which eventually leads to similarly low KL factor values after 25 CAD aTDC. Similar decay in the pyrometry temperature values is observed for both engine configurations, which suggests similar contributing factors, explained in §7.1.2, affect the soot cloud temperature in the combustion chamber of the thermodynamic engine.

In addition to the higher compression ratio and continuous firing, lower radiation heat losses in the all-metal engine in the absence of the quartz window, could be a contributing factor for the higher estimated temperatures. A simplified radiation heat loss model for comparison of the two engine configuration suggested a 45% lower heat loss in the all-metal engine. Details of this analysis is presented in Appendix H. However, the quartz window also leads to lower conductive heat losses compared to the metal piston crown. Investigation of the effect of the lower conductivity of the optical window is reported to significantly affect the heat release rate characteristics [5]. Considering these opposing effects and limited available information in this regard, it would be difficult to confidently comment on the effect of total heat transfer loss through the quartz window.

It should also be noted that light reflection off the metal surfaces, higher in the absence of the transparent quartz window in the all-metal engine, might be considered as a contributing factor to a higher pyrometry temperature calculation. However, the wall reflection was shown to be more significant when two-color pyrometry measurement wavelengths in the IR range is utilized [96]. Under low soot concentration diesel operating conditions, that investigation showed temperature and KL errors of less than 1 and 10%, respectively, for visible wavelengths, whereas errors of less than 8 and 50% in temperature and KL estimates were observed for IR measurements.

Comparison of other operating points in Table 7.2 is presented in Figure 7.11 and shows similar behaviors in the HRR and two-color pyrometry results. In all cases, the combustion phasing and peak HRR crank positions are advanced in thermodynamic measurements, despite the similar NG cGSOI, which as explained above leads to an earlier onset of soot signal, suggested by the advanced pyrometry KL factor and temperature curves. The pyrometry temperature values are also higher under thermodynamic configuration and show similar decay to those of the optical engine.

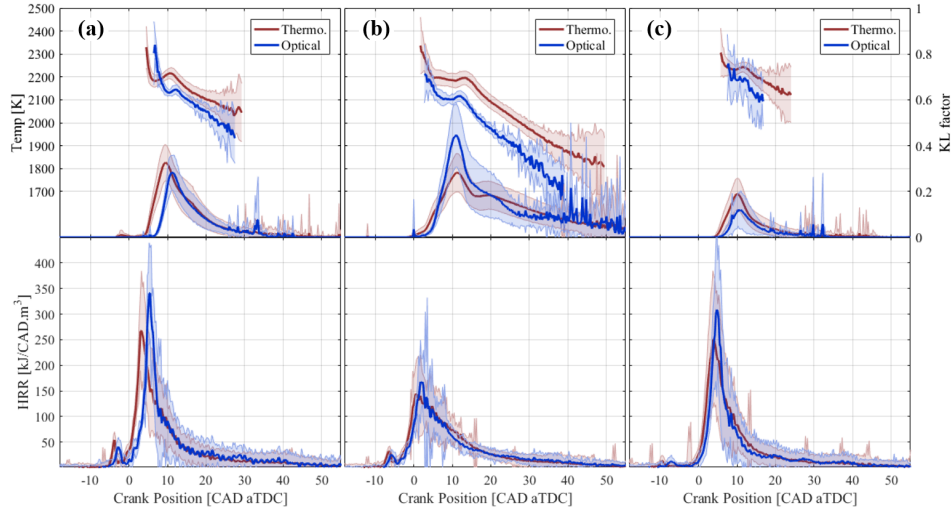


Figure 7.11: OD probe two-color pyrometry results (top row), and HRR results (bottom row) for: (a) $P_{inj}=220$ bar, (b) $P_{inj}=140$ bar, and (c) long RIT operating conditions under optical and thermodynamic engine configurations described in Table 7.2.

The pilot combustion HRR results in Figure 7.11 are advanced for the thermodynamic engine configuration, due to the described combustion chamber temperature effects in combination with more advanced cPSOI ($P_{inj}=140$ bar and long RIT cases) or higher mass and momentum flow rate (in the case of $P_{inj}=220$ bar), relative to the baseline. It is worth noting that the injected pilot mass might also be lower in the thermodynamic engine due to higher compression ratio. At $P_{inj}=220$ bar, the more significant pilot combustion HRR peak leads to small traces of soot formation detected in the ensemble average KL factor results. However, the signal was still too weak for a reliable temperature estimation within the selected uncertainty limit (standard deviation <150 K). In all three cases in Figure 7.11 the partially-premixed peak HRR is lower in the thermodynamic engine, despite the higher engine loads. Similar to the baseline, the higher fraction of NG conversion through the more mixing-rate limited processes leads to a higher peak KL factor for $P_{inj}=220$ bar and long RIT operating conditions. However, the $P_{inj}=140$ bar operating point, which showed significant heterogeneity in soot concentration distributions in the 2D optical pyrometry results, shows a lower KL factor peak and

more extended signal under thermodynamic configuration. This is attributed to the toroidal bowl design, which prevents accumulation of rich regions at the wall region through better guiding of the lower momentum NG jets and enhanced mixing after impingement on the walls. Nevertheless, the higher temperature suggests higher late-cycle soot oxidation rates, which leads to similar KL factor values after 40 CAD aTDC.

Overall, a good agreement between the thermodynamic and optical results, in terms of describing the influence of fueling parameters on soot trends, is observed across the operating points in Table 7.2. NG EOI prior to the peak HRR at long RIT shows a predominantly partially-premixed fuel conversion and low soot signal within a limited crank position range; extended injection of NG beyond the peak HRR, with a lower momentum flow rate, leads to higher KL factor peak relative to baseline and a more heterogeneous soot cloud distribution, inferred from the shape of the KL factor curves; and at higher P_{inj} (220 bar), higher mass flow rate NG jets and soot formation rates lead to a higher KL factor peak relative to baseline. Similar to the P_{inj} sweep analysis in the optical engine configuration (Chapter 6), $P_{inj}=220$ bar here also leads to a higher engine load. Therefore, direct comparison of in-cylinder soot processes to describe the previously observed lower engine-out soot emissions at increased P_{inj} , where the load was held constant, [34, 98] was not possible.

7.3 Concluding Remarks

0D optical probe two-color pyrometry measurements under optical and thermodynamic engine configurations were considered in this chapter. A simplified weighted spatially averaging (WSA) technique for 2D measurements was introduced to account for FOV differences during optical engine measurements. WSA results improved the agreement between 2D and 0D results and explained the discrepancies in the two signals originating from the more localized nature of the probe light collection technique. As such, more insight into temperature and KL estimates from the optical probe was provided. The higher pyrometry temperature estimates from optical probe were attributed to more heavily weighted light collection from regions closer to the walls, where higher concentration of high temperature reactions

were previously observed. Similarly, delayed soot signal detection was explained by the soot cloud formation and development until it reaches the optical probe FOV. An initial temperature drop was explained by WSA results and corresponded to continued NG injection and formation of higher optical thickness soot cloud and lower heat release during more mixing-rate limited fuel conversion. However, the consistent temperature decay in probe results later in the cycle could not be reproduced by the proposed WSA technique and was in part attributed to the soot signal leaving the probe FOV with higher soot oxidation rates in those regions.

0D optical probe pyrometry measurements from optical and thermodynamic engines showed good agreement in the results, considering the inherent differences between the two engine configuration designs and operating procedures. This afforded interpretation of the thermodynamic engine in-cylinder soot processes in a similar fashion to the optical engine configuration. However, the higher compression ratios and continuous firing under thermodynamic engine configuration, consistently resulted in shorter ignition delays, higher pyrometry temperature estimations and advanced the onset of soot processes, and higher engine load with generally a lower partially-premixed HRR peak, followed by slightly higher peak KL factor. Nevertheless, the higher temperature values later in the cycle and the toroidal bowl geometry appear to compensate for the higher peak and result in similar KL factor values during the late-cycle oxidation stage.

Chapter 8

Conclusions and Future Work

The presented work focused on developing optical characterization techniques to study in-cylinder processes in cleaner combustion strategies, leading to relatively lower yet non-negligible soot formation, such as those involving natural gas. Specifically, conventional diesel-ignited dual-fuel (DIDF) combustion of NG and pilot-ignited direct-injected natural gas (PIDING) combustion strategies were optically investigated through natural luminosity, two-color pyrometry, and OH* chemiluminescence measurements. In this final chapter the major findings from various investigations carried out in this work are presented and some prospects of future investigations in continuation are presented.

8.1 Summary of the Significant Findings

Optical investigations pursued in this work were primarily executed in an experimental facility that supported spatially resolved optical measurements via a Bowditch piston arrangement in a 2-litre, single-cylinder research engine. The complete optical measurement system is illustrated in Figure 8.1, with all optical diagnostics utilized in different chapters of this work. The development of the 2D optical measurement systems were accomplished in this work and the 0D optical probe design was the focus of a previous work [156].

In what follows, a summary of the significant results and novel contributions to the topic from individual chapters of the current work is presented.

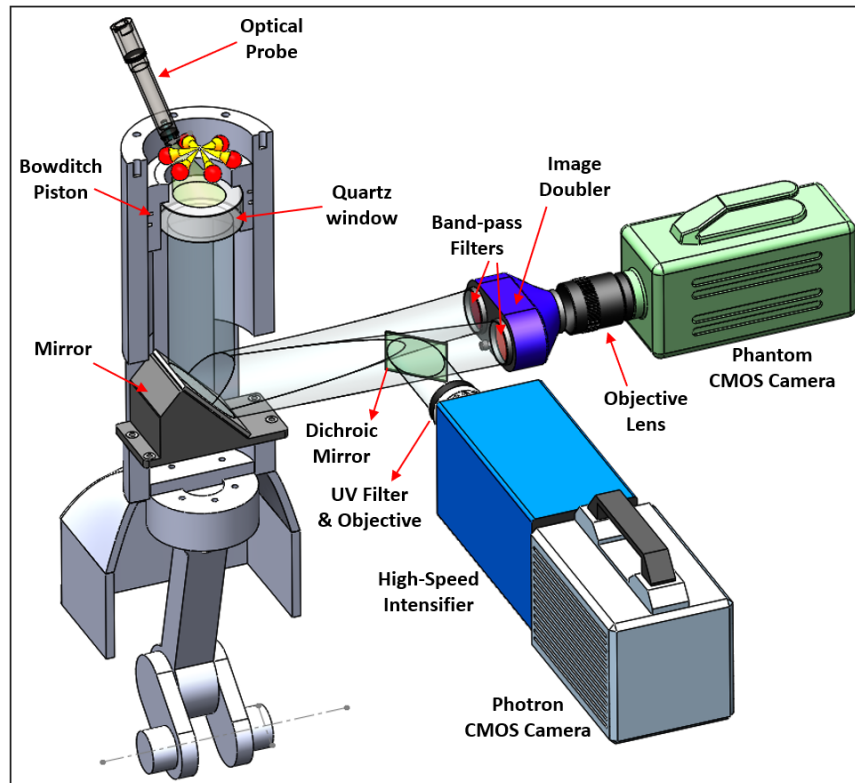


Figure 8.1: 2D and 0D natural luminosity/two-color pyrometry and OH* chemiluminescence measurement system on optical engine configuration.

8.1.1 Optical Investigation of DIFD combustion

A simultaneous high-speed natural luminosity (NL) and OH* chemiluminescence imaging system was developed to assess the influence of fueling control parameters on the fuel conversion processes in DIFD combustion. These measurements revealed the potential to manipulate combustion of premixed natural gas (ignition sites locations and reaction zone growth mechanisms) through controlling pilot injection pressure P_{inj} and relative diesel-CH₄ ratios, which were noted as the key dual-fuel operating control metrics. At higher P_{inj} the auto-ignition sites were concentrated around the piston bowl periphery and the reaction zone propagated towards the center of the bowl. Concentration of high temperature reaction zones

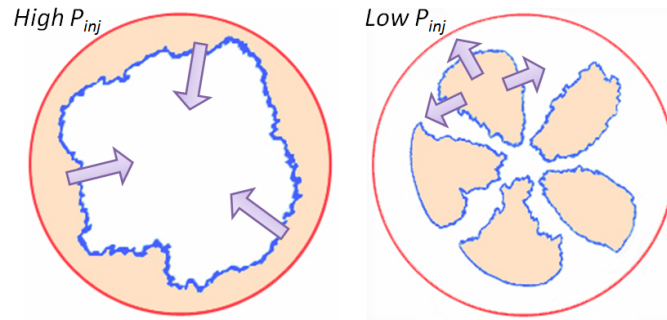


Figure 8.2: Conceptual effect of pilot fuel injection pressure on reaction zone growth mechanism (left: high pressure; right: low pressure) on DF combustion mode

around the edges promotes more effective fuel conversion at these critical, wall-influenced regions. Reducing P_{inj} caused ignition to initiate in the vicinity of the pilot fuel jet structures and resulted in a more heterogeneous fuel conversion process with regions of intense natural luminosity, attributed to soot. The conceptual representation of the described P_{inj} effects is presented in Figure 8.2, which is based on OH^* images from representative high and low pilot injection pressure operating points. An increase in diesel fraction in the charge resulted in a more aggressive combustion event, due to a larger fraction of energy released in a premixed auto-ignition event, coupled with a decrease in the fraction of the combustion chamber with significant OH^* or NL light emission, indicating incomplete fuel conversion in these regions.

8.1.2 Two-Color Pyrometry Method Improvement

The two-color pyrometry technique, being an unstimulated method relying on natural light emissions from target species, is susceptible to low signal-to-noise ratio effects imposed by the lower soot emissions of the cleaner combustion strategies. As such, the performance of the pyrometric method was enhanced to facilitate quantitative soot analysis in the low soot signal conditions, such as those of the DDF and PIDING combustion strategies. This was achieved through modifications to the numerical algorithm, increasing the detection envelope during measurements, performing perspective adjustments, accounting for non-uniform and

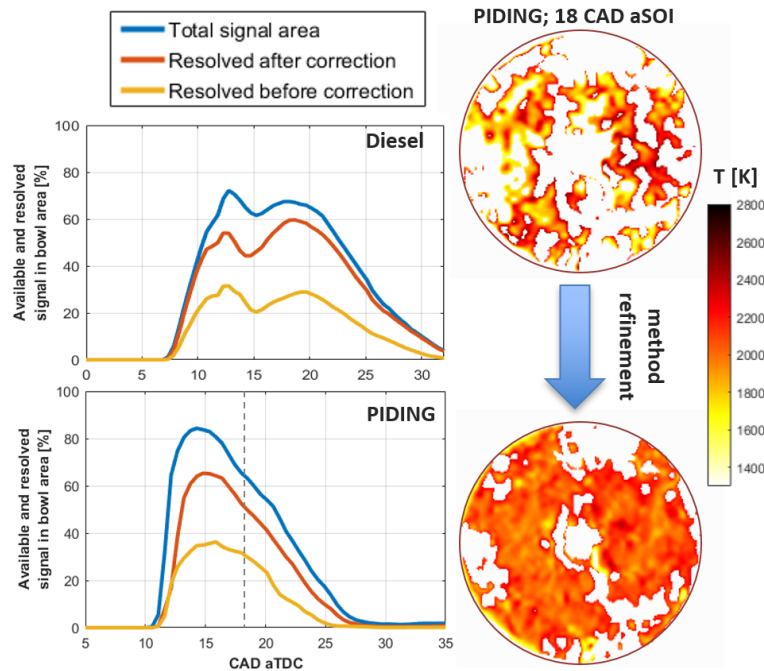


Figure 8.3: Two-color pyrometry method enhanced performance depicted as improvements in the resolved signal fraction throughout the ensemble averaged cycle (left) and at a sample crank position for PIDING combustion (right)

non-linear system response, as well as localized signal-to-noise ratio enhancement through image filtering. Figure 8.3 compares the resolved signal fraction from sample diesel and PIDING combustion operating conditions and sample PIDING pyrometric results with and without the proposed enhancements. The improved pyrometric method provided a nearly 40% increase in the resolved signal fraction. The achieved improvements are of particular significance for the PIDING combustion strategy, which had a 75% lower signal intensity than the considered diesel combustion. Furthermore, the improved method affords pyrometric investigation of other low soot signal strategies, such as LTC, as well as late-cycle soot oxidation processes in various combustion strategies, with proper adjustments to the detection envelope. The latter is particularly important for providing the link between in-cylinder and engine-out soot trends.

8.1.3 Optical Investigation of PIDING Combustion

The enhanced two-color pyrometry method was implemented simultaneously with high-speed OH* chemiluminescence imaging to PIDING combustion in order to better understand in-cylinder soot formation and oxidation processes. The results revealed that a standard PIDING operation can be characterized as low-sooting, non-premixed combustion of the natural gas (NG) along the gas jets and of a partially-premixed reaction zone near the wall. The first detectable soot is observed at the points of NG jet impingement on the wall, in the partially-premixed reaction zone. This results in formation of a soot cloud at the wall region which then grows towards the center due to continued soot formation and reflected momentum of the NG jets impinging on the bowl wall. With higher temperature reactions remaining more concentrated closer to the wall, the soot cloud signal decay initiates in those regions, due to higher oxidation rates, and disappears latest in the central bowl regions. These primary stages are summarized in Figure 8.4 for a typical PIDING combustion event.

The relative timing between NG injection pulse and the peak HRR, and P_{inj} , showed strong influence in the rate and extent of soot formation and peak concentration levels. Fuel injection timings that led to an end-of-injection of NG prior to the peak HRR resulted in predominantly partially-premixed fuel conversion with lower KL and smaller soot cloud, while with increased injection durations continuing after the peak HRR, fuel conversion was more mixing-rate limited and resulted in higher soot formation and peak concentration levels and extended growth and late-cycle signal.

8.1.4 Thermo-Optical Analysis Tool-Kit

With the developed imaging diagnostics, the final chapter focused on characterizing the signal from optical probe based 0D measurements. The rugged probe design affords optical measurements from all-metal engine configurations and could be used to extend the findings of 2D measurements to 0D optical measurements from an all-metal engine under higher loads. These operating conditions would be more relevant to real-world on-road operating conditions.

Comparisons between 2D and 0D two-color pyrometry measurements were

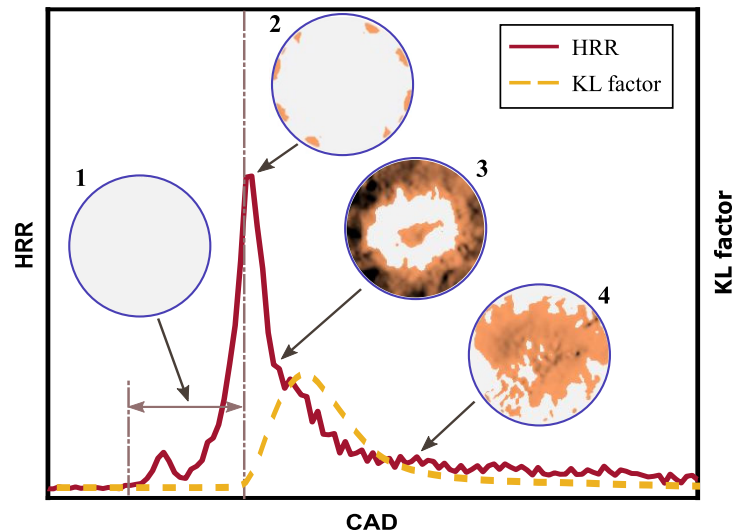


Figure 8.4: The four principal stages of soot processes during a typical PID-ING combustion event: 1-pilot combustion and NG ignition, 2-partially-premixed NG combustion and soot formation, 3-soot cloud growth, and 4-oxidation; The illustration is based on the baseline operating condition (see Table 6.1) and images show KL distribution at select crank positions.

made under optical engine configuration in order to better understand and interpret the 0D results. A novel weighted spatially averaging (WSA) technique for the 2D measurements was introduced to account for field-of-view (FOV) geometry differences between the two measurement approaches. The 0D and WSA results showed reasonable agreement and explained some of the discrepancies between the 0D and mean 2D results. Figure 8.5 illustrates these comparisons for select operating conditions along with the weighted spatially averaging mask for a sample crank position. 0D pyrometry temperature estimates before peak soot concentration are higher in response to the light collection more heavily from regions closer to the walls where higher concentration of high temperature reactions was evident in 2D measurements. The indication of onset of soot processes is also slightly delayed in 0D measurements; As illustrated by the 2D results, detectable soot signal is formed at the proximity of the wall and outside probe FOV, and the delay is in response to the soot cloud growth until signal reaches probe FOV. Furthermore, KL values in

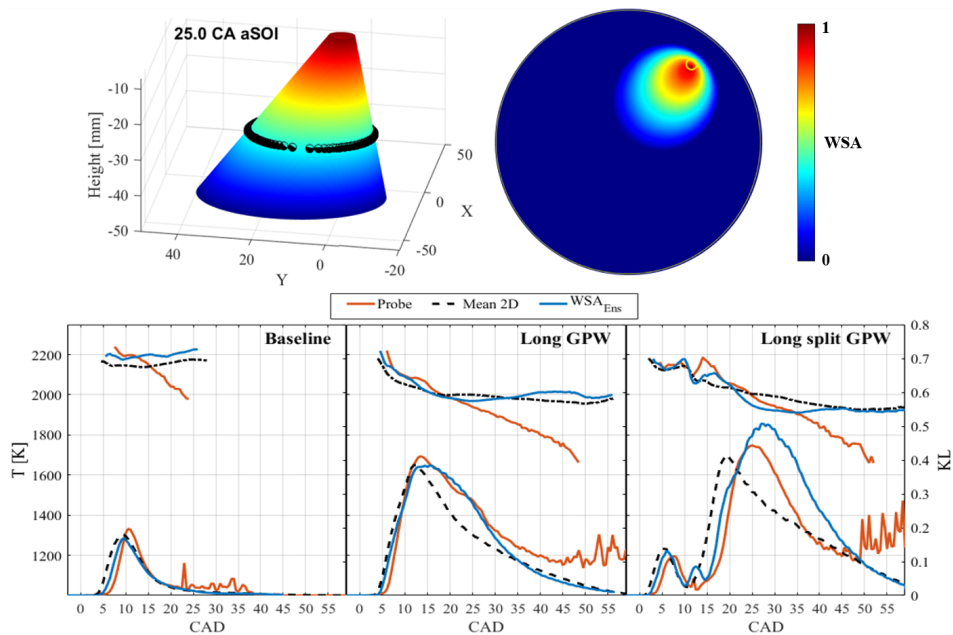


Figure 8.5: WSA mask at 25 CAD aTDC (top) and comparison of the WSA 2D and 0D optical measurements for select operating points (bottom, see Table 7.1); The surrounding ring on the WSA cone depicts the intersection with the quartz window surface at this crank position.

0D measurements are higher after the peak KL in response to transition of the high concentration soot cloud towards the center due to reflected momentum of NG jets after impingement on the walls. The consistent decay in 0D temperatures and deviation from WSA results was partially explained by soot cloud movement and soot leaving probe FOV, as well as the decreasing gas temperature due to downward piston motion. However, further investigation of this phenomenon was deemed necessary to provide a more clear understanding.

0D pyrometry measurements were carried out under thermodynamic and optical engine configurations in order to evaluate the effects of the two inherently different combustion environments and assess the extensibility of the 2D measurements findings to in-cylinder processes of a thermodynamic engine. 0D pyrometry measurements of similar operating conditions in the all-metal engine showed similar temperature and soot concentration trends to those from optical engine. As such,

these results led to similar conclusions regarding soot in-cylinder processes, despite the influences from geometric and operational differences, namely the higher compression ratio, toroidal bowl geometry, and continuous firing. Higher compression ratios and continuous firing led to higher pyrometry temperatures in thermodynamic engine and an earlier onset of soot processes in response to advanced peak HRR due to the shorter ignition delays. Slightly lower peak HRR and higher peak soot concentrations were obtained due to lower partially-premixed fraction, although higher temperatures and toroidal bowl geometry, led to signs of enhanced late-cycle soot oxidation, which resulted in similar soot concentration signal.

8.1.5 Concluding Remarks

Summaries of the major results from different chapters of this work was presented above. To summarize the work as whole, the principal novel contributions can be listed as follows:

1. Enhancement of the two-color pyrometry technique to extend its applicability for modern cleaner combustion strategies with less naturally emitted PM signal.
2. Present a conceptual understanding of the in-cylinder soot formation and oxidation processes during a standard PIDING combustion event and elucidate the influence of fueling control parameters on PIDING in-cylinder processes.
3. Characterization of OD signal from an optical probe design, in accordance with the detailed information provided in a 2D optical measurements, to extend optical results interpretations to more-representative higher load operating conditions in all-metal engines.

With the provided insight into in-cylinder fuel conversion and soot formation and oxidation processes and better characterization of the OD measurements, the current study sets the groundwork for extensive investigation of combustion in-cylinder processes under more realistic higher load operating conditions of DIDF and PIDING combustion strategies. The analysis methods and introduced metrics, however, are not restricted to NG combustion and can be implemented in assessment of other combustion scenarios.

Further characterization of the optical probe signal could be possible through additional investigations and analyses discussed in the next section, which would complete the set of tools for characterization of in-cylinder processes relevant to cleaner combustion strategies. The characterized optical probe measurements, in conjunction with HRR results and engine boundary conditions and exhaust emission measurements, would constitute a valuable and effective “Thermo-Optical” analysis toolkit to provide more insight into combustion in-cylinder processes and optimize the operating protocols and future designs of the combustion strategy under investigation. As such, the modern cleaner CI combustion strategies could conform to ever-increasing stringent emission regulations, while maintaining high performance and efficiencies resembling those of their diesel engine ancestors.

8.2 Future Work

In addition to the provided insight into in-cylinder combustion phenomena, the investigation results presented in this work also identified several areas potentially worthwhile to further investigate.

8.2.1 2D optical DIFD combustion analysis

Optical investigation of the fueling control parameter effects in DIFD combustion demonstrated potential to significantly affect fuel conversion processes and motivated more extensive assessment of such effects on known DIFD combustion drawbacks. Simultaneous 2D OH* chemiluminescence and natural luminosity measurements of DIFD combustion identified areas of localized high intensity natural luminosity without overlapping high intensity OH* chemiluminescence signal, for higher diesel pilot fraction in the charge or at lower pilot injection pressures. Although engine-out soot emissions of DIFD combustion is generally not significant, pyrometric imaging measurements of such operating conditions could provide a better understanding of the influence of these key fueling control parameters on in-cylinder processes and is not reported in literature.

8.2.2 2D optical PIDING combustion analysis

Study of soot formation and oxidation processes during PIDING combustion over a range of operating conditions identified several characteristic behaviors. Investigation of the NG injection duration effects suggested that a shorter NG injection duration and end-of-injection (EOI) before the peak HRR, leads to a predominantly partially-premixed combustion, with a lower peak HRR and soot signal level, which remains concentrated at wall. Increasing the injection duration, past the peak HRR crank position, increased the peak HRR and the normalized net soot formation rates to a point, beyond which both these metrics remained constant. It would be interesting to investigate the hypothesis that a “maximum partial-premixedness” metric at a certain injection pressure and start-of-injection timings could be considered, after which the same soot formation mechanisms, with the same normalized rates, are only extended to reach higher concentration peaks.

Investigating the fuel injection pressure effects also showed a higher soot concentration peak at higher injection pressure, which was attributed to higher mass flow rate and richer charge mixture around NG jet axes, and traces of enhanced late-cycle soot oxidation relative to the baseline operating condition was not observed. However, the tested higher fuel injection pressure operating condition also led to a higher engine load with a slightly different combustion phasing. Measurements from more closely relevant “high injection pressure” cases would be necessary to optically investigate the in-cylinder soot processes leading to the previously demonstrated soot emission advantages of operating under higher injection pressures.

As part of the analyses for PIDING soot processes characterization in this work, a basic image thresholding approach was implemented for tracking high concentration soot pockets to illustrate NG jet reflection and soot cloud advection effects. A properly developed image feature tracking algorithm, similar to combustion image velocimetry [27], could be applied to the provided higher spatial and temporal resolution two-color pyrometry results so as to provide a quantitative metric for soot cloud dynamics within the combustion chamber.

Correlations between temporal evolution of the soot cloud and OH* chemiluminescence signal depicts OH* signal attenuation by the growing soot cloud.

Knowing the spatial distribution of the soot concentration parameter (KL factor) and making simplifying assumptions to the radiative transfer equation 7.1, the feasibility of correcting the OH^* signal could be assessed. If possible to achieve, the result of this analysis would extend the crank position range for which the comparison of relative OH^* signal magnitudes could be practical.

8.2.3 Exhaust Gas recirculation (EGR)

A commonly used approach for additional control on pollutant emissions from CI engines is intake charge dilution through implementing EGR [72, 100]. Application of EGR on PENDING combustion, for instance, reduced the NO_x emissions, albeit at the cost of increased hydrocarbons, CO, and PM emissions at higher EGR levels. Nevertheless, manipulation of fueling control parameters was shown to be able to mitigate these side effects [100]. In addition to engine-out PM, reintroducing exhaust gases and oxygen dilution, and the consequent lower in-cylinder temperatures, are expected to significantly affect in-cylinder soot processes. The engine facility used in the current work, similar to most other optical engines, did not allow EGR. Further development of the engine facility to implement EGR in the thermodynamic and optical engine configurations would be useful to characterize the imposed modifications to the in-cylinder processes. Under the optical engine configuration, introducing a simulated EGR mixture of CO_2 and N_2 is a common approach to mimic the EGR effects in all-metal engines [54]. However, it has also been shown that the simulated EGR gas composition, in particular fraction of the major species, i.e., N_2 , CO_2 , H_2O , CO and uHC, could influence in-cylinder processes [23]. Considering the complexities associated with imaging diagnostics of EGR effects, optical probe pyrometric and chemiluminescence measurements (using the third fibre-optic channel) would be particularly valuable to provide more insight into the altered in-cylinder processes.

8.2.4 Optical probe OD signal characterization

As discussed in Chapter 7, several measures can be considered towards an improved interpretation of the OD signal provided by the optical probe. In this work, the two-color pyrometry results obtained from OD optical probe measurements

were in part characterized through simultaneous 2D and 0D measurements using the optical engine configuration and application of a FOV based weighted averaging function (WSA). The proposed averaging method, however, poses caveats as it assumes a homogeneous soot cloud. As such, the pyrometric temperature decay in 0D probe measurements could not be explained by the proposed approach. Several investigative paths could be considered for further exploration of the 0D optical probe signal behavior, such as computational fluid dynamic and Monte Carlo simulations, or adding a third 0D pyrometry signal channel.

Reactive computational fluid dynamics (CFD) simulations of the in-cylinder combustion phenomena is a valuable characterization tool which has demonstrated its utility in numerous studies [54, 90, 114]. The estimated three-dimensional distributions of various species and their properties, including PM and temperature values, could be used to fill the gap of the lost information due to the line-of-sight (LOS) nature of the two-color pyrometry measurements. After introducing assumptions for optical properties of the soot particle distribution, the vertical projection of the calculated cell spectral incandescence signals on the quartz window could be estimated. Comparison of the projected intensity distribution to those of the 2D optical measurements could be used to assess the LOS effects and improve the correlation between 2D and 0D measurements for better understanding of the optical probe signal.

Alternatively, as a higher fidelity investigation approach, 3D Monte Carlo ray tracing simulations based on the reactive CFD results could be considered. To perform those simulations, instantaneous gaseous flame and PM distributions from numerical simulations and modelled geometry of combustion chamber at the corresponding crank position are used as inputs to the Monte Carlo simulation algorithm for the 3D participating medium. Rays of particle emission intensities are then tracked while undergoing repeated absorption, transmission, reflection, scattering and re-emission in interaction with suspended particles and the boundaries. The simulated light collection from modelled “camera views” for the probe conical FOV and quartz window would then provide a metric for comparison of the recorded signal through the two measurement systems.

From an experimental two-color pyrometry measurement standpoint, 0D optical measurements within a narrow spectral pass-band around a third wavelength

could be considered. Introducing the third signal channel could potentially help further characterization of the OD signal in comparison of the results acquired from three separate pairs of spectral radiant intensities. Specifically, it would be interesting to assess the feasibility of isolating the effects of signal escaping probe FOV vs. high uncertainly late cycle signal, given different wavelength sensitivities towards low SNR signal. Once the optical probe signal behavior understanding is improved through these comparisons, the third optical probe channel can be used for OD OH* or CH* chemiluminescence measurements as an additional investigative metric for in-cylinder processes within thermodynamic engine configuration.

In comparison of the OD two-color pyrometry measurements from thermodynamic and optical engines, certain differences in the results could be attributed to the more optimized toroidal piston crown geometry in the thermodynamic engine. As an example, a lower soot concentration peak was obtained at a lower fuel injection pressures for PIDING combustion, which suggested enhanced mixing with better guided NG jets, preventing accumulation of high concentration soot cloud at the proximity of the bowl walls. This could be addressed through substituting the flat quartz window for a toroidal shaped one. This more representative window geometry introduces complexities for analysis and interpretation of 2D results and necessitates additional image-preprocessing stages, e.g., ray-tracing algorithms [79], to correct for image distortion due to curved window surfaces. Nevertheless, OD probe measurements would not encounter these challenges and the more representative geometry affords closer comparison of the thermodynamic and optical engine results.

8.2.5 Linking in-cylinder to engine-out soot measurements

The ultimate goal of the research and development efforts on combustion diagnostics is reducing engine-out emissions while maintaining or improving thermal and fuel efficiencies. Application of the developed tools in this work was only focused on understanding the primary in-cylinder soot formation and oxidation processes of PIDING combustion in an optical engine, as well as characterizing the optical probe signal for further investigation of those processes under more realistic operating conditions in all-metal engines. Hence, the imaging system settings were

optimized to capture spatially resolved and integrated signals throughout a combustion event with high SNR, while avoiding sensor saturation. Given the limited dynamic range of these sensors, lower incandescence and chemiluminescence signals during the late-cycle oxidation stage was inevitably lost to low SNRs. Dedicated optical measurements focusing at late-cycle soot oxidation events would be necessary in order to make the link to engine-out soot emissions.

In addition to the conventional, cycle cumulative, engine-out soot measurement apparatus, a Fast Exhaust Nephelometer design is being developed within the group [73], which affords cycle resolved exhaust stream soot measurements. Correlating dedicated pyrometric measurements of the late-cycle in-cylinder events to engine-out soot measurements, on a cycle-by-cycle level, isolating the corresponding variability effects, could be substantial in providing insight into soot emission characteristics of different combustion strategies working under various operating conditions.

Bibliography

- [1] V. Aesoy and H. Valland. Hot surface assisted compression ignition of natural gas in a direct injection diesel engine. *SAE*, (960767), 1996. → page 7
- [2] E. E. Agency. Air pollution statistics: Emissions of air pollutants, eu-28, 1990-2016, 2017. → page 11
- [3] P. Aleiferis, Y. Hardalupas, A. Taylor, K. Ishii, and Y. Urata. Flame chemiluminescence studies of cyclic combustion variations and air-to-fuel ratio of the reacting mixture in a lean-burn stratified-charge spark-ignition engine. *Combustion and Flame*, 136:72–90, 2004. → pages 22, 25
- [4] C. Arcoumanis, P. Cutter, D. Whitelaw, and B. Flannery. Heat Transfer Processes in Diesel Engines. *Chemical Engineering Research and Design*, 76(2):124–132, 1998. → page 30
- [5] U. Aronsson, C. Chartier, U. Horn, O. Andersson, B. Johansson, and R. Egnell. Heat release comparison between optical and all-metal hsd diesel engines. *SAE*, (2008-01-1062), 2008. → pages 18, 19, 46, 180
- [6] B. Ayoola, R. Balachandran, J. Frankc, E. Mastorakos, and C. Kaminski. Spatially resolved heat release rate measurements in turbulent premixed flames. *Combustion and Flame*, 144:1–16, 2006. → pages 22, 23, 24, 25
- [7] O. Badr, G. Karim, and B. Liu. An examination of the flame spread limits in a dual fuel engine. *Applied Thermal Engineering*, 19(10):1071 – 1080, 1999. → page 37
- [8] H. Baker and E. Ryder. *Temperature Measurement in Engineering*. John Wiley, New York, 1961. → page 30
- [9] J. Ballester and T. García-Armingol. Diagnostic techniques for the monitoring and control of practical flames. *Progress in Energy and Combustion Science*, 36(4):375 – 411, 2010. → pages 22, 23, 25

- [10] C. R. F. Barbosa, M. R. da Silva, and S. W. Celere. The performance of an otto cycle bi-fuel engine with natural gas direct injection. *SAE*, (962381), 1996. → page 7
- [11] M. Bell, D. Davis, and T. Fletcher. A retrospective assessment of mortality from the london smog episode of 1952: the role of influenza and pollution. *Environmental Health Perspectives*, 112:6–8, 2004. → page 8
- [12] D. Bertsch. *Experimentelle Untersuchungen zum Einfluß gemischbildungsseitiger Maßnahmen auf den Zündprozeß, Verbrennung und Schadstoffbildung an einem optisch zugänglichen DE-Dieselmotor*. Phd dissertation, University of Karlsruhe, 1999. → page 24
- [13] N. J. Birger and S. N. Rogak. Flow characteristics of a gas-blast fuel injector for direct-injection compression-ignition engines. *SAE*, (2009-01-1857), 2009. → page 7
- [14] M. K. Bobba, C. L. Genzale, and M. P. B. Musculus. Effect of ignition delay on in-cylinder soot characteristics of a heavy duty diesel engine operating at low temperature conditions. *SAE International Journal of Engines*, 2(1):911–924, 2009. → pages 35, 144
- [15] M. A. Boumehdi, S. A. Stepanyan, P. Desgroux, G. Vanhove, and S. M. Starikovskaia. Ignition of methane- and n-butane-containing mixtures at high pressures by pulsed nanosecond discharge. *Combustion and Flame*, 162(4):1336 – 1349, 2015. → page 7
- [16] F. W. Bowditch. A new tool for combustion research a quartz piston engine. *SAE*, (610002), 1961. → pages 16, 18
- [17] R. P. Brent. *Algorithms for Function Minimization without Derivatives*. Prentice-Hall, Englewood Cliffs, NJ, 1973. → page 95
- [18] A. P. Carlucci, D. Laforgia, R. Saracino, and G. Toto. Study of combustion development in methane-diesel dual fuel engines, based on the analysis of in-cylinder luminance. *SAE*, (2010-01-1297), 2010. → pages 18, 38, 82
- [19] F. Catapano, S. Di Iorio, P. Sementa, and B. M. Vaglieco. Characterization of ch₄ and ch₄/h₂ mixtures combustion in a small displacement optical engine. *SAE International Journal of Fuels and Lubricants*, 6(1):24–33, 2013. → pages 7, 22, 23, 24, 25
- [20] Y. Cengel and M. Boles. *Thermodynamics: An Engineering Approach*. McGraw-Hill, Boston, 6th ed. edition, 2001. → page 5

- [21] H. M. Cho and B. Q. He. Combustion and emission characteristics of a lean burn natural gas engine. *International Journal of Automotive Technology*, 9(4):415–422, 2008. → page 7
- [22] J. Chong, A. Tsolakis, S. Gill, K. Theinnoi, and S. Golunski. Enhancing the no₂/nox ratio in compression ignition engines by hydrogen and reformat combustion, for improved aftertreatment performance. *International Journal of Hydrogen Energy*, 35(16):8723 – 8732, 2010. → page 9
- [23] W. F. Colban, D. Kim, P. C. Miles, S. Oh, R. Opat, R. Krieger, D. E. Foster, R. P. Durrett, A. Manuel, and D. Gonzalez. A detailed comparison of emissions and combustion performance between optical and metal single-cylinder diesel engines at low temperature combustion conditions. *SAE International Journal of Engines*, pages 1–15, 2008. → pages 46, 194
- [24] J. E. Dec. A Conceptual Model of DI Diesel Combustion Based on Laser-Sheet Imaging. *SAE*, (970873), 1997. → pages 111, 158
- [25] J. E. Dec and C. Espey. Chemiluminescence Imaging of Autoignition in a DI Diesel Engine. *SAE*, (982685), 1998. → pages 24, 118
- [26] T. J. Dekker. Finding a Zero by Means of Successive Linear Interpolation. In B. Dejon and P. Henrici, editors, *Constructive Aspects of the Fundamental Theorem of Algebra*. Wiley-Interscience, London, 1969. → page 95
- [27] H. Dembinski. *In-cylinder Flow Characterisation of Heavy Duty Diesel Engines Using Combustion Image Velocimetry*. Phd dissertation, KTH Royal Institute of Technology, 2013. → pages 19, 193
- [28] J. M. Densmore, M. M. Biss, K. L. McNesby, and B. E. Homan. High-speed digital color imaging pyrometry. *Appl. Opt.*, 50(17): 2659–2665, 2011. → page 102
- [29] S. Di Iorio, P. Sementa, and B. M. Vaglieco. Experimental Investigation of a Methane-Gasoline Dual-Fuel Combustion in a Small Displacement Optical Engine. *SAE*, (2013-24-0046), 2013. → pages 20, 21, 23, 31
- [30] S. di Stasio and P. Massoli. Influence of the Soot Property Uncertainties in Temperature and Volume-Fraction Measurements by Two-Colour Pyrometry. *Measurement Science and Technology*, 5(12):1453–1465, 1999. → page 31

- [31] D. Dockery, C. r. Pope, X. Xu, J. Spengler, J. Ware, M. Fay, B. Ferris, and F. Speizer. An association between air pollution and mortality in six u.s. cities. *New England Journal of Medicie*, 329(24):1753 – 1759, 1993. → page 10
- [32] Y. Dong, C. M. Vagelopoulos, G. R. Spedding, and F. N. Egoalpoulos. Measurement of laminar flame speeds through digital particle image velocimetry: Mixtures of methane and ethane with hydrogen, oxygen, nitrogen, and helium. *Proceedings of the Combustion Institute*, 29(2):1419 – 1426, 2002. → page 39
- [33] N. Dronniou, J. Kashdan, B. Lecointe, K. Sauve, and D. Soleri. Optical investigation of dual-fuel cng/diesel combustion strategies to reduce co2 emissions. *SAE International Journal of Engines*, 7(2):873–887, 2014. → pages 38, 39, 40, 44, 74, 80, 90
- [34] S. Dumitrescu, P. G. Hill, G. Li, and P. Ouellette. Effects of injection changes on efficiency and emissions of a diesel engine fueled by direct injection of natural gas. *SAE*, (2000-01-1805), 2000. → pages 41, 42, 43, 139, 149, 152, 182
- [35] N. Englert. Fine particles and human health—a review of epidemiological studies. *Toxicology Letters*, 149(1):235 – 242, 2004. Proceedings of EUROTOX 2003. The XLI European Congress of Toxicology. Science for Safety. → pages 6, 10
- [36] J. F. Epperson. *An Introduction to Numerical Methods and Analysis*. John Wiley & Sons, Inc., Hoboken, New Jersey, 2nd editio edition, 2013. → page 95
- [37] E. Faghani, P. Kirchen, and S. N. Rogak. Application of Fuel Momentum Measurement Device for Direct Injection Natural Gas Engines. *SAE*, (2015-01-0915), 2015. → pages 120, 220
- [38] E. Faghani, P. Kheirkhah, C. W. Mabson, G. McTaggart-Cowan, P. Kirchen, and S. Rogak. Effect of Injection Strategies on Emissions from a Pilot-Ignited Direct-Injection Natural-Gas Engine- Part II: Slightly Premixed Combustion. *SAE*, (2017-01-0763), 2017. → pages 41, 100
- [39] E. Faghani, P. Kheirkhah, C. W. Mabson, G. McTaggart-Cowan, P. Kirchen, and S. Rogak. Effect of injection strategies on emissions from a pilot-ignited direct-injection natural-gas engine- part i: Late post injection. *SAE*, (2017-01-0774):1–16, 2017. → pages 168, 169

- [40] T. H. Fereja, A. Hymete, and T. Gunasekaran. A Recent Review on Chemiluminescence Reaction, Principle and Application on Pharmaceutical Analysis. *ISRN Spectroscopy*, pages 1–12, 2013. → page 22
- [41] C. Ferguson, D. Tree, D. DeWitt, and S. Wahiduzzaman. Design, Calibration and Error Analysis of Instruments for Heat Transfer Measurements in Internal Combustion Engines. *ASME reprint from developments in experimental techniques*, 71, 1987. → pages 28, 32
- [42] R.-C. Florea. *Optical Ethanol and n-heptane Dual-Fuel Partially Premixed Combustion in a Reciprocating Engine*. PhD thesis, Wayne State University, 2012. → page 40
- [43] O. for Economic Co-Operation and D. (OECD). Strategies to reduce greenhouse gas emissions from road transport: analytical methods, 2002. → page 10
- [44] P. Forster, V. Ramaswamy, P. Artaxo, T. Berntsen, R. Betts, D. Fahey, J. Haywood, J. Lean, D. Lowe, G. Myhre, J. Nganga, R. Prinn, G. Raga, M. Schulz, and R. V. Dorland. *Changes in Atmospheric Constituents and in Radiative Forcing. Climate Change 2007*, chapter 1.2. Cambridge University Press, 2008. → page 37
- [45] N. L. Garland and D. R. Crosley. On the collisional quenching of electronically excited oh, nh and ch in flames. *Symposium (International) on Combustion*, 21(1):1693 – 1702, 1988. Twenty-First Symposium (International on Combustion). → page 24
- [46] A. Gaydon. *The Spectroscopy of Flames*. Chapman and Hall, London, 2nd ed. edition, 1974. → pages 20, 22, 23, 24, 25
- [47] A. Gaydon and H. Wolfhard. *Flames, Their Structure, Radiation and Temperature*. Chapman and Hall, London, 1978. → page 22
- [48] B. Grandin, I. Denbratt, J. Bood, C. Brackmann, and P.-E. Bengtsson. The effect of knock on the heat transfer in an si engine: Thermal boundary layer investigation using cars temperature measurements and heat flux measurements. *SAE*, (2000-01-2831), 2000. → page 4
- [49] B. Group. Statistical review of world energy, 2018. → page 6

- [50] S. B. Gupta, B. P. Bihari, M. S. Biruduganti, R. R. Sekar, and J. Zigan. On use of CO_2^* chemiluminescence for combustion metrics in natural gas fired reciprocating engines. *Proceedings of the Combustion Institute*, 33(2):3131 – 3139, 2011. → pages 3, 22
- [51] D. Guyot, F. Guethe, B. Schuermans, A. Lacarelle, and C. Paschereit. CH^*/OH^* chemiluminescence response of an atmospheric premixed flame under varying operating conditions. In *ASME Turbo Expo 2010: Power for Land, Sea, and Air*, Glasgow, UK, 2010. Volume 2: Combustion, Fuels and Emissions, Parts A and B. → page 22
- [52] Y. Han, K. Lee, and K. Min. A study on the measurement of temperature and soot in a constant-volume chamber and a visualized diesel engine using the two-color method. *Journal of Mechanical Science and Technology*, 23(11):3114–3123, 2010. → pages 30, 57, 58
- [53] Y. Hardalupas and M. Orain. Local measurements of the time-dependent heat release rate and equivalence ratio using chemiluminescent emission from a flame. *Combustion and Flame*, 139:188–207, 2004. → pages 22, 23, 25
- [54] A. Hatzipanagiotou, F. Marko, G. Koenig, C. Krueger, P. Wenzel, and T. Koch. Numerical and optical analysis of heterogeneous gas combustion with diesel pilot ignition in a commercial vehicle engine. *International Journal of Engine Research*, 19(1):109–119, 2018. → pages 21, 41, 42, 45, 111, 124, 136, 142, 176, 194, 195
- [55] B. Higgins, M. McQuay, F. Lacas, J. Rolon, N. Darabiha, and S. Candel. Systematic measurements of OH chemiluminescence for fuel-lean, high-pressure, premixed, laminar flames. *Fuel*, 80(1):67 – 74, 2001. → page 25
- [56] S. K. Hoekman and C. Robbins. Review of the effects of biodiesel on NO_x emissions. *Fuel Processing Technology*, 96:237 – 249, 2012. → pages 9, 10
- [57] H. G. Hottel and F. P. Broughton. Determination of True Temperature and Total Radiation from Luminous Gas Flames. *Ind. Eng. Chem. Anal.*, 4(2): 166–175, 1932. → page 28
- [58] J. Howell, R. Siegel, and P. Menguc. *Thermal Radiation Heat Transfer*. CRC Press, Taylor and Francis, Boca Raton, 5th ed. edition, 2010. → page 167

- [59] Q. Huang, F. Wang, J. Yan, and Y. Chi. Simultaneous estimation of the 3-d soot temperature and volume fraction distributions in asymmetric flames using high-speed stereoscopic images. *Appl. Opt.*, 51(15):2968–2978, 2012. → page 102
- [60] E. Huestis, P. A. Erickson, and M. P. B. Musculus. In-cylinder and exhaust soot in low-temperature combustion using a wide-range of egr in a heavy-duty diesel engine. *SAE*, (2007-01-4017), 2007. → page 35
- [61] Y. Ikeda, J. Kojima, T. Nakajima, F. Akamatsu, and M. Katsuki. Measurement of the local flamefront structure of turbulent premixed flames by local chemiluminescence. *Proceedings of the Combustion Institute*, 28(1):343 – 350, 2000. → pages 22, 23
- [62] T. Ito and T. Kitamura. Effects of Flame Lift-Off and Flame Temperature on Soot Formation in Oxygenated Fuel Sprays. *SAE*, (2003-01-0073), 2003. → pages 16, 30, 108
- [63] M. Jakob, T. Hülser, A. Janssen, P. Adomeit, S. Pischinger, and G. Grünefeld. Simultaneous high-speed visualization of soot luminosity and oh* chemiluminescence of alternative-fuel combustion in a hsd diesel engine under realistic operating conditions. *Combustion and Flame*, 159(7):2516 – 2529, 2012. → page 25
- [64] M. Jakob, P. Lehnen, P. Adomeit, and S. Pischinger. Development and Application of a Stereoscopic 3-Color High-Speed Ratio-Pyrometry. *Combustion and Flame*, 161(11):2825–2841, 2014. → pages 30, 57, 58, 102
- [65] W. Jing, W. Roberts, and T. Fang. Comparison of Soot Formation For Diesel and Jet-A in a Constant Volume Combustion Chamber Using Two-Color Pyrometry. *SAE*, (2014-01-1251), 2014. → page 30
- [66] R. Johnson. The structure and origin of the swan band spectrum of carbon. *Philosophical Transactions of the Royal Society A*, 226:157–230, 1927. → pages 3, 23
- [67] T. Kamimoto and Y. Murayama. Re-examination of the emissivity of diesel flames. *International Journal of Engine Research*, 12(6):580–600, 2011. → page 28
- [68] T. Kamimoto, N. Uchida, T. Aizawa, K. Kondo, and T. Kuboyama. Diesel flame imaging and quantitative analysis of in-cylinder soot oxidation.

International Journal of Engine Research, 18(5-6):422–435, 2017. →
pages 31, 33, 35, 36

- [69] G. Karim. Combustion in gas fueled compression: Ignition engines of the dual fuel type. *Journal of Engineering for Gas Turbines and Power*, 125(3):827–836, 2003. → pages 37, 43, 83, 88, 90
- [70] G. A. Karim and I. Wierzba. Comparative studies of methane and propane as fuels for spark ignition and compression ignition engines. *SAE*, (831196):676–688, 1983. → page 7
- [71] S. Karnani and D. Dunn-Rankin. Visualizing ch^* chemiluminescence in sooting flames. *Combustion and Flame*, 160(10):2275 – 2278, 2013. → page 25
- [72] J. T. Kashdan and B. Thirouard. A comparison of combustion and emissions behaviour in optical and metal single-cylinder diesel engines. *SAE International Journal of Engines*, 2(1):1857–1872, 2009. → pages 18, 19, 46, 194
- [73] P. Kheirkhah, P. Kirchen, and S. Rogak. Fast exhaust nephelometer (fen): A new instrument for measuring cycle-resolved engine particulate emission. *SAE*, (2016-01-2329), 2016. → page 197
- [74] M. Khosravi and P. Kirchen. Refinement of the Two-Color Method for Application in a Direct Injection Diesel and Natural Gas Compression Ignition Engine. *Proc IMechE Part D: J Automobile Engineering*, 2019. → page 161
- [75] M. Khosravi, J. Rochussen, J. Yeo, P. Kirchen, G. McTaggart-Cowan, and N. Wu. Effect of Fuelling Control Parameters on Combustion Characteristics of Diesel-Ignited Natural Gas Dual-Fuel Combustion in an Optical Engine. In *ASME 2016 Internal Combustion Engine Fall Technical Conference, ICEF 2016*, Greenville, SC, 2016. → pages 21, 40, 73
- [76] P. Kirchen, P. Obrecht, K. Boulouchos, and A. Bertola. Exhaust-stream and in-cylinder measurements and analysis of the soot emissions from a common rail diesel engine using two fuels. *ASME. J. Eng. Gas Turbines Power*, 132(11):1128041–1128048, 2010. → page 112
- [77] J. Kojima, Y. Ikeda, and T. Nakajima. Spatially resolved measurement of oh^* , ch^* , and c2^* chemiluminescence in the reaction zone of laminar methane/air premixed flames. *Proceedings of the Combustion Institute*, 28(2):1757 – 1764, 2000. → pages 23, 25

- [78] H. Kosaka, T. Aizawa, and T. Kamimoto. Two-Dimensional Imaging of Ignition and Soot Formation Processes in a Diesel Flame. *International Journal of Engine Research*, 6(1):21–42, 2005. → page 27
- [79] K. Koyanagi, H. Öing, G. Renner, and R. Maly. Optimizing common rail-injection by optical diagnostics in a transparent production type diesel engine. *SAE*, (1999-01-3646), 1999. → pages 24, 46, 196
- [80] J. Kubesh and D. D. Brehob. Analysis of knock in a dual-fuel engine. *SAE*, (922367), 1992. → pages 7, 40
- [81] N. Ladommatos and H. Zhao. A Guide to Measurement of Flame Temperature and Soot Concentration in Diesel Engines Using the Two-Colour Method Part I: Principles. *SAE*, (941956), 1994. → page 31
- [82] P. J. Langhorne. Reheat buzz: an acoustically coupled combustion instability. part 1. experiment. *Journal of Fluid Mechanics*, 193:417–443, 1988. → page 23
- [83] A. Larsson. Optical Studies in a DI Diesel Engine. *SAE*, (1999-01-3650), 1999. → page 30
- [84] J. Lee, H. Oh, and C. Bae. Combustion process of jp-8 and fossil diesel fuel in a heavy duty diesel engine using two-color thermometry. *Fuel*, 102: 264 – 273, 2012. Special Section: ACS Clean Coal. → page 159
- [85] J. G. Lee, K. Kim, and D. Santavicca. Measurement of equivalence ratio fluctuation and its effect on heat release during unstable combustion. *Proceedings of the Combustion Institute*, 28(1):415 – 421, 2000. → page 22
- [86] T. Lee, J. Park, S. Kwon, J. Lee, and J. Kim. Variability in operation-based nox emission factors with different test routes, and its effects on the real-driving emissions of light diesel vehicles. *Science of the Total Environment*, 461-462:377 – 385, 2013. → page 9
- [87] W. Lee, C. E. Solbrig, T. A. Litzinger, and R. J. Santoro. Planar laser light scattering for the in-cylinder study of soot in a diesel engine. *SAE*, (902125), 1990. → page 26
- [88] C. A. Leermakers and M. P. Musculus. In-Cylinder Soot Precursor Growth in a Low-Temperature Combustion Diesel Engine: Laser-Induced Fluorescence of Polycyclic Aromatic Hydrocarbons. *Proceedings of the Combustion Institute*, 35(3):3079–3086, 2015. → pages 26, 27, 124

- [89] M. D. Leo, A. Saveliev, L. A. Kennedy, and S. A. Zelepouga. Oh and ch luminescence in opposed flow methane oxy-flames. *Combustion and Flame*, 149(4):435 – 447, 2007. → page 23
- [90] G. Li, P. Ouellette, S. Dumitrescu, and P. G. Hill. Optimization study of pilot-ignited natural gas direct-injection in diesel engines. *SAE*, (1999-01-3556), 1999. → pages 41, 124, 195
- [91] Z. Liu and G. A. Karim. The ignition delay period in dual fuel engines. *SAE*, (950466), 1995. → page 43
- [92] H. Ma, R. Stevens, and R. Stone. In-Cylinder Temperature Estimation from an Optical Spray-Guided DISI Engine with Color-Ratio Pyrometry (CRP). *SAE*, (2006-01-1198), 2006. → pages 30, 31, 34, 57, 58
- [93] E. Mancaruso and B. M. Vaglieco. Uv-visible spectroscopic measurements of dual-fuel pcci engine. *SAE International Journal of Fuels and Lubricants*, 4(2):271–281, 2011. → pages 40, 81
- [94] E. Mancaruso, B. Vaglieco, and C. Ciaravino. Combustion Analysis in an Optical Diesel Engine Operating with Low Compression Ratio and Biodiesel Fuels. *SAE*, (2010-01-0865), 2010. → pages 24, 118, 159
- [95] Y. Matsui, T. Kamimoto, and S. Matsuoka. A Study on the Time and Space Resolved Measurement of Flame Temperature and Soot Concentration in a D. I. Diesel Engine by the Two-Color Method. *SAE*, (790491), 1979. → page 31
- [96] Y. Matsui, T. Kamimoto, and S. Matsuoka. A Study on the Application of the Two-Color Method to the Measurement of Flame Temperature and Soot Concentration in Diesel Engines, 1980. → pages 28, 30, 31, 180
- [97] G. McTaggart-Cowan. *Pollutant formation in a gaseous-fuelled, direct injection engine*. Phd dissertation, University of British Columbia, 2006. → pages 6, 9, 10, 41
- [98] G. McTaggart-Cowan, K. Mann, J. Huang, A. Singh, B. Patychuk, Z. X. Zheng, and S. Munshi. Direct injection of natural gas at up to 600 bar in a pilot-ignited heavy-duty engine. *SAE International Journal of Engines*, 8(3):981–996, 2015. → pages 41, 42, 139, 149, 182
- [99] G. P. McTaggart-Cowan, W. K. Bushe, S. N. Rogak, P. G. Hill, and S. R. Munshi. Injection Parameter Effects on a Direct Injected, Pilot Ignited,

Heavy Duty Natural Gas Engine with EGR. *SAE*, (2003-01-3089), 2003.
→ pages 41, 100, 133, 139

- [100] G. P. McTaggart-Cowan, W. K. Bushe, S. N. Rogak, P. G. Hill, and S. R. Munshi. PM and NO_x reduction by injection parameter alterations in a direct injected, pilot ignited, heavy duty natural gas engine with EGR at various operating conditions. *SAE*, (2005-01-1733), 2005. → pages 41, 152, 194
- [101] S. S. Merola and B. M. Vaglieco. Optical investigations of fuel deposition burning in ported fuel injection (PFI) spark-ignition (SI) engine. *Energy*, 34(12):2108–2115, 2009. → pages 22, 23, 24, 25
- [102] T. I. Mohamad, A. Yusoff, S. Abdullah, M. Jermy, M. Harrison, and H. H. Geok. The combustion and performance of a converted direct injection compressed natural gas engine using spark plug fuel injector. *SAE*, (2010-32-0078), 2010. → page 7
- [103] I. Mudway and F. Kelly. Ozone and the lung: a sensitive issue. *Molecular Aspects of Medicine*, 21(1):1 – 48, 2000. → page 10
- [104] C. J. Mueller and G. C. Martin. Effects of oxygenated compounds on combustion and soot evolution in a di diesel engine:broadband natural luminosity imaging. *SAE*, (2002-01-1631):1–20, 2002. → pages 20, 21
- [105] U. Muller. *Reduzierter Reaktionsmechanismen fur die Zundung von n-Heptan und iso-Oktan unter motorrelevanten Bedingungen*. Phd dissertation, RWTH-Aachen, 1993. → page 24
- [106] T. Muruganandam, B.-H. Kim, M. Morrell, V. Nori, M. Patel, B. Romig, and J. Seitzman. Optical equivalence ratio sensors for gas turbine combustors. *Proceedings of the Combustion Institute*, 30(1):1601 – 1609, 2005. → page 22
- [107] M. P. Musculus, J. E. Dec, and D. R. Tree. Effects of Fuel Parameters and Diffusion Flame Lift-Off on Soot Formation in a Heavy-Duty DI Diesel Engine. *SAE*, (2002-01-0889), 2002. → page 27
- [108] M. P. Musculus, S. Singh, and R. D. Reitz. Gradient Effects on Two-Color Soot Optical Pyrometry in a Heavy-Duty DI Diesel Engine. *Combustion and Flame*, 153(1-2):216–227, 2008. → pages 21, 30, 31, 45, 147

- [109] M. P. B. Musculus. Multiple simultaneous optical diagnostic imaging of early-injection low-temperature combustion in a heavy-duty diesel engine. *SAE*, (2006-01-0079), 2006. → page 20
- [110] M. Nesbit, M. Fergusson, A. Colsa, J. Ohlendorf, C. Hayes, K. Paquel, and J.-P. Schweitzer. Comparative study on the differences between the eu and us legislation on emissions in the automotive sector, 2016. → page 11
- [111] J. Nocedal and S. J. Wright. *Numerical Optimization*. Springer Series in Operations Research and Financial Engineering. Springer, New York, 2nd ed. edition, 2006. → page 95
- [112] P. Ouellette, D. Goudie, and G. McTaggart-Cowan. Progress in the development of natural gas high pressure direct injection for Euro VI heavy-duty trucks. In J. Liebl and C. Beidl, editors, *Internationaler Motorenkongress 2016: Mit Konferenz Nfz-Motorentechnologie*, pages 591–607. Springer Fachmedien Wiesbaden, Wiesbaden, 2016. → pages 8, 41, 43, 45, 158
- [113] P. Ouellette and P. Hill. Turbulent transient gas injections. *Journal of Fluids Engineering*, 122(4):743–752, 2000. → page 148
- [114] P. Ouellette, P. L. Mtui, and P. G. Hill. Numerical simulations of directly injected natural gas and pilot diesel fuel in a two-stroke compression ignition engine. *SAE*, (981400), 1998. → pages 41, 195
- [115] R. Papagiannakis and D. Hountalas. Experimental investigation concerning the effect of natural gas percentage on performance and emissions of a dual fuel diesel engine. *Applied Thermal Engineering*, 23(3):353 – 365, 2003. → page 43
- [116] B. D. Patychuk. *Particulate matter emission characterization from a natural-gas high-pressure direct-injection engine*. PhD thesis, University of British Columbia, 2013. → page 7
- [117] F. Payri, J. V. Pastor, J. M. García, and J. M. Pastor. Contribution to the Application of Two-Colour Imaging to Diesel Combustion. *Measurement Science and Technology*, 18(8):2579–2598, 2007. → pages 30, 31, 57, 58, 111
- [118] R. Pearce and A. Gaydon. *Identification of Molecular spectra*. Routledge publishers, London, 4th ed. edition, 1976. → page 23

- [119] J. A. Pinson, T. Ni, and T. A. Litzinger. Quantitative Imaging Study of the Effects of Intake Air Temperature on Soot Evolution in an Optically-Accessible D.I. Diesel Engine. *SAE*, (942044), 1994. → page 27
- [120] C. Potera. Air pollution: Salt mist is the right seasoning for ozone. *Environmental Health Perspectives*, 116:A288, 2008. → page 8
- [121] M. Powell. A Fortran Subroutine for Solving Systems of Nonlinear Algebraic Equations. In P. Rabinowitz, editor, *Numerical methods for nonlinear algebraic equations*, page 199. Gordon and Breach Science Publishers, 1970. → page 95
- [122] W. H. Press, S. A. Teukolsky, W. T. Vetterling, and B. P. Flannery. *Numerical Recipes in FORTRAN : the Art of Scientific Computing*. Cambridge University Press, New York, 1993. → page 95
- [123] R. Price, I. Hurle, and T. Sugden. Optical studies of the generation of noise in turbulent flames. *Symposium (International) on Combustion*, 12(1):1093 – 1102, 1969. → page 23
- [124] J. Rochussen. *Thermodynamic and Optical Investigation of the Combustion Mechanisms of Diesel-Ignited Dual-Fuel Natural Gas Combustion*. Masters dissertation, University of British Columbia, 2015. → pages 37, 50, 71
- [125] J. Rochussen and P. Kirchen. Characterization of reaction zone growth in an optically accessible heavy-duty diesel/methane dual-fuel engine. *International Journal of Engine Research*, 0(0):1468087418756538, 2018. → page 122
- [126] J. Rochussen and P. Kirchen. Parametric study of pilot-ignited direct-injection natural gas combustion in an optically-accessible heavy-duty engine. *International Journal of Engine Research*, 0(0):1–20, 2019. → pages 117, 122, 124, 141, 142, 143, 146, 149, 152, 154, 161, 221
- [127] J. Rochussen, J. Yeo, and P. Kirchen. Effect of fueling control parameters on combustion and emissions characteristics of diesel-ignited methane dual-fuel combustion. *SAE*, (2016-01-0792), 2016. → pages 37, 73, 74, 75, 79, 83, 84, 90
- [128] J. Rochussen, J. Son, J. Yeo, M. Khosravi, P. Kirchen, and G. McTaggart-Cowan. Development of a Research-Oriented Cylinder Head with Modular Injector Mounting and Access for Multiple In-Cylinder Diagnostics. *SAE*, (2017-24-0044), 2017. → pages 63, 64, 174

- [129] A. M. Rothrock. Photographic study of combustion in compression-ignition engine. *SAE*, (340094):203–211, 1934. → page 20
- [130] B. Sahoo, N. Sahoo, and U. Saha. Effect of engine parameters and type of gaseous fuel on the performance of dual-fuel gas diesel engines—a critical review. *Renewable and Sustainable Energy Reviews*, 13(6):1151 – 1184, 2009. → pages 36, 37
- [131] J.-M. SAMANIEGO, F. N. EGOLFOPOULOS, and C. T. BOWMAN. Co₂* chemiluminescence in premixed flames. *Combustion Science and Technology*, 109(1-6):183–203, 1995. → page 23
- [132] A. Sarvi, J. Lyyräinen, J. Jokiniemi, and R. Zevenhoven. Particulate emissions from large-scale medium-speed diesel engines: 1. particle size distribution. *Fuel Processing Technology*, 92(10):1855 – 1861, 2011. → pages 9, 10
- [133] S. Schlatter, B. Schneider, Y. Wright, and K. Boulouchos. Experimental study of ignition and combustion characteristics of a diesel pilot spray in a lean premixed methane/air charge using a rapid compression expansion machine. *SAE*, (2012-01-0825), 2012. → pages 16, 34, 38, 39, 44, 86, 89, 90, 91
- [134] J. Seinfeld and S. Pandis. *Atmospheric Chemistry and Physics: From Air Pollution to Climate Change*. Wiley, 2011. → page 9
- [135] J. S. Shakal and J. K. Martin. Imaging and Spatially Resolve Two-Color Temperature Measurements Through a Coherent Fiberoptic: Observation of Auxiliary Fuel Injection Effects on Combustion in a Two-Stroke DI Diesel. *SAE*, (940903), 1994. → page 18
- [136] S. Singh, R. D. Reitz, and M. P. Musculus. 2-Color Thermometry Experiments and High-Speed Imaging of Multi-Mode Diesel Engine Combustion. *SAE*, (2005-01-3842), 2005. → pages 21, 30, 33, 34, 45, 158, 159
- [137] H. A. Stadler, M. Förster, and R. Kneer. Experimental investigation of ch-chemiluminescence in an oxyfuel flame. In *3rd European Combustion Meeting : ECM 2007, Chania, Crete, Greece 11 - 13 April 2007 ; proceedings / Mediterranean Agronomic Institute of Chania. Combustion Institute Greek Section*, Chania, 2007. MAICh. → pages 22, 23

- [138] A. Starikovskiy and N. Aleksandrov. Plasma-assisted ignition and combustion. *Progress in Energy and Combustion Science*, 39(1):61 – 110, 2013. → page 7
- [139] R. R. Steeper and E. J. Stevens. Characterization of combustion, piston temperatures, fuel sprays, and fuel-air mixing in a disi optical engine. *SAE*, (2000-01-2900), 2000. → page 46
- [140] B. D. Stojkovic, T. D. Fansler, M. C. Drake, and V. Sick. High-speed imaging of OH* and soot temperature and concentration in a stratified-charge direct-injection gasoline engine. *Proceedings of the Combustion Institute*, 30 II(2):2657–2665, 2005. → pages 21, 22, 23
- [141] K. I. Svensson, A. J. Mackrory, M. J. Richards, and D. R. Tree. Calibration of an RGB, CCD Camera and Interpretation of its Two-Color Images for KL and Temperature. *SAE*, (2005-01-0648), 2005. → page 31
- [142] M. Taschek, P. Koch, J. Egermann, and A. Leipertz. Simultaneous optical diagnostics of hsdiesel combustion processes. *SAE*, (2005-01-3845): 1–13, 2005. → pages 19, 21, 24
- [143] H. Tian. *Noise Analysis in CMOS Image Sensors*. Phd dissertation, Stanford University, 2000. → page 103
- [144] C. Tighe, M. Twigg, A. Hayhurst, and J. Dennis. The kinetics of oxidation of diesel soots by no₂. *Combustion and Flame*, 159(1):77 – 90, 2012. → page 9
- [145] C. Tornatore, S. Merola, and P. Sementa. Combustion Process Investigation in a Small SI Engine using Optical Diagnostics. *SAE*, (2010-01-2262), 2010. → pages 22, 23
- [146] D. R. Tree and J. E. Dec. Extinction Measurements of in-Cylinder Soot Deposition in a Heavy-Duty DI Diesel Engine. *SAE*, (2001-01-1296), 2001. → pages 26, 27
- [147] D. R. Tree and K. I. Svensson. Soot Processes in Compression Ignition Engines. *Progress in Energy and Combustion Science*, 33(3):272–309, 2007. → pages 26, 27, 28, 29, 31, 32
- [148] K. Walsh, M. Long, M. Tanoff, and M. Smooke. Experimental and computational study of ch*, ch*, and oh* in an axisymmetric laminar diffusion flame. *Symposium (International) on Combustion*, 27(1):615 –

623, 1998. Twenty-Seventh Symposium (International) on Combustion
Volume One. → page 24

- [149] M. Walsh. *Mobile Source Related Air Pollution: Effects on Health and the Environment*, pages 803–809. Elsevier, 12 2011. → page 10
- [150] F. Wang, J. B. Liu, J. Sinibaldi, C. Brophy, A. Kuthi, C. Jiang, P. Ronney, and M. A. Gundersen. Transient plasma ignition of quiescent and flowing air/fuel mixtures. *IEEE Transactions on Plasma Science*, 33(2):844–849, 2005. → page 7
- [151] X. Wang, D. Westerdahl, J. Hu, Y. Wu, H. Yin, X. Pan, and K. M. Zhang. On-road diesel vehicle emission factors for nitrogen oxides and black carbon in two chinese cities. *Atmospheric Environment*, 46:45 – 55, 2012. → page 9
- [152] J. Warnatz, U. Maas, and R. Dibble. *Combustion; Physical and Chemical Fundamentals, Modeling and Simulation, Experiments, Pollutant Formation*. Springer, Berlin, Germany, 2006. → page 7
- [153] C. S. Weaver and S. H. Turner. Dual fuel natural gas/diesel engines: Technology, performance, and emissions. *SAE*, (940548), 1994. → pages 7, 36, 40
- [154] L. Wei and P. Geng. A review on natural gas/diesel dual fuel combustion, emissions and performance. *Fuel Processing Technology*, 142:264 – 278, 2016. → pages 36, 43
- [155] J. Yan and G. L. Borman. Analysis and in-cylinder measurement of particulate radiant emissions and temperature in a direct injection diesel engine. *SAE*, (881315), 1988. → pages 17, 64, 65
- [156] J. Yeo. *Development and application of in-cylinder fuel concentration and pyrometry optical diagnostic tools in diesel-ignited dual-fuel natural gas engines*. Masters dissertation, University of British Columbia, 2017. → pages 49, 50, 63, 64, 65, 66, 67, 142, 184
- [157] A. I. Zayed. Weierstrass Transform. In *Handbook of function and generalized function transformations*, chapter 18, page 643. CRC Press, Boca Raton, FL, 1996. → page 108
- [158] K. Zha, R.-C. Florea, and M. Jansons. Soot Evolution With Cyclic Crank-Angle-Resolved Two-Color Thermometry in an Optical Diesel

Engine Fueled With Biodiesel Blend and ULSD. *Journal of Engineering for Gas Turbines and Power-Transactions of the Asme*, 134(9):1–7, 2012. → pages 30, 31, 35, 36, 57, 58

- [159] J. Zhang, W. Jing, and T. Fang. High speed imaging of OH* chemiluminescence and natural luminosity of low temperature diesel spray combustion. *Fuel*, 99:226–234, 2012. → pages 16, 24, 118
- [160] J. Zhang, W. Jing, W. L. Roberts, and T. Fang. Soot Temperature and KL Factor for Biodiesel and Diesel Spray Combustion in a Constant Volume Combustion Chamber. *Applied Energy*, 107:52–65, 2013. → pages 30, 31, 57, 58
- [161] Q. Zhang, Y. Gong, Q. Guo, X. Song, and G. Yu. Experimental study on ch* chemiluminescence characteristics of impinging flames in an opposed multi-burner gasifier. *AIChE Journal*, 63(6):2007–2018, 2017. → page 25
- [162] H. Zhao and N. Ladommatos. Optical Diagnostics for Soot and Temperature Measurement in Diesel Engines. *Progress in Energy and Combustion Science*, 24(3):221–255, 1998. → pages 26, 28, 30, 31, 147
- [163] P. Zoldak, J. John Joseph, W. Shelley, J. Johnson, and J. Naber. Characterization of partially stratified direct injection of natural gas for spark-ignited engines. *SAE*, (2015-01-0937), 2015. → page 7

Appendix A

High-Speed Imaging System Considerations

The design of the CMOS (complementary metal-oxide-semiconductor) sensors, with each photodiode being paired with an amplifier, making each pixel a separate light detection unit, allows high frame rates of 4,800 and 5,400 frames-per-second (fps) at the full resolution for the Phantom V7.1 and Photron SA-1 cameras used in this work, respectively. This is in contrast with the CCD (charged-coupled device) sensors, where one or more amplifiers are located at the edges of the sensor to read out the pixel charges successively, making the process slower and more energy demanding.

The combination of the camera sensor resolution and the focal length of the objective lens, determines the stand-off distance of the camera from the combustion chamber to maximize the recorded image resolution and spatial information. The maximum frame rate of the camera, on the other hand, is determined by the adjustable pixel resolution. Therefore, the final resolution of the camera sensor, and consequently the recorded image, are reduced to allow recording images at higher frame rates than the maximum values at the full resolution and reach higher temporal resolutions of 0.25-0.5 CAD/frame. Managing the amount of light reaching the camera sensor is the other important camera setting and the only way to physically control the SNR (as opposed to the image post-processing considerations). It is worth noting here that the commonly used ISO setting in photography as a

means to adjust the “sensitivity” of the the sensor is merely adjusting the dynamic range of the output image through applying a post-senor gain to the signal from the sensor. The sensitivity of the sensor is constant and determined by the quantum efficiency of the CMOS photodiode arrays. The amount of light reaching the camera sensor is controlled by the camera exposure duration and the lens aperture. The exposure duration in scientific high-speed CMOS cameras, such as the ones used in this work, is tightly controlled by the high shutter rates of $\sim 1 \mu\text{sec}$, afforded by the on-chip global electronic shutter design. This shutter rate also defines the lower limit for the possible exposure duration settings. The upper limit for exposure duration is determined by the image recording frame rate (i.e., the interval of two consecutive image frames), which can be reached at lower light intensity cases, leaving the lens aperture the only sensor exposure control factor.

To present an estimate of the range of light intensities to expect on the imaging system, a natural luminosity imaging (with no spectral/neutral density filters) of a low-load diesel combustion, using the HPDI injector, nearly saturated the sensor of the Phantom camera (ISO: 4,800) at $10 \mu\text{sec}$ exposure duration and $f/5.6$ lens aperture setting.

Images of a rapid phenomena captured by the high-speed cameras are usually stored on the internal memory of the camera, referred to as the camera buffer, limiting the number of image frames that can be recorded for the incident. As a result, partitioning capabilities are considered in the camera system design to optimize the use of the limited camera buffer and minimize “empty” frames captured before and after the phenomena of interest. The V7.1 Phantom camera used in the current work provided up to 15 partitions, accommodating image sequences from 15 individual combustion cycles to examine cycle-to-cycle variability and for ensemble averaging purposes.

Appendix B

Ensemble Averaging of Results vs. Raw signal

The spatially resolved two-color pyrometry results presented in this work were acquired from application of the two-color pyrometry algorithm on the ensemble average raw image frames at each crank position (SNR enhancement approach). As depicted in Figure B.1, ensemble averaging of the two-color pyrometry results instead would lead to inaccurate temperature estimations due to cycle-to-cycle variability effects on distribution of the soot cloud signal and “0” values. The unresolved regions within individually resolved 2D two-color pyrometry results is caused by missing incandescent soot cloud signal, low SNR signal below the detection limit of the current imaging system, method imperfections, or a combination of these factors.

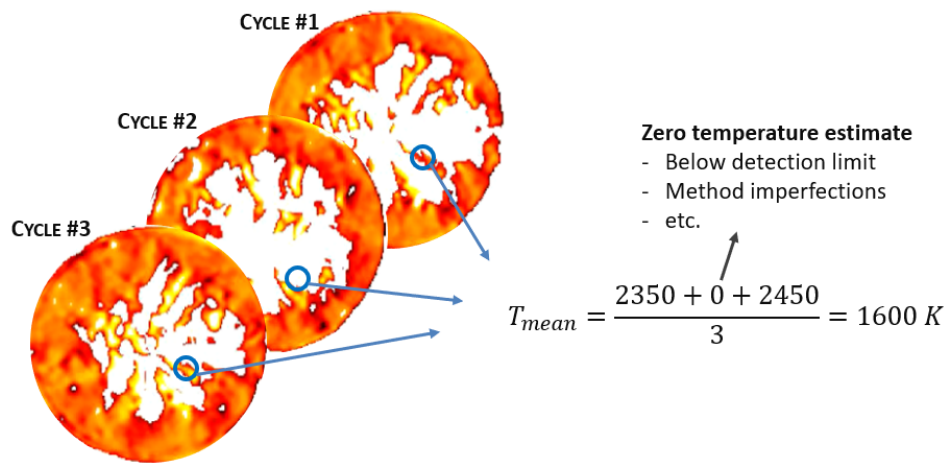


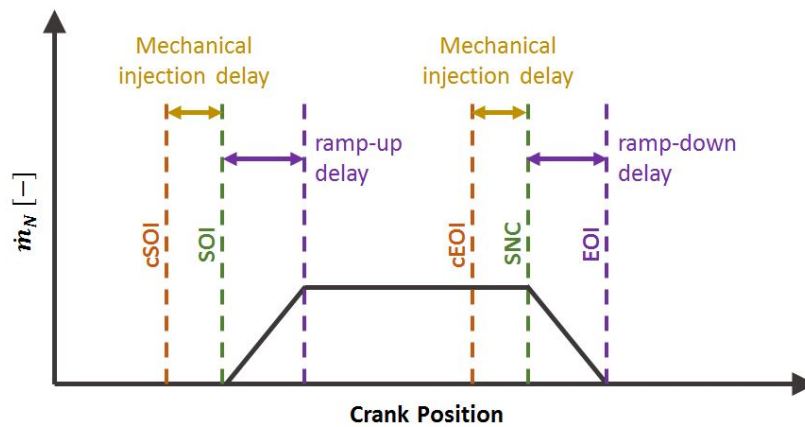
Figure B.1: Effect of ensemble averaging on the two-color pyrometry temperature distributions instead of using it as a SNR enhancement approach for the raw data

Appendix C

PIDING Fuel Injection Profile

The estimated fuel injection profiles for PIDING combustion are presented in Figure C.1. The pulse magnitudes are presented in terms of estimated mass flow rates normalized by the baseline value (see Table 6.1).

cSOI: command of start of injection **SOI:** start of injection
cEOI: command of end of injection **SNC:** start of needle closing
EOI: end of injection



$$\dot{m}_N = \frac{\dot{m}_i}{\dot{m}_{NG@Baseline}} ; i = \text{Operating condition under consideration}$$

Figure C.1: Estimated PIDING fuel injection profile. Mechanical injection delay was estimated through illuminated combustion chamber optical measurements and needle ramp-up and ramp-down timings were estimated in a previous work [37]

Appendix D

Optical and Thermodynamic Ignition Delays

The optical and thermodynamic ignition delay (τ_{ign}) values for the operating points described in Table 6.1 can be compared in Table D.1. The optical ignition delays were evaluated in this work based on the first indication of the OH*-CL signal in 2D measurements. A single frame delay was considered for all optical ignition delay values in order to ensure distinguishing between the OH*-CL signal from pilot combustion vs. NG ignition. The absolute values of the optical ignition delay is dependant on the optical imaging settings. The thermodynamic ignition delays for the considered operating conditions were evaluated in conceptual combustion mode analysis of the same campaign [126]. Comparison of the ignition delay values in this table shows consistent influence trends for the considered PIDING fueling parameter sweeps.

Table D.1: Comparison of optical and thermodynamic ignition delays for operating points described in Table 6.1

Point	Pilot τ_{ign} [CAD]		NG τ_{ign} [CAD]	
	Optical	Thermo.	Optical	Thermo.
Baseline	13	8.2	10	7.0
Short GPW	13	8.2	10	7.0
Long GPW	13	8.2	10	7.0
Short RIT	11.5	6.8	12.5	9.2
Long RIT	16	10.9	10.5	6.9
Negative RIT	13	8.5	19-22	19.8
High P_{inj}	12	7.0	10	5.7
Low P_{inj}	15	10.3	11.5	8.7

Appendix E

NG Jet Momentum Reflection Effects

Following the formation and merging of the initial soot pockets to form a toroidal soot cloud, it grows towards the central bowl region (see §6.2.1). Small high concentration soot pockets, depicted as black regions in KL factor distributions of Figure E.1, can be traced during this process. This phenomenon reveals that advection effects due to the reflected NG jets momentum after impingement is a contributing factor in soot cloud growth process, in addition to the continued formation and accumulation effects.

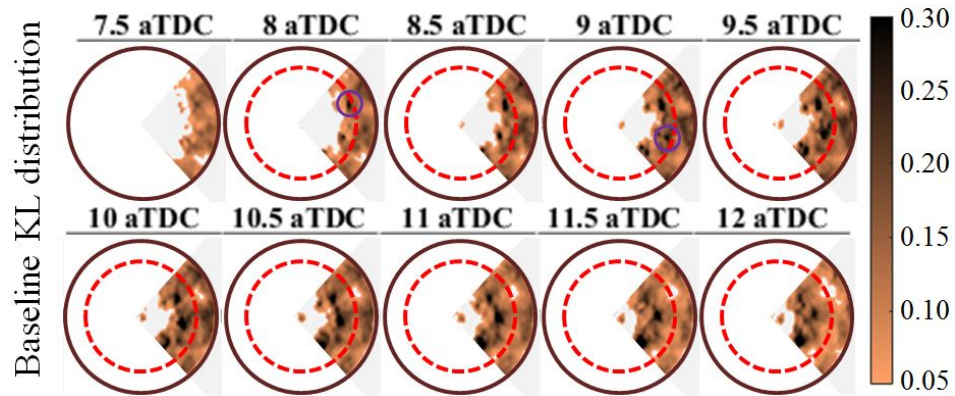


Figure E.1: Soot cloud advection effects with reflected NG jet momentum after impingement onto the walls. Image frames show KL factor distribution from the baseline operating condition described in Table 6.1

Appendix F

Mean Soot Cloud Growth Rate

2D two-color pyrometry temperature distributions, shown in Figure F.1, were used to evaluate soot cloud growth rates. The mean soot cloud growth rate was calculated based on 1000 rpm engine speed and the crank position after onset of soot signal (CAD aOS) where the soot cloud front (R_{SCF}) reaches a marked (imaginary) ring with a radius equal to 30% of the visible bowl radius (83 mm). Note that at 0 CAD aOS initial soot cloud pockets are adjacent to the wall ($R_{SCF,0} = R_{bowl}$)

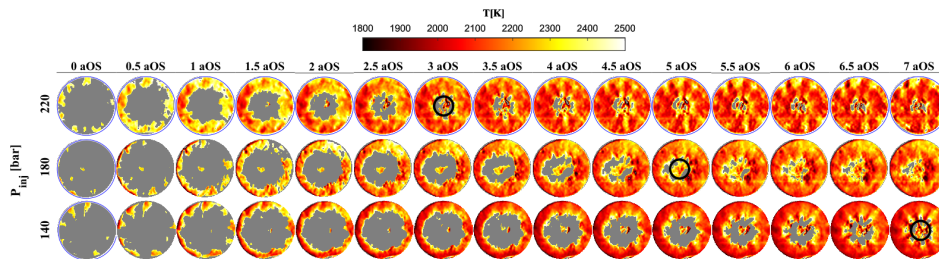


Figure F.1: The influence of P_{inj} on 2D two-color pyrometry temperature distribution. The crank positions are relative to onset of soot signal and the black rings mark 30% visible bowl radius (see Table 6.1 for operating point specifications)

Appendix G

Ensemble Averaging of Results vs. Raw signal

Alternative approaches towards application of the weighted spatial averaging function on the 2D two-color pyrometry results are illustrated in Figure G.1. The corresponding WSA results from these approaches for the long GPW operating condition described in Table 7.1 are compared in Figure G.2. Temperature values reported are restricted to the range where the mean KL factor is higher than 0.025, which is ~5% of the peak KL value. It is clear from this figure that the EWP approach leads to incorrect temperature and KL factor results. The WPE, WEP, EPW approaches lead to very similar results before late cycles stage at >40 CAD aTDC. Similar to the probe results, WPE and WEP approaches lead show a drop in temperature values during the late-cycle stage and the KL signal does not reduce to near zero values as it does for the PWE and EPW approaches. The KL factor values for this and other investigated operating conditions show closer agreement with the results acquired using the PWE approach.

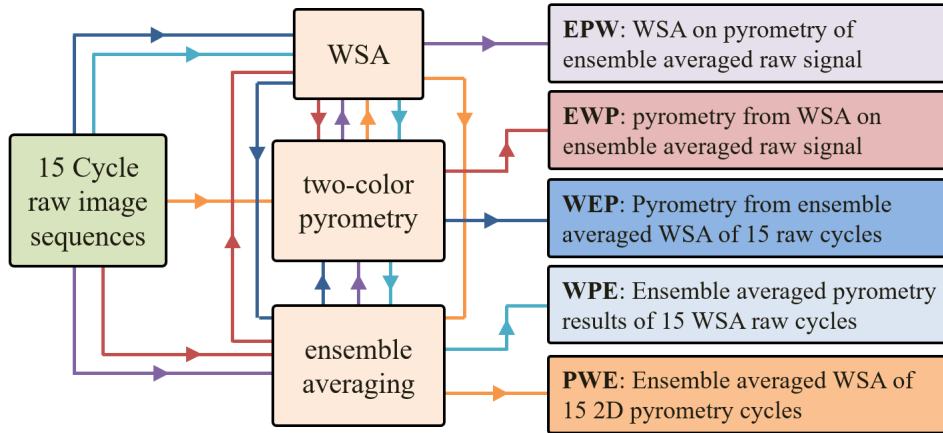


Figure G.1: Alternative WSA procedures flowchart

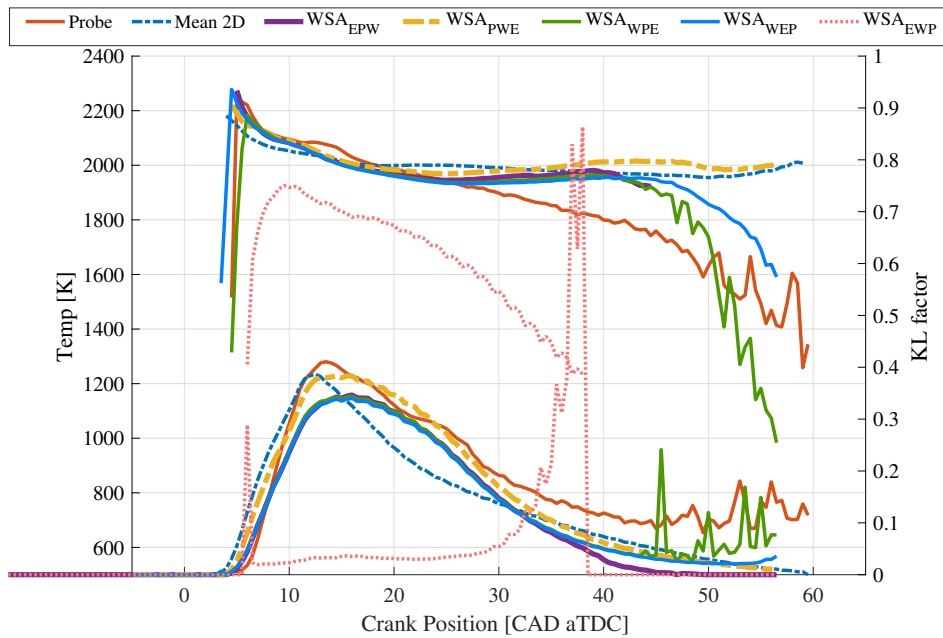


Figure G.2: Alternative WSA procedures; Sample results on long GPW operating point in Table 7.1

Appendix H

Radiation Heat Loss through Quartz Window

In the absence of the quartz window in the all-metal engine, lower radiation heat losses can be thought as a contributing factor for higher estimated in-cylinder temperatures. A simplified radiation heat loss model for comparison of the two engine configurations is shown in Figure H.1, which suggests a 45% lower heat loss in the all-metal engine.

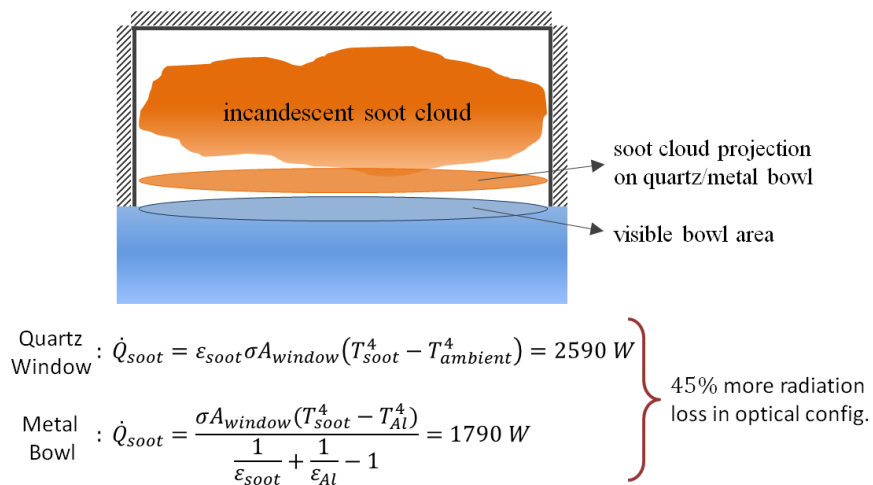


Figure H.1: A simplified radiation heat loss model for comparison of the two engine configurations